ESTIMATION OF MECHANOPATHOLOGICAL PARAMETERS USING ULTRASOUND POROELASTOGRAPHY

A Dissertation

by

MD TAUHIDUL ISLAM

Submitted to the Office of Graduate and Professional Studies of
Texas A&M University
in partial fulfillment of the requirements for the degree of

DOCTOR OF PHILOSOPHY

Chair of Committee,	Raffaella Righetti
Committee Members,	Steve Wright
	Jun Zou
	J. N. Reddy
Head of Department,	Miroslav M. Begovic

December 2018

Major Subject: Electrical Engineering

ABSTRACT

Mechanical microenvironment of cancerous tumors plays an important role in the growth, metastasis and treatment of the tumors. Elevated interstitial fluid pressure (IFP) is an important component of the mechanical microenvironment of the tumor and a mechanopathological parameter of great clinical significance. Interstitial and vascular permeabilities are two other mechanopathological parameters of soft tissues that are clinically relevant and can provide useful information for cancer diagnosis and prognosis. There are a few invasive techniques that can measure IFP and the interstitial and vascular permeabilities in tissues but no non invasive imaging techniques that can assess or quantify them. In this dissertation, I propose novel, non invasive techniques based on ultrasound poroelastography, which can image these mechanopathological parameters in cancers in vivo. To achieve the goal, I developed analytical models, novel strain estimation techniques and reconstruction method for estimating the Young's modulus and Poisson's ratio of tumors and normal tissues. I applied my techniques on a few treated and untreated mice in a small in vivo study. The reconstructed IFP, interstitial permeability and vascular permeability were found to increase in untreated tumors with time, whereas to decrease or remain almost same in treated tumors with time. These results correlate with the results available in the literature. Based on the importance of the IFP, interstitial and vascular permeability in diagnosis, prognosis and treatment of cancers, the proposed methodology may keep important impact in quantitative cancer imaging.

DEDICATION

To my ever caring aunt (‘fufu’) and uncle (‘fufa’) whose inspirations are behind my every success.

ACKNOWLEDGMENTS

First of all, I would like to thank my committee chair Dr. Raffaella Righetti for her support, encouragement, guidance and useful suggestions throughout this research work. The discussions we had and her constructive comments and ideas not only helped me to complete the thesis, but also gave me a new perspective for my future career. She supported me both in my good and bad times and never gave me the chance to feel demotivated through her inspiration and motivation.

I would also like to thank the rest of the members of my dissertation committee: Dr. Steve Wright, Dr. Jun Zou and Dr. J. N. Reddy for their encouragement and insightful comments. Dr. Reddy's comments on the theoretical and finite element methods of biomechanics were priceless to solve many of the problems in this thesis. I thank him for his valuable time and patience to my ignorance.

I would thank Dr. Anuj Chaudhry for his constant support and Songyuan for helping with experimental data collection. I also thank Dr. Ennio Tasciotti and his team at Houston Methodist Research Institute for helping with the animal data collection.

I would also like to thank my thesis supervisors in undergraduate and Master's studies: Dr. Md. Kamrul Hasan and Dr. Celia Shahnaz. Without their guidance, it was never possible for me to come this far to pursue my dream.

My acknowledgments will be incomplete without the final word of gratitude to my aunt and uncle who have been always the wind beneath my wings. Thanks to my parents and other family members for their constant motivation and support. I would also like to thank my roommate Sajib Saha, who was a true friend and guide throughout my doctoral study.

CONTRIBUTORS AND FUNDING SOURCES

Contributors

This work was supported by a dissertation committee consisting of Professors Dr. Raffaella Righetti, Dr. Steve Wright and Dr. Jun Zou of the Department of Electrical and Computer Engineering and Professor Dr. J. N. Reddy of the Department of Mechanical Engineering.

All work conducted for the dissertation was completed by the student independently.

Funding Sources

Graduate study of Md Tauhidul Islam was partially funded by the U.S. Department of Defense grants W81XWH-18-1-0544 (BC171600) and W81XWH-15-1-0718.

NOMENCLATURE

E_b	Young's modulus of background
E_i	Young's modulus of inclusion
H_{Ab}	aggregate modulus of background
H_{Ai}	aggregate modulus of inclusion
ν_b	Poisson's ratio of background
ν_i	Poisson's ratio of inclusion
k_b	interstitial permeability of background
k_i	interstitial permeability of inclusion
χ_b	microfiltration coefficient of background
χ_i	microfiltration coefficient of inclusion
p_b	fluid pressure inside background
p_i	fluid pressure inside inclusion
C_b	gel diffusion constant of background
C_i	gel diffusion constant of inclusion
γ_f	volumetric weight of the pore fluid
J_n	Bessel function of first kind of order n
I_n	modified Bessel function of first kind of order n
Y_n	Bessel function of second kind of order n

TABLE OF CONTENTS

Page

LIST OF FIGURES

FIGURE Page

LIST OF TABLES

TABLE Page

1. INTRODUCTION

1.1 Background of ultrasound elastography

Ultrasonography is a widely used imaging technique for its ease of use, real-time capability, portability and low-cost in comparison to other imaging modalities available such as MRI, CT etc [1]. Based on the propagation of ultrasound waves inside tissues, this imaging technique can reconstruct the morphology of human organs. However, this modality does not provide quantitative estimates of the mechanical properties of tissue, which are important in diagnosis of different diseases such as cancer.

Ultrasound elastography is an imaging modality used for assessing the mechanical properties of biological tissues in numerous clinical applications [2–5]. This methodology originated in the early 1990s [2] and, over the past few decades, different elastographic techniques have been developed. These include both quasi-static elastography and dynamic elastography techniques, which typically rely on shear wave propagation [1].

In quasi-static elastography, the local strains experienced by a tissue due to an external quasi-static compression are imaged with the intent of obtaining information about the tissues' pathology [2, 3]. Quasi-static ultrasound has the advantage of being inexpensive, portable and easily implementable in diagnostic ultrasound systems. This imaging modality is being widely used for diagnosis and prognosis of different diseases such as breast cancer, prostate cancer and others [6,7].

In dynamic elastography, a time-varying force is applied to the tissue, which can be either a short transient mechanical force or an oscillatory force with fixed frequency. The time-varying mechanical force creates either a compressional wave, which is very fast (~ 1500 ms^{-1}) or a shear wave, which is relatively slow ($1 - 50$ ms^{-1}) in solid materials. The speed of the shear wave can be determined by computing the displacements of ultrasound speckles in tissue caused by the shear wave propagation, which in turn can be used to estimate the shear modulus of tissue ($\mu = \rho V_s^2$), where ρ is the density of soft tissue (~ 1000 kgm^{-3}) and V_s is the speed of the shear wave. In

shear wave imaging techniques, the tissue is assumed to be incompressible, and the stiffness of the tissue is estimated in terms of Young's modulus (as 3 times the shear modulus).

1.2 Physics principles in quasi-static elastography

Quasi-static elastography techniques rely on a common protocol: acquire pre-compressed radio-frequency (RF) data from a sample, apply a compression to it, record post-compressed RF data and compute the induced axial and/or lateral strain from the pre-compressed and post-compressed RF data. An elastography experiment has been shown in Fig. 1.1, where we see that two sets of data are acquired in elastography experiments. The first set is before applying any compression to the sample (pre-compression) and the second set is acquired after application compression (post-compression). The induced strain in tissue then can be computed by correlating these two sets of data. Two elastic mechanical parameters, i.e., Young's modulus and Poisson's ratio can be determined from the applied compression and strain data. In the assumption that the tissue behaves as a linear elastic material, the applied stress σ_y and induced strain ϵ_y can be related using the following equation

$$\sigma_y = E \cdot \epsilon_y, \tag{1.1}$$

where E is the Young's modulus of the elastic material. The stress-strain relationship in a linear elastic material is shown in Fig. 1.2. The induced lateral and axial strain can be related as

$$\epsilon_x = -\nu \epsilon_y, \tag{1.2}$$

where ν is the Poisson's ratio of the material.

1.3 Physics principles in ultrasound poroelastography

Poroelastography is an elastographic technique, which is based on the same principles of quasi-static elastography in terms of wave propagation but focuses on the estimation of the temporal response of tissues to sustained compressions [8, 9]. In poroelastography, a tissue is modeled as

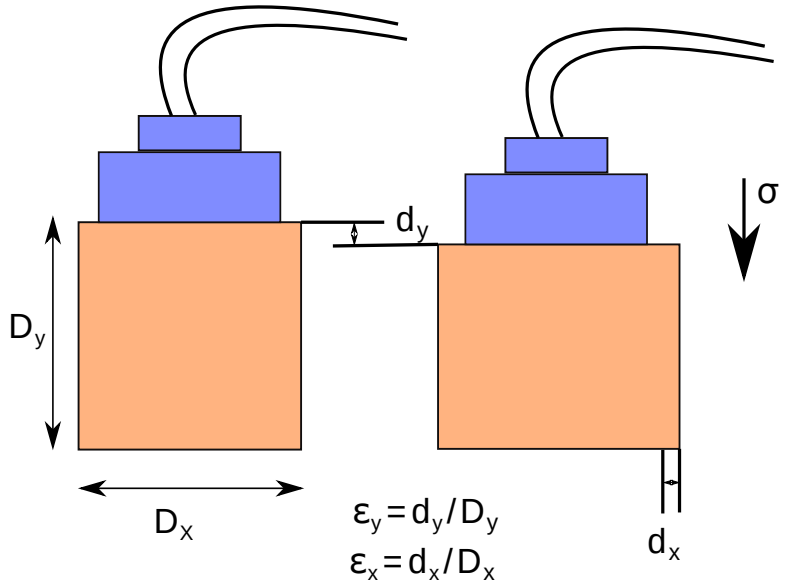

Figure 1.1: Elastography experiment

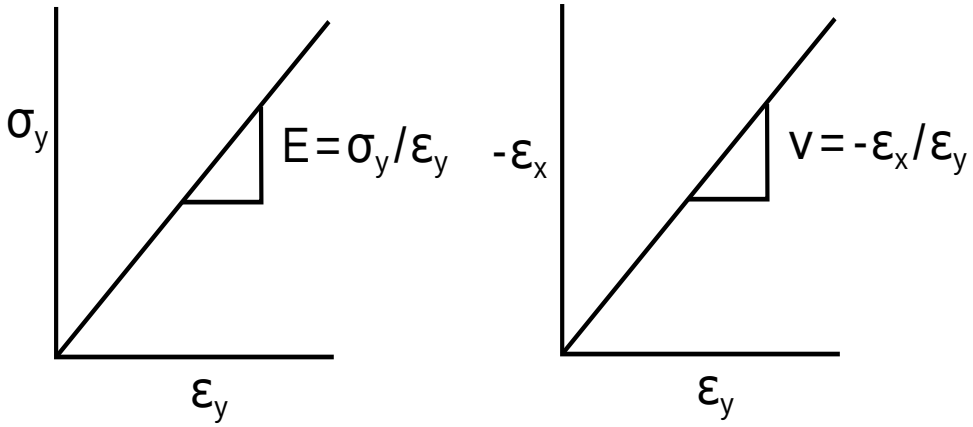

Figure 1.2: Stress-strain relationship in elastography

a poroelastic compressible material. Poroelastic materials are solid structures comprised of pores filled with fluid, and their deformation depends on the applied load as well as the fluid flow inside the pores. The motivation at the basis of the development of poroelastography is that underlying pathologies such as cancers and lymphedema affect the established interstitial pressure gradients. These, in turn, alter the tissue's fluid content and flow patterns [10, 11] and, consequently, its poroelastic response to a uniaxial sustained compression. Poroelastography techniques aim at

imaging the time-dependent behavior of the local axial strains and the lateral-to-axial strain ratios, also referred to as effective Poisson's ratio (EPR) [8, 9, 12, 13].

A block diagram for a poroleastography experiment is shown in Fig. 1.3. In this figure, we see that in a poroleastography experiment, a number of RF datasets are acquired with time, while the tissue is under compression. The axial and lateral strains computed from these RF datasets result in strains, which are time-varying in nature.

The equation for the lateral strain in a uniform cylindrical poroelastic sample can be written as [14, 15]

$$\epsilon_{rr}(r,t) = -\frac{\sigma_0}{E}\left[\frac{1-2\nu}{2} + \frac{(1+\nu)(1-2\nu)}{1-\nu}\sum_{n=1}^{\infty}\frac{J_0(\alpha_n\frac{r}{a}) - \frac{J_1(\alpha_n\frac{r}{a})}{\alpha_n\frac{r}{a}}}{\frac{1+\nu}{1-\nu}J_0(\alpha_n) - \frac{3}{2}\alpha_n J_1(\alpha_n)}\exp(-\frac{\alpha_n^2 H_A k t}{a^2})\exp(-H_A\chi t)\right] - \frac{\epsilon_{zz}(t)}{2}, \tag{1.3}$$

where H_A, k and χ are the aggregate modulus, interstitial permeability and vascular permeability of the poroelastic material. Here α_n are the roots of the characteristics function, $C_0(x) = J_0(x) - \frac{4(1-2\nu)}{3(1-\nu)}\frac{J_1(x)}{x} = 0$. We can write the time domain expression of the axial strain as [14, 15]

$$\epsilon_{zz}(t) = -\frac{\sigma_0}{E}\left[1 + 2(1+\nu)\sum_{n=1}^{\infty}\frac{J_0(\alpha_n) - \frac{1-2\nu}{1-\nu}\frac{J_1(\alpha_n)}{\alpha_n}}{\frac{1+\nu}{1-\nu}J_0(\alpha_n) - \frac{3}{2}\alpha_n J_1(\alpha_n)}\exp(-\frac{\alpha_n^2 H_A k t}{a^2})\exp(-H_A\chi t)\right]. \tag{1.4}$$

From eqs. (1.3) and (1.4), we see that the steady state behavior of axial and lateral strains in poroelastic sample depends on the Young's modulus and Poisson's ratio of the sample. On the other hand, the temporal behavior of lateral and axial strains in poroelastic material depends on the interstitial and vascular permeabilities of the sample along with Young's modulus and Poisson's ratio. This allows us to estimate all the four mechanical properties (Young's modulus, Poisson's ratio, interstitial permeability and vascular permeability) of a poroelastic sample from a poroelastography experiment.

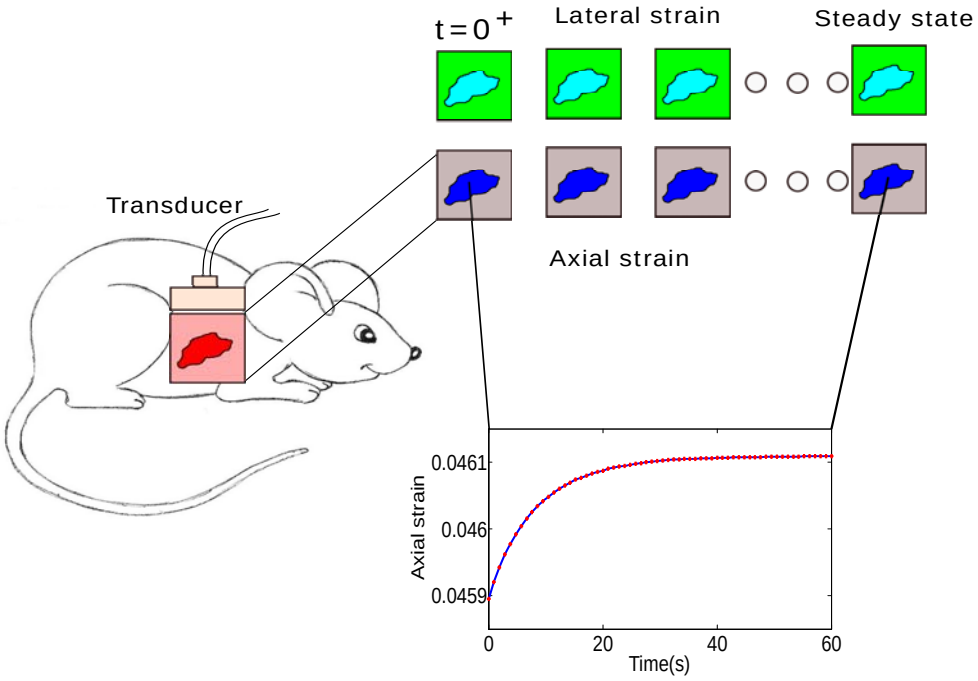

Figure 1.3: Poroelastography experiment

1.4 Importance of mechanopathological parameters

The mechanical micro environment of the soft tissue tumor plays an important role in its growth, invasion and malignancy [16–19]. The interstitial fluid pressure (IFP) and solid stress are two main components of the mechanical micro environment of the tumor [20]. The presence of IFP inside cancer tumor was proven three decades ago, and the role of IFP in cancer progression and treatment has been studied extensively both theoretically and experimentally [21–23]. The proof of the existence of solid stress inside the tumor is relatively recent and has come from the discovery that the blood and lymphatic vessels inside the tumor are mechanically compressed [24–26].

When a solid tumor initially grows, it makes use of existing vasculature, but further of its growth requires angiogenesis, i.e., formation of new blood vessels. These newly formed blood vessels are leaky, highly irregular and tortuous [27, 28]. This increases the vascular permeability of the tumor and decreases its perfusion. The uncontrolled proliferation of cancer cells, increment of collagen increase the resistance of fluid flow in the interstitium of the tumor, which in turn

decreases the interstitial permeability. The proliferating cells in the growing tumor increases the microvascular pressure. The ill-conditioned lymphatic system cannot allow the drainage of fluid and thus reduces fluid movement through the interstitium. All these phenomena causes the elevation of the interstitial fluid pressure in cancer tumors in comparison to the normal tissues [27]. Normally, in experimental models of tumors, the IFP is assumed to be constant along the whole radius of the tumor and zero at the periphery of the tumor [27]. However, in clinical studies, IFP has been found heterogeneous across the radius of the tumor [29]. The mechanopatholgy of a tumor is shown in Fig. 1.4.

High IFP has been found to be a significant therapeutic problem in several experimental and clinical studies [30, 31]. First of all, high elevated IFP can cause serious obstacle to success of chemotherapy, immunotherapy through causing low and hetergeneous uptake of chemical therapeutic agents [32, 33]. Secondly, interstitial hypertension caused by the elevated IFP can cause failure to radiation therapy, which has been shown in several studies [34, 35]. In these studies, the high IFP has been connected to the poor radiocurability by both hypoxia-dependent and hypoxia-independent mechanisms. Thirdly, the metastatic spread of the cancer tumor can be induced by the high elevated IFP. The pulmonary and lymph node metastases have been shown connected to the IFP of the cancer tumor in mice bearing melanoma and cervical carcinoma xenografts [36, 37]. Lastly, the elevated IFP can be an independent prognostic parameter for some cases like advanced cervical carcinoma, where the conventional prognostic factors, such as tumor size, stage, and lymph node status failed to do so [29, 38, 39].

The interstitial and vascular permeabilities of cancer tumor are reported to be important factors for drug delivery inside the tumor. The values of the convection and consolidation time of the drug molecules depend on the vascular and interstitial permeabilities inside the tumor [40]. The values of the permeabilities are also important for determining the treatment type to be used. The vascular normalization technique is more effective in highly permeable tumor whereas the stress normalization technique is more effective in less permeable tumors.

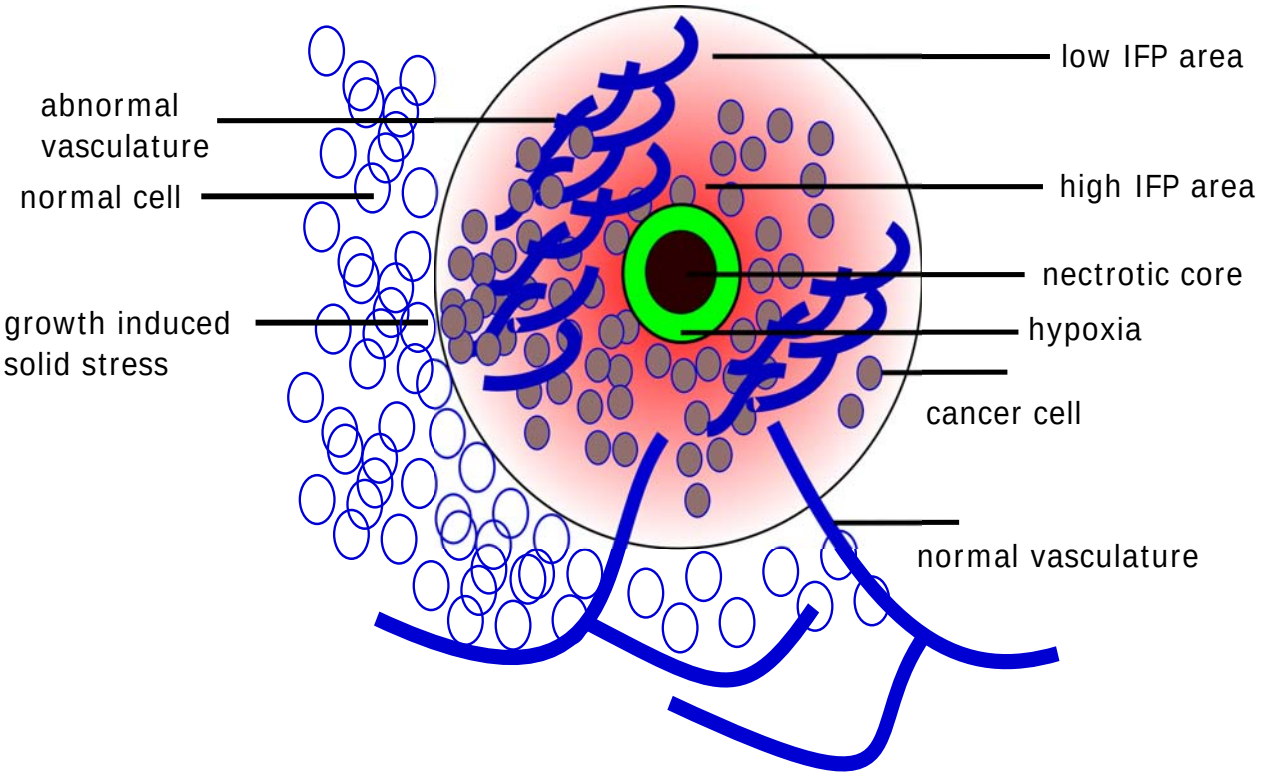

Figure 1.4: Tumor mechanopathology

1.5 Previous methods for estimation of mechanopathological parameters

There are several invasive methods to estimate the IFP in cancer tumor: transducer-tipped catheter and a precision glide needle [41], wick catheter [42–44], modified wick technique (wick-in-needle technique) [45, 46], servo-micropipette [47] and subcutaneous capsule implantation for $4-6$ weeks [48] etc. The most popular of these techniques are the wick and needle and micro-puncture methods, which only measure the IFP in discrete locations inside the tumor [41, 49]. Currently, there is no invasive method available for estimation of the IFV inside the tumor [50].

A noninvasive imaging method for assessment of the IFP and IFV of tumors can be solution to the limitations of the invasive methods. The possibility of using dynamic contrast-enhanced MRI (DCE-MRI) has been explored in a limited number of studies [51–54]. But the values obtained from these studies have been found to have weak or no correlation with the actual values [52, 53, 55].

There are a few invasive and non invasive techniques that can image the interstitial and vascular permeabilities. Among the invasive ones, the methods proposed in [56–60] are the prominent ones. Swab et al. [58] used glycosaminoglycan content of tissue to measure its interstitial permeability, whereas Netti et al. used the confined compression to estimate the interstitial permeability of the tumor tissues [59]. The 'Miles assay' is the classical invasive technique for measuring the vascular permeability [56]. In this technique, the leakage of 'visible dye' from the vasculature to the normal tissues is estimated spectrophotometrically, by taking the relative vascular permeability as ratio of extravasated versus intravascular dye. The cannulation of a single microvessel with a micropipette is another prominent invasive technique to measure the vascular permeability, which involves the perfusion of capillaries through a micro pipette with a solution of known composition in which a few human red blood cells are suspended [57]. The techniques proposed in [61–64] are the important non invasive ones for estimating the vascular permeability. However, these techniques are contrast agent based and requires long time, heavy computation and time consuming pre-processing of the sample.

1.6 Objective of the dissertation

The main objective of this dissertation is to propose a technique based on ultrasound poroelastography, which is non-invasive and can accurately map cancer mechanopathological parameters, i.e., IFP, interstitial permeability and vascular permeability inside the tumor. To determine IFP and the interstitial and vascular permeability inside the tumor, knowledge of Young's modulus and Poisson's ratio of the tumor is necessary [13]. In this dissertation, we propose a three dimensional technique to reconstruct the Young's modulus and Poisson's ratio of tumor accurately. We also propose a new technique for estimating both the axial and lateral strains efficiently and with high accuracy, which are required to estimate all these mechanical parameters from the ultrasound elastography data. To validate our methods, we design a novel finite element model of the tumors considering all the mechanical parameters and IFP. Finally, animal cancer data are collected and analyzed to prove the feasibility of the methods in vivo.

1.7 Overview of the dissertation

This dissertation is organized as follows. In Section 2, we focus on the analytical models of poroelastic samples containing inclusions of cylindrical and spherical shapes. The analytical models have been developed for both stress relaxation and creep experiments. In Section 3, we describe the methods for accurate estimation of lateral strain from a poroelastography experiment. In Section 4, a novel method for estimation of Young's modulus and Poisson's ratio of tumors embedded inside normal tissues is described. The finite element model of tumors is described in Section 5. The estimation procedure of the IFP has been described in Section 6. Section 7 presents concluding remarks.

2. ANALYTICAL MODEL OF ELASTOGRAPHIC PARAMETERS IN CANCERS [1,2,3,4]

2.1 Past related work

The mechanical behavior of biological tissues under small strain compression can be modeled using poroelastic models [13, 65, 66]. Poroelastic materials can be described using biphasic theories, which take into consideration the coupling of interstitial fluid flow and solid matrix deformation [67–70]. When a poroelastic material is subjected to stress relaxation, during the compression phase, fluid exudation causes the stress to rise above the equilibrium value. In the relaxation phase, no fluid exudation occurs and the internal fluid relocates inside the sample [71]. The stress relaxation occurs through a diffusion mechanism also referred to as "gel diffusion", which controls the displacement of the solid matrix [14]. The first work reporting theoretical developments on the stress relaxation analysis of poroelastic materials can be found in [69], where expressions of the deformation, strain and fluid pressure fields were determined. Based on this theory, Armstrong et al. [14] developed a complete set of analytic expressions for a uniform cylindrical sample compressed from the top and the bottom with two frictionless plates.

The set of expressions for the axial and volumetric strains in a homogeneous cylindrical sample under constant compression (both for a constant displacement and for a constant pressure) is first developed by Armstrong et al. [14]. In this work, the authors reported that, in a homogeneous cylindrical sample subjected to a creep compression, the rate of fluid exudation controls the rate of the creep. Immediately after compression, the sample behaves as a nearly incompressible material

[1]Islam, M.T., Chaudhry, A., Unnikrishnan, G., Reddy, J.N. and Righetti, R., 2018. An analytical poroelastic model for ultrasound elastography imaging of tumors. Physics in Medicine & Biology, 63(2), p.025031, ©Institute of Physics and Engineering in Medicine. Reproduced with permission. All rights reserved.

[2]Reprinted with permission from “An analytical poroelastic model of a non-homogeneous medium under creep compression for ultrasound poroelastography applications-Part I" by Islam, M.T., Reddy, J.N. and Righetti, R., 2018. Journal of biomechanical engineering, doi:10.1115/1.4040603, ©2018 by ASME.

[3]Reprinted with permission from “An analytical poroelastic model of a non-homogeneous medium under creep compression for ultrasound poroelastography applications-Part II" by Islam, M.T., Reddy, J.N. and Righetti, R., 2018. Journal of biomechanical engineering, doi:10.1115/1.4040604, ©2018 by ASME.

[4]Reprinted with permission from “An analytical model of tumors with higher permeability than surrounding tissues for ultrasound elastography imaging" by Islam, M.T., Chaudhry, A., Unnikrishnan, G., Reddy, J. and Righetti, R., 2018. Journal of Engineering and Science in Medical Diagnostics and Therapy, 1(3), p.031006031006, ©2018 by ASME.

with no change in volume, as the fluid cannot instantaneously move out of the material. The transient phase of the response of the material depends on the interstitial fluid flow through the solid matrix. At equilibrium, internal fluid flow ceases and the sample behaves as a linearly elastic solid. While this work marks an important milestone toward the understanding of the mechanical behavior of tissues that behave as poroelastic materials, it is limited to homogeneous samples of known geometry.

The first exemplary work on modeling the elastic behavior of an inclusion inside another elastic medium can be found in [72]. In this seminal work, the author derived the formulations for the strains inside the elastic inclusion dependently on the geometry of the inclusion and Poisson's ratio of the background. For poroelastic materials, Rice et al. [73] reported the displacements, strains and fluid pressure inside a poroelastic inclusion embedded in a poroelastic material. Later, the same group published several works dealing with the determination of the shear modulus of cylindrical and spherical poroelastic inclusions inside another poroelastic material [74, 75]. In these studies, the mathematical formulation is given in the Laplace domain, and no closed form analytical solutions are reported in the space and time domains. Additional work on the response of an inclusion in a porous medium is reported in [76–78]. The behavior of two poroelastic layers has been analyzed in [79], where the authors obtained analytical formulations for the displacement and fluid pressure fields at the contact of two poroelastic materials.

Mathematical modeling of abnormal tissues such as tumor tissues and cancers has been of interest to scientists and engineers for the last three decades [18, 21–23, 40, 50, 58, 59, 80–83]. Several models to depict the biomechanical behavior of tumors have been developed. Previous studies incorporate fluid transport mechanisms in the interstitial space [21,84–86]. Growth models, which account for residual stress of the solid due to volumetric expansion, have also been reported [87–89]. In [21–23], the authors used a poroelastic model to describe the stress, strains and fluid pressure behavior of tumors. However, their developments refer only to residual fluid pressure and stress inside the tumor, and no analysis has been reported for applied stress or strain.

Tumors have often been modeled as cylindrical or circular inclusions inside a uniform back-

ground [18, 21, 80, 90–92]. Given the fluid transport mechanisms occurring in tissues, a cancer could be more realistically modeled as a poroelastic inclusion embedded inside another poroelastic material [18, 80, 86]. To our knowledge, however, there is no complete work on the determination of a full set of analytical expressions for the displacements, strains and fluid pressure in a poroelastic inclusion embedded in a poroelastic background subjected to an external applied strain or stress. In [15, 93], we develop a cylindrical model of a tumor and present a complete set of analytical solutions for this model. These analytical expressions can be helpful to understand the inter-dependence of displacements, strains and fluid pressure to different poroelastic mechanical parameters. In the literature, a wide range of measured and estimated values of tumor interstitial permeability has been reported. In many cases the tumor has been considered to be less permeable than the normal tissue [16, 71, 94] and in many other cases the tumor has been considered to be more permeable than the normal tissue [18, 21, 50, 58, 59, 80]. Since both these cases are equally important for applications in cancer imaging and treatment, we have treated the two cases separately. Additionally, using a cylindrical model significantly simplifies the analysis because of the radial symmetry and can be used in the future as the foundation for poroelastic models involving more complex geometries.

2.2 Poroelastic sample with cylindrical inclusion in creep experiment

2.2.1 When inclusion is less permeable than the background

The poroelastic sample containing an inclusion used for the analysis reported in this paper is shown in Fig. 2.1. For convenience, the sample has been assumed to have cylindrical shape, and cylindrical polar coordinates are used throughout the paper. The radial direction is along the r direction and the circumferential direction is along the angle θ. The experimental setup that the model refers to is shown in Fig. 2.2. The cylindrical sample is compressed from the top and the bottom side is fixed. Two frictionless compressor plates are used for holding up the sample and exert compression upon it.

The first basic equation for cylindrical symmetric poroelasticity is the continuity equation of

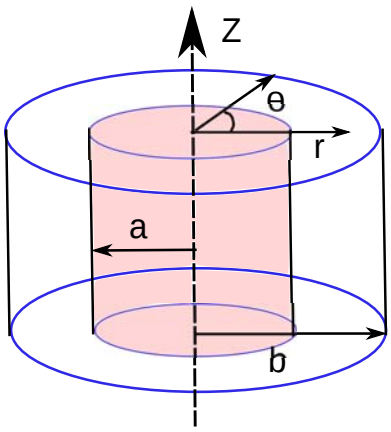

Figure 2.1: A cylindrical sample of a poroelastic material of radius b with a cylindrical inclusion of radius a. Axial direction is along the z direction, radial direction is along the r direction and the circumferential direction is along the angle θ.

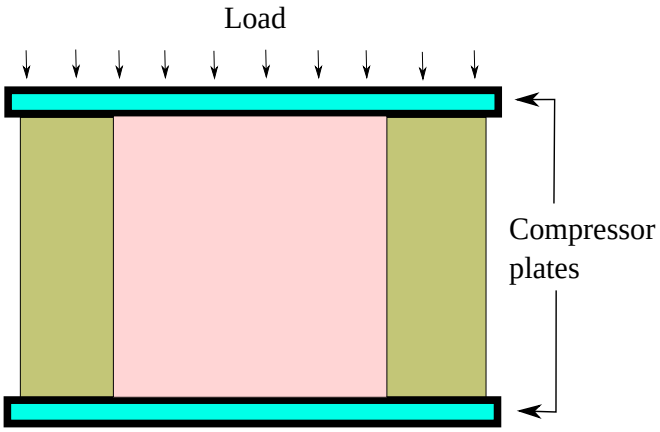

Figure 2.2: 2D view of the setup of a creep experiment where a poroelastic sample is compressed between two compressor plates

the pore fluid which can be written as [13] [95, p. 67]

$$\zeta\frac{\delta\epsilon}{\delta t} + S\frac{\delta p}{\delta t} + \chi p = \frac{k}{\gamma_f}(\frac{\delta^2 p}{\delta r^2} + \frac{1}{r}\frac{\delta p}{\delta r}), \tag{2.1}$$

where χ is the average microfiltration coefficient, ϵ is the volumetric strain, p is the fluid pressure, ζ is Biot's coefficient, S is the storage coefficient, k is the coefficient of interstitial permeability and γ_f is the volumetric weight of the pore fluid. Here, $\chi = \chi_V + \chi_L$, with $\chi_V = \frac{L_p S_V}{V_V}$ and $\chi_L = \frac{L_{PL} S_L}{V_L}$.

L_p and L_{pL} are the hydraulic conductivities of capillary and lymphatic walls, respectively. $\frac{S_V}{V_V}$ and $\frac{S_L}{V_L}$ are the surface area to volume ratio of the capillary and lymphatic walls, respectively. Based on the values of the hydraulic conductivities of capillary and lymphatic walls reported in the literature, $\chi_V >> \chi_L$ [18]. This results in $\chi \approx \chi_V$, and the microfiltration coefficient becomes the hydraulic conductivity of the capillary wall (vascular hydraulic conductivity) multiplied by the surface area to volume ratio. The volumetric strain ϵ is related to the radial displacement u by

$$\epsilon = \frac{\delta u}{\delta r} + \frac{u}{r} + \epsilon_{zz} = \frac{1}{r}\frac{\delta(ur)}{\delta r} + \epsilon_{zz}, \tag{2.2}$$

where ϵ_{zz} is the axial strain.

The second basic equation is the equation of radial equilibrium, which can be expressed as

$$\frac{\delta \sigma_{rr}}{\delta r} + \frac{\sigma_{rr} - \sigma_{\theta\theta}}{r} = 0, \tag{2.3}$$

where σ_{rr} and $\sigma_{\theta\theta}$ are the total stresses in the radial and tangential directions. The total stresses can be separated into the effective stresses and the pore pressure by

$$\sigma_{rr} = \sigma^e_{rr} + \zeta p, \;\; \sigma_{\theta\theta} = \sigma^e_{\theta\theta} + \zeta p. \tag{2.4}$$

The equation of radial equilibrium then can be written as

$$\frac{\delta \sigma^e_{rr}}{\delta r} + \frac{\sigma^e_{rr} - \sigma^e_{\theta\theta}}{r} + \zeta \frac{\delta p}{\delta r} = 0. \tag{2.5}$$

Using eq. (2.2) and the stress-strain relations

$$\sigma^e_{rr} = -(K - \frac{2}{3}G)\epsilon - 2G\frac{\delta u}{\delta r}, \tag{2.6}$$

$$\sigma^e_{\theta\theta} = -(K - \frac{2}{3}G)\epsilon - 2G\frac{u}{r}, \tag{2.7}$$

where K and G are the bulk modulus and shear modulus, respectively, the equation of equilibrium

can be expressed in terms of the volumetric strain as

$$(K + \frac{4}{3}G)\frac{\delta\epsilon}{\delta r} = \zeta\frac{\delta p}{\delta r}. \tag{2.8}$$

The constant $H_A = K + \frac{4}{3}G$ represents the aggregate modulus of the poroelastic material, which results eq. (2.8) in

$$H_A\frac{\delta\epsilon}{\delta r} = \zeta\frac{\delta p}{\delta r}. \tag{2.9}$$

Integrating eq. (2.9) with respect to r, we obtain

$$H_A\epsilon = \zeta p + Q \tag{2.10}$$

and

$$\epsilon = \frac{1}{H_A}(\zeta p + Q), \tag{2.11}$$

where Q is an integration constant.

The remaining of our analysis is for incompressible fluid and solid for which $\zeta = 1$ and $S = 0$. The fluid of interest in our analysis is assumed to have a unit specific weight, i.e., $\gamma_f = 1$. Taking $S = 0$, $\zeta = 1$, $\gamma_f = 1$, we can write eq. (2.1) as

$$\frac{\delta\epsilon}{\delta t} + \chi p = k(\frac{\delta^2 p}{\delta r^2} + \frac{1}{r}\frac{\delta p}{\delta r}). \tag{2.12}$$

Using eq. (2.11), we can write eq. (2.12) as

$$\frac{1}{H_A}\frac{\delta p}{\delta t} + \frac{1}{H_A}\frac{\delta Q}{\delta t} + \chi p = k(\frac{\delta^2 p}{\delta r^2} + \frac{1}{r}\frac{\delta p}{\delta r}), \tag{2.13}$$

which can also be written as

$$\frac{\delta p}{\delta t} + \frac{\delta Q}{\delta t} + H_A \chi p = C(\frac{\delta^2 p}{\delta r^2} + \frac{1}{r}\frac{\delta p}{\delta r}), \tag{2.14}$$

where $C = H_A k$. Let us assume two new variables p' and ϵ' which can be related to the fluid pressure p and volumetric strain ϵ as $p = p' e^{-H_A \chi t}$, $\epsilon = \epsilon' e^{-H_A \chi t}$. Based on the relationship of p' and ϵ' with fluid pressure and volumetric strain, p' and ϵ' are also fluid pressure and volumetric strain but in a different time coordinate system than p and ϵ. p' and ϵ' have same spatial dependencies as p and ϵ. We also assume that Q and Q' are functions of time such that $\frac{\delta Q}{\delta t} = e^{-H_A \chi t}\frac{\delta Q'}{\delta t}$. By performing integration by parts, the relationship between Q and Q' can be found. As Q is an integration constant, the relationship between Q and Q' is not important for further development of the theory. We will denote all the variables related to p' and ϵ' with those variables with a prime. Replacing p and ϵ with p' and ϵ', we get from eq. (2.14)

$$-H_A \chi p' e^{-H_A \chi t} + \frac{\delta p'}{\delta t} e^{-H_A \chi t} + e^{-H_A \chi t}\frac{\delta Q'}{\delta t} + H_A \chi p' e^{-H_A \chi t} = e^{-H_A \chi t} C\left(\frac{\delta^2 p'}{\delta r^2} + \frac{1}{r}\frac{\delta p'}{\delta r}\right), \tag{2.15}$$

which results in

$$\frac{\delta p'}{\delta t} + \frac{\delta Q'}{\delta t} = C\left(\frac{\delta^2 p'}{\delta r^2} + \frac{1}{r}\frac{\delta p'}{\delta r}\right). \tag{2.16}$$

Taking the Laplace transform of eq. (2.16) and putting it in a compact form, we obtain

$$\nabla_r^2 \bar{p'} = s\frac{\bar{p'}}{C} + s\frac{\bar{Q'}}{C}. \tag{2.17}$$

2.2.1.1 Analytical solution inside the inclusion

In the following analysis, we will assume that, at steady state, the fluid pressure inside and outside the inclusion is zero everywhere. This is a common assumption in problems of this kind

[96]. Inside the inclusion, the radial displacement is finite and material flow is zero in the center of the sample. These boundary conditions inside the inclusion can be expressed as

$$r = 0, \frac{\delta \bar{p'}_i}{\delta r} = 0, \tag{2.18}$$

$$r = 0, u'_i = \text{finite}, \tag{2.19}$$

where p'_i and u'_i are the fluid pressure and the radial displacement inside the inclusion, respectively.

The radial displacement, fluid pressure and total radial stress are continuous at the interface between the inclusion and the background and the total radial stress outside the inclusion is zero, i.e.,

$$r = a, \sigma'_{rr,i} = \sigma'_{rr,b} \approx 0, u'_i = u'_b, p'_i = p'_b. \tag{2.20}$$

Here, p'_b, $\sigma'_{rr,b}$ and u'_b are the fluid pressure, total radial stress and the radial displacement outside the inclusion. $\sigma'_{rr,i}$ is the total radial stress inside the inclusion. Considering the first boundary condition, the general solution of eq. (2.17) for the fluid pressure can be written as ([95] p.69)

$$\bar{p'}_i(r, s) = A_i I_0(\xi_i r) - \bar{Q'}_i(s), \tag{2.21}$$

where $\xi_i^2 = sC_i$ and $\bar{Q}'_i$ is the integration constant inside the inclusion. C_i is the product of the aggregate modulus and interstitial permeability inside the inclusion, i.e., $C_i = H_{Ai}k_i$. By using the relationship between the volumetric strain and fluid pressure shown in eq. (2.11), the volumetric strain can be written as

$$\bar{\epsilon'}_i(r, s) = \frac{1}{H_{Ai}} A_i I_0(\xi_i r). \tag{2.22}$$

Considering the second boundary condition (eq. (2.19)), we can express the radial displacement

inside the inclusion as ([95] p. 69)

$$\bar{u'}_i(r,s) = \frac{1}{H_{Ai}} A_i \frac{I_1(\xi_i r)}{\xi_i} - \frac{\bar{\epsilon'}_{zz,i}(s) r}{2}. \tag{2.23}$$

The radial strain can be determined by taking the derivative of u'_i with respect to r as

$$\bar{\epsilon'}_{rr,i}(r,s) = \frac{\delta \bar{u'}_i(r,s)}{\delta r} = \frac{1}{H_{Ai}} A_i \left[I_0(\xi_i r) - \frac{I_1(\xi_i r)}{\xi_i r} \right] - \frac{\bar{\epsilon'}_{zz,i}(s)}{2}. \tag{2.24}$$

The third boundary condition states that $\sigma'_{rr,i} = 0$ at $r = a$, which results in a relationship among the fluid pressure, axial strain and radial displacement as [97]

$$-\bar{p'}_i(a,t) + \lambda_i \left(\frac{d\bar{u'}_i(r,s)}{dr} + \frac{\bar{u'}_i(r,s)}{r} + \bar{\epsilon'}_{zz,i}(s) \right) \Bigg|_{r=a} + 2\mu_i \frac{d\bar{u'}_i(r,s)}{dr} \Bigg|_{r=a} = 0, \tag{2.25}$$

where λ_i and μ_i are the first and second Lame parameters of the inclusion material. λ_i and μ_i are related to the Young's modulus and drained Poisson's ratio of the inclusion as $\lambda_i = \frac{\nu_i E_i}{(1+\nu_i)(1-2\nu_i)}$ and $\mu_i = \frac{E_i}{2(1+\nu_i)}$. For the case of $k_b >> k_i$, eq. (2.25) can be written as [97]

$$\lambda_i \left(\frac{\delta \bar{u'}_i(r,s)}{\delta r} + \frac{\bar{u'}_i(r,s)}{r} + \bar{\epsilon'}_{zz,i}(s) \right) \Bigg|_{r=a} + 2\mu_i \frac{\delta \bar{u'}_i(r,s)}{\delta r} \Bigg|_{r=a} = 0. \tag{2.26}$$

As the volumetric strain, $\bar{\epsilon'}_i(r,s) = \frac{\delta \bar{u'}_i(r,s)}{\delta r} + \frac{\bar{u'}_i(r,s)}{r} + \bar{\epsilon'}_{zz,i}(s)$, eq. (2.26) can also be written as

$$\lambda_i \bar{\epsilon'}_i(r,s) \Big|_{r=a} + 2\mu_i \frac{\delta \bar{u'}_i(r,s)}{\delta r} \Bigg|_{r=a} = 0. \tag{2.27}$$

Using the expressions of the volumetric strain from eq. (2.22) and of radial displacement from eq. (2.23), we can write eq. (2.27) as

$$\lambda_i \frac{1}{H_{Ai}} A_i I_0(\xi_i a) + 2\mu_i \left[\frac{1}{H_{Ai}} A_i \left(I_0(\xi_i a) - \frac{I_1(\xi_i a)}{\xi_i a} \right) - \frac{\bar{\epsilon'}_{zz,i}(s)}{2} \right] = 0. \tag{2.28}$$

Solving this, we get the value of A_i as

$$A_i = \frac{\mu_i \bar{\epsilon'}_{zz,i}(s)}{I_0(\xi_i a) - 2\frac{\mu_i}{H_{Ai}}\frac{I_1(\xi_i a)}{\xi_i a}}. \tag{2.29}$$

Inserting the expression of A_i from eq. (2.29) in eq. (2.21), we obtain the expression of the fluid pressure inside the inclusion as

$$\bar{p'}_i(r,s) = \frac{\mu_i \bar{\epsilon'}_{zz,i}(s)}{I_0(\xi_i a) - 2\frac{\mu_i}{H_{Ai}}\frac{I_1(\xi_i a)}{\xi_i a}} I_0(\xi_i r) - \bar{Q'}_i(r,s). \tag{2.30}$$

Using the expression of A_i from eq. (2.29) in eq. (2.23), the radial displacement can be derived as

$$\bar{u'}_i(r,s) = \frac{1}{H_{Ai}} \frac{\mu_i \bar{\epsilon'}_{zz,i}(s)}{I_0(\xi_i a) - 2\frac{\mu_i}{H_{Ai}}\frac{I_1(\xi_i a)}{\xi_i a}} \frac{I_1(\xi_i r)}{\xi_i} - r\frac{\bar{\epsilon'}_{zz,i}(s)}{2}. \tag{2.31}$$

For an applied uniaxial constant compression, the relationship between the axial pressure and the axial strain in the Laplace domain can be written as [14]

$$\bar{\sigma'}_{zz,i}(s) = \frac{\mu_i \bar{\epsilon'}_{zz,i}(s)(3I_0(\xi_i a) - \frac{8\mu_i}{H_{Ai}}\frac{I_1(\xi_i a)}{\xi_i a})}{I_0(\xi_i a) - \frac{2\mu_i}{H_{Ai}}\frac{I_1(\xi_i a)}{\xi_i a}}. \tag{2.32}$$

From eq. (2.32), the equation for the axial strain can be written as

$$\bar{\epsilon'}_{zz,i}(s) = \frac{\bar{\sigma'}_{zz,i}(s)(I_0(\xi_i a) - \frac{2\mu_i}{H_{Ai}}\frac{I_1(\xi_i a)}{\xi_i a})}{\mu_i(3I_0(\xi_i a) - \frac{8\mu_i}{H_{Ai}}\frac{I_1(\xi_i a)}{\xi_i a})}. \tag{2.33}$$

In our current problem, the applied axial pressure can be defined as $\sigma'_{zz,i}(t) = -\sigma_0 H(t)$, where $H(t)$ is the Heaviside step function. Substituting the expression for the axial strain from eq. (2.33) in the first part of eq. (2.31), we obtain the radial displacement as

$$\bar{u'}_i(r,s) = \frac{1}{H_{Ai}} \frac{\bar{\sigma'}_{zz,i}(s)}{3I_0(\xi_i a) - 8\frac{\mu_i}{H_{Ai}}\frac{I_1(\xi_i a)}{\xi_i a}} \frac{I_1(\xi_i r)}{\xi_i} - r\frac{\bar{\epsilon'}_{zz,i}(s)}{2}. \tag{2.34}$$

The inverse Laplace transform of (2.34) can be written as

$$u_i'(r,t) = -r\frac{\sigma_0}{E_i}\left[\frac{1-2\nu_i}{2} + \frac{(1+\nu_i)(1-2\nu_i)}{1-\nu_i}\sum_{n=1}^{\infty}\frac{\frac{J_1(\alpha_n\frac{r}{a})}{\alpha_n\frac{r}{a}}}{\frac{1+\nu_i}{1-\nu_i}J_0(\alpha_n) - \frac{3}{2}\alpha_n J_1(\alpha_n)}\exp(-\frac{\alpha_n^2 H_{Ai}k_i t}{a^2})\right] - r\frac{\epsilon_{zz,i}'(t)}{2}, \quad (2.35)$$

where α_n are the roots of the characteristics function, $C_0(x) = J_0(x) - \frac{4(1-2\nu_i)}{3(1-\nu_i)}\frac{J_1(x)}{x} = 0$.

Converting u_i' to u_i, we obtain the expression of the radial displacement inside the inclusion as

$$u_i(r,t) = -r\frac{\sigma_0}{E_i}\left[\frac{1-2\nu_i}{2} + \frac{(1+\nu_i)(1-2\nu_i)}{1-\nu_i}\sum_{n=1}^{\infty}\frac{\frac{J_1(\alpha_n\frac{r}{a})}{\alpha_n\frac{r}{a}}}{\frac{1+\nu_i}{1-\nu_i}J_0(\alpha_n) - \frac{3}{2}\alpha_n J_1(\alpha_n)}\exp(-\frac{\alpha_n^2 H_{Ai}k_i t}{a^2})\exp(-H_{Ai}\chi_i t)\right] - r\frac{\epsilon_{zz,i}(t)}{2}. \quad (2.36)$$

The equation for the radial strain can be derived by taking the derivative of eq. (2.36) with respect to r, i.e.,

$$\epsilon_{rr,i}(r,t) = -\frac{\sigma_0}{E_i}\left[\frac{1-2\nu_i}{2} + \frac{(1+\nu_i)(1-2\nu_i)}{1-\nu_i}\sum_{n=1}^{\infty}\frac{J_0(\alpha_n\frac{r}{a}) - \frac{J_1(\alpha_n\frac{r}{a})}{\alpha_n\frac{r}{a}}}{\frac{1+\nu_i}{1-\nu_i}J_0(\alpha_n) - \frac{3}{2}\alpha_n J_1(\alpha_n)}\exp(-\frac{\alpha_n^2 H_{Ai}k_i t}{a^2})\exp(-H_{Ai}\chi_i t)\right] - \frac{\epsilon_{zz,i}(t)}{2}. \quad (2.37)$$

Taking the inverse transform of the Laplace-domain expression of the axial strain from eq. (2.33), we can write the time domain expression of the axial strain as

$$\epsilon_{zz,i}(t) = -\frac{\sigma_0}{E_i}\left[1 + 2(1+\nu_i)\sum_{n=1}^{\infty}\frac{J_0(\alpha_n) - \frac{1-2\nu_i}{1-\nu_i}\frac{J_1(\alpha_n)}{\alpha_n}}{\frac{1+\nu_i}{1-\nu_i}J_0(\alpha_n) - \frac{3}{2}\alpha_n J_1(\alpha_n)}\exp(-\frac{\alpha_n^2 H_{Ai}k_i t}{a^2})\exp(-H_{Ai}\chi_i t)\right]. \quad (2.38)$$

By integrating eq. (2.38) with respect to z and using zero displacement ($u_{zz,i} = 0$) at the bottom of the sample ($z = 0$), we obtain the equation for the axial displacement as

$$u_{zz,i}(z,t) = -\frac{z\sigma_0}{E_i}\left[1 + 2(1+\nu_i)\sum_{n=1}^{\infty}\frac{J_0(\alpha_n) - \frac{1-2\nu_i}{1-\nu_i}\frac{J_1(\alpha_n)}{\alpha_n}}{\frac{1+\nu_i}{1-\nu_i}J_0(\alpha_n) - \frac{3}{2}\alpha_n J_1(\alpha_n)}\exp(-\frac{\alpha_n^2 H_{Ai}k_i t}{a^2})\exp(-H_{Ai}\chi_i t)\right]. \quad (2.39)$$

By using the expression of the radial strain from eq. (2.37) and of the axial strain from eq. (2.38), the effective Poisson's ratio (EPR) inside the inclusion can be expressed as

$$\Psi_i(r,t) = -\frac{\epsilon_{rr,i}(r,t)}{\epsilon_{zz,i}(t)} \tag{2.40}$$

$$= \frac{1}{2} - \frac{\frac{1-2\nu_i}{2} + \frac{(1+\nu_i)(1-2\nu_i)}{1-\nu_i}\sum_{n=1}^{\infty} \frac{J_0(\alpha_n \frac{r}{a}) - \frac{J_1(\alpha_n \frac{r}{a})}{\alpha_n \frac{r}{a}}}{\frac{1+\nu_i}{1-\nu_i}J_0(\alpha_n) - \frac{3}{2}\alpha_n J_1(\alpha_n)} \exp(-\frac{\alpha_n^2 H_{Ai} k_i t}{a^2}) \exp(-H_{Ai}\chi_i t)}{1 + 2(1+\nu_i)\sum_{n=1}^{\infty} \frac{J_0(\alpha_n) - \frac{1-2\nu_i}{1-\nu_i}\frac{J_1(\alpha_n)}{\alpha_n}}{\frac{1+\nu_i}{1-\nu_i}J_0(\alpha_n) - \frac{3}{2}\alpha_n J_1(\alpha_n)} \exp(-\frac{\alpha_n^2 H_{Ai} k_i t}{a^2}) \exp(-H_{Ai}\chi_i t)}. \tag{2.41}$$

We will derive the expression for the fluid pressure for two cases: (a) when the radius of the inclusion is large, i.e., it is comparable to the radius of the overall sample and (b) when the radius of the inclusion is much smaller than the background, i.e., $a << b$. In case (a), the fluid pressure at the boundary of the inclusion can be taken as zero, which results in $\bar{Q'}_i = -A_i I_0(\xi_i a)$ in eq. (2.30). Taking the inverse Laplace transform of eq. (2.30) with $\bar{Q'}_i = -A_i I_0(\xi_i a)$, we obtain the expression of the fluid pressure inside the inclusion as [96]

$$p_i(r,t) = \sigma_0 \sum_{n=1}^{\infty} \frac{J_0(\alpha_n) - J_0(\alpha_n \frac{r}{a})}{\frac{1+\nu_i}{1-\nu_i}J_0(\alpha_n) - \frac{3}{2}\alpha_n J_1(\alpha_n)} \exp(-\frac{\alpha_n^2 H_{Ai} k_i t}{a^2}) \exp(-H_{Ai}\chi_i t). \tag{2.42}$$

In case (b), $\bar{Q'} = 0$ in eq. (2.30). Considering $\bar{Q'} = 0$ in and taking the inverse Laplace transform of eq. (2.30), the fluid pressure inside the inclusion can be expressed as

$$p_i(r,t) = -\sigma_0 \sum_{n=1}^{\infty} \frac{J_0(\alpha_n \frac{r}{a})}{\frac{1+\nu_i}{1-\nu_i}J_0(\alpha_n) - \frac{3}{2}\alpha_n J_1(\alpha_n)} \exp(-\frac{\alpha_n^2 H_{Ai} k_i t}{a^2}) \exp(-H_{Ai}\chi_i t). \tag{2.43}$$

2.2.1.2 Analytical solution outside the tumor

The equation for the fluid pressure in the outside region of the tumor can be written from eq. (2.17) as

$$\frac{\delta^2 p'_b}{\delta r^2} + \frac{1}{r}\frac{\delta p'_b}{\delta r} = \frac{1}{C_b}\frac{\delta p'_b}{\delta t} + \frac{1}{C_b}\frac{\delta Q'_b}{\delta t}. \tag{2.44}$$

where $p_b = p'_b e^{-H_{Ab}\chi_b t}$. In [14], it has been reported that, for an applied axial load of $\sigma'_{zz,b} = -\sigma_0 H(t)$, at $t = 0^+$, the fluid pressure rises to $\frac{\sigma_0}{3}$. This value can be used as the initial value of the fluid pressure in the background region of the sample. After application of the axial compression, the fluid starts to redistribute inside the sample, and a specific fluid pressure $p_i(a,t)$ is created at the interface between the two materials. This can be used as the boundary condition for the fluid pressure in the background region. The boundary and initial conditions for this problem can then be written as

$$p'_b(r,t) = p_i(r,t)e^{H_{Ab}\chi_b t}, r = a, t > 0, \tag{2.45}$$

$$= 0, r = b, \tag{2.46}$$

$$= \frac{\sigma_0}{3}, t = 0. \tag{2.47}$$

Our goal is to find a solution of p'_b that satisfies the differential equation eq. (2.44), initial conditions and boundary conditions expressed by the eqs. (2.45)-(2.47). As Q'_b is a constant that depends on initial and boundary conditions, if a solution p'_b is found that satisfies the differential equation with the initial and boundary conditions, Q'_b becomes zero. Note that the solution to this problem can be found by finding two independent solutions - one for the initial condition of $p'_b(r,0) = \frac{\sigma_0}{3}$ with zero fluid pressure at $r = a$ and $r = b$ and the other one for the boundary condition at the interface, $p'_b(a,t) = p_i(a,t)e^{H_{Ab}\chi_b t}$ with zero initial condition and zero fluid pressure at $r = b$. For the initial condition of $p'_b(r,0) = \frac{\sigma_0}{3}$ with zero fluid pressure at $r = a$ and $r = b$, the solution can be readily written as ([98] p.207)

$$p'_{b,1}(r,t) = \frac{\sigma_0}{3}\pi \sum_{n=1}^{\infty} \frac{J_0(\beta_n a)U(\beta_n r)e^{-\beta_n^2 C_b t}}{J_0(\beta_n a) + J_0(\beta_n b)}, \tag{2.48}$$

where $U(\beta_n r) = J_0(\beta_n r)Y_0(\beta_n b) - Y_0(\beta_n r)J_0(\beta_n b)$. Eq. (2.48) satisfies the condition of zero fluid pressure at $r = a$, provided that β_n are the roots of $C_1(x) = J_0(xa)Y_0(xb) - Y_0(xa)J_0(xb) = 0$.

For the solution of the fluid pressure for boundary condition at the interface, $p'_b(a,t) = p_i(a,t)e^{H_{Ab}\chi_b t}$, we refer to ([98] p.207) and [99]. From ([98] p.207), we know that, for the following boundary

and initial conditions

$$\begin{aligned}\phi(r,t) =& 1, r = a, t > 0,\\ =& 0, r = b,\\ =& 0, t = 0,\end{aligned} \tag{2.49}$$

the solution of eq. (2.44) with ϕ as the variable can be written as

$$\phi(r,t) = \frac{\log(r/b)}{\log(a/b)} + \pi \sum_{n=1}^{\infty} \frac{J_0(\beta_n a) J_0(\beta_n b) U(\beta_n r)}{J_0^2(\beta_n a) - J_0^2(\beta_n b)} e^{-\beta_n^2 C_b t}. \tag{2.50}$$

Considering a sum of time decaying exponential functions $h(t) = p_i(a,t) e^{H_{Ab}\chi_b t} f(t)$ at the interface of the inclusion and background, where $f(t)$ is a function defined as

$$f(t) = \begin{cases} 0, \ t \leq 0, \\ 1, \ t > 0, \end{cases} \tag{2.51}$$

the solution of eq. (2.44) can be determined using the following form of the Duhamel's integral [99, 100]

$$p'_{b,2}(r,t) = \int_0^t \frac{\delta h(\tau)}{\delta \tau} \phi(r, t-\tau) d\tau. \tag{2.52}$$

Use of eq. (2.52) requires that the material properties are independent of the applied strain and fluid pressure, $h(0) = 0$ and that the initial fluid pressure is zero. Using eq. (2.50) for $\phi(r,t)$ and replacing the derivative of $h(t)$ into eq. (2.52) and integrating and considering the boundary conditions stated in eqs. (2.45) and (2.46) with zero initial condition, the fluid pressure as a function

of the radius and time can be found as

$$
\begin{aligned}
p'_{b,2}(r,t) &= \sigma_0\pi\sum_{n=1}^{\infty}\frac{\beta_n^2 J_0(\beta_n a)J_0(\beta_n b)U(\beta_n r)}{J_0^2(\beta_n a)-J_0^2(\beta_n b)}\\
&\times C_b\sum_{m=1}^{\infty}\frac{J_0(\alpha_m)}{\frac{1+\nu_i}{1-\nu_i}J_0(\alpha_m)-\frac{3}{2}\alpha_m J_1(\alpha_m)}\times\frac{e^{-(\frac{\alpha_m^2}{a^2}C_i+H_{Ai}\chi_i-H_{Ab}\chi_b)t}-e^{-\beta_n^2 C_b t}}{\beta_n^2 C_b-(\frac{\alpha_m^2}{a^2}C_i+H_{Ai}\chi_i-H_{Ab}\chi_b)}f(t)\\
&-\sigma_0\frac{\log(r/b)}{\log(a/b)}\sum_{m=1}^{\infty}\frac{J_0(\alpha_m)}{\frac{1+\nu_i}{1-\nu_i}J_0(\alpha_m)-\frac{3}{2}\alpha_m J_1(\alpha_m)}e^{-(\frac{\alpha_m^2}{a^2}C_i+H_{Ai}\chi_i-H_{Ab}\chi_b)t}f(t).
\end{aligned}
\tag{2.53}
$$

Therefore, the total solution for the fluid pressure outside the inclusion can be written as

$$
\begin{aligned}
p'_b(r,t) &= \sigma_0\pi\sum_{n=1}^{\infty}\frac{\beta_n^2 J_0(\beta_n a)J_0(\beta_n b)U(\beta_n r)}{J_0^2(\beta_n a)-J_0^2(\beta_n b)}\\
&\times C_b\sum_{m=1}^{\infty}\frac{J_0(\alpha_m)}{\frac{1+\nu_i}{1-\nu_i}J_0(\alpha_m)-\frac{3}{2}\alpha_m J_1(\alpha_m)}\times\frac{e^{-(\frac{\alpha_m^2}{a^2}C_i+H_{Ai}\chi_i-H_{Ab}\chi_b)t}-e^{-\beta_n^2 C_b t}}{\beta_n^2 C_b-(\frac{\alpha_m^2}{a^2}C_i+H_{Ai}\chi_i-H_{Ab}\chi_b)}f(t)\\
&-\sigma_0\frac{\log(r/b)}{\log(a/b)}\sum_{m=1}^{\infty}\frac{J_0(\alpha_m)}{\frac{1+\nu_i}{1-\nu_i}J_0(\alpha_m)-\frac{3}{2}\alpha_m J_1(\alpha_m)}e^{-(\frac{\alpha_m^2}{a^2}C_i+H_{Ai}\chi_i-H_{Ab}\chi_b)t}f(t)\\
&+\frac{\sigma_0}{3}\pi\sum_{n=1}^{\infty}\frac{J_0(\beta_n a)U(\beta_n r)e^{-\beta_n^2 C_b t}}{J_0(\beta_n a)+J_0(\beta_n b)}.
\end{aligned}
\tag{2.54}
$$

Changing to the relevant variable p_b, we obtain

$$
\begin{aligned}
p_b(r,t) &= \Bigg(\sigma_0\pi\sum_{n=1}^{\infty}\frac{\beta_n^2 J_0(\beta_n a)J_0(\beta_n b)U(\beta_n r)}{J_0^2(\beta_n a)-J_0^2(\beta_n b)}\\
&\times C_b\sum_{m=1}^{\infty}\frac{J_0(\alpha_m)}{\frac{1+\nu_i}{1-\nu_i}J_0(\alpha_m)-\frac{3}{2}\alpha_m J_1(\alpha_m)}\times\frac{e^{-(\frac{\alpha_m^2}{a^2}C_i+H_{Ai}\chi_i-H_{Ab}\chi_b)t}-e^{-\beta_n^2 C_b t}}{\beta_n^2 C_b-(\frac{\alpha_m^2}{a^2}C_i+H_{Ai}\chi_i-H_{Ab}\chi_b)}f(t)\\
&-\sigma_0\frac{\log(r/b)}{\log(a/b)}\sum_{m=1}^{\infty}\frac{J_0(\alpha_m)}{\frac{1+\nu_i}{1-\nu_i}J_0(\alpha_m)-\frac{3}{2}\alpha_m J_1(\alpha_m)}e^{-(\frac{\alpha_m^2}{a^2}C_i+H_{Ai}\chi_i-H_{Ab}\chi_b)t}f(t)\\
&+\frac{\sigma_0}{3}\pi\sum_{n=1}^{\infty}\frac{J_0(\beta_n a)U(\beta_n r)e^{-\beta_n^2 C_b t}}{J_0(\beta_n a)+J_0(\beta_n b)}\Bigg)e^{-H_{Ab}\chi_b t}.
\end{aligned}
\tag{2.55}
$$

Simplifying eq. (2.55), we get the expression of the fluid pressure in the background region as

$$
\begin{aligned}
p_b(r,t) &= \sigma_0 \pi \sum_{n=1}^{\infty} \frac{\beta_n^2 J_0(\beta_n a) J_0(\beta_n b) U(\beta_n r)}{J_0^2(\beta_n a) - J_0^2(\beta_n b)} \\
&\times C_b \sum_{m=1}^{\infty} \frac{J_0(\alpha_m)}{\frac{1+\nu_i}{1-\nu_i} J_0(\alpha_m) - \frac{3}{2}\alpha_m J_1(\alpha_m)} \times \frac{e^{-(\frac{\alpha_m^2}{a^2} C_i + H_{Ai}\chi_i)t} - e^{-(\beta_n^2 C_b + H_{Ab}\chi_b)t}}{\beta_n^2 C_b - (\frac{\alpha_m^2}{a^2} C_i + H_{Ai}\chi_i - H_{Ab}\chi_b)} f(t) \\
&- \sigma_0 \frac{\log(r/b)}{\log(a/b)} \sum_{m=1}^{\infty} \frac{J_0(\alpha_m)}{\frac{1+\nu_i}{1-\nu_i} J_0(\alpha_m) - \frac{3}{2}\alpha_m J_1(\alpha_m)} e^{-(\frac{\alpha_m^2}{a^2} C_i + H_{Ai}\chi_i)t} f(t) \\
&+ \frac{\sigma_0}{3} \pi \sum_{n=1}^{\infty} \frac{J_0(\beta_n a) U(\beta_n r) e^{-(\beta_n^2 C_b + H_{Ab}\chi_b)t}}{J_0(\beta_n a) + J_0(\beta_n b)}.
\end{aligned} \tag{2.56}
$$

We will derive the expression of the EPR for the following two different scenarios: (a) when the radius of the inclusion is large, i.e., it is comparable to the radius of the sample, and (b) when the radius of the inclusion is much smaller than the background, i.e., $a << b$. In the case (a), for the solution of the EPR close to the interface between the inclusion and the background, we can take a general solution of the radial displacement in the background region as [101]

$$u_b(r,t) = r\epsilon_{rr,b}(r,t) + D_b(t). \tag{2.57}$$

Taking the total radial stress in the background region ($a < r < b$) as zero, we can write [14]

$$-p_b(r,t) + \lambda_b(\frac{1}{r}\frac{\delta}{\delta r}(r u_b(r,t)) + \epsilon_{zz,b}(r,t)) + 2\mu_b \epsilon_{rr,b}(r,t) = 0, \quad a < r < b. \tag{2.58}$$

If we substitute eq. (2.57) in the equation of the radial stress in (2.58) for $a < r < b$, we obtain the expression of the radial strain in the background region as

$$\epsilon_{rr,b}(r,t) = \frac{1-\nu_b}{H_{Ab}} p_b(r,t) - \nu_b \epsilon_{zz,b}(r,t) - \nu_b \frac{D_b(t)}{r}. \tag{2.59}$$

Here, we used the following relationship

$$\begin{aligned}\frac{1}{r}\frac{\delta}{\delta r}(ru_b(r,t)) =& \frac{1}{r}(r\frac{\delta u_b(r,t)}{\delta r} + u_b(r,t)) \\ =& 2\epsilon_{rr,b}(r,t) + \frac{D_b(t)}{r}.\end{aligned} \tag{2.60}$$

Imposing the condition of continuous displacement at $r = a$, i.e., $u_i(a,t) = u_b(a,t)$, we get from eq. (2.57)

$$u_i(a,t) = \left(\frac{1-\nu_b}{H_{Ab}}p_b(a,t) - \nu_b\epsilon_{zz,b} - \nu_b\frac{D_b(t)}{a}\right)a + D_b(t), \tag{2.61}$$

which results in

$$D_b(t) = a\frac{1}{\nu_b - 1}\big(\frac{1-\nu_b}{H_{Ab}}p_b(a,t) - \nu_b\epsilon_{zz,b}(a,t) - \frac{1}{a}u_i(a,t)\big). \tag{2.62}$$

The final expression for the radial strain outside the inclusion can be written from eq. (2.59) as

$$\epsilon_{rr,b}(r,t) = \frac{1-\nu_b}{H_{Ab}}p_b(r,t) - \nu_b\epsilon_{zz,b}(r,t) - \frac{a\nu_b}{(\nu_b-1)r}\left(\frac{1-\nu_b}{H_{Ab}}p_b(a,t) - \nu_b\epsilon_{zz,b}(a,t) - \frac{1}{a}u_i(a,t)\right). \tag{2.63}$$

As the axial strain close to the interface is mostly controlled by the axial strain induced inside the inclusion [101], the axial strain outside the inclusion but close to the interface can be approximated by eq. (2.38).

In this case, the fluid pressure outside the inclusion is very small , i.e., $\frac{1-\nu_b}{H_{Ab}}p_b(r,t) << \nu_b\epsilon_{zz,b}(r,t)$. Therefore, the expression for the EPR can be written as

$$\Psi_b(r,t) = -\frac{\epsilon_{rr,b}}{\epsilon_{zz,b}}(r,t) = \nu_b - \frac{a\nu_b}{(\nu_b-1)r}\left(\nu_b + \frac{1}{a\epsilon_{zz,b}(a,t)}u_i(a,t)\right). \tag{2.64}$$

In the case (b), when the inclusion is small in comparison to the sample size, we can determine the EPR in the background region far away from the interface. In this case, the radial strain can be

written from [97] as

$$\epsilon_{rr,b}(r,t) = \frac{1-2\nu_b}{E_b} p_b(r,t) + \nu_b \frac{\sigma_0}{E_b}. \tag{2.65}$$

The axial strain can be written from [97] as

$$\epsilon_{zz,b}(r,t) = \epsilon_{rr,b}(r,t) - (1+\nu_b)\frac{\sigma_0}{E_b}. \tag{2.66}$$

By integrating eq. (2.66) with respect to z and using zero displacement ($u_{zz,b} = 0$) at the bottom of the sample ($z = 0$), we obtain the equation for the axial displacement in background region as

$$u_{zz,b}(z,t) = z\big[\epsilon_{rr,b}(r,t) - (1+\nu_b)\frac{\sigma_0}{E_b}\big]. \tag{2.67}$$

The expression of the EPR can be found by dividing the expression of the radial strain by the axial strain as

$$\begin{aligned}\Psi_b(r,t) =& -\frac{\epsilon_{rr,b}}{\epsilon_{zz,b}}(r,t) \\ =& -\frac{\frac{1-2\nu_b}{E_b} p_b(r,t) + \nu_b \frac{\sigma_0}{E_b}}{\frac{1-2\nu_b}{E_b} p_b(r,t) + \nu_b \frac{\sigma_0}{E_b} - (1+\nu_b)\frac{\sigma_0}{E_b}}.\end{aligned} \tag{2.68}$$

2.2.1.3 Validation using finite element simulation

The commercial finite element simulation software Abaqus, Dassault Systemes Simulia Corp., Providence, RI, USA was used to validate the theory developed in this section. An 'effective stress' principle is used in Abaqus [102], whereby the total stress acting at a point is assumed to be made up by the average pressure in the wetting fluid and an 'effective stress' on the solid matrix. Both the inclusion and background of the sample were modeled as a linearly elastic, isotropic, permeable solid phase fully saturated with fluid.

Four different samples were simulated in our study, as explained below. The exact same geom-

etry and set up shown in Figs. 2.1 and 2.2 were considered. An instantaneous load of 1 kPa was applied to each sample and then kept constant while the sample was under compression [103]. The interstitial permeability of the sample was assumed to be independent of the strain and void ratio. The mesh used to model the sample was CAX4RP with $63,801$ elements in the solution plane. No mesh refinement was applied while meshing the sample geometry in Abaqus. We used a 2D axisymmetric model in Abaqus to represent the 3D cylindrical sample. As the used 2D rectangular geometry is regular without any curvature, mesh refinement was not necessary. A perfect bonding is assumed between the inclusion and surrounding tissue. A portion of the meshed sample along with the mesh seeds is shown in Fig. 2.3. The dimension of the solution plane of the sample was 2 cm in radius and 10 cm in height. A zero fluid pressure boundary condition on the right hand side of the sample was imposed. The specific weight of the fluid was as assumed to be 1Nm^{-3} to match the definitions of interstitial permeability in Abaqus and in the developed model. Under the assumption of unit specific weight of the pore fluid, the hydraulic conductivity and permeability become equal [96]. In Abaqus, the microfiltration coefficient (vascular hydraulic conductivity or permeability) is modeled with the seepage coefficient. The void ratio used in all samples was 0.4. The time response of each sample was recorded for 60 second with a 0.3 sampling interval. The instantaneous load of 1 kPa was applied in the first 0.01 second. This load was then kept constant for 60.01 s.

The mechanical properties of the samples used in our simulations were chosen following [13, 40]. In all cases, the Poisson's ratio was assumed to be 0.49 in the background (normal) tissue and 0.47 in the inclusion (tumor) [13]. As several values of the Young's modulus for tumors have been reported in the literature, two cases for the inclusion were considered: a Young's modulus of 97.02 kPa [13] and a Young's modulus of 40 kPa [104]. The Young's modulus of the normal tissue was assumed to be in all cases 32.78 kPa [13]. The interstitial permeability of the normal tissue was always assumed to be 1000 times higher than the interstitial permeability of the tumor to comply with the assumption of the developed theory. Similar values of interstitial permeability contrast between tumor and surrounding tissue have been previously considered in the literature

[16] (supplementary p. 17). Two samples were chosen with an inclusion radius of 4 mm (i.e., much smaller than the background) and two samples were chosen with an inclusion radius of 18 mm (i.e., comparable to the background radius). In two samples, the vascular permeability (hydraulic conductivity) was dominant over the interstitial permeability, while in the other two samples the interstitial and vascular permeabilities had comparable values. Table 2.1 provides a detailed description of the samples used for the simulation study.

Table 2.1: Description of the samples used in the simulation study

Sample name	E_b (kPa)	E_i (kPa)	k_b (m$^4N^{-1}s^{-1}$)	k_i (m$^4N^{-1}s^{-1}$)	χ_b ((Pa s)$^{-1}$)	χ_i ((Pa s)$^{-1}$)	ν_b	ν_i	a (mm)	b (mm)
A	32.78	97.02	3.1×10^{-11}	3.1×10^{-14}	1.89×10^{-8}	5.67×10^{-7}	0.49	0.47	18	20
B	32.78	97.02	3.1×10^{-8}	6.1×10^{-11}	1.89×10^{-8}	5.67×10^{-7}	0.49	0.47	18	20
C	32.78	40	2.1×10^{-11}	2.1×10^{-14}	3.33×10^{-7}	5.67×10^{-7}	0.49	0.47	4	20
D	32.78	40	3.12×10^{-9}	3.12×10^{-12}	1.89×10^{-8}	5.67×10^{-7}	0.49	0.47	4	20

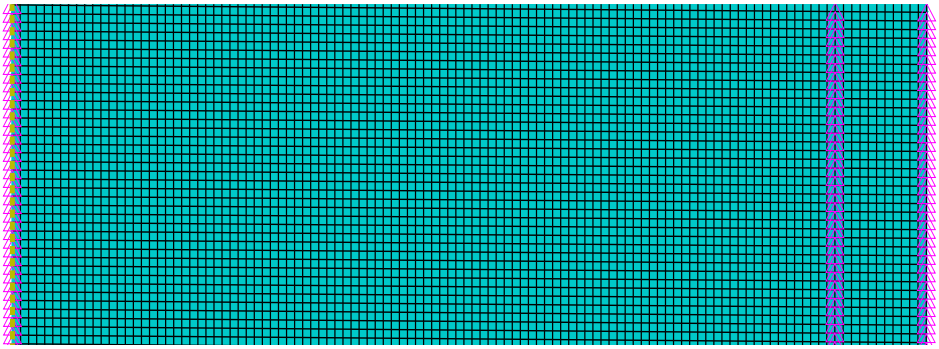

Figure 2.3: Mesh in selected portion of the 2D rectangular sample plane in Abaqus

2.2.1.4 Error analysis

Error analyses were carried out to statistically compare the results obtained using the proposed theoretical model and the simulation results from Abaqus. The following formula was used to calculate the root mean squared error (RMSE) for the estimation of the effective Poisson's ratio

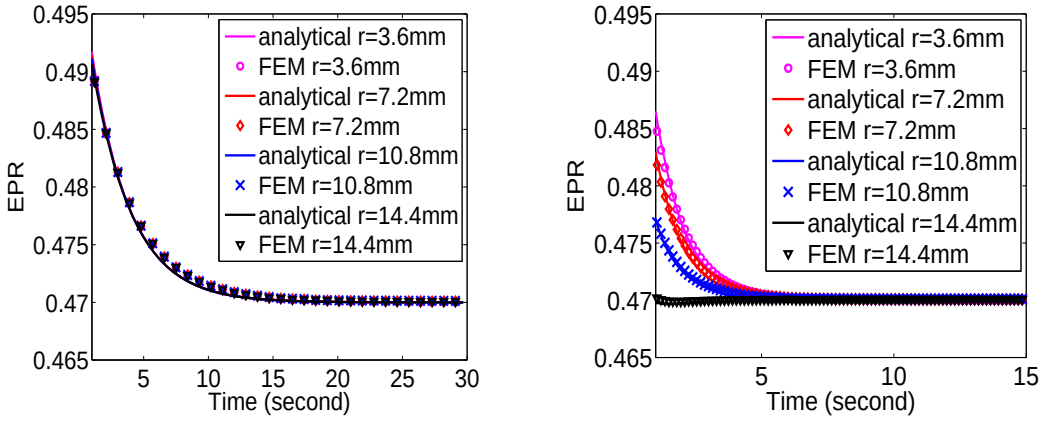

(A) (B)

Figure 2.4: EPR at different positions inside the inclusion for sample A (A) and sample B (B)

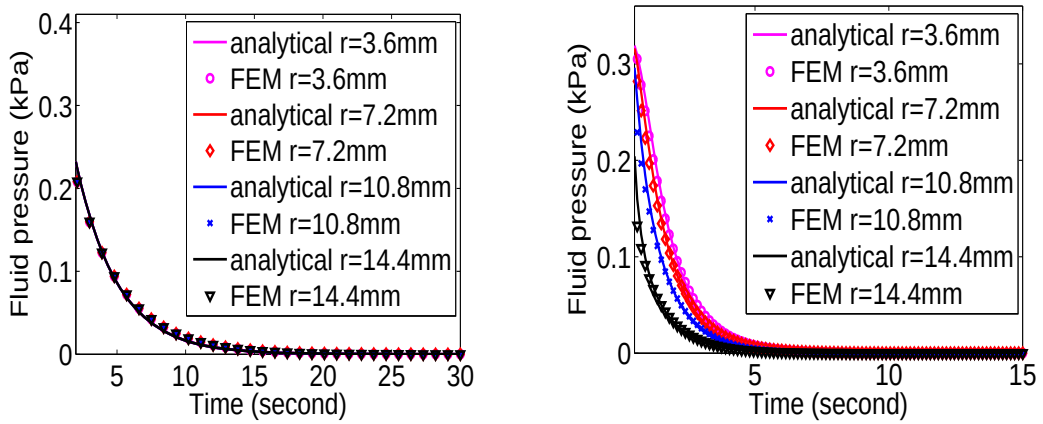

(A) (B)

Figure 2.5: Fluid pressure at different positions inside the inclusion for sample A (A) and sample B (B)

and fluid pressure.

$$\text{RMSE} = \sqrt{\frac{\sum_t^M \sum_r^R (\rho_a(t,r) - \rho_f(t,r))^2}{M \times R}} \times \frac{100 \times R}{\sum_r^R \rho_f(0^+, r)}, \tag{2.69}$$

where M is the total number of time samples considered and R is the number of considered points along radial direction of the sample. ρ_a is the EPR/fluid pressure estimated by the analytical model

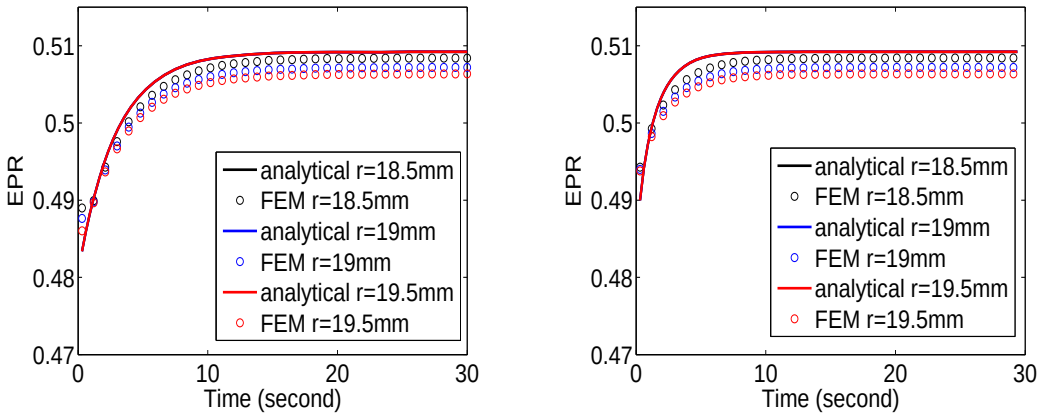

Figure 2.6: EPRs at different positions outside the inclusion for sample A (A) and sample B (B)

and ρ_f is the EPR/fluid pressure estimated by the FEM. $\rho_f(0^+, r)$ is the instantaneous value of ρ_f at radial position r. The RMSE was evaluated on the first 100 samples, i.e., $M = 100$ and for 4 radial positions: for the positions inside the inclusion, we used $0.2a, 0.4a, 0.6a, 0.8a$ for all samples; for the positions outside the inclusion, we used $1.025a, 1.05a, 1.075a, 1.1a$ for samples A and B and $3a, 3.3a, 3.6a, 4a$ for samples C and D. Therefore, in eq. (2.69), R=4.

2.2.1.5 Results

The instantaneous responses of the effective Poisson's ratio (EPR) and fluid pressure inside the inclusion can be found using the initial value theorem in Laplace domain expressions shown in eqs. (2.34) and (2.30). Taking the derivative of eq. (2.34) with respect to r and dividing by the axial strain, we can obtain the Laplace domain expression of the EPR. Letting $s \longrightarrow \infty$ in the expression of $s\Psi_i(r, s)$, we get $\Psi_i(r, 0^+) = \frac{\epsilon_{rr,i}}{\epsilon_{zz,i}}(r, t = 0^+) = \frac{1}{2}$ [14]. Letting $s \longrightarrow \infty$ in $sp_i(r, s)$ from (2.30) with $\bar{Q}_i = -A_i I_0({}_i a)$, we get the instantaneous fluid pressure $p_i(r, 0^+) = \sigma_0/3$ [14]. As the fluid pressure at outer boundary of the sample is zero, for $t > 0s$, a fluid pressure gradient is created. The pressure gradient causes fluid exudation and facilitates fluid flow toward the sample boundary. As radial stress in the solid matrix of the sample is along the opposite direction of the fluid flow, the radial stress in the solid matrix of the sample pulls the tissue back toward the center. Since the

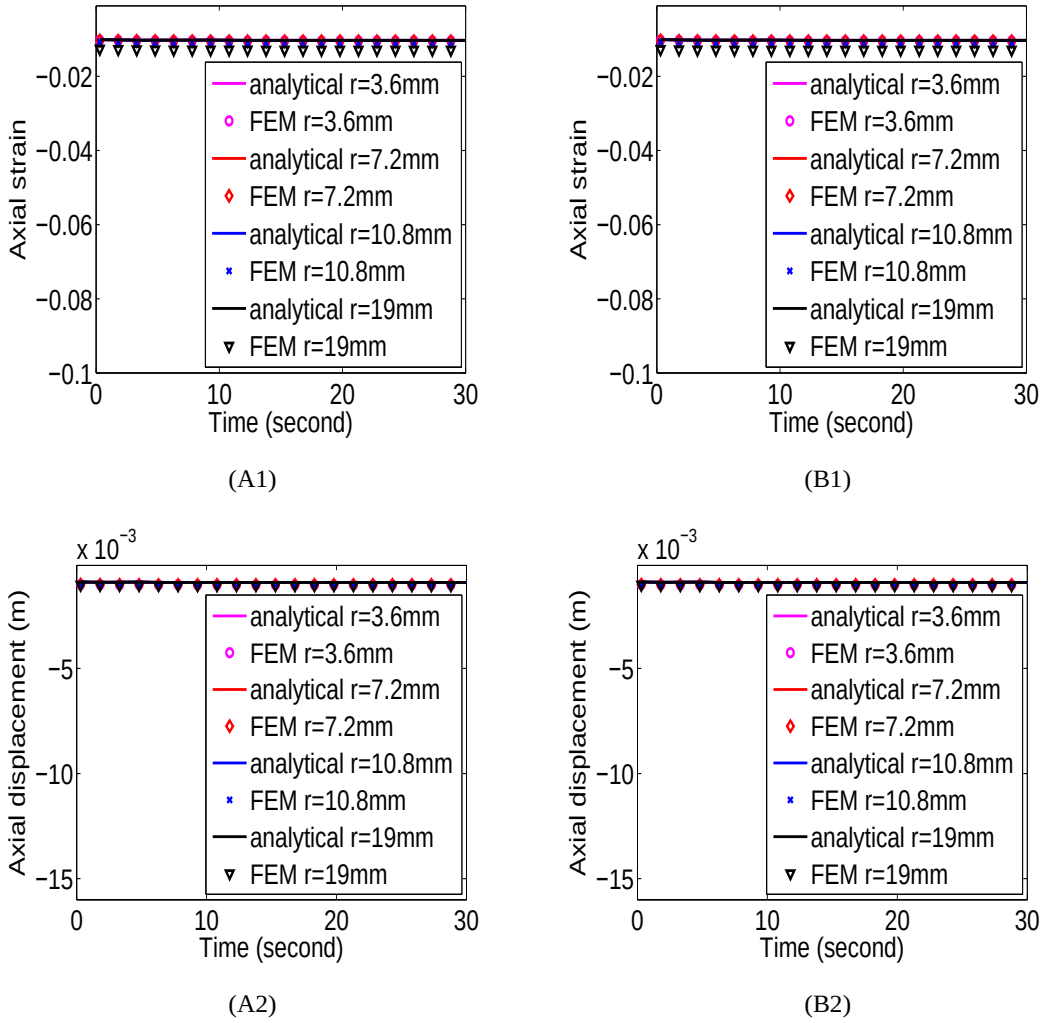

Figure 2.7: Axial strains at different positions inside and outside the inclusion for sample A (A1) and sample B (B1). Axial displacements at different positions inside and outside the inclusion for sample A (A2) and sample B (B2).

interstitial permeability of the background tissue is much higher than the interstitial permeability of the tissue, the fluid exudes through the outer boundary of the sample in a faster way than the inclusion. When the solid matrix of the inclusion and background are fully relaxed, the EPRs of the inclusion and background become the drained Poisson's ratio of the corresponding materials, which can be found by letting $t \longrightarrow \infty$ in eqs. (2.41) and (2.68). Close to the interface of the inclusion and background, the EPR in background region assumes value higher than the drained Poisson's ratio of the background which can be found by letting $t \longrightarrow \infty$ in eq. (2.64). The fluid

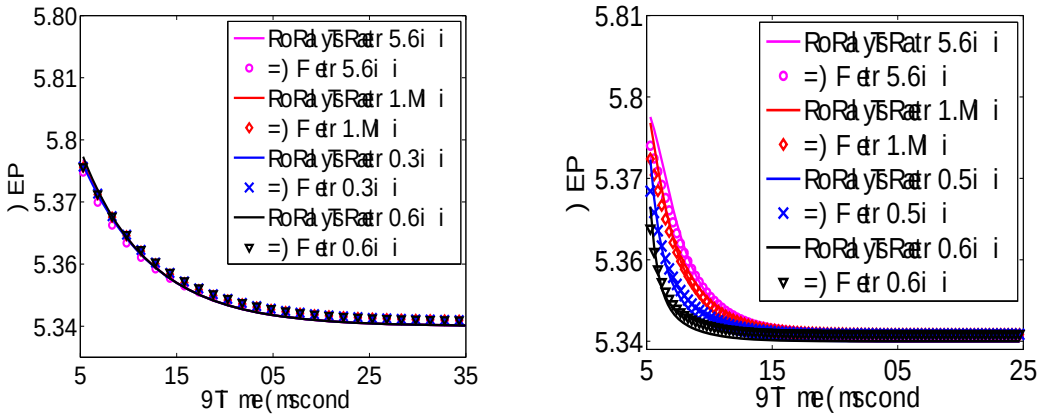

Figure 2.8: EPR at different positions inside the inclusion for sample C (A) and sample D (B)

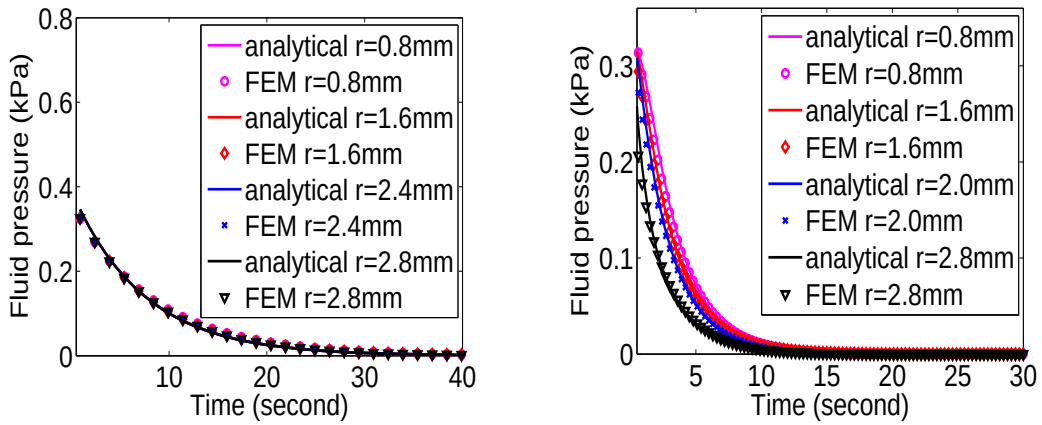

Figure 2.9: Fluid pressure at different positions inside the inclusion for sample C (A) and sample D (B)

pressure everywhere becomes zero, as expected, and this is demonstrated if we let $t \longrightarrow \infty$ in eqs. (2.42) or (2.43) and (2.56).

Next, we show the responses of the inclusion and background in terms of EPR and fluid pressure computed both from the analytical theory and the FEM simulations for different samples. The EPRs for samples A and B for positions inside the inclusion are shown in Fig. 2.4 (A) and (B). From these figures, we see that the EPR starts at around 0.5 at $t = 0^+$ and goes to the drained

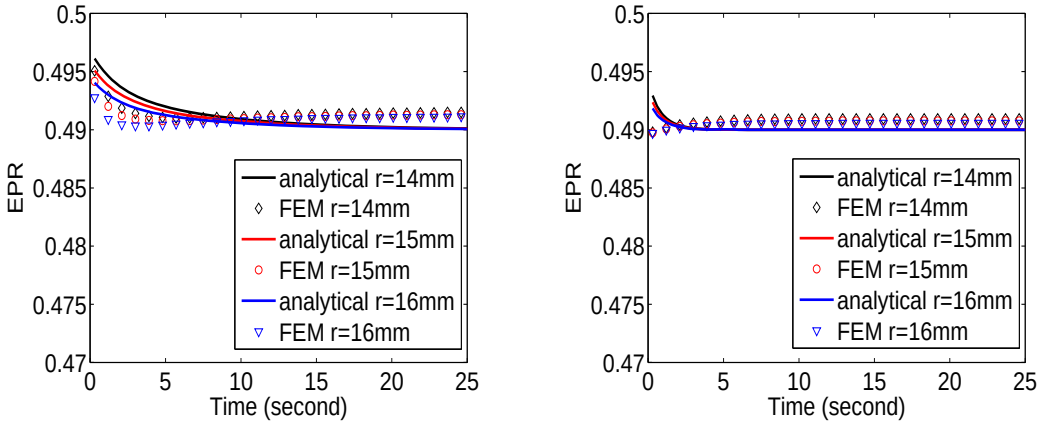

(A) (B)

Figure 2.10: EPR at different positions outside the inclusion for sample C (A) and sample D (B)

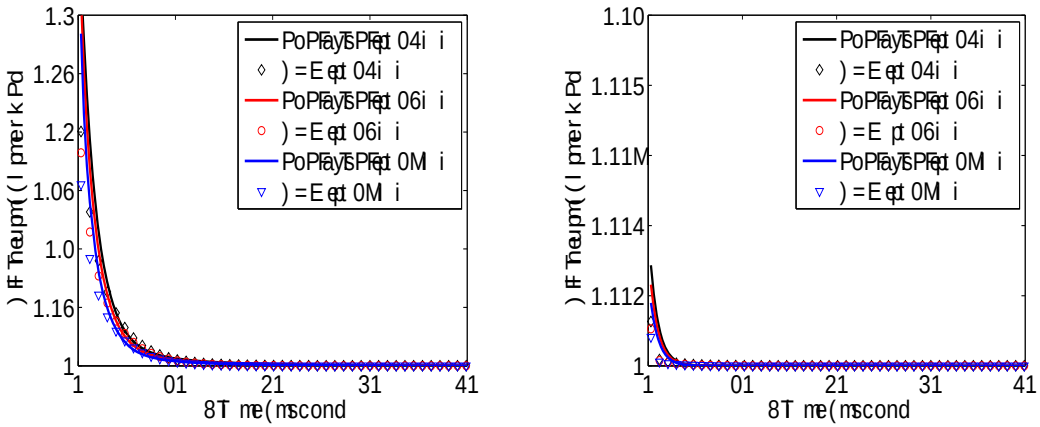

(A) (B)

Figure 2.11: Fluid pressure at different positions outside the inclusion for sample C (A) and sample D (B)

Poisson's ratio of the inclusion material at steady state. For sample A, as the vascular permeability is dominant over the interstitial permeability, we see that there is no spatial dependence of the EPR. This is because the vascular walls are distributed throughout the inclusion (as it is the case in real tumors) and, consequently, the fluid flow and pressure are same everywhere inside the inclusion. In sample B, instead, the EPR varies with the radius. This is due to the fact that, in this sample, the interstitial permeability is dominant over the vascular permeability. When the interstitial

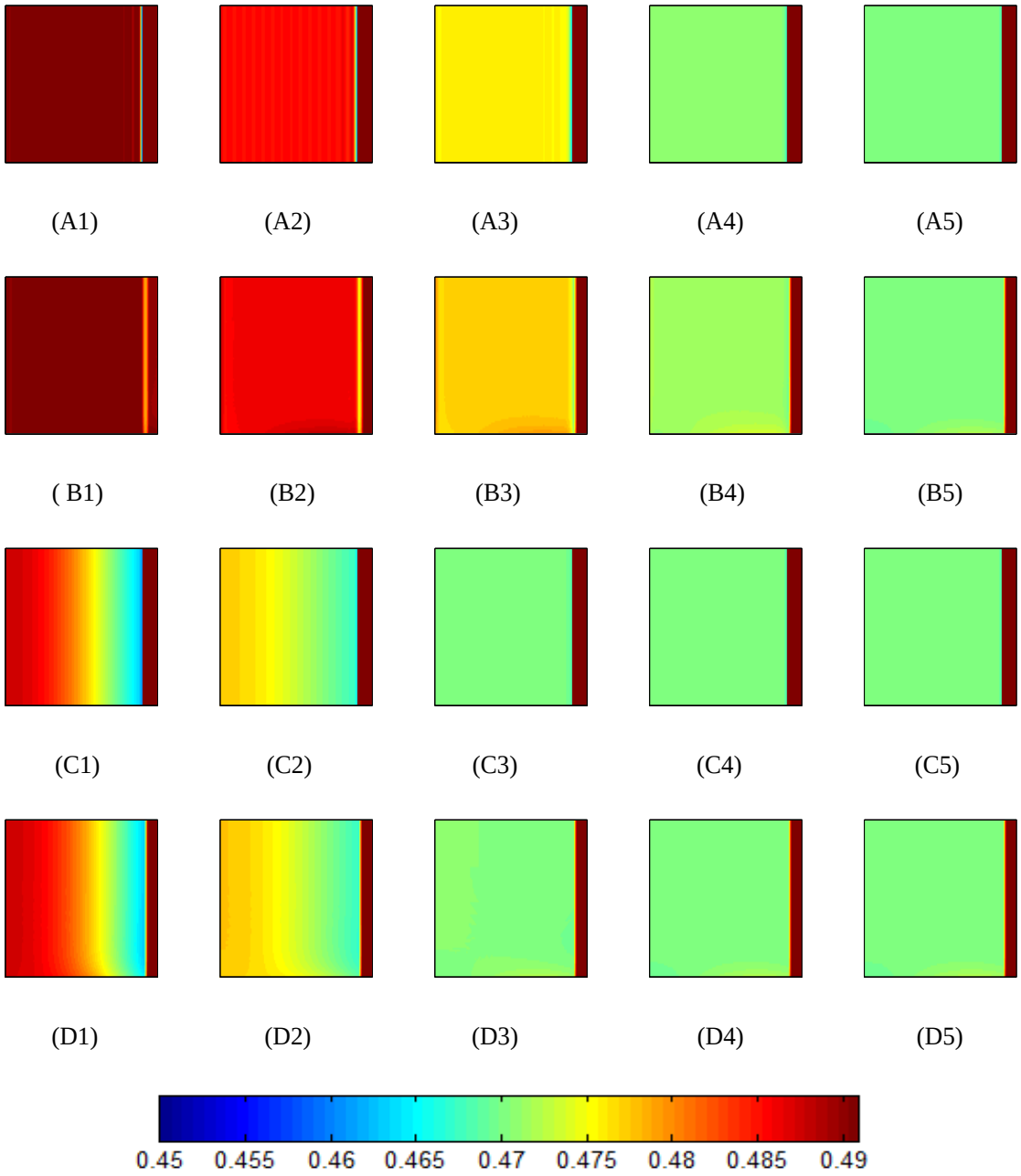

Figure 2.12: Sample A: (A1), (A2), (A3), (A4), (A5) show the EPR images at different time points (1s, 2s, 5s, 10s and 15s) as obtained from the developed analytical model; (B1), (B2), (B3), (B4), (B5) show the corresponding EPR images obtained from the FEM model. Sample B: (C1), (C2), (C3), (C4), (C5) show the EPR images at different time points (1s, 2s, 5s, 10s and 15s) as obtained from the developed analytical model; (D1), (D2), (D3), (D4), (D5) show the corresponding EPR images obtained from the FEM model.

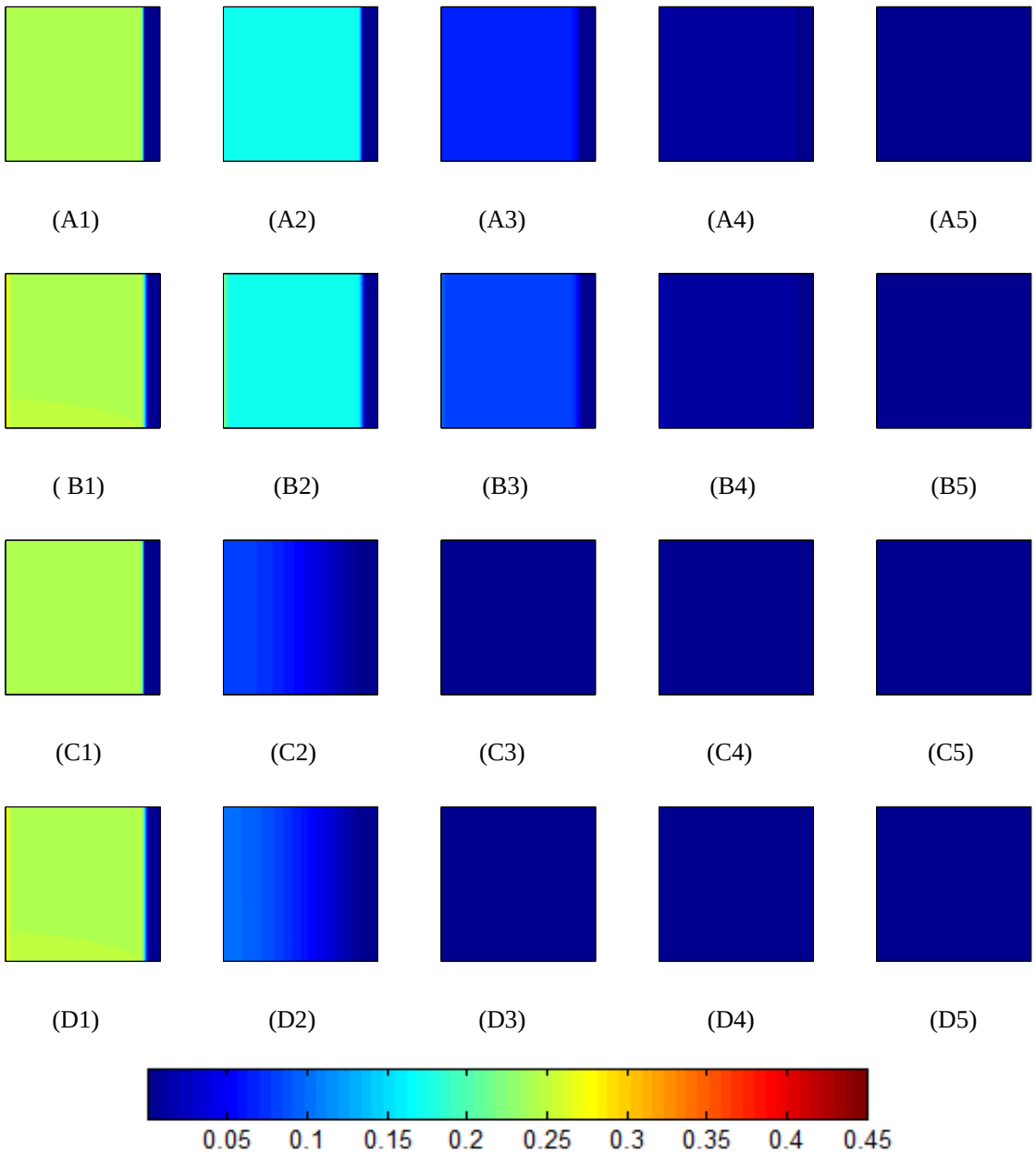

Figure 2.13: Sample A: (A1), (A2), (A3), (A4), (A5) show the fluid pressure (kPa) at different time points (1s, 2s, 5s, 10s and 15s) as obtained from the developed analytical model; (B1), (B2), (B3), (B4), (B5) show the corresponding the fluid pressure (kPa) obtained from the FEM model. Sample B: (C1), (C2), (C3), (C4), (C5) show the fluid pressure (kPa) at different time points (1s, 2s, 5s, 10s and 15s) as obtained from the developed analytical model; (D1), (D2), (D3), (D4), (D5) show the corresponding fluid pressure (kPa) obtained from the FEM model.

permeability becomes dominant over the vascular permeability, the fluid needs to cross a certain path to exude, which gives rise to non-uniformly distributed fluid flow and pressure fields inside

the inclusion. This makes the EPR spatially dependent as the EPR depends on the fluid pressure inside the inclusion. This result is in agreement with previous literature [13]. The fluid pressures for samples A and B are shown in Fig. 2.5 (A) and (B) for positions inside the inclusion. The fluid pressure starts at a value close to $\sigma_0/3$ at $t = 0^+$ and goes to zero at steady state. These observations are consistent with the results reported in [14]. Similar to the EPR, the fluid pressure inside the inclusion is spatially constant in sample A and spatially variant in sample B.

The EPRs for samples A and B for positions outside the inclusion are shown in Fig. 2.6 (A) and (B). From these figures, we see that the EPRs start at a lower value than the Poisson's ratio of the background at $t = 0^+$ and reach at a higher value than the drained Poisson's ratio of the background at steady state. The fluid pressure outside the inclusion in samples A and B is close to zero as these samples have an inclusion of radius comparable to the radius of the overall sample.

The axial strain and displacement inside and outside the inclusion for samples A and B are shown in Fig. 2.7. We see that the axial strain and displacements at different radius values in both samples, inside and outside the inclusion, are almost identical and almost time-invariant. It should be noted that the axial and lateral shear strains are zero for the analyzed cases according to both the analytical model and FEM. Axial and lateral shear strains from the analytical model can be computed by taking derivatives of eqs. (2.39) and (2.67) with respect to r and eqs. (2.36) and (2.57) with respect to z, respectively, inside and outside the inclusion.

Samples C and D have inclusions of much smaller radii than samples A and B. The EPR and fluid pressure at different locations inside the inclusion are shown in Figs. 2.8 and 2.9. As for samples A and B, the EPR starts at a value close to 0.5 and goes to the drained Poisson's ratio of the inclusion in samples C and D. On the other hand, the fluid pressure starts at a value close to $\frac{\sigma_0}{3}$ and goes to zero at steady state. In sample C, the vascular permeability is dominant over the interstitial permeability, and the EPR and fluid pressure have no spatial variance inside the inclusion. EPR and fluid pressure demonstrate a spatial dependence in the case of sample D, where the interstitial permeability and vascular permeability are of comparable values.

The EPR and the fluid pressure outside the inclusion in samples C and D are shown in Figs. 2.10

and 2.11. As the radius of the tumor in sample C and D is smaller than that of sample A and B, the fluid pressure should have higher values than that of sample A and B. This is seen for sample C. But since the interstitial permeability in sample D is very high, the fluid exudes within a few seconds. Consequently, the fluid pressure and EPR go to the steady state within a few seconds as indicated in Figs. 2.10 (B) and 2.11 (B).

The time evolution of the EPR in samples A and B is shown in Fig. 2.12. From these images, we see that, for all the samples, at time $t = 0^+$, the EPR in the inclusion remains 0.5. However, in the background, the EPR is not 0.5 rather it has a value lower than 0.5. The EPR in the inclusion gradually decreases from 0.5 with time and reaches the drained Poisson's ratio ν_i of the inclusion material at very large time. On the other hand, in the background, the EPR starts at lower value than the drained Poisson's ratio of the background and, with time, increases to the drained Poisson's ratio of the background material, ν_b in the background region far from the interface and even to a higher value than the drained Poisson's ratio close to the interface.

Fig. 2.13 shows the fluid pressure image at different time points for samples A and B. From these images, we see that, at time $t = 0^+$, the fluid pressure remains higher than $\sigma_0/3$ in the inclusion, while it is almost zero in the background because of the high permeability of the background and quick exudation of the fluid along the right boundary of the sample. The material properties of the inclusion affect the time taken for the fluid pressure to go to the steady state value (i.e., zero).

Table 2.2 summarizes the results of the error analyses. From this table, we observe that: with respect to the EPR, the error is below 0.29% in the inclusion and below 0.53% in the background; with respect to the fluid pressure, the error is below 1.85% in the inclusion while it becomes larger outside the inclusion, but still below 2.11%. These results demonstrate the correctness of the proposed theoretical model with respect to an established FEM software.

Table 2.2: Root mean squared error computed between the results obtained from the analytical model and the corresponding FEM results

Sample name	Error in EPR estimation inside inclusion (%)	Error in EPR estimation outside inclusion (%)	Error in fluid pressure estimation inside inclusion (%)	Error in fluid pressure estimation outside inclusion (%)
A	0.09	0.45	1.71	NA
B	0.10	0.51	1.64	NA
C	0.02	0.53	1.85	2.11
D	0.29	0.36	1.51	0.92

2.2.2 When inclusion is more permeable than the background

Following the same reasoning used in first part (inclusion less permeable than the background), we can write the following differential equation for the fluid pressure

$$\frac{1}{H_A}\frac{\delta p}{\delta t} + \frac{1}{H_A}\frac{\delta Q}{\delta t} + \chi p = k(\frac{\delta^2 p}{\delta r^2} + \frac{1}{r}\frac{\delta p}{\delta r}), \tag{2.70}$$

which can also be written as

$$\frac{\delta p}{\delta t} + \frac{\delta Q}{\delta t} + H_A \chi p = C(\frac{\delta^2 p}{\delta r^2} + \frac{1}{r}\frac{\delta p}{\delta r}), \tag{2.71}$$

where $C = H_A k$, H_A is the aggregate modulus of the poroelastic material. Let us assume that $p = p' e^{-H_A \chi t}$, $\epsilon = \epsilon' e^{-H_A \chi t}$. We also assume that Q and Q' are functions of time such that $\frac{\delta Q}{\delta t} = e^{-H_A \chi t}\frac{\delta Q'}{\delta t}$. By performing integration by parts, the relationship between Q and Q' can be found. As Q is an integration constant and depends on time only, the relationship between Q and Q' is not important for further development of the theory. All the variables related to p' and ϵ' will be denoted with a prime. Replacing p and ϵ with p' and ϵ', we obtain

$$-H_A \chi p' e^{-H_A \chi t} + \frac{\delta p'}{\delta t} e^{-H_A \chi t} + e^{-H_A \chi t}\frac{\delta Q'}{\delta t} + H_A \chi p' e^{-H_A \chi t} = e^{-H_A \chi t} C(\frac{\delta^2 p'}{\delta r^2} + \frac{1}{r}\frac{\delta p'}{\delta r}), \tag{2.72}$$

which results in

$$\frac{\delta p'}{\delta t} + \frac{\delta Q'}{\delta t} = C\left(\frac{\delta^2 p'}{\delta r^2} + \frac{1}{r}\frac{\delta p'}{\delta r}\right). \tag{2.73}$$

This equation can be written in terms of the volumetric strain as

$$\frac{\delta \epsilon'}{\delta t} + \frac{\delta Q''}{\delta t} = C\left(\frac{\delta^2 \epsilon'}{\delta r^2} + \frac{1}{r}\frac{\delta \epsilon'}{\delta r}\right), \tag{2.74}$$

where Q'' is another constant, which depends on time only. Eq. (2.74) can be written in terms of the radial strain, circumferential strain ($\epsilon'_{\theta\theta}$) and axial strain as

$$\frac{\delta}{\delta t}(\epsilon'_{rr} + \epsilon'_{\theta\theta} + \epsilon'_{zz}) + \frac{\delta Q''}{\delta t} = C\left(\frac{\delta^2}{\delta r^2}(\epsilon'_{rr} + \epsilon'_{\theta\theta} + \epsilon'_{zz}) + \frac{1}{r}\frac{\delta}{\delta r}(\epsilon'_{rr} + \epsilon'_{\theta\theta} + \epsilon'_{zz})\right). \tag{2.75}$$

After taking the integral with respect to r, this equation can be written in terms of the radial displacement inside the inclusion as [14, 97]

$$\frac{\delta^2 u'_i}{\delta r^2} + \frac{1}{r}\frac{\delta u'_i}{\delta r} - \frac{u'_i}{r^2} - \frac{1}{H_{Ai}k_i}\frac{\delta u'_i}{\delta t} = \frac{1}{H_{Ai}k_i}\frac{r}{2}\frac{\delta \epsilon'_{zz,i}(t)}{\delta t} - \frac{1}{H_{Ai}k_i}\frac{\delta Q''}{\delta t}. \tag{2.76}$$

We will consider the limiting case where the permeability of the inclusion is much higher than the permeability of the background, i.e., $\frac{ak_b}{hk_i} << 1$ [97]. Here the background thickness $h = b - a$. Multiplying eq. (2.76) by $a\frac{k_b}{h}$ and neglecting the terms with $\frac{ak_b}{hk_i}$, we obtain

$$\frac{\delta^2 u'_i}{\delta r^2} + \frac{1}{r}\frac{\delta u'_i}{\delta r} - \frac{u'_i}{r^2} = \frac{\delta}{\delta r}\left[\frac{1}{r}\frac{\delta}{\delta r}(r u'_i)\right] = 0. \tag{2.77}$$

We can write for the filtration in the background region as

$$w'_{r,b} = -k_b\frac{\delta p''_b}{\delta r}, \tag{2.78}$$

where p''_b is the fluid pressure outside the inclusion associated with p'_i and ϵ'_i. For a background

of thickness $h = b - a$, where $h << b$, the pressure gradient normal to the background is given by [97]

$$-\frac{\delta p_b''}{\delta r} \approx \frac{\Delta p_b''}{h}, \tag{2.79}$$

where $\Delta p_b'' = p_b''(x) - p_b''(x+h)$ is the pressure difference between a point at the interface background/inclusion and a point at external boundary of the sample. Therefore, we can write

$$w_{r,b}' = \frac{k_b}{h}\Delta p_b''. \tag{2.80}$$

2.2.2.1 Analytical solution inside the inclusion

The solution of eq. (2.77) is given by

$$u_i'(r,t) = \Lambda(t)r, \tag{2.81}$$

where $\Lambda(t)$ is a function of time only. Taking derivative of eq. (2.81), we find that the radial strain strain inside inclusion can be written as $\epsilon_{rr,i}'(t) = \Lambda(t)$. This shows that under the specified condition of lower interstitial permeability of inclusion than the background, the radial strain inside the inclusion is uniform.

Using the relationship between the volumetric strain and the fluid pressure [15], we can write the following equation relating the fluid pressure and radial displacement

$$-\frac{\delta p_i'}{\delta r} + H_{Ai}\left(\frac{\delta^2 u_i'}{\delta r^2} + \frac{1}{r}\frac{\delta u_i'}{\delta r} - \frac{u_i'}{r^2}\right) = 0. \tag{2.82}$$

Substituting the expression of the radial displacement from eq. (2.81) in eq. (2.82), we find that the fluid pressure inside the inclusion is also constant with respect to the radius, i.e., $p_i'(r,t) = p_i'(t)$.

Let us assume that the total radial stress along the radius of the inclusion is zero [50]. This

results in

$$-p_i'(a,t) + \lambda_i \left[\frac{1}{r}\frac{\delta}{\delta r}(ru_i') + \epsilon'_{zz,i}(t)\right]_{r=a} + 2\mu_i \left[\frac{\delta u_i'}{\delta r}\right]_{r=a} = 0. \tag{2.83}$$

Using the zero fluid pressure condition at the outer boundary and the conditions of continuity of fluid pressure and filtration at the interface between the inclusion and the background, i.e., $p_i'(a,t) = p_b''(a,t)$ and $w_{r,i}'(a,t) = w_{r,b}'(a,t)$, we can write from eq. (2.80)

$$\frac{k_b}{h}p_b''(a,t) = \frac{k_b}{h}p_i'(a,t) = w_{r,i}'(a,t) = w_{r,b}'(a,t). \tag{2.84}$$

For the filtration inside the inclusion, we can write [97]

$$w_{r,i}'(a,t) = \left(-\frac{\delta u_i'(r,t)}{\delta t} - \frac{r}{2}\dot{\epsilon'}_{zz,i}(t)\right)_{r=a}. \tag{2.85}$$

Using eqs. (2.85) and (2.84), we can express $\frac{k_b}{h}p_i'(a,t)$ as

$$\frac{k_b}{h}p_i'(a,t) = \left(-\frac{\delta u_i'(r,t)}{\delta t} - \frac{r}{2}\dot{\epsilon'}_{zz,i}(t)\right)_{r=a}. \tag{2.86}$$

Using the expression of $p_i'(a,t)$ from eq. (2.86), we obtain from eq. (2.83),

$$\frac{h}{k_b}\left[\dot{\epsilon'}_{rr,i}(t)a + \frac{a}{2}\dot{\epsilon'}_{zz,i}(t)\right] + \big(2\lambda_i + 2\mu_i\big)\epsilon'_{rr,i}(t) + \lambda_i \epsilon'_{zz,i}(t) = 0. \tag{2.87}$$

As $2\lambda_i + 2\mu_i = \frac{\lambda_i}{\nu_i}$, dividing eq. (2.87) by $2\lambda_i + 2\mu_i$, we obtain

$$\frac{ah(1-\nu_i)}{H_{Ai}k_b}\left[\dot{\epsilon'}_{rr,i}(t) + \frac{1}{2}\dot{\epsilon'}_{zz,i}(t)\right] + \epsilon'_{rr,i}(t) + \nu_i \epsilon'_{zz,i}(t) = 0. \tag{2.88}$$

Taking $\tau_{\epsilon,i} = \frac{ah(1-\nu_i)}{H_{Ai}k_b}$, we can write

$$\tau_\epsilon\left[\dot{\epsilon'}_{rr,i}(t) + \frac{1}{2}\dot{\epsilon'}_{zz,i}(t)\right] + \epsilon'_{rr,i}(t) + \nu_i \epsilon'_{zz,i}(t) = 0. \tag{2.89}$$

The axial normal stress $\sigma'_{zz,i}(t)$ acting on the loading plates is given by [97]

$$\frac{\sigma'_{zz,i}(t)}{H_A} = -\frac{p'_i(t)}{H_A} + \frac{2\nu_i}{1-\nu_i}\epsilon'_{rr,i}(t) + \epsilon'_{zz,i}(t). \tag{2.90}$$

To get the fluid pressure, we use eq. (2.83), which gives

$$-p'_i(a,t) + \frac{H_{Ai}}{1-\nu_i}\epsilon'_{rr,i}(t) + \lambda_i\epsilon'_{zz,i}(t) = 0. \tag{2.91}$$

As the fluid pressure does not depend on the radial position, i.e., $p'_i(t) = p'_i(a,t)$, the fluid pressure can be written as

$$\frac{p'_i(t)}{H_{Ai}} = \frac{\epsilon'_{rr,i}(t) + \nu_i\epsilon'_{zz,i}(t)}{1-\nu_i}. \tag{2.92}$$

Using eq. (2.92) in eq. (2.90), we get the expression of the axial normal stress as

$$\frac{\sigma'_{zz,i}(t)}{H_{Ai}} = \frac{1-2\nu_i}{1-\nu_i}\left[\epsilon'_{zz,i}(t) - \epsilon'_{rr,i}(t)\right]. \tag{2.93}$$

For a creep compression experiment with applied load $\sigma'_{zz,i} = -\sigma_0 H(t)$, where $H(t)$ is a Heaviside step function, eq. (2.93) yields

$$\epsilon'_{zz,i}(t) = -\frac{1-\nu_i}{1-2\nu_i}\frac{\sigma_0}{H_{Ai}} + \epsilon'_{rr,i}(t). \tag{2.94}$$

If we substitute the expression of axial strain from eq. (2.94) into eq. (2.89), we obtain

$$\frac{3}{2}\tau_{\epsilon,i}\dot{\epsilon}'_{rr,i}(t) + (1+\nu_i)\epsilon'_{rr,i}(t) - \frac{\nu_i(1-\nu_i)}{1-2\nu_i}\frac{\sigma_0}{H_{Ai}} = 0. \tag{2.95}$$

This ordinary differential equation is to be solved subjected to the initial condition of zero volu-

metric strain, which results in

$$2\epsilon'_{rr,i}(0^+) + \epsilon'_{zz,i}(0^+) = 3\epsilon'_{rr,i}(0^+) - \frac{(1-\nu_i)}{1-2\nu_i}\frac{\sigma_0}{H_{Ai}} = 0. \tag{2.96}$$

The solution is given by

$$\epsilon'_{rr,i}(t) = \left(\nu_i + \frac{1-2\nu_i}{3}\exp\left(-\frac{t}{\tau_{\sigma,i}}\right)\right)\frac{\sigma_0}{E_i}, \tag{2.97}$$

where

$$\tau_{\sigma,i} = \frac{3\tau_{\epsilon,i}}{2(1+\nu_i)} = \frac{3ah(1-2\nu_i)}{2E_i k_b}. \tag{2.98}$$

Converting to $\epsilon_{rr,i}$, we obtain the expression of the radial strain inside the inclusion as

$$\epsilon_{rr,i}(t) = \left(\nu_i + \frac{1-2\nu_i}{3}\exp\left(-\frac{t}{\tau_{\sigma,i}} - H_{Ai}\chi_i t\right)\right)\frac{\sigma_0}{E_i}. \tag{2.99}$$

To write eq. (2.99) from eq. (2.97), we have used the fact that $\epsilon_{rr,i}(\infty) = \epsilon'_{rr,i}(\infty) = \frac{\nu_i\sigma_0}{E_i}$. Using the expression of the radial strain from eq. (2.99) in eq. (2.81), the lateral displacement inside the inclusion can be written as

$$u_i(r,t) = r\left(\nu_i + \frac{1-2\nu_i}{3}\exp\left(-\frac{t}{\tau_{\sigma,i}} - H_{Ai}\chi_i t\right)\right)\frac{\sigma_0}{E_i}. \tag{2.100}$$

Using eqs. (2.99) and (2.94), we obtain the expression of the axial strain as

$$\epsilon_{zz,i}(t) = -\left(1 - \frac{1-2\nu_i}{3}\exp\left(-\frac{t}{\tau_{\sigma,i}} - H_{Ai}\chi_i t\right)\right)\frac{\sigma_0}{E_i}. \tag{2.101}$$

By integrating eq. (2.101) with respect to z and using zero displacement ($u_{zz,i} = 0$) at the bottom

of the sample ($z = 0$), we obtain the equation for the axial displacement as

$$u_{zz,i}(z,t) = -\left(1 - \frac{1-2\nu_i}{3}\exp\left(-\frac{t}{\tau_{\sigma,i}} - H_{Ai}\chi_i t\right)\right)\frac{z\sigma_0}{E_i}. \tag{2.102}$$

Using eqs. (2.99) and (2.101), the volumetric strain inside the inclusion for the creep compression can be expressed as

$$e_i(t) = 2\epsilon_{rr,i}(t) + \epsilon_{zz,i}(t) = -(1-2\nu_i)(1 - \exp\left(-\frac{t}{\tau_{\sigma,i}} - H_{Ai}\chi_i t\right))\frac{\sigma_0}{E_i}. \tag{2.103}$$

By using the expressions of the radial and axial strains in eq. (2.92), the fluid pressure inside the inclusion can be expressed as

$$p_i(t) = \frac{\sigma_0}{3}\exp\left(-\frac{t}{\tau_{\sigma,i}} - H_{Ai}\chi_i t\right). \tag{2.104}$$

Using the expressions of the radial strain from eq. (2.99) and axial strain from eq. (2.101), the EPR can be expressed as

$$\Psi_i(t) = -\frac{\epsilon_{rr,i}}{\epsilon_{zz,i}}(t) = \frac{\nu_i + \frac{1-2\nu_i}{3}\exp\left(-\frac{t}{\tau_{\sigma,i}} - H_{Ai}\chi_i t\right)}{1 - \frac{1-2\nu_i}{3}\exp\left(-\frac{t}{\tau_{\sigma,i}} - H_{Ai}\chi_i t\right)}. \tag{2.105}$$

2.2.2.2 Analytical solution outside the inclusion

The differential equation for the fluid pressure outside the inclusion can be written from eq. (2.73) as

$$\frac{\delta^2 p_b'}{\delta r^2} + \frac{1}{r}\frac{\delta p_b'}{\delta r} = \frac{1}{C_b}\frac{\delta p_b'}{\delta t} + \frac{1}{C_b}\frac{\delta(Q_b)}{\delta t}, \tag{2.106}$$

where we have assumed that $p_b = p'_b e^{-H_{Ab}\chi_b t}$. The 'gel diffusion' constant C_b can be written as [105]

$$C_b = H_{Ab} k_b. \tag{2.107}$$

It has been reported in [14] that, for an applied axial load of $\sigma'_{zz,b} = -\sigma_0 H(t)$, at $t = 0^+$, the fluid pressure rises to $\frac{\sigma_0}{3}$. This value can be used as the initial value of the fluid pressure in the background region of the sample. After application of the axial strain, the fluid starts to redistribute inside the sample, and a specific fluid pressure $p_i(a,t)$ is created at the interface between the two materials. This can be imposed as the boundary condition for the fluid pressure in the background region. The boundary and initial conditions for this problem can be written as

$$p'_b(r,t) = p_i(r,t) e^{H_{Ab}\chi_b t},\ r = a,\ t > 0, \tag{2.108}$$

$$= 0,\ r = b, \tag{2.109}$$

$$= \frac{\sigma_0}{3},\ t = 0. \tag{2.110}$$

The solution can be constructed by setting up the following individual solutions for each one of the conditions and then adding them up:

$$(p'_{b,1}, p'_{b,2}) = (p_i(t) e^{H_{Ab}\chi_b t}, 0),\ r = a, \tag{2.111}$$

$$= (0, \frac{\sigma_0}{3}),\ t = 0, \tag{2.112}$$

$$= (0,0),\ r = b. \tag{2.113}$$

If we construct a solution as

$$p'_b(r,t) = p'_{b,1}(r,t) + p'_{b,2}(r,t) \tag{2.114}$$

and $p'_{b,1}$ and $p'_{b,2}$ satisfies eq. (2.106) with $Q_b = 0$, the resulting fluid pressure satisfies eq. (2.106) along with the initial condition and all the boundary conditions.

We introduce the function

$$U(\beta r) = J_0(\beta r)Y_0(\beta b) - Y_0(\beta r)J_0(\beta b). \tag{2.115}$$

This function vanishes when $r = a$, provided that β is root of

$$J_0(\beta a)Y_0(\beta b) - Y_0(\beta a)J_0(\beta b) = 0. \tag{2.116}$$

$p'_{b,1}$ and $p'_{b,2}$ can be expressed as [106, p. 634], [107], [98, p. 207], [108, p. 623]

$$p'_{b,1} = -\frac{\sigma_0}{3}C_b\pi\sum_{n=1}^{\infty}\frac{\beta_n^2 J_0(\beta_n a)J_0(\beta_n b)U(\beta_n r)}{J_0^2(\beta_n a) - J_0^2(\beta_n b)}\frac{e^{(-\frac{1}{\tau_{\sigma,i}} - H_{Ai}\chi_i + H_{Ab}\chi_b)t} - e^{-\beta_n^2 C_b t}}{\beta_n^2 C_b - \frac{1}{\tau_{\sigma,i}} - H_{Ai}\chi_i + H_{Ab}\chi_b}, \tag{2.117}$$

$$p'_{b,2} = \frac{\sigma_0}{3}\pi\sum_{n=1}^{\infty}\frac{J_0(\beta_n a)U(\beta_n r)e^{-\beta_n^2 Ct}}{J_0(\beta_n a) + J_0(\beta_n b)}. \tag{2.118}$$

The total solution can then be written as

$$\begin{aligned} p'_b(r,t) = -\frac{\sigma_0}{3}C_b\pi\sum_{n=1}^{\infty}\frac{\beta_n^2 J_0(\beta_n a)J_0(\beta_n b)U(\beta_n r)}{J_0^2(\beta_n a) - J_0^2(\beta_n b)}\frac{e^{(-\frac{1}{\tau_{\sigma,i}} - H_{Ai}\chi_i + H_{Ab}\chi_b)t} - e^{-\beta_n^2 C_b t}}{\beta_n^2 C_b - \frac{1}{\tau_{\sigma,i}} - H_{Ai}\chi_i + H_{Ab}\chi_b} \\ +\frac{\sigma_0}{3}\pi\sum_{n=1}^{\infty}\frac{J_0(\beta_n a)U(\beta_n r)e^{-\beta_n^2 Ct}}{J_0(\beta_n a) + J_0(\beta_n b)}. \end{aligned} \tag{2.119}$$

The solution for $p_b(r,t)$ can be written as

$$\begin{aligned} p_b(r,t) = \Bigg(-\frac{\sigma_0}{3}C_b\pi\sum_{n=1}^{\infty}\frac{\beta_n^2 J_0(\beta_n a)J_0(\beta_n b)U(\beta_n r)}{J_0^2(\beta_n a) - J_0^2(\beta_n b)}\frac{e^{(-\frac{1}{\tau_{\sigma,i}} - H_{Ai}\chi_i + H_{Ab}\chi_b)t} - e^{-\beta_n^2 C_b t}}{\beta_n^2 C_b - \frac{1}{\tau_{\sigma,i}} - H_{Ai}\chi_i + H_{Ab}\chi_b} \\ +\frac{\sigma_0}{3}\pi\sum_{n=1}^{\infty}\frac{J_0(\beta_n a)U(\beta_n r)e^{-\beta_n^2 Ct}}{J_0(\beta_n a) + J_0(\beta_n b)}\Bigg)e^{-H_{Ab}\chi_b t}. \end{aligned} \tag{2.120}$$

Simplifying eq. (2.120), we obtain

$$p_b(r,t) = -\frac{\sigma_0}{3}C_b\pi\sum_{n=1}^{\infty}\frac{\beta_n^2 J_0(\beta_n a)J_0(\beta_n b)U(\beta_n r)}{J_0^2(\beta_n a)-J_0^2(\beta_n b)}\frac{e^{-(\frac{1}{\tau_{\sigma,i}}+H_{Ai}\chi_i)t}-e^{-(\beta_n^2 C_b+H_{Ab}\chi_b)t}}{\beta_n^2 C_b-\frac{1}{\tau_{\sigma,i}}-H_{Ai}\chi_i+H_{Ab}\chi_b}$$
$$+\frac{\sigma_0}{3}\pi\sum_{n=1}^{\infty}\frac{J_0(\beta_n a)U(\beta_n r)e^{-(\beta_n^2 C_b+H_{Ab}\chi_b)t}}{J_0(\beta_n a)+J_0(\beta_n b)}. \quad (2.121)$$

Taking the total radial stress at $a < r < b$ as zero, we can write

$$-p_b(r,t)+\lambda_b(\frac{1}{r}\frac{\delta}{\delta r}(ru_b(r,t))+\epsilon_{zz,b}(r,t))+2\mu_b\epsilon_{rr,b}(r,t)=0. \quad (2.122)$$

Following the expression of the radial displacement inside the inclusion as shown in eq. (2.81), we take a general solution of the radial displacement in the background region as

$$u_b(r,t) = r\epsilon_{rr,b}(r,t). \quad (2.123)$$

Following the same derivation used for the radial strain inside the inclusion, we can write the radial and axial strains in the background region as

$$\epsilon_{rr,b}(r,t) = \frac{1-2\nu_b}{E_b}p_b(r,t)+\nu_b\frac{\sigma_0}{E_b} \quad (2.124)$$

and

$$\epsilon_{zz,b}(r,t) = \epsilon_{rr,b}(r,t)-(1+\nu_b)\frac{\sigma_0}{E_b}. \quad (2.125)$$

By integrating eq. (2.125) with respect to z and using zero displacement ($u_{zz,b}=0$) at the bottom of the sample ($z=0$), we obtain the equation for the axial displacement as

$$u_{zz,b}(r,z,t) = z\big[\epsilon_{rr,b}(r,t)-(1+\nu_b)\frac{\sigma_0}{E_b}\big]. \quad (2.126)$$

The expression of the EPR can be found by dividing the expression of the radial strain by the axial strain as

$$\begin{aligned}\Psi_b(r,t) &= -\frac{\epsilon_{rr,b}}{\epsilon_{zz,b}}(r,t) \\ &= -\frac{\frac{1-2\nu_b}{E_b}p_b(r,t) + \nu_b\frac{\sigma_0}{E_b}}{\frac{1-2\nu_b}{E_b}p_b(r,t) + \nu_b\frac{\sigma_0}{E_b} - (1+\nu_b)\frac{\sigma_0}{E_b}}.\end{aligned} \tag{2.127}$$

2.2.2.3 Validation using finite element simulation

Abaqus has been used to validate the analytical formulations developed in this section. The sample was compressed from the top and the bottom side was kept static. An instantaneous load of 1 kPa was applied to the sample instantaneously and kept constant thereafter. The permeability of the sample was assumed to be independent of the strain and void ratio. The mesh used to model the sample was CAX4RP with $63,801$ elements in the solution plane. The dimension of the solution plane of the sample was 2 cm in radius and 10 cm in height. The zero fluid pressure boundary condition on the right hand side of the sample was imposed. The time response was recorded for 60 second in interval time steps of 0.3 s. The total analysis is done in two steps. In the first step of duration 0.01 second, an instantaneous load of 1 kPa is applied. In the second step, the load is kept constant for 60.01 s. The specific weight of the fluid was as assumed to be 1Nm^{-3} to match the definitions of interstitial permeability in Abaqus and in the developed model. Under the assumption of unit specific weight of the pore fluid, the hydraulic conductivity and permeability become equal [96]. In Abaqus, the microfiltration coefficient (vascular hydraulic conductivity or permeability) was modeled with the seepage coefficient. The void ratio used in all samples was 0.4.

The material properties of the three samples A, B and C used in the simulation were chosen based on previous literature [13, 40]. Some of the properties were then adjusted to create different scenarios, i.e., dominance of vascular permeability (hydraulic conductivity) or interstitial permeability or to bring the responses within a fixed time scale. The Poisson's ratio of both the

background and inclusion was assumed to be 0.47. The Young's moduli of the inclusion and background were assumed to be 32.78 kPa and 50 kPa, respectively. In all cases, the interstitial permeability of the inclusion was assumed to be 1000 times higher than the interstitial permeability of the background. In all cases, the radius of the inclusion was assumed to be 18.75 mm. The properties of the samples are described in Table 2.3.

We note that, in sample A, inside the inclusion, the interstitial permeability is dominant over the vascular permeability. In sample B, interstitial permeability is comparable to the vascular permeability. In sample C, the vascular permeability is dominant over the interstitial permeability.

2.2.2.4 Error analysis

Error analyses were carried out to statistically compare the results obtained using the proposed theoretical model and the simulation results from Abaqus. Eq. (2.69) was used to calculate the RMSE for the estimation of the effective Poisson's ratio and fluid pressure. For producing the error values in Table 2.4, we used the first 100 samples, i.e., $M = 100$ and considered 4 radial positions, i.e., $0.2a, 0.4a, 0.6a, 0.8a$ inside the inclusion and $1.015a, 1.03a, 1.045a, 1.06a$ outside the inclusion for all the samples, which implies that $R = 4$.

Table 2.3: Description of the samples used in current study

Sample name	E_b (kPa)	E_i (kPa)	k_b (m$^4N^{-1}s^{-1}$)	k_i (m$^4N^{-1}s^{-1}$)	χ_b ((Pa s)$^{-1}$)	χ_i ((Pa s)$^{-1}$)	ν_b	ν_i	a (mm)	b (mm)
A	32.78	50	1×10^{-11}	1×10^{-8}	1.41×10^{-8}	6.67×10^{-8}	0.47	0.47	18.75	20
B	32.78	50	1×10^{-11}	1×10^{-8}	1.41×10^{-7}	6.67×10^{-7}	0.47	0.47	18.75	20
C	32.78	50	1×10^{-12}	1×10^{-9}	1.41×10^{-7}	6.67×10^{-7}	0.47	0.47	18.75	20

2.2.2.5 Results

The instantaneous response of the fluid pressure and the EPR can be found from the developed formulations. Putting $t \longrightarrow 0$ in the equation of the fluid pressure in eq. (2.104) and eq. (2.121), we obtain the fluid pressure inside the inclusion and outside the inclusion as $\sigma_0/3$ at $t = 0^+$. The EPR inside and outside the inclusion at $t = 0^+$ can be found from eq. (2.105) and eq. (2.127) as

0.5 by inserting $t \longrightarrow 0$. At the steady state, we find the fluid pressure inside and outside the inclusion as zero if we put $t \longrightarrow \infty$ in eq. (2.104) and eq. (2.121). The EPRs in the inclusion and background region can be found as ν_i and ν_b at the steady state by putting $t \longrightarrow \infty$ in eq. (2.105) and eq. (2.127).

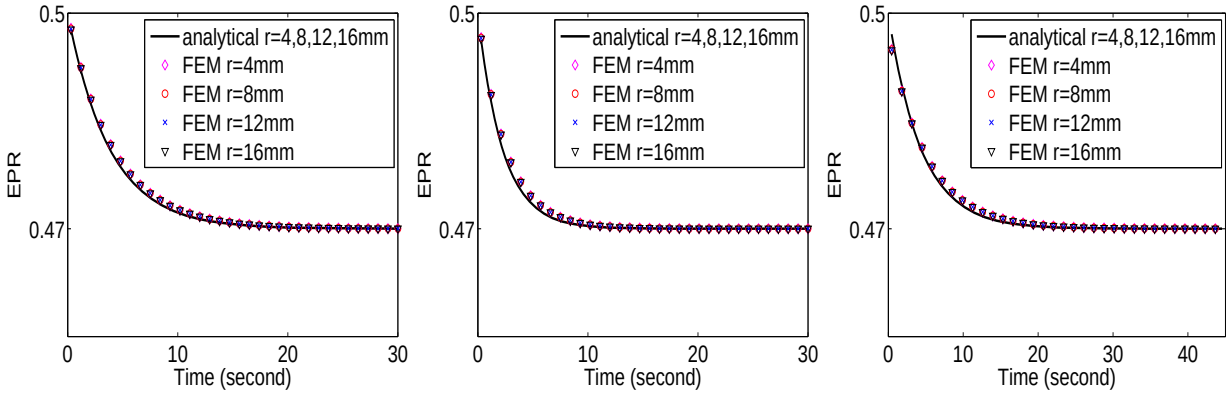

(A) (B) (C)

Figure 2.14: EPR inside the inclusion of sample A (A), sample B (B) and sample C (C)

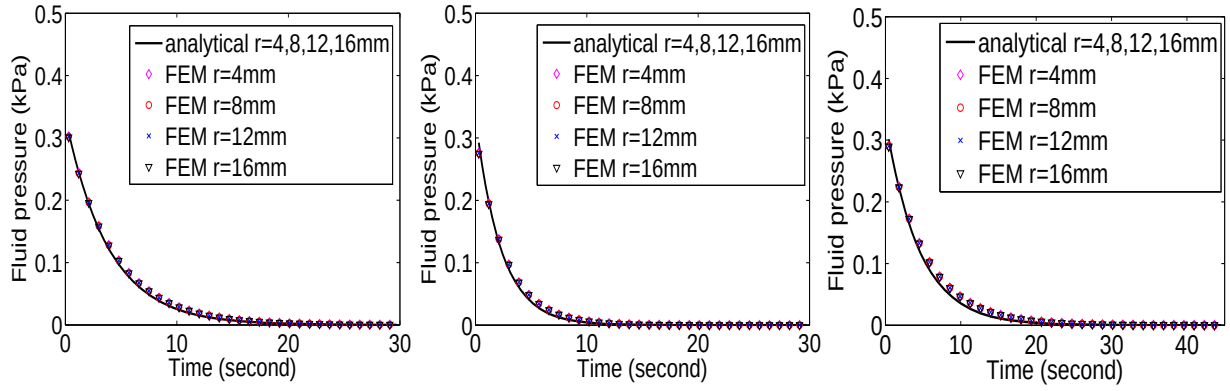

(A) (B) (C)

Figure 2.15: Fluid pressure inside the inclusion of sample A (A), sample B (B) and sample C (C).

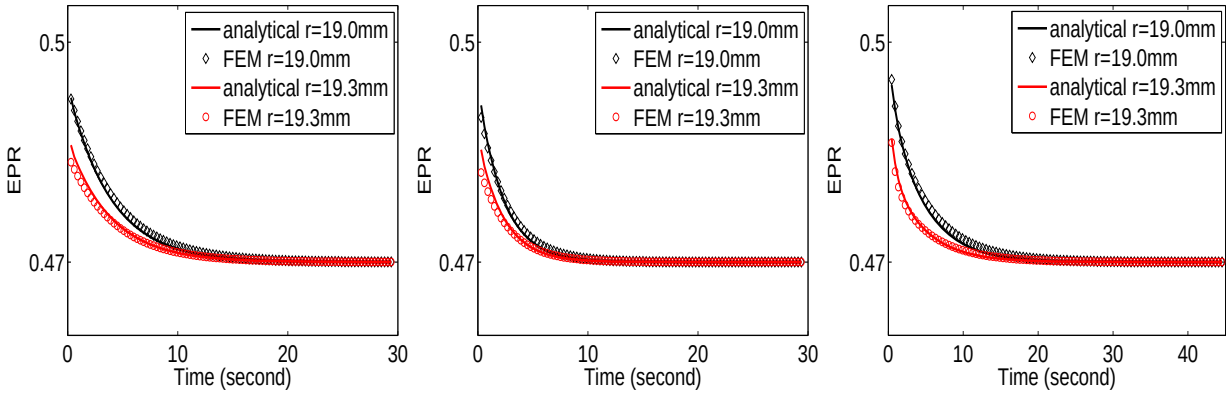

(A) (B) (C)

Figure 2.16: EPRs outside the inclusion of sample A (A), sample B (B) and sample C (C).

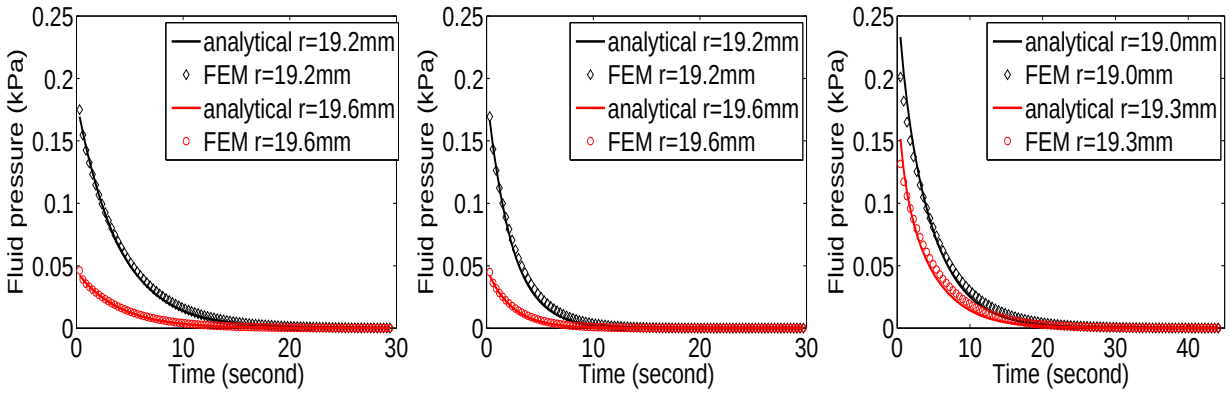

(A) (B) (C)

Figure 2.17: Fluid pressure outside the inclusion of sample A (A), sample B (B) and sample C (C).

In this section, evaluations of the developed analytical expressions of the EPR and fluid pressure are provided for the three samples A, B and C with FEM comparison. Fig. 2.14 (A), (B) and (C) shows the EPR with time at different positions inside the inclusion for samples A, B and C. In these figures, we see that at time $t = 0^+$, the EPR is 0.5 and goes to the drained Poisson's ratio of the material at steady state for all the samples which is consistent with [14]. The time required for the EPR to go to the steady state differs from sample to sample. For sample A, the EPR goes to steady state around 10 second. As in sample A, the effect of interstitial permeability is much

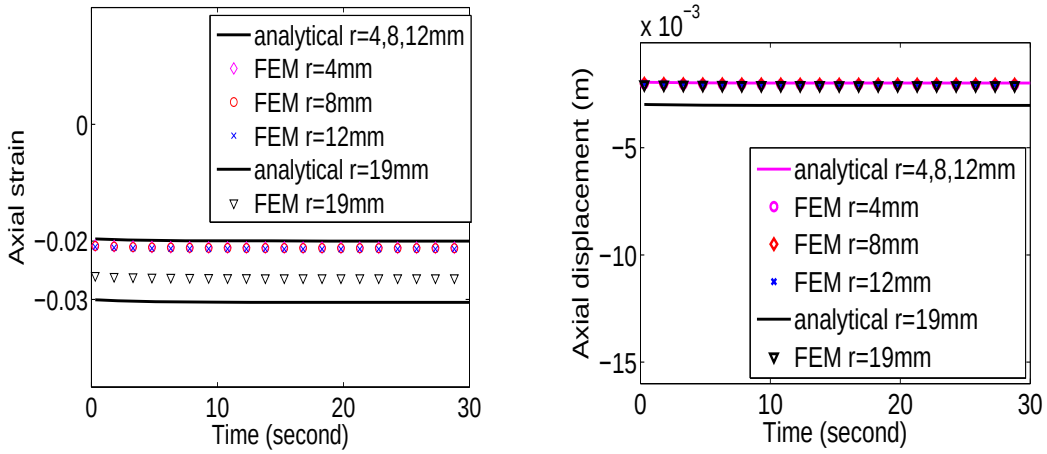

(A) (B)

Figure 2.18: Axial strain (A) and displacement (B) at different positions inside and outside the inclusion for sample A.

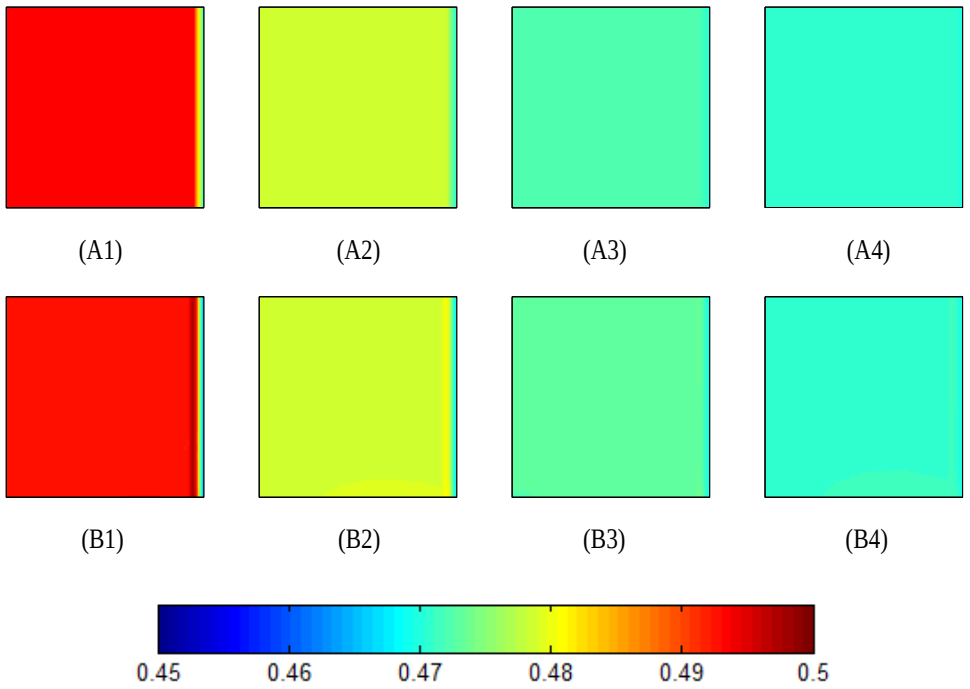

Figure 2.19: EPR at different time points of 1 s, 5 s, 10 s and 15 s from developed analytical model are shown in (A1), (A2), (A3), (A4) and from FEM in (B1), (B2), (B3), (B4) for sample A.

stronger than the effect of vascular permeability, this response can be assumed to be the result from the exudation of the fluid through the interstitium and the fluid flow through vasculatures can be

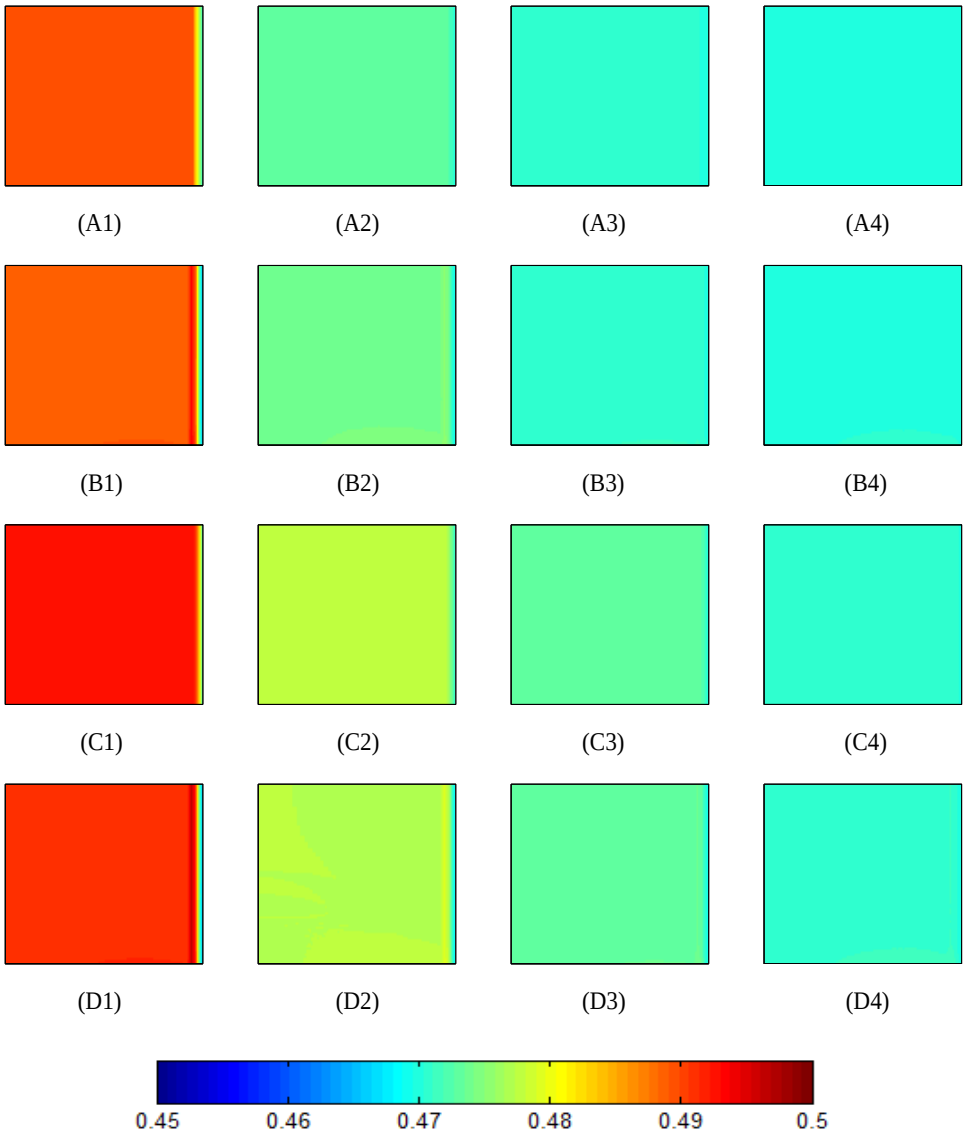

Figure 2.20: EPR at different time points of 1 s, 5 s, 10 s and 15 s from developed analytical model are shown in (A1), (A2), (A3), (A4) from FEM in (B1), (B2), (B3), (B4) for sample B and from developed analytical model in (C1), (C2), (C3), (C4) and from FEM in (D1), (D2), (D3), (D4) for sample C.

assumed to play insignificant role in determining the temporal behavior of EPR inside the inclusion in sample A. For sample B, we see that the EPR goes to steady state around 6 second, which is much faster than sample A. This is because in sample B, the effect of interstitial permeability and vascular permeability are comparable and their impacts add up to dictate the behavior of EPR inside the tumor. For sample C, the vascular permeability dominates and we see that the EPR goes

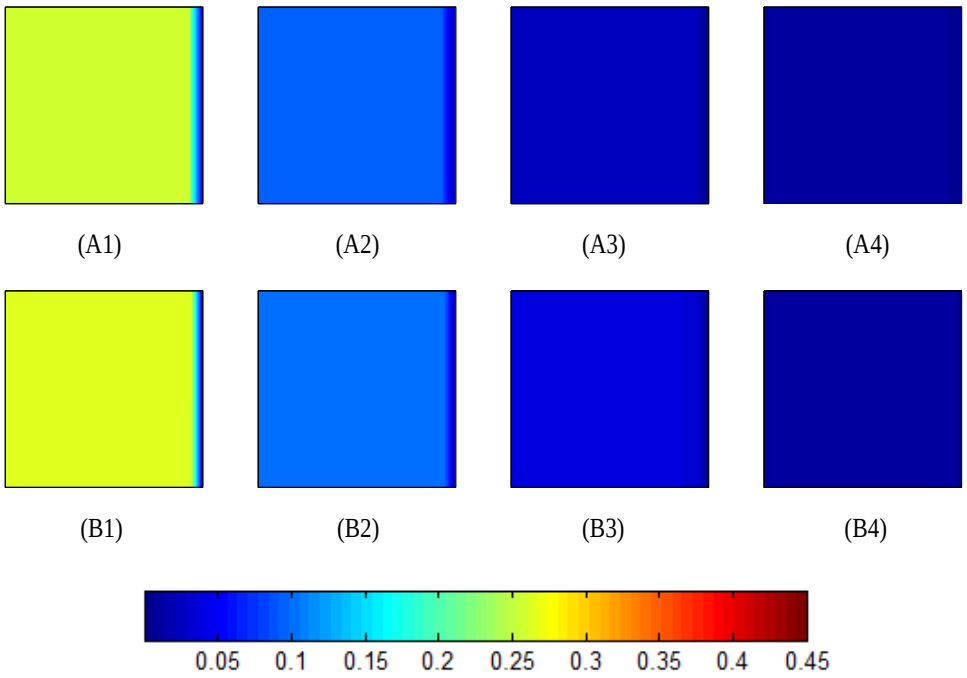

Figure 2.21: Fluid pressures (in kPa) at different time points of 1 s, 5 s, 10 s and 15 s from developed analytical model are shown in (A1), (A2), (A3), (A4) and from FEM in (B1), (B2), (B3), (B4) for sample A.

to the steady state around 12 s. For all the samples, A, B and C, the EPRs inside the inclusion are spatially constant, which corroborate with the results found in [13, 97]. Fig. 2.15 (A), (B) and (C) shows the fluid pressure with time at different positions inside the inclusion for samples A, B and C. The fluid pressure is $\sigma_0/3$ at $t = 0^+$, which goes to zero at steady state. The temporal response of the fluid pressure also matches with the temporal behavior of the EPR for all the samples.

Fig. 2.16 (A), (B) and (C) shows the EPR with time at different positions outside the inclusion. At time $t = 0^+$, the EPR outside the inclusion is close to 0.5, and goes to the drained Poisson's ratio of the material at steady state. The EPR outside the inclusion is seen as spatially dependent for all the samples, whereas we saw that the EPR inside the inclusion is independent of the spatial position. This is because of the zero fluid pressure condition at the periphery of the sample. Fig. 2.17 (A), (B) and (C) shows the fluid pressure with time at different positions outside the inclusion. The fluid pressure is less than $\sigma_0/3$ at $t = 0^+$, which goes to zero at large time. The reduced value

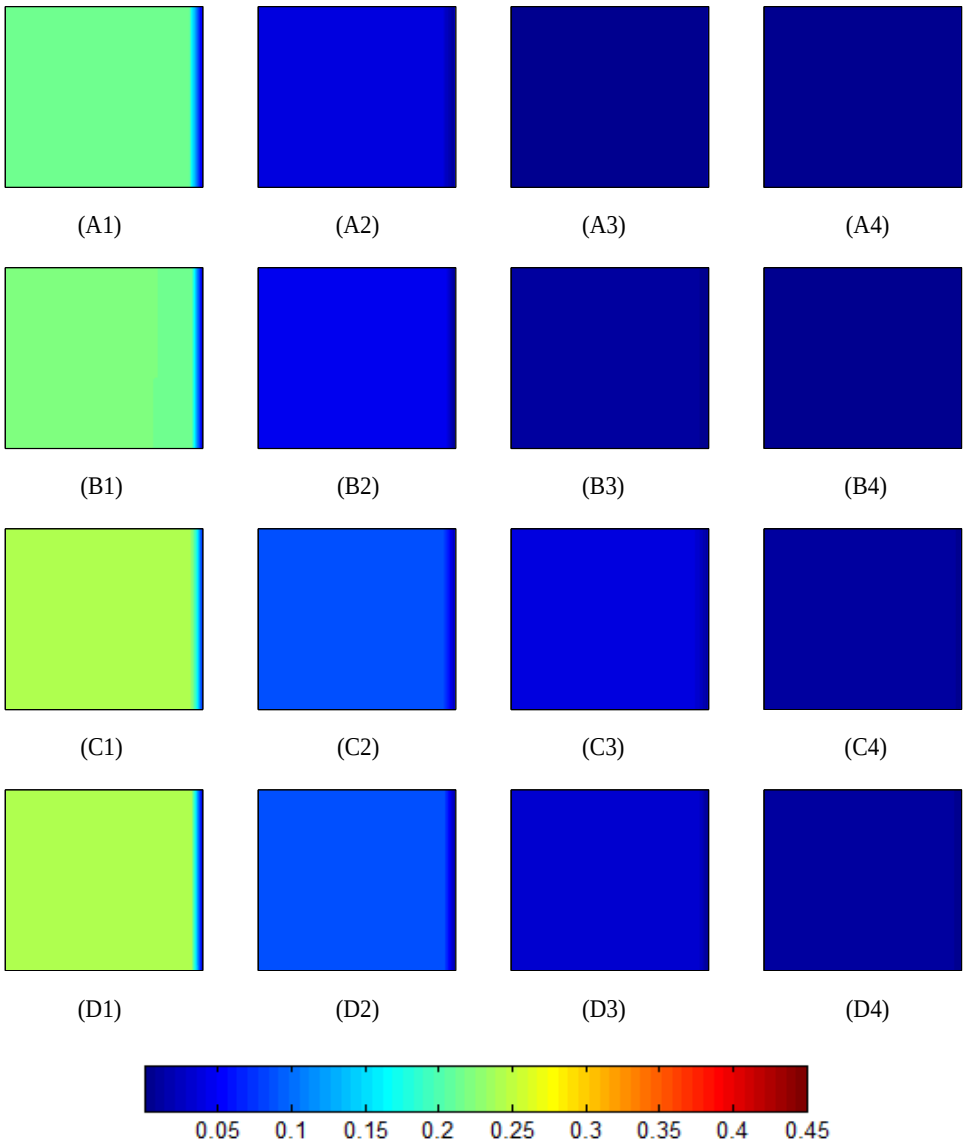

Figure 2.22: Fluid pressures (in kPa) at different time points of 1 s, 5 s, 10 s and 15 s from developed analytical model are shown in (A1), (A2), (A3), (A4) from FEM in (B1), (B2), (B3), (B4) for sample B and from developed analytical model in (C1), (C2), (C3), (C4) and from FEM in (D1), (D2), (D3), (D4) for sample C.

of the fluid pressure from $\sigma_0/3$ at $t = 0^+$ is because of the additional term in eq. (2.121), which incorporates the impact of the fluid pressure inside the inclusion region on fluid pressure in the outside region. The fluid pressure outside the inclusion is also spatially dependent like the EPR outside the inclusion.

The axial strain and displacement inside and outside the inclusion for sample A are shown in

Fig. 2.18. In this figure, it is demonstrated that the axial strain and displacements at different radius values of the sample inside and outside the inclusion are almost identical and almost time-invariant. A small deviation between the results from the analytical model and the FEM for the axial strain and displacement can be observed outside the inclusion. It should be noted that the axial shear and lateral shear strains are zero (or negligible) both inside and outside the inclusion for the analyzed cases.

Fig. 2.19 and Fig. 2.20 shows the time evolution of the EPR for each of the samples described in Table 2.3. From these images, we see that for all the samples, at time $t = 0^+$, the EPR remains 0.5 in the inclusion and background regions and assumes the value of drained Poisson's ratio at large time. The time evolution of fluid pressure for analytical model and FEM are plotted for samples A, B and C in Fig. 2.21 and Fig. 2.22. The fluid pressure starts at $\sigma_0/3$ in the inclusion region and less than $\sigma_0/3$ in the background region and goes to zero at steady state. The temporal nature of the EPR and fluid pressure images are dependent on the material properties of the inclusion and background of the sample.

Table 2.4 summarizes the results of the error analyses. From this table, we observe that, with respect to the effective Poisson's ratio, the error is below 0.03% in the inclusion and below 0.46% in the background. With respect to the fluid pressure, the error is below 0.11% in the inclusion while it becomes larger outside the inclusion, but still below 0.54%. These results demonstrates the correctness of the proposed theoretical model with respect to an established FEM software.

Table 2.4: RMSE results

Sample name	Error in EPR estimation inside inclusion (%)	Error in EPR estimation outside inclusion (%)	Error in fluid pressure estimation inside inclusion (%)	Error in fluid pressure estimation outside inclusion (%)
A	0.02	0.43	0.09	0.44
B	0.02	0.46	0.11	0.53
C	0.03	0.45	0.05	0.54

2.2.3 Poroelastic sample with cylindrical inclusion in stress relaxation experiment

2.2.3.1 When inclusion is less permeable than the background

The analytical expression for the radial effective Poisson's ratio inside the inclusion can be written as [101]

$$\begin{aligned}\Psi_i(r,t) &= \frac{\epsilon_{rr,i}}{\epsilon_0}(r,t) \\ &= \nu_i + \sum_{n=1}^{\infty} \frac{J_0(\alpha_n) - \frac{1-2\nu_i}{1-\nu_i}\left\{J_0(\alpha_n\frac{r}{a}) - \frac{J_1(\alpha_n\frac{r}{a})}{\alpha_n\frac{r}{a}} + \frac{J_1(\alpha_n)}{\alpha_n}\right\}}{\frac{1}{1-\nu_i}J_0(\alpha_n) - \alpha_n J_1(\alpha_n)} \times \exp(-\frac{\alpha_n^2 H_{Ai} k_i t}{a^2}),\end{aligned} \tag{2.128}$$

where ϵ_0 is the applied strain, α_n are the roots of $J_1(x) - \frac{1-\nu_i}{1-2\nu_i}xJ_0(x) = 0$, J_0 and J_1 are the Bessel functions of zeroth and first order. The fluid pressure inside the inclusion can be expressed as

$$p_i(r,t) = \mu_i\epsilon_0 \sum_{n=1}^{\infty} \frac{J_0(\alpha_n\frac{r}{a})}{\frac{1}{2(1-\nu_i)}J_0(\alpha_n) - \frac{\alpha_n}{2}J_1(\alpha_n)} \exp(-\frac{\alpha_n^2 H_{Ai} k_i t}{a^2}), \tag{2.129}$$

where μ_i is the shear modulus of the inclusion.

The solution for the fluid pressure outside the inclusion can be written as

$$\begin{aligned}p_b(r,t) &= -\mu_i\epsilon_0\pi \sum_{n=1}^{\infty} \frac{J_0(\beta_n a)J_0(\beta_n b)U(\beta_n r)}{J_0^2(\beta_n a) - J_0^2(\beta_n b)} \\ &\times \sum_{m=1}^{\infty} \frac{J_0(\alpha_m)}{\frac{1}{1-\nu_i}J_0(\alpha_m) - \alpha_m J_1(\alpha_m)} \frac{e^{-\frac{\alpha_m^2}{a^2}C_i t} - e^{-\beta_n^2 C_b t}}{\frac{\beta_n^2 C_b a^2}{\alpha_m^2 C_i} - 1} f(t) \\ &+ \mu_i\epsilon_0 \frac{\log(r/b)}{\log(a/b)} \sum_{m=1}^{\infty} \frac{J_0(\alpha_m)}{\frac{1}{1-\nu_i}J_0(\alpha_m) - \alpha_m J_1(\alpha_m)} e^{-\frac{\alpha_m^2}{a^2}C_i t} f(t) \\ &+ \mu_b\epsilon_0\pi \sum_{n=1}^{\infty} \frac{J_0(\beta_n a)U(\beta_n r)e^{-\beta_n^2 C_b t}}{J_0(\beta_n a) + J_0(\beta_n b)},\end{aligned} \tag{2.130}$$

where μ_b is the shear modulus of the background, β_n are the roots of $C_1(x) = J_0(xa)Y_0(xb) - Y_0(xa)J_0(xb) = 0$. Y_0 is the modified Bessel function of first order. $C_b = H_{Ab}k_b$, H_{Ab} and k_b are the aggregate modulus and interstitial permeability of the background and b is the radius of the

Table 2.5: Description of the simulated cylindrical media (where inclusion has lower permeability than the background) used in the study

Sample name	E_b (kPa)	E_i (kPa)	k_b (m$^4N^{-1}s^{-1}$)	k_i (m$^4N^{-1}s^{-1}$)	ν_b	ν_i	a (mm)	b (mm)
A	1	1.29	1.37×10^{-8}	1.37×10^{-11}	0.3	0.3	10	20
B	1	1.29	1.37×10^{-8}	1.37×10^{-11}	0.3	0.3	8	40
C	1	2	1.37×10^{-8}	1.37×10^{-11}	0.2	0.2	8	40

sample.

We can write the expression for the effective Poisson's ratio outside the inclusion as

$$\Psi_b(r,t) = \frac{\epsilon_{rr,b}(r,t)}{\epsilon_0} = \nu_b - \frac{a\nu_b}{(\nu_b - 1)r}\left(\nu_b - \frac{1}{a\epsilon_0}u_i(a,t)\right), \tag{2.131}$$

where ν_b is the Poisson's ratio of the background and u_i is the displacement inside the inclusion. This equation demonstrates that temporal behavior of the effective Poisson's ratio in the background region is controlled by the radial displacement at the interface of the inclusion and the background.

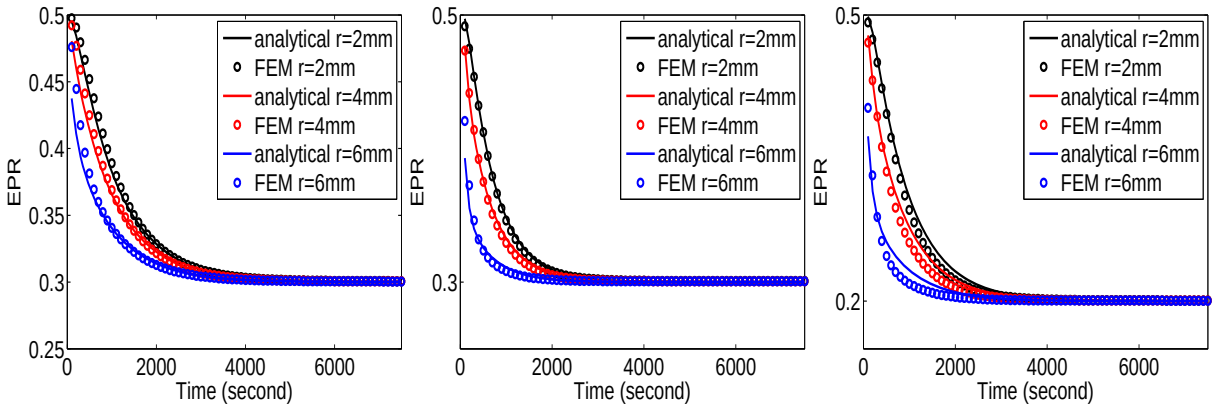

Figure 2.23: Effective Poisson's ratio inside the inclusion at different positions for sample A (A), sample B (B) and sample C (C).

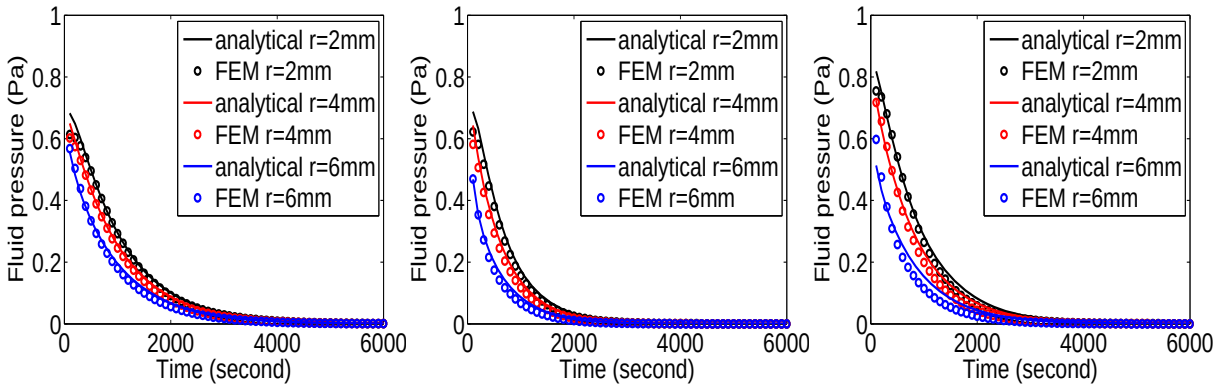

Figure 2.24: Fluid pressure inside the inclusion at different positions for sample A (A), sample B (B) and sample C (C).

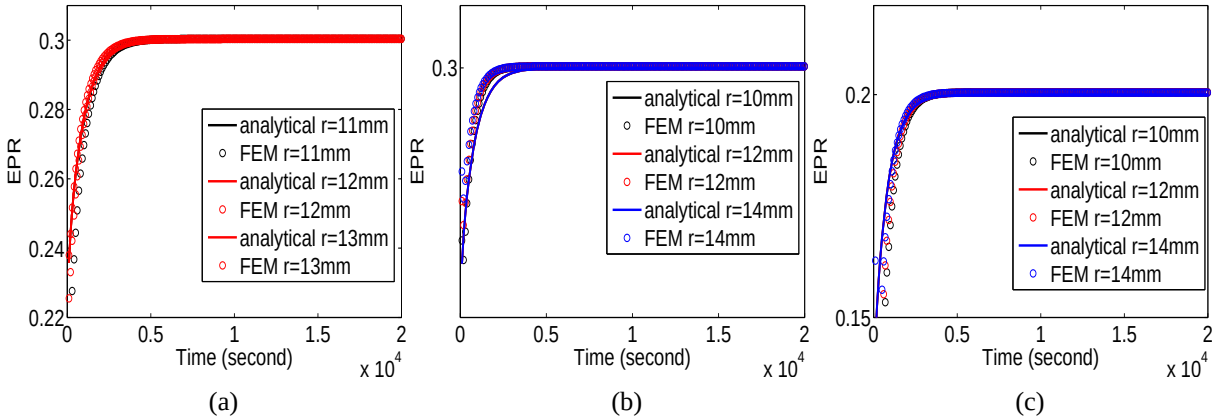

Figure 2.25: Effective Poisson's ratio outside the inclusion at different positions for sample A (A), sample B (B) and sample C (C).

Results The effective Poisson's ratios for samples A, B and C at 3 different radial positions inside the inclusion are shown in Figs. 2.23 (A), (B) and (C). In these figures, we see that the effective Poisson's ratios computed by the analytical model (solid lines) and measured from the corresponding finite element method (FEM) simulations (dotted lines) start at 0.5 at $t = 0^+$ and reach the drained Poisson's ratio of the material at steady state. The detail of FEM simulations can be found in [101]. The corresponding fluid pressures predicted by the analytical model and those

computed by the FEM simulations for samples A, B and C are shown in Figs. 2.24 (A), (B) and (C). The fluid pressures start at a value slightly higher than $\mu_i\epsilon_0$ at $t = 0^+$ and reach zero at steady state. These observations are consistent with [14] for uniform poroelastic cylinders.

Figs. 2.25 (A), (B) and (C) show the results obtained for the effective Poisson's ratio in the background (i.e., outside the inclusion) for samples A, B and C. Specifically, the figures show the effective Poisson's ratio predicted by the theoretical model (solid lines) and the effective Poisson's ratio from the corresponding simulations (dotted lines) at 3 different radial distances. In all cases, the effective Poisson's ratio is at its lowest value at $t = 0^+$ and then reaches the drained Poisson's ratio value of the material at steady state ($t = \infty$).

2.2.3.2 When inclusion is more permeable than the background

The equation for the effective Poisson's ratio (EPR) inside the inclusion can be written as [109]

$$\Psi_i(t) = \frac{\epsilon_{rr,i}(t)}{\epsilon_0} = \nu_i + \frac{1-2\nu_i}{2}\exp\left(-\frac{t}{\tau_\epsilon}\right), \tag{2.132}$$

where $\tau_{\epsilon,i} = \frac{a(1-\nu_i)}{H_{Ai}\frac{k_b}{b-a}}$.

The fluid pressure inside the inclusion can be determined as

$$p_i(t) = \frac{E_i}{2(1+\nu_i)}\epsilon_0\exp\left(-\frac{t}{\tau_{\epsilon,i}}\right) = \mu_i\epsilon_0\exp\left(-\frac{t}{\tau_{\epsilon,i}}\right). \tag{2.133}$$

The solution for the fluid pressure outside the inclusion can be written as

$$\begin{aligned} p_b(r,t) = \mu_i\epsilon_0\pi\sum_{n=1}^{\infty}\frac{\beta_n^2 J_0(\beta_n a)J_0(\beta_n b)U(\beta_n r)}{J_0^2(\beta_n a) - J_0^2(\beta_n b)}\frac{e^{-\frac{t}{\tau_{\epsilon,i}}} - e^{-\beta_n^2 C_b t}}{\beta_n^2 - \frac{1}{\tau_{\epsilon,i}C_b}} \\ +\mu_b\epsilon_0\pi\sum_{n=1}^{\infty}\frac{J_0(\beta_n a)U(\beta_n r)e^{-\beta_n^2 C_b t}}{J_0(\beta_n) + J_0(b\beta_n)}. \end{aligned} \tag{2.134}$$

Table 2.6: Description of the cylindrical samples (where inclusion has higher permeability than the background) used in the current study

Sample name	E_b (kPa)	E_i (kPa)	k_b $(m^4N^{-1}s^{-1})$	k_i $(m^4N^{-1}s^{-1})$	ν_b	ν_i	a (mm)	b (mm)
F	32.78	42.28	1.875×10^{-13}	1.875×10^{-10}	0.30	0.30	3.6	4
G	32.78	42.28	1.875×10^{-13}	9.375×10^{-12}	0.20	0.20	3.6	4
H	32.78	65.56	1.875×10^{-13}	3.75×10^{-12}	0.30	0.30	3.6	4

The equation for the EPR in the background region can be written as

$$\Psi_b(t) = \frac{\epsilon_{rr,b}(t)}{\epsilon_0} = \nu_b + \frac{1-\nu_b}{H_{Ab}\epsilon_0} p_b(r,t). \tag{2.135}$$

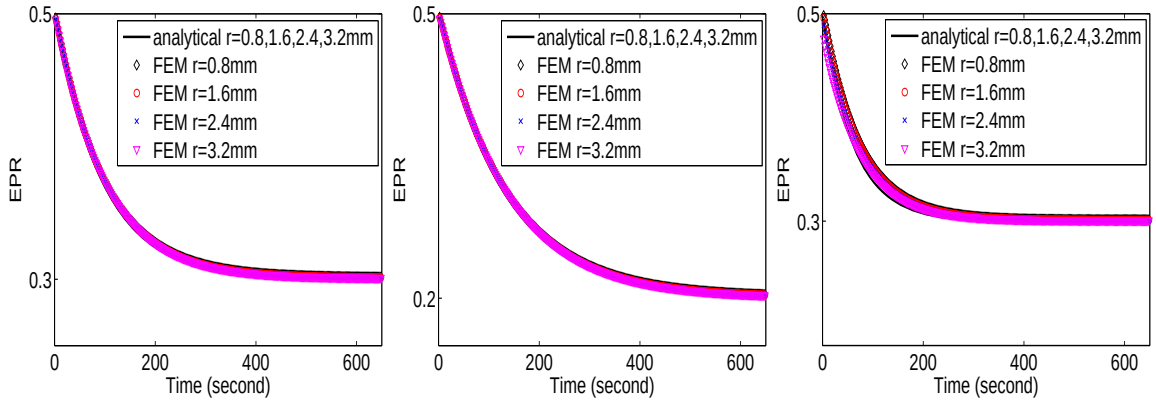

(a) (b) (c)

Figure 2.26: EPR inside the inclusion at different positions for sample F (a), sample G (b) and sample H (c).

Results Fig. 2.26 shows the EPR as a function of time at different positions inside the inclusion computed from the developed analytical model and FEM for samples F, G and H. The inclusion in sample F has 1000 times higher interstitial permeability than the background, whereas the inclusion in sample G has 50 times higher interstitial permeability than the background and the inclusion in sample H has 20 times higher interstitial permeability than the background . Samples F and H

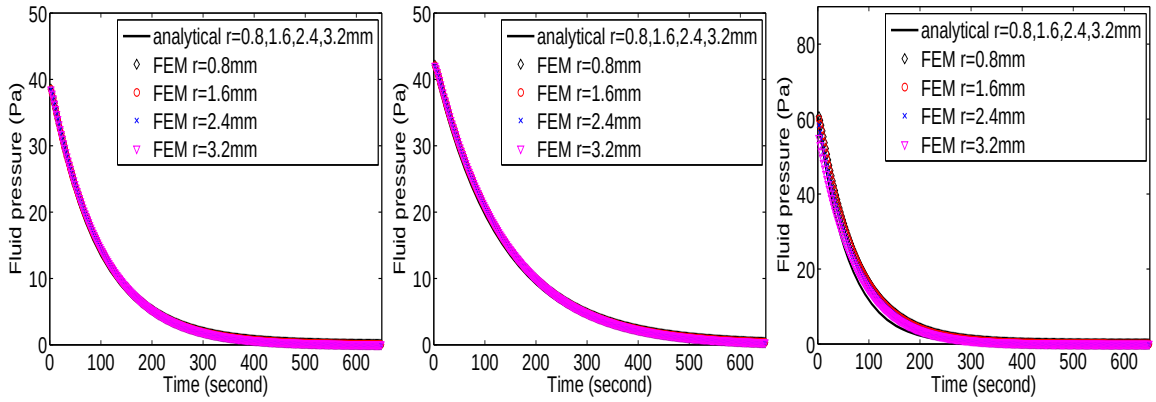

(a) (b) (c)

Figure 2.27: Fluid pressure inside the inclusion at different positions for sample F (a), sample G (b) and sample H (c).

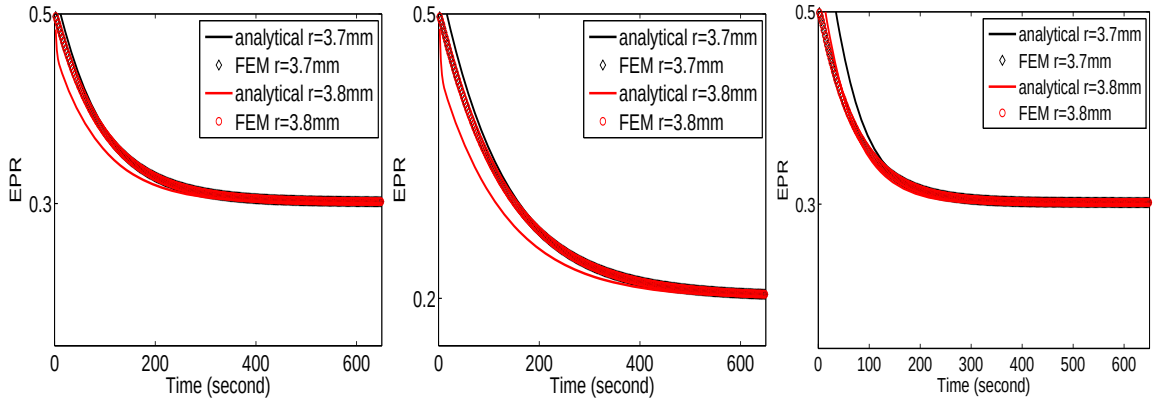

(a) (b) (c)

Figure 2.28: EPR outside the inclusion at different positions for sample F (a), sample G (b) and sample H (c).

have Poisson's ratio of 0.3 and sample G has Poisson's ratio of 0.2 for both the background and the inclusion. Young's modulus contrast between the inclusion and background is 1.29 in sample F and G and 2 in sample H. In Fig. 2.26, we see that, for both the analytical model and FEM, the EPR inside the inclusion does not vary spatially, and we obtain the same time profiles of EPR for all the radial positions. From these curves, we also see that at time $t = 0^+$, the EPR is 0.5 and tends to the drained Poisson's ratio of the material at steady state, which is consistent with previous

literature [14].

Fig. 2.27 shows the fluid pressure as a function of time at different positions inside the inclusion from the analytical model and FEM. We see from this figure that the fluid pressure is also spatially invariant, and fluid pressures at different radial positions inside the inclusion change in the same manner with time. We also observe that the fluid pressure is $\mu_i \epsilon_0$ at $t = 0^+$ and goes to zero at steady state for each sample. Fig. 2.28 shows the EPR as a function of time at different positions outside the inclusion. At time $t = 0^+$, the EPR outside the inclusion is 0.5 and tends to the drained Poisson's ratio of the material at steady state. The time profile of the EPR outside the inclusion is dependent on the radial position. Fig. 2.29 shows the fluid pressure as a function of time at different positions outside the inclusion. The fluid pressure is lower than $\mu_b \epsilon_0$ at $t = 0$ and goes to zero as time increases. The fluid pressure is lower than $\mu_b \epsilon_0$ at $t = 0^+$ because of the additional term in eq. (2.134), which incorporates the impact of the fluid pressure inside the inclusion region on the fluid pressure in the outside region. The time profile of the fluid pressure outside the inclusion is also spatially variant.

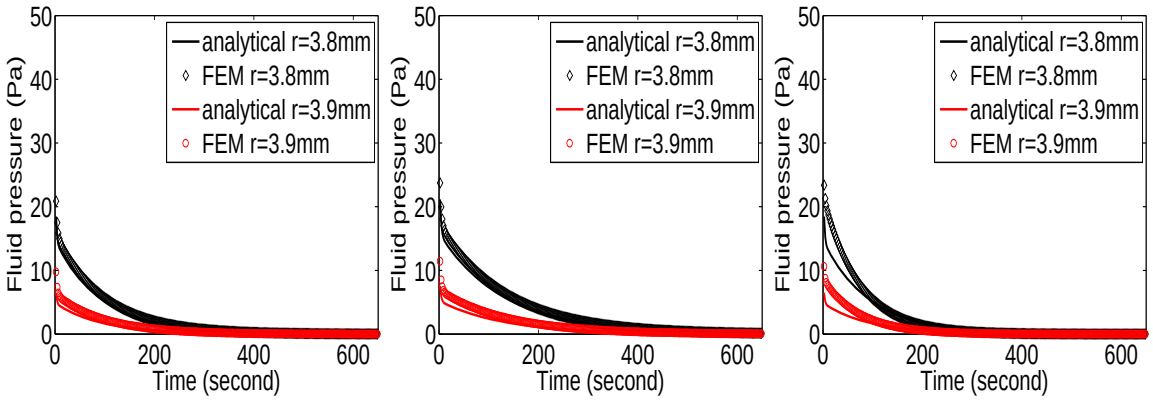

Figure 2.29: Fluid pressure outside the inclusion at different positions for sample F (a), sample G (b) and sample H (c).

2.3 Poroelastic sample with spherical inclusion in creep experiment

2.3.1 Analytical model

The poroelastic sample with a spherical inclusion inside it used in the analysis of this paper is shown in Fig. 2.30. In this figure, we see that sample is of cylindrical shape, where the inclusion inside the sample is of spherical shape.

Based on the theory of Eshelby, the applied uniaxial stress (σ) from the top of the sample in an elastography experiment (see Fig. 2.30) is inflicted over the full outer surface of the spherical inclusion (tumor) [110]. Therefore, when we are interested in the analysis of strains, fluid pressure inside the tumor, the problem can be thought as one of a poroelastic sphere under a uniform compressive stress (σ_T) over its outer surface. The stress σ_T over the sphere can be computed using Eshelby's theory from the applied stress σ, geometry and Young's modulus and Poisson's ratio of the tumor. In such case, the volumetric strain and fluid pressure become functions of only R and t inside the poroelastic tumor [111]. Consequently, the problem can be simplified from cylindrical coordinate system to spherical coordinate system. Based on that, we derive the formulations for different parameters inside the inclusion in spherical coordinate below.

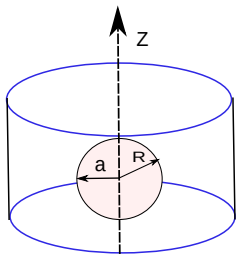

Figure 2.30: A schematic of a cylindrical sample of a poroelastic material with a spherical poroelastic inclusion of radius a.

The first basic equation for spherical symmetric poroelasticity is the continuity equation of the

pore fluid which can be written as [13, 93]

$$\alpha \frac{d\epsilon}{dt} + S\frac{dp}{dt} + \chi(p) = \frac{k}{\gamma_f}\frac{1}{R}\frac{d^2(pR)}{dR^2}, \tag{2.136}$$

where ϵ is the volume strain, p is the fluid pressure, α is Biot's coefficient, k is the coefficient of permeability, γ_f is the volumetric weight of the pore fluid and S is the storage coefficient. Here $\chi = \chi_V + \chi_L$, with $\chi_V = \frac{L_p S_V}{V}$ and $\chi_L = \frac{L_{PL} S_L}{V}$. L_p and L_{pL} are the permeabilities of the capillary and lymphatic walls. $\frac{S_V}{V}$ and $\frac{S_L}{V}$ are the surface area to volume ratio of the capillary and lymphatic walls. The storage coefficient S is defined as

$$S = \psi C_f + (\alpha - \psi) C_s, \tag{2.137}$$

where ψ is porosity, C_f is the compressibility of the fluid, and C_s is the compressibility of the solid particles. In the case of incompressible constituents, $S = 0$ and $\alpha = 1$. It should be noted that eq. (2.136) can be written for the fluid pressure inside the inclusion, only if the interstitial permeability of the inclusion is much lower than the interstitial permeability of the background, when the interstitial permeability has comparable or dominant effect as the vascular permeability on the mechanical behavior of the inclusion. Eq. (2.136) is applicable in all conditions when the vascular permeability is dominant over the interstitial permeability inside the inclusion.

The volumetric strain ϵ is related to the radial displacement u by

$$\epsilon = \frac{du}{dR} + \frac{2u}{R} = \frac{1}{R^2}\frac{d(uR^2)}{dR}. \tag{2.138}$$

The second basic equation is the equation of radial equilibrium, which can be expressed as

$$\frac{d\sigma_{RR}}{dR} + 2\frac{\sigma_{RR} - \sigma_{TT}}{R} = 0, \tag{2.139}$$

where σ_{RR} and σ_{TT} are the total stresses in radial and tangential directions.

The total stresses can be separated into the effective stresses and the fluid pressure by

$$\sigma_{RR} = \sigma'_{RR} + \alpha p, \;\; \sigma_{TT} = \sigma'_{TT} + \alpha p. \tag{2.140}$$

The equation of radial equilibrium can be written now as

$$\frac{d\sigma'_{RR}}{dR} + 2\frac{\sigma'_{RR} - \sigma'_{TT}}{R} + \alpha\frac{dp}{dR} = 0. \tag{2.141}$$

Using eq. (2.138) and the stress-strain relations

$$\sigma'_{RR} = -\,(K - \frac{2}{3}G)\epsilon - 2G\frac{du}{dR}, \tag{2.142}$$

$$\sigma'_{TT} = -\,(K - \frac{2}{3}G)\epsilon - 2G\frac{u}{R}, \tag{2.143}$$

the equation of equilibrium can be expressed in terms of the volume strain as

$$(K + \frac{4}{3}G)\frac{d\epsilon}{dR} = \alpha\frac{dp}{dR}, \tag{2.144}$$

where K is the compression modulus of the poroelastic material in fully drained conditions, and G is the its shear modulus.

Let the aggregate modulus be $H_A = K + \frac{4}{3}G$ [14]. So, we can write from eq. (2.144)

$$H_A\frac{d\bar{\epsilon}}{dR} = \alpha\frac{d\bar{p}}{dR}. \tag{2.145}$$

Integrating with respect to R,

$$\begin{aligned} H_A\epsilon &= \alpha\bar{p} + P_T \\ \epsilon &= \frac{1}{H_A}(\alpha\bar{p} + P_T), \end{aligned} \tag{2.146}$$

where P_T is an integration constant. Using $S = 0, \alpha = 1$, the continuity equation in eq. (2.136)

can be written as

$$\frac{d\epsilon}{dt} = \frac{k}{\gamma_f}\left(\frac{d^2p}{dR^2} + \frac{2}{R}\frac{dp}{dR}\right) - \chi(p). \tag{2.147}$$

If we replace the volumetric strain with the fluid pressure using eq. (2.146), we obtain

$$\frac{1}{H_A}\frac{d(p+Q)}{dt} = k\left(\frac{d^2p}{dR^2} + \frac{2}{R}\frac{dp}{dR}\right) - \chi(p), \tag{2.148}$$

which results in

$$\frac{d(p+Q)}{dt} = H_A k\left(\frac{d^2p}{dR^2} + \frac{2}{R}\frac{dp}{dR}\right) - H_A\chi(p). \tag{2.149}$$

Let us assume that $p = p'e^{-H_A\chi t}$, $Q = Q'e^{-H_A\chi t}$, $\epsilon = \epsilon' e^{-H_A\chi t}$. Using these new variables, we get

$$-H_A\chi(p'+Q')e^{-H_A\chi t} + e^{-H_A\chi t}\frac{d(p+Q)}{dt} + H_A\chi p'e^{-H_A\chi t} = H_A k e^{-H_A\chi t}\left(\frac{d^2p}{dR^2} + \frac{2}{R}\frac{dp}{dR}\right). \tag{2.150}$$

Simplifying this equation, we obtain

$$-H_A\chi Q' + \frac{d\epsilon'}{dt} = H_A k\left(\frac{d^2\epsilon'}{dR^2} + \frac{2}{R}\frac{d\epsilon'}{dR}\right). \tag{2.151}$$

In this equation, Q' is a constant which depends on the boundary condition. If it is possible to find a solution for the volumetric strain, which satisfies

$$\left(\frac{d^2\epsilon'}{dR^2} + \frac{2}{R}\frac{d\epsilon'}{dR}\right) - \frac{1}{H_A k}\frac{d\epsilon'}{dt} = 0 \tag{2.152}$$

and all the boundary and initial conditions, Q' becomes zero. Eq. (2.152) is comparable with eq. (14) of supplementary material of [16], eq. (2) of [18] and eq. (1) of [22].

We now define the following dimensionless variables,

$$\hat{R} = \frac{R}{a}, \hat{t} = \frac{a^2 t}{H_A k}. \tag{2.153}$$

With help of these dimensionless variables, we can write for the volumetric strain from eq. (2.152)

$$\frac{\partial \epsilon'}{\partial \hat{t}} = \left(\frac{\partial^2 \epsilon'}{\partial \hat{R}^2} + \frac{2}{\hat{R}} \frac{\partial \epsilon'}{d\hat{R}} \right). \tag{2.154}$$

To remove the partial derivative in $\hat{R}$, we introduce

$$\epsilon'(\hat{R}, t) = \frac{1}{\hat{R}} \psi(\hat{R}, t). \tag{2.155}$$

Based on this, eq. (2.154) simplifies to

$$\frac{\partial \psi}{\partial \hat{t}} = \frac{\partial^2 \psi}{\partial \hat{R}^2}. \tag{2.156}$$

Taking Laplace transform of eq. (2.156), we obtain

$$\frac{d^2 \bar{\psi}}{d\hat{R}^2} - s\bar{\psi} = 0. \tag{2.157}$$

In this equation, $\bar{\psi}$ denotes the Laplace transform of ψ and the initial condition $\psi(\hat{R}, 0) = 0$ has been used. The general solution of eq. (2.157) can be written as

$$\bar{\psi}(\hat{R}, s) = A(s) \cosh(\sqrt{s}\hat{R}) + B(s) \sinh(\sqrt{s}\hat{R}). \tag{2.158}$$

Therefore using eq. (2.155), expression for the volumetric strain $\bar{\epsilon}(\hat{R}, s)$ can be written as

$$\bar{\epsilon'}(\hat{R}, s) = \frac{A(s)}{\hat{R}} \cosh(\sqrt{s}\hat{R}) + \frac{B(s)}{\hat{R}} \sinh(\sqrt{s}\hat{R}). \tag{2.159}$$

2.3.2 Solution inside the inclusion

The first boundary condition for the volumetric strain inside the inclusion can be written as [111]

$$\hat{R} = 1, \quad \epsilon_i(1, \hat{t}) = -\frac{(1+\nu_e)(1-2\nu_e)}{(1-\nu_e)} \frac{\sigma_T}{E_e}, \hat{t} > 0. \tag{2.160}$$

where ν_e is the lateral to axial strain ratio inside the tumor, E_e is the effective Young modulus calculated inside the tumor by taking ratio of σ_T to axial strain inside the tumor and σ_T is a constant normal traction measured per unit bulk area of the surface of the inclusion. The second boundary condition states that the volumetric strain is not infinite at the canter of the inclusion, i.e.,

$$\hat{R} = 0, \quad |\epsilon_i(0, \hat{t})| < \infty, \hat{t} \geq 0. \tag{2.161}$$

Using eqs. (2.160) and (2.161), we can write for the volumetric strain inside the inclusion from eq. (2.159) as [111]

$$\bar{\epsilon_i'}(\hat{R}, s) = -\frac{\sigma_T}{E_e} \frac{(1+\nu_e)(1-2\nu_e)}{\{[(1-\nu_e)s + 2(1-2\nu_e)\sinh(\sqrt{s}) - 2(2-2\nu_e)\sqrt{s}\cosh(\sqrt{s})]\}} \frac{\sinh(\sqrt{s}\hat{R})}{\hat{R}}. \tag{2.162}$$

The inverse Laplace transform of this equation can be written as [111]

$$\epsilon_i'(\hat{R}, \hat{t}) = -\frac{3(1-2\nu_e)}{E_e}\sigma_T \times \left(1 + \frac{4}{3}\sum_{n=1}^{\infty} \frac{(1-2\nu_e)(1+\nu_e)}{[2(1+\nu_e)(1-2\nu_e) - (1-\nu_e)^2 x_n]} \times \frac{\sinh(\hat{R}\sqrt{x_n})\exp(-x_n\hat{t})}{\hat{R}\sinh(\sqrt{x_n})}\right), \tag{2.163}$$

where x_n are the roots of of the characteristics function

$$C(x) = \tan(\sqrt{x}) - \frac{2(1-2\nu_e)\sqrt{x}}{[2(1-2\nu_e) - (1-\nu_e)x]}. \tag{2.164}$$

The characteristics function and the roots are shown in Fig. 2.31. Using (2.153), (2.163) can be

written in time variable t and space variable R as

$$\epsilon_i'(R,t) = -\frac{\sigma_T}{K_e} \times \left(1 + \frac{4}{3}\sum_{n=1}^{\infty} \frac{(1-2\nu_e)(1+\nu_e)}{[2(1+\nu_e)(1-2\nu_e) - (1-\nu_e)^2 x_n]} \times \frac{\sinh(\frac{R}{a}\sqrt{x_n})\exp\left(-x_n \frac{H_{Ai} k_i t}{a^2}\right)}{\frac{R}{a}\sinh(\sqrt{x_n})}\right), \quad (2.165)$$

where $K_e = \frac{E_e}{3(1-\nu_e)}$. Eshelby's inclusion formulation can be used to calculate σ_e and K_e, i.e., E_e and ν_e [72] from applied load σ_0, the Young's moduli and Poisson's ratios of the inclusion and background.

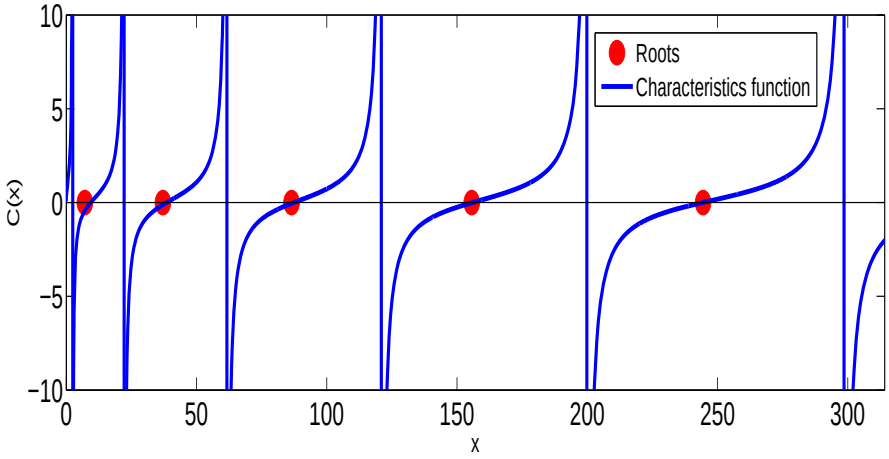

Figure 2.31: The characteristics function and roots

By changing the variable from ϵ' to ϵ, in true variable, the equation for the volumetric strain can be written as

$$\epsilon_i(R,t) = -\frac{\sigma_T}{K_e} \times \left(1 + \frac{4}{3}\sum_{n=1}^{\infty} \frac{(1-2\nu_e)(1+\nu_e)}{[2(1+\nu_e)(1-2\nu_e) - (1-\nu_e)^2 x_n]} \times \frac{\sinh(\frac{R}{a}\sqrt{x_n})\exp\left(-x_n \frac{H_{Ai} k_i t}{a^2}\right)}{\frac{R}{a}\sinh(\sqrt{x_n})} \exp\left(-H_{Ai}\chi t\right)\right). \quad (2.166)$$

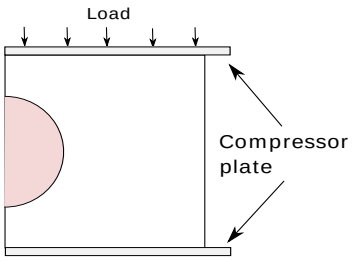

Figure 2.32: The 2D solution plane for the three dimensional sample shown in Fig. 2.30. The sample is compressed between two compressor plates.

2.3.3 Finite element simulation

A commercial finite element simulation software namely ABAQUS, Abaqus Inc, Providence, RI, USA has been used to verify the analytical theories developed in this paper. An “effective stress" principle is used in ABAQUS [102]. In this principle, the total stress acting at a point is assumed to be made up of an average pressure stress in the wetting liquid and an “effective stress" on the solid matrix. Both the inclusion and background of the sample were modeled as a linearly elastic, isotropic, incompressible, permeable solid phase saturated with an incompressible fluid. The sample is compressed from the top and the bottom side was kept static. An instantaneous load of 1 kPa has been applied and kept constant after that. The permeability of the sample was assumed independent of strain and void ratio. Because of cylindrical and spherical symmetry of the sample and inclusion, a 2D solution plane has been analyzed in ABAQUS, which is shown in Fig. 2.32. In this figure, the method of applying compression is also shown. We see that the compression is applied from top and the bottom side is fixed. Two frictionless compressor plates have been used for holding up the sample and exert compression upon it.

The mesh used to model the sample was CAX4RP and has 20718 elements in the solution plane. The dimension of the sample was 20 mm in radius and 40 mm in height. The radius of the spherical inclusion was 7.5 mm. The zero fluid pressure boundary condition on the right hand side of the sample is imposed. The vascular permeability was modeled using seepage coefficient as described in [112].

Nine samples were chosen with different material properties for examining the theories developed in this paper, which are described in Table 2.7. Young's modulus of the normal tissue was chosen as 32.78 kPa based on previous literature [13, 40]. As the tumors can have a broad range of Young's moduli [113, 114], we chose up to ten inclusion-to-background contrasts. The Poisson's ratio is reported in the literature to have a range of values between $0.2 - 0.49$ for both tumors and normal tissues [16, 115, 116]. Poisson's ratio values of $0.4, 0.45$ and 0.47 for the tumors and normal tissues were used. Based on previous literature (Netti et al. [59], [94]), the tumors can have a broad range of interstitial permeability. We used different values of inclusion-to-background permeability contrast $(1, 10, 1000)$ for the different samples. It should be noted that, in most of the literature, the tumor is assumed to be at least five times more permeable than the normal tissue [18, 21–23, 40, 58, 59, 80]. Swartz et al. [94] provides a list of values of interstitial permeability for different types of tumor and normal tissue with a contrast between the interstitial permeability of tumor and the interstitial permeability of the normal tissue of the order of 0 to 3. Jain et al. [50] assumed an equal value of interstitial permeability in the tumor and normal tissue. The vascular permeability of the tumor and normal tissue was chosen based on the reported values in [13, 40].

The time response was recorded for 300 second for each 1 second time step. The total analysis is done in two steps. In the first step, an instantaneous displacement/load is applied which is constant for the next step. The first step is of 1 s and the second step continues upto 300 s. The specific weight of the fluid was taken as $1\text{N}m^{-3}$ to match the definitions of permeability in ABAQUS and in our developed theory.

2.3.4 Error analysis

An error analysis has been done to find the error in results from the developed analytical model in comparison to the results from FEM. The following formula has been used for calculation of root mean squared error (RMSE) in computed volumetric strain from the analytical model.

$$\text{RMSE} = \sqrt{\frac{\sum_t^T \sum_r^R (v_a(t,r) - v_f(t,r))^2}{T \times R}} \times \frac{100 \times R}{\sum_r^R v_f(100,r)}, \tag{2.167}$$

where T is the total number of time samples considered and R is the number of point along radial direction of the inclusion. v_a is the volumetric strain estimated by the analytical model and v_f is the volumetric strain estimated by the FEM. For producing the error values in Table 2.8, we used the first 100 samples, i.e., $T = 100$ and considered 3 radial positions, i.e., $0.8, 2.4$ and 4.0 mm inside the inclusion, which implies that $R = 3$.

2.3.5 Results

To get the instantaneous value of the volumetric strain from the developed analytical model, we use the initial value theorem on the Laplace domain expression shown in eq. (2.163). Putting $s \longrightarrow \infty$ in eq. (2.163), we get $\epsilon_i(t = 0^+) = 0$. The instantaneous values of total radial and circumferential stresses inside and outside the inclusion become zero at the instant the strain/load is applied for which the volumetric strain becomes zero. But the effective stress on the solid matrix is not zero, which initiates the recoiling behavior. The recoiling nature of the solid phase induces a pressure gradient which helps the fluid exudation. When the solid matrix is fully relaxed, the volumetric strain depends only on the bulk modulus of the inclusion and applied strain, which can be found by putting $t \longrightarrow \infty$ in eq. (2.166). The volumetric strain at steady state can be found as σ_e/K_e. Based on this, we can say that at time $t = 0^+$, the solid inside the inclusion acts like a incompressible solid with Poisson ratio of 0.5 and at steady state, the inclusion works as a compressible solid with Poisson ratio of its solid matrix.

Results are provided for all the nine samples with FEM comparison in Figs. 2.33, 2.34 and 2.35. Figs. 2.33-2.35 (A)-(C) show the time evolution of volume strain inside the inclusion of samples I-Q. From these figures, we see that for all the samples, at time $t = 0^+$, the volumetric strain inside the tumor remains 0. With time, the negative volumetric strain increases and reaches to a value that is dependent on the elastic bulk modulus of the tumor and applied compression on the sample. Matching between the results from FEM and developed analytical model can be clearly seen for all the samples.

In Table 2.8, the error in computed volumetric strain from the developed analytical model in comparison to the FEM results are shown. From this table, we see that the error is overall

Table 2.7: Description of the samples used in current study

Sample name	E_b (kPa)	E_i(kPa)	k_b $(m^4N^{-1}s^{-1})$	k_i $(m^4N^{-1}s^{-1})$	χ_b $((Pas)^{-1})$	χ_i $((Pas)^{-1})$	ν_b	ν_i
I	32.78	97.02	1.125×10^{-9}	1.125×10^{-12}	9×10^{-9}	5×10^{-9}	0.47	0.45
J	32.78	97.02	3.189×10^{-9}	3.189×10^{-12}	1.89×10^{-8}	5.67×10^{-8}	0.47	0.45
K	32.78	97.02	1.276×10^{-10}	1.276×10^{-13}	1.89×10^{-8}	5.67×10^{-8}	0.47	0.45
L	32.78	163.90	3.189×10^{-9}	3.189×10^{-12}	1.89×10^{-8}	5.67×10^{-8}	0.47	0.40
M	32.78	327.80	3.189×10^{-9}	3.189×10^{-12}	3.78×10^{-8}	5.67×10^{-8}	0.45	0.40
N	32.78	97.02	1.276×10^{-14}	1.276×10^{-14}	1.89×10^{-7}	5.67×10^{-7}	0.47	0.45
O	32.78	97.02	0.742×10^{-9}	0.742×10^{-12}	5.94×10^{-9}	3.3×10^{-9}	0.47	0.45
P	32.78	97.02	2.54×10^{-14}	1.27×10^{-14}	5.94×10^{-8}	2.83×10^{-7}	0.47	0.45
Q	32.78	163.90	6.38×10^{-9}	6.38×10^{-12}	3.78×10^{-8}	1.134×10^{-7}	0.47	0.40

very small which proves the correctness of the proposed model. The error increases inside the samples, where the inclusion and background has higher contrast in values of Young's modulus and/or Poisson's ratio.

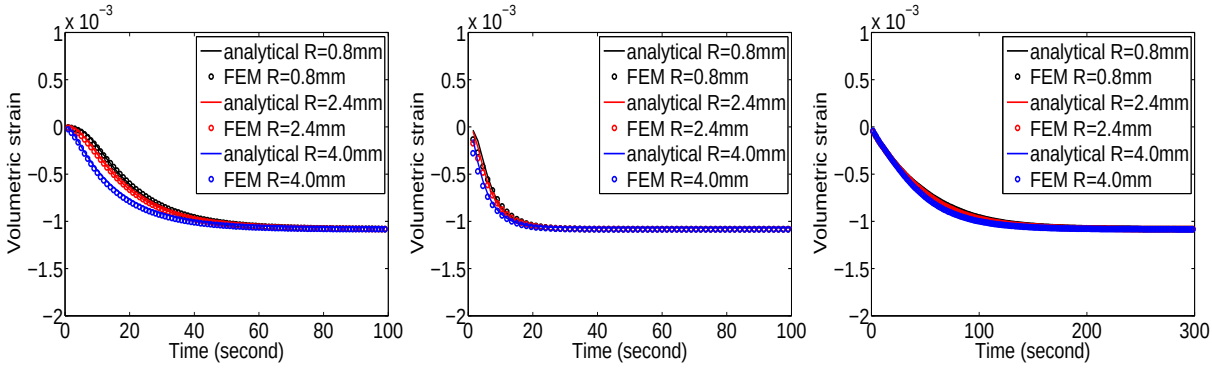

(A) (B) (C)

Figure 2.33: Volumetric strain inside the tumor at different positions for sample I (A), sample J (B) and sample K (C).

2.4 Conclusion

Closed-form analytical expressions are developed for the strains inside a cylindrical/spherical poroelastic inclusion embedded inside a cylindrical poroelastic sample under constant pressure. These model can be thought of general models for the solid tumor embedded inside normal tissues

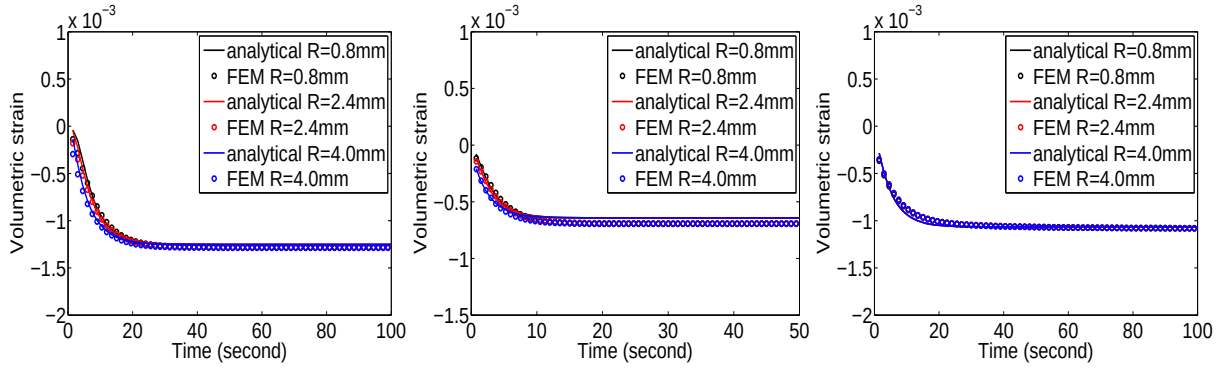

(A) (B) (C)

Figure 2.34: Volumetric strain inside the tumor at different positions for sample L (A), sample M (B) and sample N (C).

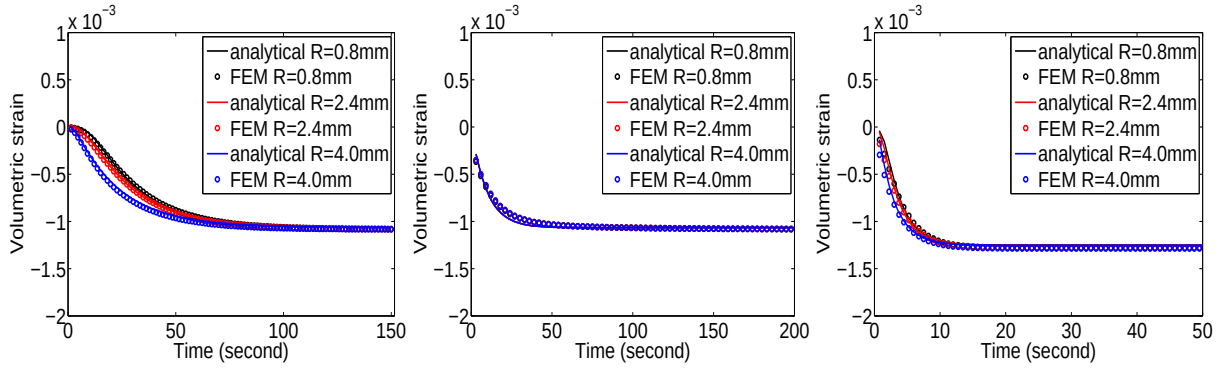

(A) (B) (C)

Figure 2.35: Volumetric strain inside the tumor at different positions for sample O (A), sample P (B) and sample Q (C).

in an elastography experiment. Thus, the developed models can be useful in extraction of the material properties of tumor tissue, which can be helpful in diagnostics and treatment of cancer. Although the models have been developed for application in ultrasound poroelastography, it can be used in fields like rock mechanics, ceramic engineering, soil and petroleum engineering, where such scenario of a poroelastic inclusion embedded inside a poroelastic material frequently rises.

Table 2.8: Root mean squared error between results from analytical model and FEM

Sample name	Error in volumetric strain estimation inside tumor (%)
I	2.05
J	2.52
K	1.22
L	2.93
M	6.84
N	2.17
O	2.08
P	2.19
Q	2.91

3. ESTIMATION OF LATERAL STRAIN [1]

3.1 Background

The majority of the poroelastography works retrievable in the literature refers to axial strain rather than lateral strain. In the past decade, many methods have been proposed to estimate and image the axial strains experienced by a tissue due to compression. These methods can be divided into two main categories: direct strain estimators [117, 118] and gradient-based strain estimators [119–122]. In direct strain estimation methods, a stretch factor is obtained by minimizing a cost function, and the strain is measured directly from the stretch factor. In gradient-based strain estimation methods, a displacement map is obtained first, and the strain is then computed as the gradient of the displacement. Gradient-based estimation methods include: correlation-based techniques, cost function minimization techniques and block matching algorithms.

Correlation-based techniques [123, 124] are by far the most widely employed strain estimation methods in ultrasound elastography. These techniques, however, are limited in resolution by the choice of the cross-correlation window, which also affects the resulting signal-to-noise ratio, and they are very sensitive to tissue motion [125].

Prominent cost function minimization techniques for strain estimation include the ones proposed by [119, 120, 126]. The general problem of these techniques is the high computational cost. In [119], DPE is proposed to speed up the process of strain estimation. In DPE, a 2D strain map is estimated through the minimization of a cost function using dynamic programming. The cost function incorporates similarity of the pre- and post-compressed radio frequency (RF) data and displacement continuity. Since tissue deformations are smooth, the incorporation of the smoothness into the cost function results in reduced decorrelation noise. DPE provides integer axial and lateral displacements only. Estimation of subsample displacements is possible but at the expense of additional computational time [119].

[1] ©2018 IEEE. Reprinted, with permission, from Islam, M.T., Chaudhry, A., Tang, S., Tasciotti, E. and Righetti, R., A new method for estimating the effective Poisson's ratio in ultrasound poroelastography, IEEE transactions on medical imaging, May 2018.

Block matching algorithms [121, 127, 128] also require a high number of computations. Additionally, they typically provide elastograms with lower spatial resolution than those obtained using cross-correlation methods. Recently, an optical flow estimation technique has been proposed to refine the results of block matching algorithms, which is also robust against noise and decorrelation [121]. In [121], the authors propose a block matching algorithm to obtain the coarse axial strain estimates followed by the Lucas-Kanade technique to refine the coarse axial strain measurements. Other two-step techniques have been described in [129–134] and [122]. In [134], the authors used a HS-based technique on B-mode data of hypertensive rat carotid to obtain the axial and lateral displacement fields in the first step and the strain fields in the second step. However, the lateral strain fields obtained using this method are reported to be unreliable. In [129] and [130], the coarse estimates of strain fields are obtained using cross-correlation as applied to the RF data, and subsequently a cross-spectrum phase gradient method is used to construct the strain fields with higher spatial resolution. In [131], the axial strains inside discontinuous tissues are estimated using cross-correlation as applied to B-mode data based on a pyramidal processing approach in the first step and on RF data in the second step. In [133], a numerical optimization method based on the Quasi-Newton algorithm is adopted in the second step to improve the displacement and strain, which are estimated in the first step using cross correlation. In a two-step technique described in [122], the authors used HS-based optical flow estimation method in both the first step and the second step. However, the method is shown to be suitable for very small displacements (2.3% maximum strain) only and does not consider lateral strain while warping the pre-compressed data by the strains (axial normal and axial shear) estimated in the first step. In the aforementioned two-step methods, various techniques have been employed to improve the quality of axial strain estimation, but little or no attention has been dedicated to the lateral strain or EPR estimation.

Prior work on lateral strain estimation can be found in [120, 135–141]. In [135], the authors estimated the lateral strain by using a priori assumptions about the tissue's incompressibility. This method cannot be used for poroelastic materials, which are, by definition, compressible [14]. Correlation-based lateral strain estimation methods such as the one described in [136] are compu-

tationally intense and prone to noise [142]. In [137], the authors combined elements of multi-level correlation and phase-zero search to achieve the noise tolerance of the former and the speed of the latter. In [120], the authors computed both the axial and lateral strains. While computationally very fast, the method proposed by [120] provides lateral strain estimations of significantly lower quality than the corresponding axial strain ones. Similar to [120], the method proposed in [139] is based on optimizing a nonlinear cost function that incorporates similarity of RF data intensity and prior information of displacement continuity. In [138], the authors proposed an improved speckle tracking algorithm where axial and lateral motion estimations are simultaneously performed. In [141], the authors employed a multi-level block matching algorithm for estimating lateral strain along with axial and shear strains, where displacements tracked at coarser levels are interpolated to initialize the search region location at finer levels. Different post processing techniques have been proposed to improve the accuracy of lateral strain estimation, such as iterative interpolation along the lateral direction [136] or local affine transformation [143]. Beam forming techniques have also been proposed for improving the resolution of lateral strain [144, 145]. Recently, our group has proposed a new method for accurate and reliable estimation of EPR using multiple transducers [142]. Although this method allows lateral strain estimation with image quality and accuracy close to those obtainable for axial strain estimation, it is currently difficult to implement in clinical applications. At the present time, methods to obtain lateral strain and EPR elastograms of clinically acceptable quality are still elusive.

In [146], we propose a new two-step processing method, where DPE [119] is first used to obtain integer axial and lateral displacement estimates. This step is then followed by a motion compensation procedure and HS optical flow estimation to obtain subsample estimates of both the axial and lateral displacements. The axial and lateral displacements from the two steps are then added to obtain complete axial and lateral displacements. Axial and lateral strains are calculated from the axial and lateral displacements using a Kalman filter-based least square estimation [120]. The EPR elastogram is obtained by dividing the lateral strain elastogram by the corresponding axial strain elastogram [71]. This two-step method maintains the advantages offered by DPE and HS

and is computationally very fast. Thus, it is expected to provide EPR estimates with significantly higher quality than those obtained using methods previously proposed for poroelastography.

3.2 Proposed method

The block diagram for the proposed method is shown in Fig. 3.1. The pre- and post-compressed data are used to determine the integer axial and lateral displacements by DPE. The pre-compressed data is compensated in motion by using the integer values of lateral and axial displacements. The motion-compensated pre-compressed and the post-compressed data are then entered into the HS method to determine the sub-sample axial and lateral displacements. Integer axial and lateral displacement values obtained from DPE and subsample axial and lateral displacement values obtained from the HS method are added to obtain the complete axial and lateral displacement estimations. Axial and lateral strains are calculated from axial and lateral displacements. The EPR elastogram is obtained by point-by-point division of the lateral strain by the corresponding axial strain. Details of each of the step of the proposed method are given below.

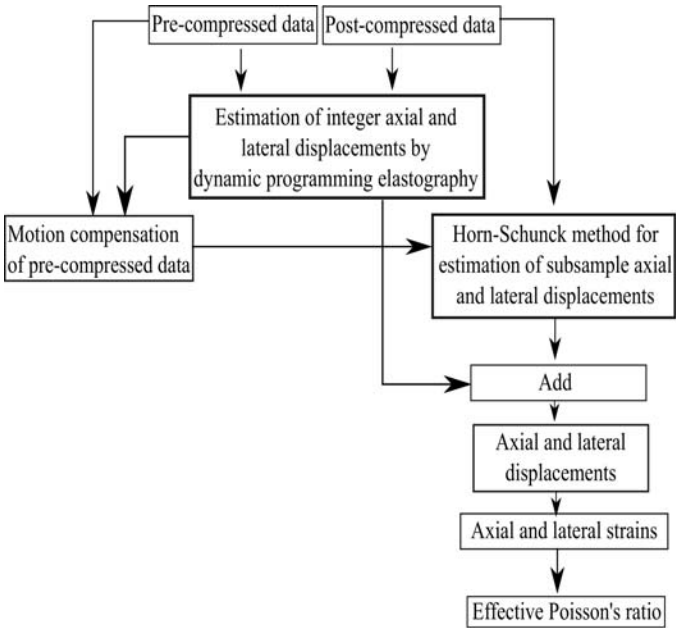

Figure 3.1: Block diagram for the proposed method.

3.2.1 Dynamic programming elastography

We consider a single column j in the pre-compressed ultrasound data I_1 of size $r \times c$, where r and c are the number of row and column of I_1. Here, r corresponds to the number of samples along one single RF-line and c corresponds to the number of RF-line. Let a_i and l_i be the integer axial and lateral displacements of the i^{th} sample in the j^{th} RF-line. In DPE [119], displacement continuity is assumed based on which a regularized cost function is created. This cost function has two terms - a regularization term consisting of prior of displacement continuity and an amplitude similarity term. For the j^{th} column, the cost function can be written as

$$C_j(a_i, l_i, i) = [I_1(i, j) - I_2(i + a_i, j + l_i)]^2 + \min_{d_a, d_l} \left\{ \frac{C_j(d_a, d_l, i-1) + C_{j-1}(d_a, d_l, i)}{2} + R_j(a_i, l_i, d_a, d_l) \right\}, \tag{3.1}$$

where I_2 is the post-compressed data and d_a and d_l are the temporary displacements along the axial and lateral directions, which are varied to minimize the term in the braces. The regularization term R_j can be written as

$$R_j(a_i, l_i, d_a, d_l) = \alpha_a (a_i - a_{i-1})^2 + \alpha_l (l_i - l_{i-1})^2, \tag{3.2}$$

where α_a and α_l are the axial and lateral regularization weights, respectively. The computation process of eq. (3.1) is initialized by taking the displacement as zero at $i = 1$ for all j and the cost function C_{j-1} is taken as zero when $j = 1$. The minimization of the regularization term in the cost function while minimizing the cost function forces the displacements (a_i and a_{i-1}, l_i and l_{i-1}) of two consecutive samples (i and $i - 1$) similar to each other. After calculating C_j for all $i = 2, \ldots, m$, C_j is minimized for $i = m$ producing the displacements at m^{th} sample, a_m and l_m. The values of a_i and l_i, $i = 1, \ldots, m - 1$, those minimize the cost function C_j are remembered in the process, which are the cost minimized displacements at $i = 1, \ldots, m - 1$ samples in the j-th line. The displacement maps are obtained for all the RF-lines in the same manner to get the

complete axial displacement D_a and lateral displacement D_l [119].

3.2.2 Horn-Schunck method

The optical flow is the apparent motion of brightness patterns of the image [147]. To estimate the optical flow, Horn and Schunck proposed the first variational approach [148], where the optical flow is computed as the solution of a minimization problem. The constraint equation of optical flow is derived based on the assumption of no change of the pixel intensities over time. This equation relates the optical flow with the derivatives of the image. The solution of this problem becomes ill-posed because there can be an infinite number of vector fields that satisfy this optical flow constraint. To overcome this problem, an additional regularity condition is introduced by Horn and Schunck that restricts the number of possible solutions. The HS method minimizes both the optical flow constraint and the magnitude of the variations of the flow field, producing smooth vector fields. As the optical flow constraint holds only for smaller (sub-sample) displacements, this technique can be used to estimate smaller displacements. Let $I(x, y, t)$ be a stack of motion-compensated pre-compressed data I_1' and post-compressed data I_2, where t is the time index, i.e., $I(x, y, 1) = I_1'$ and $I(x, y, 2) = I_2$.

For large displacement fields, the optical flow equation can be written in a non-linear formulation as [149]

$$I_1'(\mathbf{x}) - I_2(\mathbf{x} + \mathbf{w}) = 0, \tag{3.3}$$

where $\mathbf{w} = (u, v)$ is the optical flow vector and $\mathbf{x}$ denotes the space vector, i.e., $\mathbf{x} = (x, y)$. This equation still assumes the brightness constancy, but $\mathbf{w}$ can be any large value.

The energy functional can be written as [149]

$$E(\mathbf{w}) = \int_\Omega \left(I_1'(\mathbf{x}) - I_2(\mathbf{x} + \mathbf{w})\right)^2 + \beta^2(||\nabla u||^2 + ||\nabla v||^2) d\mathbf{x}. \tag{3.4}$$

The minimization of this energy functional yields the following Euler-Lagrange equations

$$0 = -(I_1'(\mathbf{x}) - I_2(\mathbf{x}+\mathbf{w}))I_{2x}(\mathbf{x}+\mathbf{w}) - \beta^2(\Delta u), \tag{3.5}$$

$$0 = -(I_1'(\mathbf{x}) - I_2(\mathbf{x}+\mathbf{w}))I_{2y}(\mathbf{x}+\mathbf{w}) - \beta^2(\Delta v). \tag{3.6}$$

These equations are nonlinear in $\mathbf{w}$ because of the warping $I_2(\mathbf{x}+\mathbf{w})$. Using the first order Taylor expansion, we can write

$$I_2(\mathbf{x}+\mathbf{w}^{n+1}) = I_2(\mathbf{x}+\mathbf{w}^n) + \nabla I_2(\mathbf{x}+\mathbf{w}^n)(\mathbf{w}^{n+1} - \mathbf{w}^n), \tag{3.7}$$

where n denotes the iteration index and difference between the values of $\mathbf{w}^n$ and $\mathbf{w}^{n+1}$ is very small.

For obtaining a linear system of equations, we replace the nonlinear terms in the Euler-Lagrange equations by their Taylor expansions to obtain

$$\begin{aligned} 0 = -(I_1'(\mathbf{x}) - I_2(\mathbf{x}+\mathbf{w}^n) &- \nabla I_2(\mathbf{x}+\mathbf{w}^n)(\mathbf{w}^{n+1} - \mathbf{w}^n)) \\ &\times I_{2x}(\mathbf{x}+\mathbf{w}^n) + \beta^2(\Delta u^n), \end{aligned} \tag{3.8}$$

$$\begin{aligned} 0 = -(I_1'(\mathbf{x}) - I_2(\mathbf{x}+\mathbf{w}^n) &- \nabla I_2(\mathbf{x}+\mathbf{w}^n)(\mathbf{w}^{n+1} - \mathbf{w}^n)) \\ &\times I_{2y}(\mathbf{x}+\mathbf{w}^n) + \beta^2(\Delta v^n). \end{aligned} \tag{3.9}$$

These equations can be solved in two steps. In the first step, a multi-scale approach can be taken to reduce the distance between $\mathbf{w}^n$ and $\mathbf{w}^{n+1}$ and in the second step, at each scale, $\mathbf{w}^n$ can be iteratively made to converge to $\mathbf{w}^{n+1}$. The main idea behind using a multi-scale strategy is to create a coarse-to-fine structure. One way to acheive this is to create a pyramid of down-sampled images [149]. The pyramid is created by reducing the images by a factor of $\eta \in (0, 1)$. A Gaussian smoothing is applied before the down-sampling. To transfer the values from a coarse scale (s) to a

fine scale $(s-1)$, the flow field is updated as

$$\mathbf{w}^{s-1}(\mathbf{x}) := \frac{1}{\eta}\mathbf{w}^{s}(\eta\mathbf{x}). \tag{3.10}$$

The details on the numerical implementation of the pyramidal approach of the HS method for recovering large displacements are discussed in [149].

3.2.3 Displacement reconstruction and strain estimation

The final axial displacement D_{ax} and lateral displacement D_{lat} are obtained as

$$\begin{aligned} D_{ax} &= D_a + v, \\ D_{lat} &= D_l + u. \end{aligned} \tag{3.11}$$

In our proposed algorithm, the estimation of the lateral and axial strains from the displacement data is performed using Kalman filter-based least square estimation [120].

In the first step of Kalman filter-based least square estimation, a noisy strain image is generated by performing the least squares regression along the axial direction for each RF-line. This is done by fitting a line to the displacement estimates in a window of length $2k+1$ around a sample i, i.e., from sample $i-k$ to $i+k$. The slope of the fitted line is the noisy strain measurement $\rho_{i,j}$ at sample i. This step ensures the prior of strain continuity along the axial direction.

In the second step, a Kalman filter is applied in the lateral direction for obtaining a denoised strain image. For this, we write the noisy strain measurement as [150, 151]

$$z_{i,j} = z_{i,j-1} + r_{i,j}, \tag{3.12}$$

$$\rho_{i,j} = z_{i,j} + g_{i,j}, \tag{3.13}$$

where $z_{i,j}$ is the underlying true strain field, $r_{i,j}$ and $g_{i,j}$ are Gaussian process and Gaussian measurement noise. Assuming $\bar{z}_{i,j}$ and $\hat{z}_{i,j}$ the a priori estimate of the strain before step j and a

posteriori estimate of the strain after step j, we can write the measurement update equations as follows [120]

$$\hat{z}_{i,j} = \bar{z}_{i,j} + \frac{\hat{q}_{i,j}}{\hat{q}_{i,j} + \sigma_g^2}(\rho_{i,j} - \bar{z}_{i,j}), \tag{3.14}$$

$$\hat{q}_{i,j} = \left(1 - \frac{\bar{q}_{i,j}}{\bar{q}_{i,j} + \sigma_g^2}\right)\bar{q}_{i,j}, \tag{3.15}$$

where $\bar{z}_{i,j} = \hat{z}_{i,j-1}$ and σ_g^2 is the variance of the measurement noise g. $\hat{q}_{i,j}$ and $\bar{q}_{i,j}$ are the variances of $\hat{z}_{i,j}$ and $\bar{z}_{i,j}$ and are related through

$$\bar{q}_{i,j} = \hat{q}_{i,j-1} + \sigma_r^2, \tag{3.16}$$

where σ_r^2 is the variance of the process noise r. $\hat{q}_{i,j-1}$ is taken as zero when $j = 1$. σ_r^2 has been determined using $\sigma_r^2 = (\mu_{j-1} - \mu_j)^2$, where μ_{j-1} and μ_j are the mean values (calculated using a Gaussian kernel of standard deviation of 0.6) of strains in 3×3 square blocks around samples $(i, j-1)$ and (i, j), respectively. σ_g^2 is the variance of the noisy strain values $\rho_{i,j}$ over the whole image and is a constant in the entire strain elastogram. It should be noted that the second step of the method ensures the prior of strain continuity along the lateral direction.

The above mentioned method of strain estimation is applicable for estimating both the axial and lateral strains. For estimating lateral strain elastogram, lateral displacement matrix needs to be transposed before applying the first step of the method to obtain the gradient along lateral direction. The resulting strain matrix from the second step of the method needs to be transposed again in the end to obtain the lateral strain elastogram.

3.3 Experiments

3.3.1 Simulation models

From the governing equations of poroelastography [71], a weak-form Galerkin finite element model (FEM) was developed with fluid pressure and displacement treated as the primary variables. The formulation was coded with an in-house finite element program [152]. An axisymmetric

model was used in this study. The model consisted of a cylindrical domain 40 mm tall and 40 mm in diameter. For the fluid phase in the domain, free flow boundary conditions (pressure = 0) were prescribed at the edges of the domain, and for the solid phase, stress free boundary conditions were prescribed at the edges of the domain. Two finite element models were used in the study. In the first model, called the "inclusion model", an inclusion of radius 7.5 mm with material properties distinct from the peripheral region was created at the center of the domain. In the second model, the "uniform model", we simulated a uniform tissue sample with a single set of poroelastic properties. For both models, we simulated an unconfined stress relaxation test between impervious surfaces. The displacement at the base of the domain was constrained along the vertical direction. The entire domain was meshed using linear quadrilateral elements. For the inclusion model used in our simulations, only a background/inclusion permeability contrast was considered, i.e., no Poisson's ratio or Young's modulus contrast was simulated. The permeability of the inclusion was set to $1.95 \times 10^{-9}\mathrm{m}^4/\mathrm{N.s}$ and the permeability of the background was set to $1.95 \times 10^{-8}\mathrm{m}^4/\mathrm{N.s}$. The Young's modulus (E), and the Poisson's ratio (ν) of the solid matrix of both the inclusion and background were set to 1.74 kPa and 0.25, respectively. In the case of the uniform model, the Poisson's ratio was assumed to be equal to 0.2, the Young's modulus equal to 1.74 kPa and the interstitial permeability equal to $1.95 \times 10^{-9}\mathrm{m}^4/\mathrm{N.s}$. The choice of these mechanical parameters is based on previous work from our lab [153, 154]. It should be noted that the inclusion-model used in this simulation study is meant to represent the case of a tumor, which has the same Young's modulus and Poisson's ratio but different permeability than the background (normal tissue). Even though tumors may differ with respect to the surrounding tissue in terms of multiple mechanical parameters, this model is suitable to study the effect that a range of permeability contrasts may have on the generated EPR elastograms [71].

3.3.2 Phantom experiments

A non-homogenous phantom was created using tofu (Banyan foods, Houston, TX) as the background and gelatin-agar as the inclusion similarly as in [8, 142]. The size of the background was 80mm x 60mm x 40mm with a cylindrical inclusion of 15 mm in diameter. The inclusion was cre-

ated by mixing 5% porcine gelatin (Sigma-Aldrich, USA) with 3% agar (Sigma-Aldrich, USA) as in [155]. The experiments were performed using our Sonix RP system (Ultrasonix, Richmond, BC, Canada) with a 38-mm linear array transducer, which operates with a center frequency of 6.6 MHz, bandwidth $5-14$ MHz and beamwidth equal to 1 mm at the focus. Compression was applied from the top using a compressor plate attached to the transducer face. The experimental setup is shown in Fig. 3.2. A multi-compression protocol was used for data acquisition [142, 156–158].

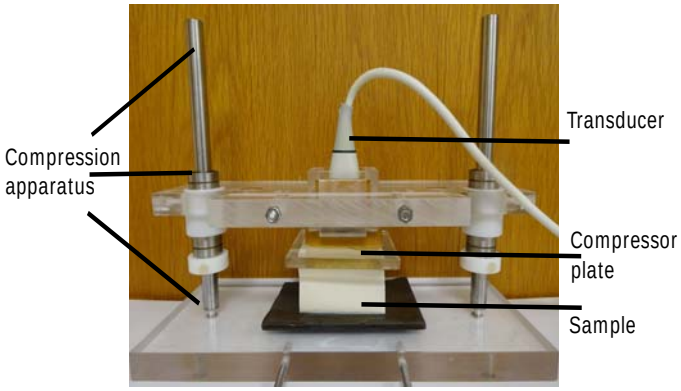

Figure 3.2: The experimental setup for poroelastic experiments.

3.3.3 In vivo experiments

In vivo experiments were performed on five mice with triple negative breast cancer. The cancers were created by our collaborators at the Houston Methodist Research Institute by injection of the cancerous cells beneath the mouse's mammary fat pad [159]. In vivo data acquisition was approved by the Houston Methodist Research Institute, Institutional Animal Care and Use Committee (ACUC-approved protocol # AUP-0614-0033).

The elastography experiments were performed using a 38-mm linear array transducer (Sonix RP, Ultrasonix, Richmond, BC, Canada) with a center frequency of 6.6 MHz, $5-14$ MHz bandwidth. To compensate for the surface geometry as well as improve the focus inside the fairly superficial tumors, an aqueous ultrasound gel pad (Aquaflex, Parker Laboratories, NJ, USA) was

placed between the compressor plate and the animal. Creep compression experiments were performed on the anesthetized animals, and the ultrasound RF data acquisition was synchronized to the compression. Data were acquired for up to 1 minute with a sampling rate of 0.1 second/sample. The total duration of each experiment was approximately 5 minutes, which resulted in up to 5 RF data acquisitions at different locations around the tumors.

3.3.4 Elastographic processing parameters

The simulated pre- and post-compression temporal ultrasound RF data were generated from the mechanical displacements (at a time interval 10 s) using a convolution model [160]. Bilinear interpolation was performed on the input mechanical displacement data prior to the computation of the simulated RF frames [9]. The simulated ultrasound transducer had 128 elements, frequency bandwidth between $5-14$ MHz, a 6.6 MHz center frequency, and 50% fractional bandwidth at -6 dB. The transducer's beamwidth was assumed to be dependent on the wavelength and to be approximately 1 mm at 6.6 MHz [8]. The sampling frequency was set at 40 MHz and Gaussian noise was added to set the SNR at 40 dB. From the same sets of simulated RF data, three different methods were used to create the axial, lateral and EPR elastograms. In addition to the proposed two-step method (DPHS) elastograms were also created using a cross-correlation method (CM) [71] and analytic minimization (AM) [120]. This allowed us to compare the performance of the proposed two-step method with more accepted and widely used elastographic methods. An explanation of the processing parameters used for the implementation of the three methods is provided below.

To compute the elastograms with DPE, the range of variation of axial displacement was limited to 0 to -100 (negative for compression) data points, the range of variation of lateral displacement was set to -4 to 4 data points (negative corresponds to the left and positive to the right) and the seed RF-line where the displacement calculation starts from was set to half of the number of RF-lines used in the simulation. The regularization weights along the axial and lateral directions, α_a and α_l were set to 0.15. For estimating the elastograms by the HS method, the trade-off (regularization) parameter β in (3.4) was set to 1. The number of pyramid levels was taken as 4, and the maximum number of warping per pyramid level was set to 3. A bi-cubic interpolation was used both for

warping and up-scaling from coarse to fine scales. To compute the temporal elastograms at a given time using correlation, the pre-compression frame was correlated with the post-compression frame corresponding to that time after compression [8]. The length of the correlation window, both for the pre- and post-compression signals, was fixed at 1.5 mm with an 80% overlap between adjacent windows. A 5×5 pixels median filter was applied to the axial and lateral displacement estimates prior to the computation of the strains. To compute the elastograms using the AM method, the axial regularization weight was taken as 5, two lateral regularization weights were taken as 10 and 0.005. The threshold of the iteratively reweighted least squares algorithm was set to 0.2 and the frequency dependent attenuation coefficient was taken as 0.63 dB/cm/MHz. The processing parameters for the CM method are chosen based on prior work from our lab [71, 154]. The parameters for the AM method are chosen based on the values suggested by [120]. The parameters for the newly proposed two-step method are chosen based on values suggested in [119] for the DPE part and in [149] for the HS part.

Each EPR elastogram was computed as the ratio between a lateral strain elastogram and corresponding axial strain elastogram [8]. EPR poroelastograms were obtained as temporal sequences of EPR elastograms.

3.3.5 Image quality analysis

Image quality of EPR elastograms and poroelastograms was quantified using three elastographic quality factors, which are typically used for elastographic studies: SNR (signal-to-noise ratio), CNRe (elastographic contrast-to-noise ratio) and RMSE (root mean square error). The SNR is defined as

$$\text{SNR} = \frac{\mu_E}{\sigma_E}, \tag{3.17}$$

where μ_E and σ_E are the mean and standard deviation of the EPR elastogram. The SNR is defined for homogeneous phantoms. The CNRe, instead, is defined for non-homogenous phantoms and gives a measure of the maximum achievable elastographic contrast for a given underlying mechanical contrast. CNRe differs from image contrast because image contrast depends only on the ratio

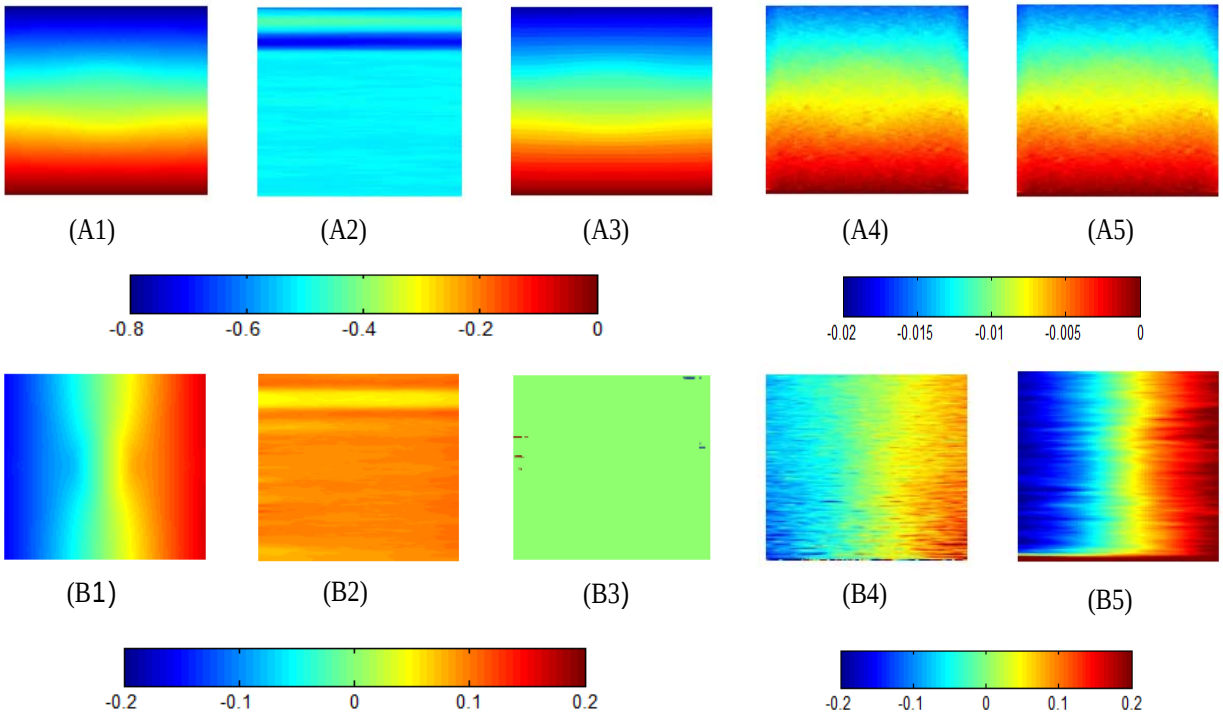

Figure 3.3: Ideal axial displacement (A1) and lateral displacement (B1) maps. Axial displacement (A2) and lateral displacement (B2) estimated by using the HS method (for large displacement). Axial displacement (A3) and lateral displacement (B3) estimated at the first step of the two-step proposed method (i.e., DPE). Axial displacement (A4) and lateral displacement (B4) estimated at the second step of the two-step proposed method (using standard HS). Axial displacement (A5) and lateral displacement (B5) estimated at the second step of the two-step proposed method (using HS for large displacement). All displacement maps are shown in unit of [mm].

of the means while CNRe depends also on the standard deviations of the noise. The EPR CNRe has been defined as [161]

$$\text{CNRe} = \frac{2(\nu_t - \nu_b)^2}{\sigma_{\nu_t}^2 + \sigma_{\nu_b}^2}, \tag{3.18}$$

where ν_t is the mean EPR in the target and ν_b is the mean EPR in the background and $\sigma_{\nu_t}^2$ and $\sigma_{\nu_b}^2$ are the corresponding variances. In elastography, the CNRe is typically defined for the axial strain [162], but it can also be defined in an analogous manner for other elastographic parameters, including the EPR [161]. It should be noted that, in general, when dealing with poroelastic media under sustained compression, both the background and target may show the presence of poroelastic patterns in the corresponding elastograms. Therefore, before computing the CNRe, each elastogram was detrended by subtracting from it the corresponding ideal strain image (generated directly from the mechanical displacement models) [9]. However, detrending is done only for the EPR elastograms resulting from simulated data (not from controlled/in vivo experimental data), because knowledge of the ideal elastogram is required for applying this technique. Detrending is often used in signal processing so that time-varying processes can be analyzed using statistical methods that assume stationarity [163].

The RMSE is defined as

$$\begin{aligned}\text{RMSE} =& \sqrt{\frac{\sum_{r=1}^{R}\sum_{c=1}^{C}(\nu_e(r,c) - \nu_f(r,c))^2}{R \times C}} \\ &\times \frac{100 \times R \times C}{\sum_{r=1}^{R}\sum_{c=1}^{C}\nu_f(r,c)},\end{aligned} \tag{3.19}$$

where ν_e is the estimated EPR elastogram and ν_f is the true EPR map from the FEM. R and C are the number of rows and columns in the estimated EPR elastogram.

3.4 Results

3.4.1 Inclusion model

Figs. 3.3-3.8 show selected results obtained from the inclusion model. Fig. 3.3 shows the ideal axial and lateral displacements (A1, B1) at a time point of 10 s during compression with

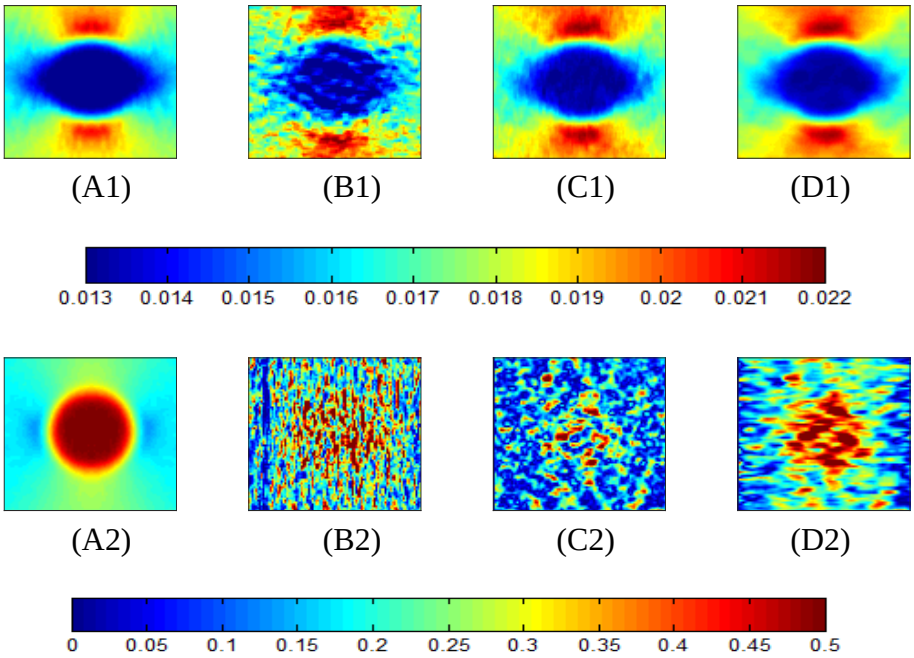

Figure 3.4: Axial strain and EPR at time point of 10 s for 2.2% applied strain compression from FEM for the inclusion model are shown in (A1) and (A2). Axial strain and EPR estimated by CM at time point of 10 s for 2.2% applied strain compression for the inclusion model are shown in (B1) and (B2), axial strain and EPR estimated by AM are shown in (C1) and (C2) and axial strain and EPR estimated by DPHS are shown in (D1) and (D2).

2.2% applied strain along with the displacement estimates obtained by the HS method (for large displacement) alone (A2, B2), the displacement estimates obtained using the DPE method (first step of DPHS) (A3, B3) and the displacement estimates obtained at the second step of the DPHS method with both standard (A4, B4) and large displacement HS (A5, B5). In all cases, no averaging was used. Note that the estimates obtained using the HS method alone have no similarity with the ideal displacements. The integer axial displacement from the DPE method (A3) is close to the ideal axial displacement but the lateral displacement (B3) is almost zero everywhere. Due to the high axial resolution of the ultrasound transducer, small axial displacements can still be detected. Along the lateral direction, instead, most of the motion/displacement is a fraction of a single pixel due to the limited lateral resolution. From Fig. 3.3 (A4), (A5), (B4) and (B5), we see that the axial sub-pixel displacements from both types of HS methods are similar but the estimates of sub-pixel lateral displacement for large displacement HS method is better than the standard HS method.

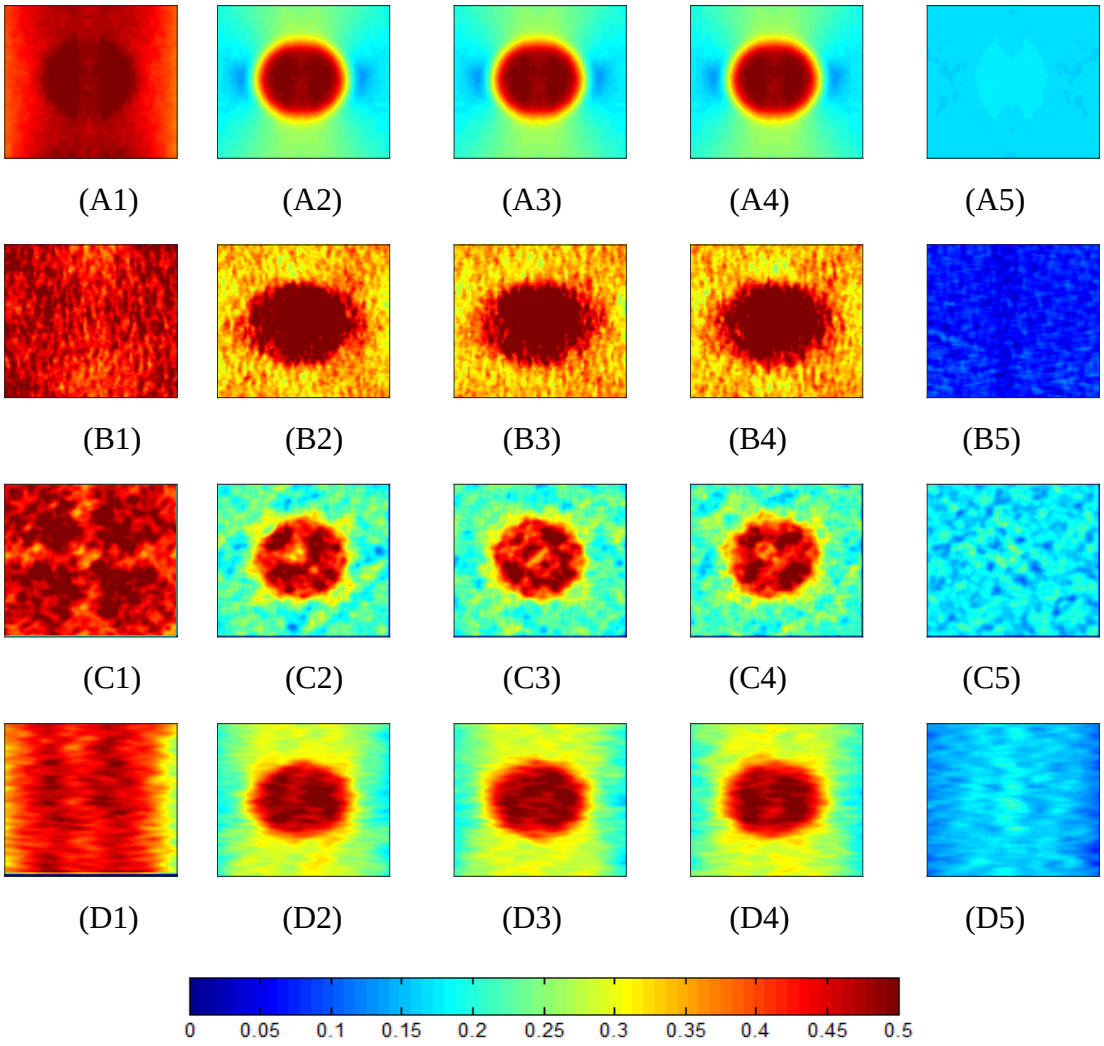

Figure 3.5: EPR elastograms at different time points of 1s, 10s, 110s, 260s and 360s from finite element modeling (FEM) for the inclusion model for applied strain compression of 2.2% are shown in (A1), (A2), (A3), (A4), (A5). EPR elastograms at different time points of 1s, 10s, 110s, 260s and 360s estimated by CM for 2.2% applied strain compression for the inclusion model are shown in (B1), (B2), (B3), (B4), (B5), estimated by AM are shown in (C1), (C2), (C3), (C4), (C5) and estimated by DPHS are shown in (D1), (D2), (D3), (D4), (D5).

Axial strain and EPR elastograms obtained using CM, AM and DPHS along with the FEM predictions for the simulated inclusion model are shown in Fig. 3.4. These elastograms represent single realizations (i.e., no temporal and spatial averaging) and refer to simulated data at time point of 10 s for 2.2% applied strain compression. The first column (A) corresponds to the ideal axial and EPR maps from FEM, the second (B), third (C) and forth (D) columns show the elastograms from

CM, AM and DPHS, respectively. The first row (A1, B1, C1, D1) shows the axial strain results. All methods seem to perform well when estimating the axial strains, even if AM and DPHS appear to outperform CM. When observing C1 and D1 in Fig. 3.4, both AM and DPHS appear to accurately estimate the axial strains. This is due to the fact that the accuracy of sub-sample estimation of axial strain by the AM and HS methods are very similar. However, the elastogram from DPHS appears slightly smoother than the elastogram from AM probably due to the nature of optical flow estimation. The second row (A2, B2, C2 and D2) in Fig. 3.4 shows the EPR elastograms obtained from the three methods as well as the ideal EPR map from FEM. In this case, only the DPHS produces a result that has some similarities with the FEM result.

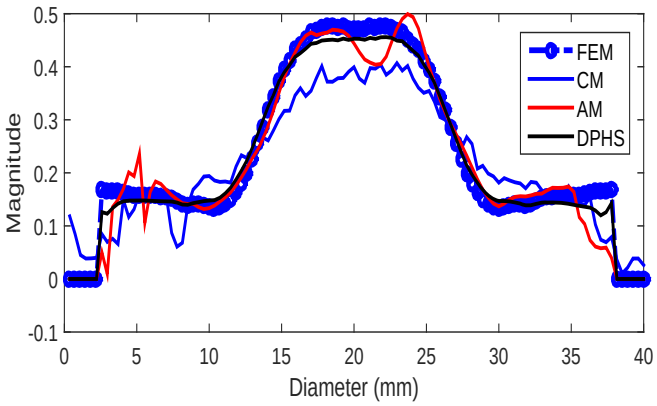

Figure 3.6: Central lines of the estimated EPRs by CM, AM and DPHS along with the FEM prediction for the inclusion model at time point of 10 s after application of 2.2% strain compression.

Fig. 3.5 shows examples of simulated EPR poroelastograms obtained from the inclusion model for applied strain compression of 2.2% using different methods and averaging results from fifty independent realizations. In Fig. 3.5, each row represents results by different methods (from top to bottom: FEM, CM, AM and DPHS). Each column corresponds to temporal EPR elastograms obtained at different time points. The first column (A1, B1, C1, D1) shows the EPR elastograms at time point of 1 s. The next columns (2, 3, 4, 5) show EPR elastograms corresponding to 10, 110, 260, and 360 s respectively. In all cases, we note that no poroelastic contrast is visible immediately

after compression. As time progresses, fluid starts to translocate at a rate that depends on the local permeability and the boundary conditions. Since fluid flow can occur from the sides of the phantom only (due to the imposed boundary conditions), the inclusion may appear elliptical in the elastograms. Since no underlying contrast of Young's modulus or Poisson's ratio exists between target and background, any poroelastographic contrast observed in the axial strains or EPRs is caused by the difference in the rate of fluid clearance in the background and in the inclusion. Fluid movement ceases when the equilibrium is reached. If we qualitatively compare the performances of the different estimation methods, we observe that the results from DPHS are the closest to the FEM ones. At 1 s (A1, B1, C1, D1), every method estimates the EPR close to 0.5 [96]. At other time points, results from AM seem to be more accurate than the corresponding ones obtained using CM. Overall, the results from DPHS are smoother than those obtained using AM and CM and have a better correspondence with the FEM ideal maps at all time points.

The central horizontal profiles of the 10 s EPR elastograms (shown in Fig. 3.5) for the various methods are shown in Fig. 3.6. The EPR profile from the DPHS elastogram matches closely the FEM result. The EPR profile from the CM elastogram is the noisiest and does not reach the true EPR value in the inclusion region. The EPR profile from the AM elastogram has a better smooth rise and fall at the boundary of the inclusion than CM but appears to be nosier and less accurate than DPHS.

Fig. 3.7 shows EPR elastograms estimated by the various methods for different strain compressions at time point of 10 s. First row shows the FEM results. The second row shows the CM results, the third row the AM results and the last row the DPHS results. Each EPR elastogram is an average over fifty realizations. The first column (1) represents the EPR elastograms obtained with an applied strain of 0.2%. The second to fifth columns (2, 3, 4, 5) represent the EPR elastograms obtained with applied strains of 1.2%, 3.2%, 4.2% and 6.2%, respectively. These results show that, at a very low compression, all methods perform poorly, and the resulting EPR elastograms have low similarity with the ideal FEM EPR maps. In general, the performances of all methods improve as the applied strain increases (up to 4.2%). At 6.2%, the performances of all methods degrade

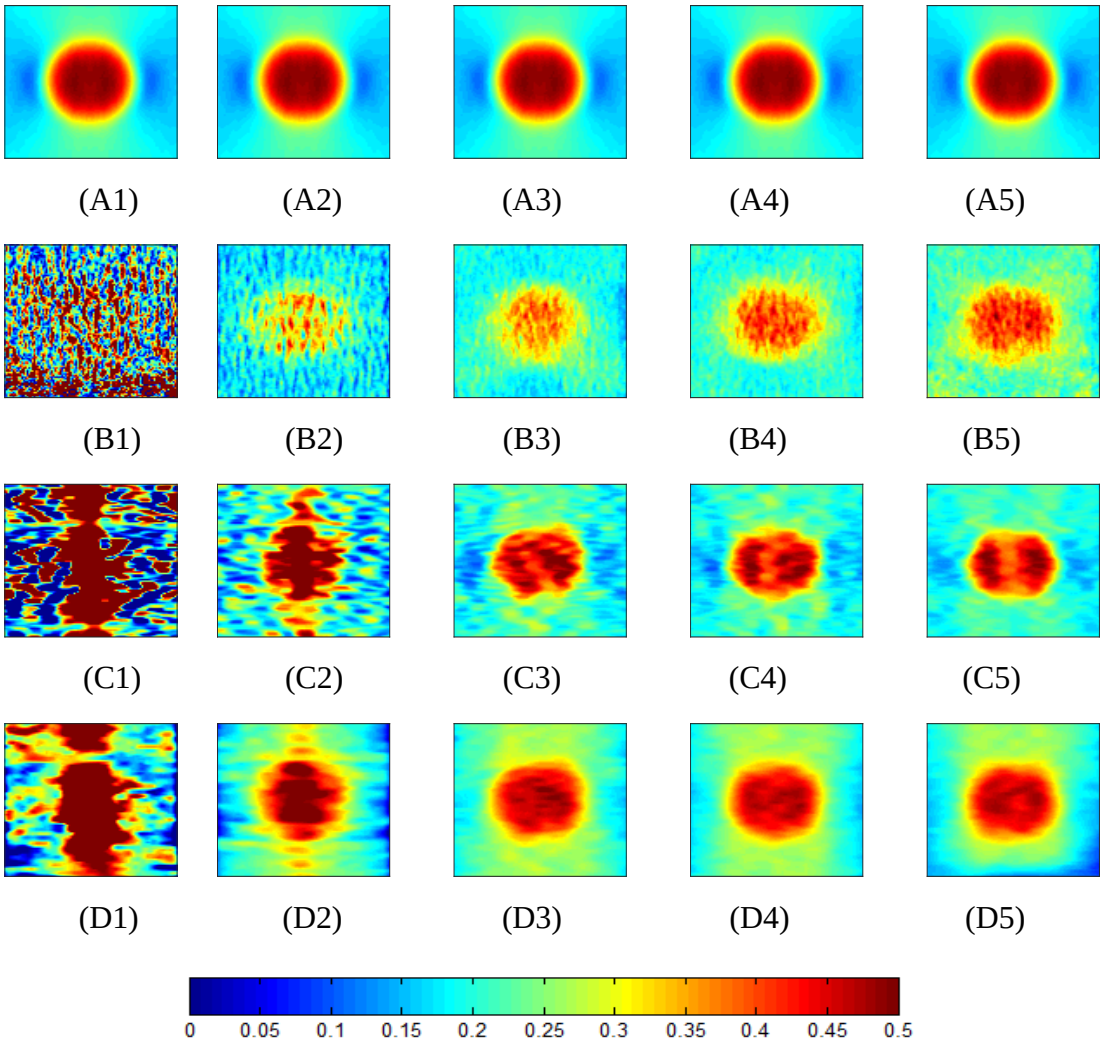

Figure 3.7: EPR elastograms for the inclusion model for applied strain compressions of 0.2%, 1.2%, 3.2%, 4.2% and 6.2% at time point of 10 s from FEM are shown in (A1), (A2), (A3), (A4), (A5). EPR elastograms for the inclusion model for applied strain compressions of 0.2%, 1.2%, 3.2%, 4.2% and 6.2% at the same time point estimated by CM are shown in (B1), (B2), (B3), (B4), (B5), estimated by AM are shown in (C1), (C2), (C3), (C4), (C5) and estimated by DPHS are shown in (D1), (D2), (D3), (D4), (D5).

slightly, most likely due to out of plane motion. As for the previous results, DPHS outperforms CM and AM in terms of image quality and accuracy.

Results of the CNRe and RMSE for the inclusion model for application of different strain compressions at time point of 10 s are shown in Figs. 3.8 (a) and (b). The proposed method outperforms the CM and AM methods with respect to these two quality factors. The classical 'strain filter' be-

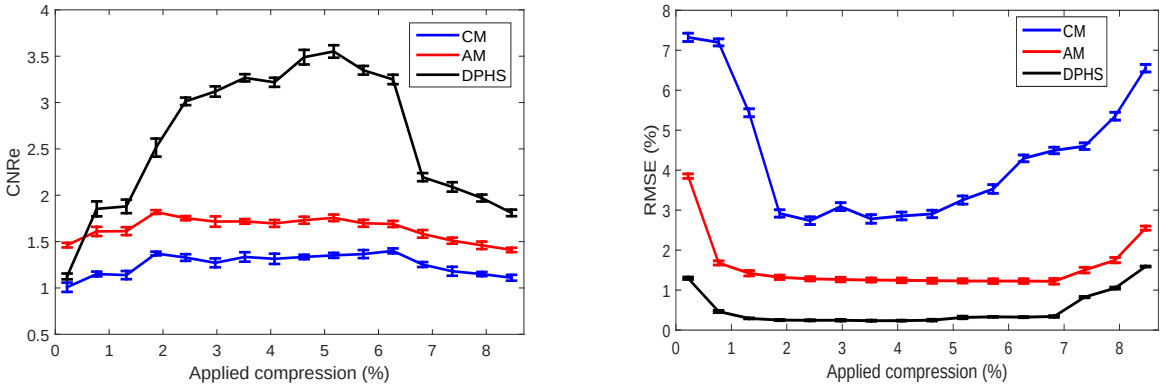

(a) (b)

Figure 3.8: (a) CNRe and (b) RMSE for different methods for the inclusion model at different strain compressions at time point of 10 s.

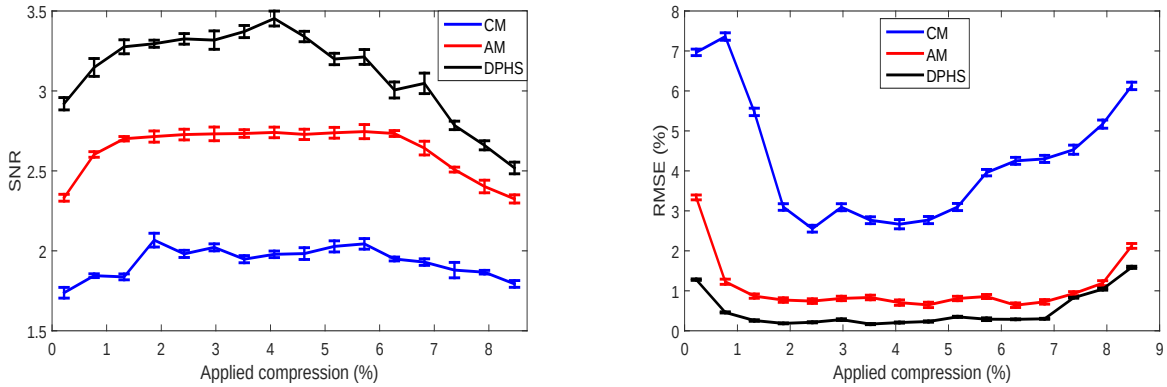

(a) (b)

Figure 3.9: (a) SNR and (b) RMSE for different methods for the uniform model for different strain compressions at time point of 10 s.

havior is observable for all methods [125]. According to the 'strain filter' theory, for very low compression, the performance of the strain estimator deteriorates because of the dominance of the electronic noise of the ultrasound imaging system. On the other hand, for large compression, the performance of the estimator degrades because of the out-of-plane motion (decorrelation noise). For a range of applied compression between the small and large compression, the estimator provides the best performance. If SNR or CNRe is plotted against the applied compression, the graph

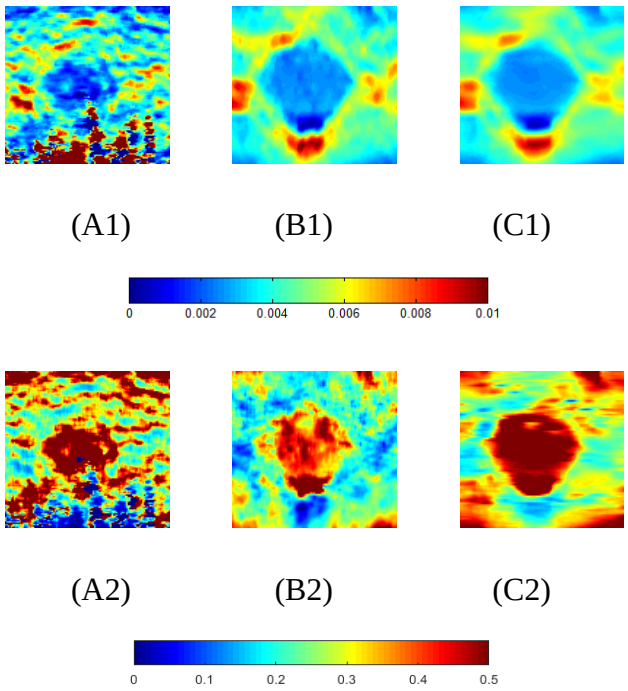

Figure 3.10: Axial strain and EPR elastogram estimated by CM are shown in (A1) and (A2) for the experimental data. Axial strain and EPR elastograms estimated by AM and DPHS for the same data are shown in (B1) and (B2) and (C1) and (C2), respectively.

looks like a bandpass filter [125]. In Fig. 3.8 (a), the CNRe for DPHS is around 2.5 times higher than the CNRe of CM and 2 times higher than the CNRe of AM for most applied strains. From the plot of RMSE shown in Fig. 3.8 (b), we see that CM has higher RMSE for all applied strains in comparison to the other two methods. DPHS has the lowest RMSE for all applied strains with very small standard deviation values. The RMSE of AM is much lower than the RMSE of CM and closer to the one of DPHS.

3.4.2 Uniform model

The RMSEs and SNRs of EPR elastograms obtained using the different methods for the uniform model for different strain compressions at time point of 10 s are given in Fig. 3.9 (a) and (b). From these figures, we see that DPHS shows better performance in terms of both SNR and RMSE in comparison to CM and AM for all the applied strain compressions. The SNR of DPHS is almost two times higher than the SNR of AM and four times higher than the SNR of CM. In terms of

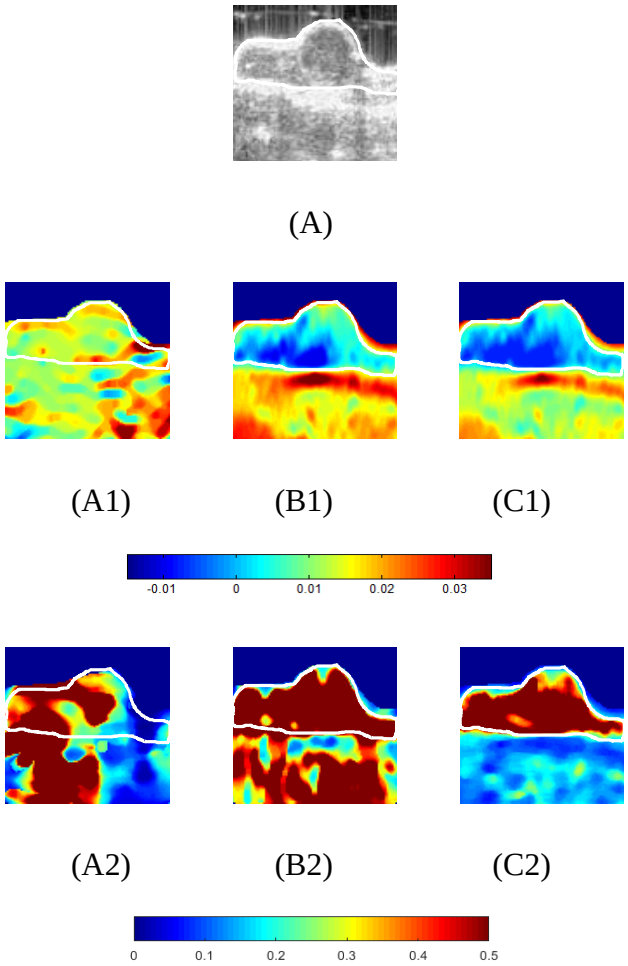

Figure 3.11: (A) B-mode image of the in vivo experimental data for mouse 1. Axial strain and EPR elastograms estimated from the in vivo experimental RF data by CM are shown in (A1) and (A2) for mouse 1. Axial strain and EPR elastograms estimated by AM and DPHS from the same data are shown in (B1) and (B2) and (C1) and (C2), respectively. The blue colored parts on top of the tumor in axial strain and EPR elastograms are from used gel pad in the experiment.

RMSE, RMSE of DPHS is one-fourth the one of AM and one-tenth the one of CM for most of the strain compressions.

3.4.3 Phantom experiments

Fig. 3.10 shows selected experimental results obtained from our tofu/agar phantom. To obtain each elastogram, we averaged all data collected up to 100 s. In this figure, the first column (A1 and A2) corresponds to the results of obtained using CM. The second (B1 and B2) and third columns

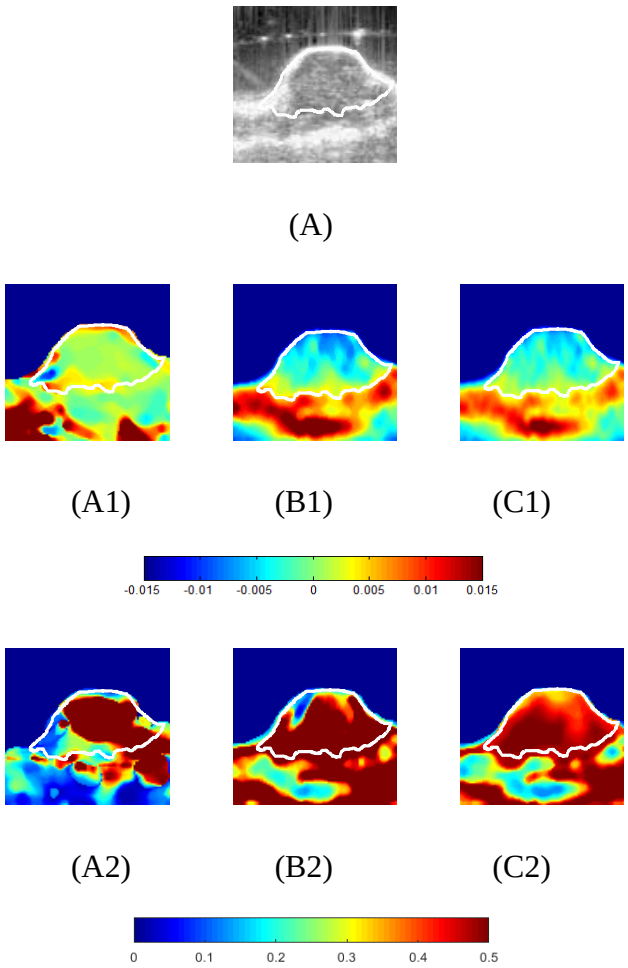

Figure 3.12: (A) B-mode image of the in vivo experimental data for mouse 2. Axial strain and EPR elastograms estimated from the in vivo experimental RF data by CM are shown in (A1) and (A2) for mouse 2. Axial strain and EPR elastograms estimated by AM and DPHS from the same data are shown in (B1) and (B2) and (C1) and (C2), respectively. The blue colored parts on top of the tumor in axial strain and EPR elastograms are from used gel pad in the experiment.

(C1 and C2) show the results obtained using the AM and DPHS methods. From these preliminary results, we observe that AM and DPHS methods have similar performance with respect to the axial strain estimation, far better than CM. Since tofu and gelatin have different poroelastic properties, the inclusion is clearly visible in the EPR elastograms [142]. In the EPR elastogram obtained using DPHS, the inclusion borders are better defined and the inclusion/background contrast appears to be higher than in the EPR elastograms obtained using both AM and CM. The CNRe calculated from the EPR elastograms of the tofu/agar phantom by CM, AM and DPHS are shown in Table 3.1. We see from this table that the EPR elastogram from the DPHS has the highest CNRe (4.91), whereas the EPR elastograms from the other two methods AM and CM have CNRe of 1.93 and 0.52, respectively.

Table 3.1: CNRe computed from EPR elastograms of controlled experiment

Sample	CM	AM	DPHS
Tofu-agar phantom	0.52	1.93	4.91

3.4.4 In vivo experiments

The in vivo results obtained from two mice experiments are shown in Figs. 3.11 and 3.12. Axial strain elastograms and EPR elastograms obtained using the CM, AM and DPHS methods along with the B-mode images are shown for both cases. From these results, we observe that AM and DPHS methods have similar performance with respect to the axial strain estimation (even if the axial strain resulting from the DPHS appears to be smoother). With respect to the EPR estimation, DPHS outperforms AM providing a better definition of the tumor borders and higher tumor/background contrast. Axial and lateral strains estimated using CM were found significantly noisier when compared to AM and DPHS. These results were consistent for all in vivo experiments performed in this study. The SNR and CNRe computed from the EPR elastograms obtained from in vivo experiments using CM, AM and DPHS are shown in Table 3.2. SNR values are calculated

from the EPR elastograms in the background tissue, away from the tumor. From Table 3.2, we see that the values of SNR and CNRe for the EPR elastograms from DPHS are higher than the SNR and CNRe values of the EPR elastograms from AM and CM in all five in vivo cases.

3.5 Discussion and future works

EPR of poroelastic materials is an important mechanical parameter, which has been linked to a number of pathological and physiological conditions of tissues. In the field of ultrasound elastography, prior studies have shown that the image quality of EPR elastograms is significantly compromised by poor lateral strain estimation. This would reduce the usefulness of these images in clinical scenarios where uncontrollable factors may further deteriorate image quality and only limited averaging may be possible.

Table 3.2: SNR and CNRe computed from EPR elastograms of in vivo experiments

Sample	SNR			CNRe		
	CM	AM	DPHS	CM	AM	DPHS
Mouse 1	0.43	1.49	2.23	1.53	4.81	7.12
Mouse 2	1.13	1.98	3.14	0.44	2.03	2.90
Mouse 3	0.95	2.73	2.89	0.82	3.82	5.22
Mouse 4	1.29	3.19	3.52	0.59	2.78	3.93
Mouse 5	0.71	1.59	1.98	0.73	1.89	5.12

In this paper, we propose a new method to obtain high quality EPR estimates in ultrasound poroelastography experiments in vivo. The proposed method uses DPE to estimate large integer-pixel motion displacements between pre- and post-compression RF data and HS to estimate the residual sub-pixel displacements using optical flow. The novelty of the proposed method lies in the combined use of these two established methods while maintaining their own distinct benefits. Although each of the method on its own has been previously investigated, the combination is novel and especially relevant for the poroelastography applications.

DPE is a robust and computationally fast method for integer axial and lateral displacement estimation [119], whereas the HS method is found to be a good choice for estimation of sub-sample axial and lateral displacements [164,165]. Specifically, the HS method has certain advantages over other optical flow based methods such as Lucas-Kanade (LK) [164] and sub-pixel displacement recovery methods [166]. In the LK method, a matrix needs to be inverted to obtain the flow field. The matrix may not be defined for many conditions, such as flat regions where the derivatives are zero and lines where x and y derivatives are linearly correlated. In the HS method, these problems are solved by imposing an additional constraint on the flow field: spatial smoothness, i.e., adjacent pixels should move together as much as possible. As discussed in [164], the HS method displays a better convergence for displacement estimation in comparison to the LK method. With increasing displacements between image frames, the HS technique shows constantly better performance, especially in the motion boundary region with respect to LK method. The HS method also generates sharper motion boundaries and offers higher robustness within deformation regions with respect to LK method. The HS method is also found to possess higher spatial resolution than the LK method. Therefore, overall, the HS method is expected to perform better than the LK method in ultrasound poroelastography applications.

Our proposed two-step method was tested with simulated and experimental data. Our results show that the proposed method can generate accurate EPR elastograms in a variety of time and applied compression conditions.

The performance of the proposed method was qualitatively and statistically compared with the performance of CM [136] and AM [120] algorithms. We chose these two comparative benchmarks for the following reasons. CM is the most widely used technique for strain estimation in elastography [124, 167]. AM is based on DPE but with sub-sample axial and lateral strain estimation capability. The better performance of DPHS in comparison to AM clearly shows the effectiveness of using HS to improve the quality of the strain images, especially that of EPR elastograms. Most of the available displacement estimation methods work well for estimating the axial displacement but perform poorly for lateral displacement estimation. Due to inherently poor lateral sampling

in standard ultrasound imaging, it is important to use a method that can very efficiently estimate sub-pixel lateral displacements, such as the HS [164]. Our study shows that HS produces accurate estimates of both sub-pixel axial and lateral displacements and the estimation of sub-pixel axial strain from HS is smoother than that of other methods. Although estimated axial strains from various methods look similar, the performance of DPHS in the EPR estimation appears to be significantly better than that of AM and CM because of the more accurate lateral strain estimation and of the smoother axial strain estimation. This is demonstrated in simulations as well as controlled and in vivo experiments.

By using the parameter estimation methods on the acquired in vivo ultrasound poroelastographic experimental data, the mechanical parameters such as Young's modulus, interstitial permeability and vascular permeability of tumor and normal tissues could be extracted with help of a proper analytical model [13]. All these parameters are known to be of great clinical value for cancer diagnosis, treatment and prognosis [27, 168]. However, for determination of these parameters, accurate estimations of the EPR and axial strain are necessary. As DPHS has been proved efficient in both controlled and in vivo experiments in our study, DPHS can be an essential tool in parameter estimation and imaging in ultrasound poroelastography in clinical settings.

The main limitation of the proposed method is the estimation of EPR for high axial compression levels. In our simulations, we have observed that, when the applied strain is larger than 7%, the results from DPHS begins to degrade presumably due to the limited performance of the HS method in estimating large displacements. In our simulations, AM and correlation methods were found to begin to deteriorate at around 9% applied strain. However, it should be noted that applied strains above 5% are not typical in in vivo ultrasound elastography studies.

In terms of computational time, current implementation of the proposed method requires about 29 second in a 3.8 GHz Core i5 CPU with 8 GB RAM to produce a EPR elastogram using for pre-compressed and post-compressed data of size 2078×128 pixels. Further improvement in speed can be obtained using multi-processors and is left for future work.

Given the results presented in this paper, we believe that the availability of the proposed DPHS

method can have a significant impact in novel applications of elastography dealing with EPR estimations, for the assessment of different strain time constants, and, in general, in ultrasound applications requiring lateral displacement information such as shear strain imaging and 3D elastographic imaging.

3.6 Conclusion

In this paper, we propose a novel technique to estimate the time varying EPR of biological tissues. Our simulation results demonstrate that the proposed method can provide better quality EPR estimates than those obtainable using standard methods such as correlation-based technique or analytic minimization method. Experimental data is used to validate the method with real data. Availability of the proposed method may be helpful for future elastographic studies requiring accurate and reliable lateral displacement and strain estimations.

4. ESTIMATION OF YOUNG'S MODULUS AND POISSON'S RATIO

4.1 Background

There are only a few non-invasive imaging modalities that are capable of generating YM maps of tissues in vivo, while there are no available methods to non-invasively image the PR in complex biological tissues. Ultrasound elastography (USE) [3], ultrasound shear wave elastography (SWE) [169] and magnetic resonance elastography (MRE) [170] techniques have shown to be able to provide YM images, under the assumption that the tissue behaves as a linearly elastic incompressible solid (i.e., as PR of 0.5) [171–176]. Recent studies have demonstrated the feasibility of imaging the lateral-to-axial strain ratio also referred to as "effective PR" (EPR) in tissues using elastography [96], [153], [10, 177], but not the actual, underlying PR of the tissue.

There are two main approaches that can be used for reconstructing the YM distribution in tissues - a direct approach and an iterative approach. In the direct approach, a partial differential equation developed using the equations of equilibrium for linear elastic solids is used for estimating the YM [178–181]. The limitation of the direct approach is that it implicitly assumes continuity of the stress and strain in the tissue. Therefore, it is not directly applicable to cases where the distribution of the YM can vary sharply such as at the interface of a tumor and surrounding tissue.

The iterative methods utilize forward and backward solutions of the differential equations of equilibrium for linear elastic solids and attempt to minimize their differences [171,172]. Generally, the iterative methods are more robust than the direct approaches but have other limitations. Firstly, these methods are computationally intensive [182, 183]. Secondly, they require a regularization term, which is often difficult to choose. The regularization parameter is used to reduce the noise and preserve the contrast of the reconstructed YM image. Inability to select a proper value of the regularization parameter can result in incorrect and noisy estimates of YM.

In most of the works pertinent to medical elasticity imaging retrievable in the literature, the YM of the tissue is reconstructed with two fundamental assumptions: 1) that the tissue (tumor and

surrounding tissue) behaves as a perfectly linearly elastic solid, and 2) that the tissue is incompressible or nearly incompressible [171–176, 184]. It is now widely believed that tissues can be more realistically represented using poroelastic models instead of linearly elastic models. Thus their strain response under loading varies with time. In that case, the YM and PR should be determined by the strain response at steady state, when the material is fully relaxed [185]. The YM estimated from the instantaneous response of soft tissue in place of steady state response can be much higher (2-4 times) than the true value as shown in Bayat et al. [186]. In all the above-mentioned works [171–176, 184], the PR of the tissue, which is needed to correctly estimate the YM of the tissue, is not estimated. Rather, it is assumed to be a given value, typically $0.495/0.499995/0.45$. Moreover, it has been demonstrated by a number of studies that the PR of tissues (including tumors) may have a value much lower than 0.495. In the works of Stylianopoulos et al. [16], Mpekris et al. [115] and Fung [116], the PR of normal tissue was assumed 0.2 and that of cancer was assumed 0.2 (compressible)/0.45 (incompressible) in works of Stylianopoulos et al. [16], Roose et al. [187] and Netti et al. [59]. Recently, Nia et al. [185] assumed a PR value for the soft tissue and tumor of 0.1 to compute the residual stress inside the tumor. In some other works [188–191], the authors reported or used values of PR for the soft tissue ranging between 0.3 and 0.45. Given the broad range of PR values for soft tissue and tumors that has been reported in the literature, the assumption that the PR is constant and equal to 0.5 or a value to close to 0.5 is not only unrealistic but can also lead to incorrect reconstructed YM values. Accurate determination of the PR is crucial to obtain accurate estimates of YM. In addition, a correct knowledge of the YM and PR is essential for the quantification of other poroelastic parameters such as vascular and interstitial permeability, which are known to be of great clinical value [13]. Finally, it is reasonable to expect that the PR itself may change with the onset of many diseases [10] as it is directly related to the compressibility of the tissue, and this information could prove useful clinically.

The estimation of the mechanical properties of tumors is inherently a three-dimensional problem. While a few three dimensional YM reconstruction methods have been reported in the literature [176, 192], in most of the prior YM reconstruction studies, the models are two dimensional

and based on the common assumption of plane strain/plane stress [171, 172, 193–195]. Furthermore, most of the above mentioned methods assume specific boundary conditions such as total uniformity of the background, stress-free lateral boundaries etc., which are rarely true in complex cancer environments. Most of these methods perform well for tumors of specific shapes such as disk (2D)/sphere (3D) [171, 192, 194, 195] but have poorer performance in tumors of other shapes such as ellipse. These methods also perform poorly when the YM contrast between the tumor and normal tissue is larger than 10 and are not applicable to the case of tumors softer than the background [195]. In many cases, the tumor is assumed to be very small so that certain ratios such as ratios of sample radius to tumor radius, compressor radius to tumor radius and distance between applied force and tumor to tumor radius are greater than a predefined value [192, 194]. Determination of heterogeneous distribution of YM inside the tumor and normal tissue is another challenge [196]. Most of these methods fail to reconstruct the YM accurately in case of non uniform axial compression, which occurs frequently in elastography experiments.

In this section, we present a three dimensional YM and PR reconstruction method based on Eshelby's inclusion formulation [110, 197]. Our proposed method overcomes the aforementioned limitations of current YM reconstruction methods. It allows simultaneous quantification and imaging of the YM and PR in both a tumor and surrounding tissue irrespective of the complex boundary conditions and/or the shape of the tumor and for a wide range of tumor/background YM contrasts ($0.1 - 50$). In our approach, the tumor and normal tissues are assumed to behave as poroelastic materials, and the YM and PR are reconstructed from knowledge of the strain responses at steady state. The proposed method is based on a cost function minimization technique, and the cost function is developed utilizing the formulations of eigen strain described in works of Eshelby [110] and Mura [197].

4.2 Materials and methods

The local stress and strain inside and outside an inclusion due to the remote stress have been determined by Eshelby [110] using the superposition principle and Green's function. The remote stress is the applied stress that creates a uniform stress over the entire background. This was done

using a virtual experiment, which is summarized in Fig. 4.1. The virtual experiment is composed by the following steps:

1. Isolate the inclusion from the background (Fig. 4.1(A)). Consequently, the inclusion is strained because of the loss of constraint imposed by the background. This strain is denoted as eigenstrain (ϵ^*).

2. Apply traction T to bring the inclusion in its original shape (Fig. 4.1(B)). The strain induced inside the inclusion should compensate the eigenstrain.

3. Insert the inclusion back in the background (Fig. 4.1(C)). The traction force is still T.

4. Remove the applied traction T (Fig. 4.1(D)). This is the same scenario as step 1 (Fig. 4.1(A)). The removal of the traction force from step 3 to step 4 is equivalent to applying a body force of $-T$ to the surface of the inclusion.

These four steps can be written mathematically in terms of the Green's function of the elastic body. The strain and stress inside the inclusion can be written as [110, 176]

$$\boldsymbol{\epsilon} = \boldsymbol{\epsilon^0} + \boldsymbol{S} : \boldsymbol{\epsilon^*}, \tag{4.1}$$

$$\boldsymbol{\sigma} = \boldsymbol{\sigma^0} + \boldsymbol{C^0} \cdot [\boldsymbol{S} - \boldsymbol{I}] : \boldsymbol{\epsilon^*}, \tag{4.2}$$

where $\boldsymbol{\epsilon^0}$ is the remote strain, $\boldsymbol{\epsilon^*}$ is the eigenstrain, $\boldsymbol{\sigma^0}$ is the remote stress, $\boldsymbol{C^0}$ is the stiffness tensor of the background, $\boldsymbol{I}$ is the identity tensor and $\boldsymbol{S}$ is the Eshelby's tensor. $\boldsymbol{\epsilon^0}$, $\boldsymbol{\epsilon^*}$ and $\boldsymbol{\sigma^0}$ are vectors of three components (axial, lateral and elevational). Based on the axisymmetric assumption, the lateral and elevational components are equal. The relationship between the remote stress $\boldsymbol{\sigma^0}$ and $\boldsymbol{\epsilon^0}$ can be expressed as

$$\boldsymbol{\sigma^0} = \boldsymbol{C^0} : \boldsymbol{\epsilon^0}. \tag{4.3}$$

The Eshelby's tensor $\boldsymbol{S}$ is a function of the geometry of the inclusion and the PR of the background.

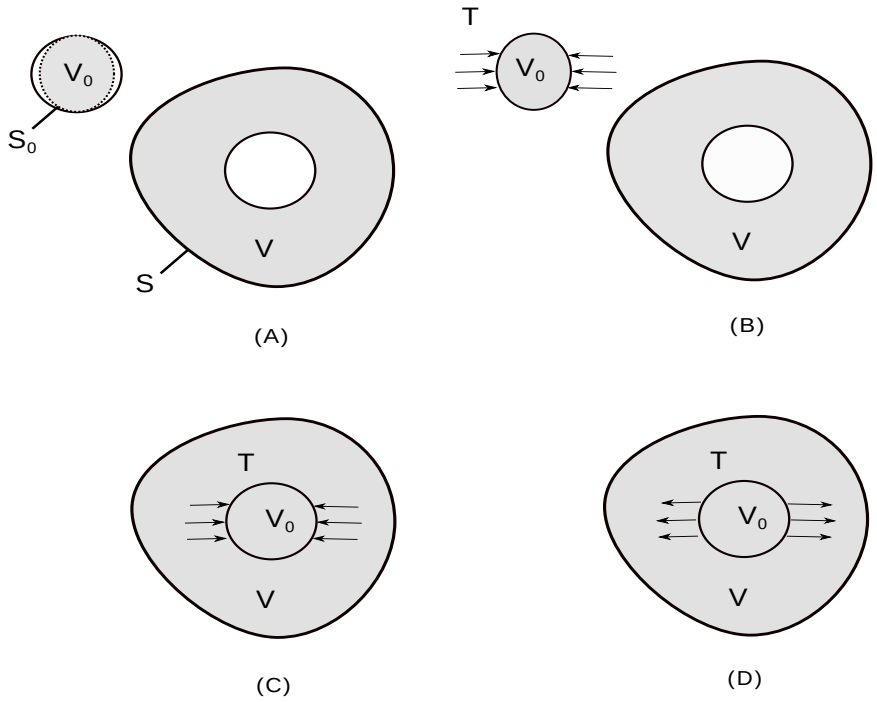

Figure 4.1: Four steps of Eshelby's virtual experiment to reach the solution. Here background is a linear elastic solid of volume V and surface S. The inclusion is also a linear elastic solid of volume V_0 and surface S_0. (A) The inclusion is removed from the background. (B) A surface traction T is applied to return V_0 in its original shape. (C) Put the inclusion back to the matrix and (D) remove the applied traction.

In eqs. (4.1) and (4.2), the eigenstrain can be written as ([197] eq. 22.13)

$$\boldsymbol{\epsilon^*} = (\boldsymbol{S} + \boldsymbol{A})^{-1} : (\boldsymbol{B} : \boldsymbol{\epsilon}^t - \boldsymbol{\epsilon^0}), \tag{4.4}$$

where ϵ^t is a prescribed eigenstrain (zero for our current problem), and the fourth-order mismatch stiffness tensors A and B can be defined as

$$\boldsymbol{A} = [\boldsymbol{C} - \boldsymbol{C^0}]^{-1} \cdot \boldsymbol{C^0}, \tag{4.5}$$

$$\boldsymbol{B} = [\boldsymbol{C} - \boldsymbol{C^0}]^{-1} \cdot \boldsymbol{C}, \tag{4.6}$$

where $\boldsymbol{C}$ is the stiffness tensor in the inclusion. The expression of $\boldsymbol{A}$ is relevant to our problem. $\boldsymbol{A}$ is determined in [198].

Let us indicate $\boldsymbol{\epsilon^*}$ in eq. (4.1) as $\boldsymbol{\epsilon_1^*}$ and $\boldsymbol{\epsilon^*}$ in eq. (4.4) as $\boldsymbol{\epsilon_2^*}$. In the expression of $\boldsymbol{\epsilon_1^*}$, only the Eshelby's tensor $\boldsymbol{S}$ is involved. This requires knowledge of the tumor (inclusion) geometry and the PR of the normal tissue (background). In the expression of $\boldsymbol{\epsilon_2^*}$, the YM and PR of the tumor and normal tissues are involved.

A cost function can be defined as

$$J(E_i, \nu_i) = (J_1(E_i, \nu_i))^2 + (J_2(E_i, \nu_i))^2, \tag{4.7}$$

where

$$J_1(E_i, \nu_i) = \boldsymbol{\epsilon_1^*}(1) - \boldsymbol{\epsilon_2^*}(1), \;\; J_2(E_i, \nu_i) = \boldsymbol{\epsilon_1^*}(2) - \boldsymbol{\epsilon_2^*}(2) \tag{4.8}$$

and by minimizing this cost function J, we can obtain the YM (E_i) and PR (ν_i) of the tumor. The YM and PR of the normal tissue can be determined by using eq. (4.3). The expressions of $\boldsymbol{\epsilon_1^*}$ and $\boldsymbol{\epsilon_2^*}$ for elliptic (prolate, oblate) and spherical tumor (inclusion) are shown in [198]. The expressions of the Eshelby's tensor $\boldsymbol{S}$ for cylindrical, flat elliptic, penny-shaped tumors are given in [198]. Using

these $\boldsymbol{S}$ in equations of $\boldsymbol{\epsilon_1^*}$ and $\boldsymbol{\epsilon_2^*}$ for elliptic tumor, $\boldsymbol{\epsilon_1^*}$ and $\boldsymbol{\epsilon_2^*}$ for these shapes can be determined (and therefore YM and PR).

4.2.1 Controlled experiments

For the controlled experiments, we used the breast phantom model 059 from Computerized Imaging Reference Systems (CIRS), Inc., Norfolk, VA, USA. As provided by the manufacturer, in this phantom, the Young's modulus of each inclusion mass is around 50 kPa, while the background has a Young's modulus of 20 ± 5 kPa [199, 200]. The PR of both inclusions and background of this phantom is 0.5 [201]. The applied compression was evaluated using a graphical user interface monitoring the force sensor. The axial and lateral strain was estimated using the pre- and post-compressed ultrasound radio frequency data acquired in the elastography experiments.

4.2.2 In vivo experiments

Experiments on nineteen mice with triple negative breast cancer cells injected in the mammary fat pad were carried out on a weekly basis for three consecutive weeks. The cancers were created at the Houston Methodist Research Institute by injection of the cancerous cells beneath the mouse's mammary fat pad [159]. In vivo data acquisition was approved by the Houston Methodist Research Institute, Institutional Animal Care and Use Committee (ACUC-approved protocol # AUP-0614-0033). Seven mice were kept untreated and twelve mice were treated by injecting them intravenously with one of the following drugs: 1. Epirubicin alone, 2. Liposomes loaded with Epirubicin and 3. Liposomes loaded with Epirubicin and conjugated with Lox antibody on the particle surface. The dose of each drug was 3 mg/kg body weight once a week. Prior to ultrasound data acquisition, each mouse was anesthetized with isoflurane. Each data acquisition session was 5 minutes long, and several RF data acquisitions could be performed during this period (for reliability purposes).

Elastography was carried out using a 38-mm linear array transducer (Sonix RP, Ultrasonix, Richmond, BC, Canada) with a center frequency of 6.6 MHz and $5 - 14$ MHz bandwidth. To compensate for the surface geometry as well as facilitate positioning the focus inside the superfi-

cial tumors, an aqueous ultrasound gel pad (Aquaflex, Parker Laboratories, NJ, USA) was placed between the compressor plate and the developed tumor. It should be noted that such use of gel pad does not change the stress distribution inside the sample significantly and thus does not change the estimated parameters. This has been proved in [198]. A force sensor (Tekscan FlexiForce) was inserted between the gel pad's top surface and the compressor plate to record the applied force during the compression. Creep compression was performed manually on the animals and monitored using the force sensor, with the duration of each compression being one minute. Duration of the experiment was selected based on the temporal behavior of the soft tissue and tumor reported in the literature [202] and to ensure that both the tumor and surrounding tissues reached steady state conditions. Ultrasound radio-frequency (RF) data acquisition was synchronized to the application of the compression. The sampling period of the data was set at 0.1 s. The axial and lateral strain data were calculated at steady state, when both the tumor and normal tissues behave as elastic materials [203]. An expert radiologist is employed to segment the in vivo axial strain elastograms in Matlab for determining the tumor areas.

4.2.3 Calculation of stress

FlexiForce OEM Development Kit manufactured by Tekscan, Inc., South Boston, MA, USA-02127 was employed to inspect and adjust the applied compression in both the controlled and in vivo experiments. A Microsoft Windows based interface software is provided with the sensor and can be used to observe and record the applied force. A temporal curve showing the applied compression in one of the in vivo experiments is reported in Fig. 4.2. The sensor used in the kit is model #A201, which senses a force range $0 - 4.4$ N in a scale of $0 - 255$. The diameter of the sensing area of the sensor is 9.53 mm. The area of the sensing area is calculated as 7.1331×10^{-5} m^2 ($A_r = \pi r^2$). The applied pressure in Pa is calculated using

$$\sigma_0 = \frac{F_r \times 4.4}{255 \times A_r}, \tag{4.9}$$

where F_r is the mean force reading obtained from the sensor during the experiments. It should be noted that σ_0 is the axial component of $\boldsymbol{\sigma^0}$ in eq. 4.3 and other two components (lateral and elevation) of $\boldsymbol{\sigma^0}$ are zero.

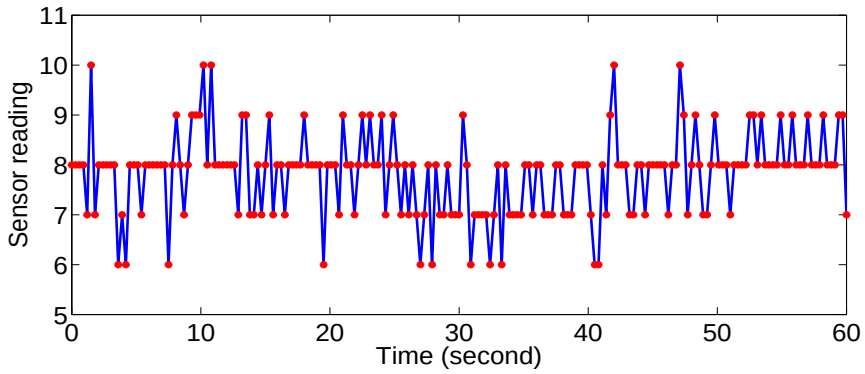

Figure 4.2: Reading from the force sensor in an in vivo elastography experiment.

4.2.4 Estimation of axial and lateral displacements and strains

To compute the axial and lateral strains in both the simulated and experimental data, a technique recently developed in our lab [146] was used.

4.2.5 Estimation of YM and PR

For FE and ultrasound simulation data, we select a square region of 5×5 pixels in the left corner of the axial and lateral strain elastograms (128×128 pixels). The mean strains of this area are assumed to be representative of the axial and lateral strains of the background region. For the in vivo and controlled experiments, we choose a square region of 10×10 pixels in the normal tissue/background region and compute the mean values of the strains in that region. For estimation of YM and PR using the proposed method, non linear least square optimization by 'trust-region-reflective' algorithm in MATLAB (The MathWorks, Natick, MA) is used to minimize the cost function J in eq. 4.7, where the maximum number of iteration is set to 100. Complex shapes such as tetragon, pentagon and hexagon are approximated with ellipses, and the cost function for

the elliptical tumor has been used for these shapes. The approximation of these complex shapes with ellipses are shown in Fig. 4.3. The lower and higher limits for the YM are set to $0.1 \times \frac{\sigma_0}{\epsilon_{zz}}$ and $100 \times \frac{\sigma_0}{\epsilon_{zz}}$ inside the tumor. The lower limit of PR in the cost function minimization process is set to $-0.8 \times \frac{\epsilon_{xx}}{\epsilon_{zz}}$ and the higher limit is set to 0.495. Here, ϵ_{zz} and ϵ_{xx} are axial and lateral strains, respectively. For reconstruction using the 3DB method, the method described in [192] is used while for 3DS method, the method described in [176] is used. When computing the YM by 3DB, the Poisson's ratios of both inclusion and background are assumed 0.495 in all cases. The correctness of the implementations of these methods is verified by matching the results obtained by our implementations with the results reported in their papers for the same simulation conditions.

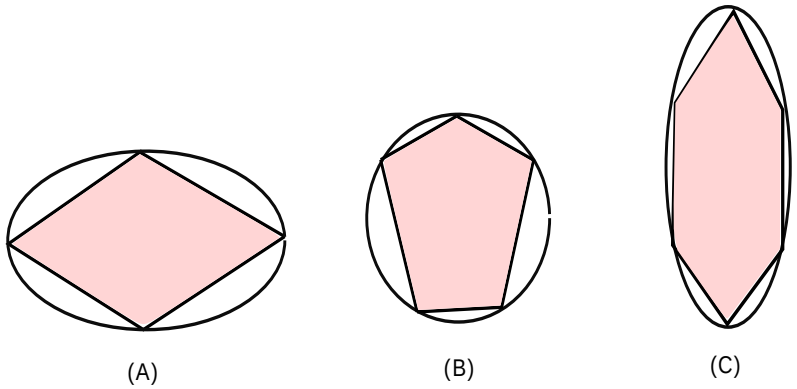

Figure 4.3: Approximation of different shapes with ellipses (A) tetragon (B) pentagon (C) hexagon. It has been assumed that in the imaging plane the tumors are of these shapes and if the plane is revolved around the center line, the shape remains same in all other planes (axisymmetry).

4.2.6 Calculation of RMSE of estimated YM and PR

Calculation of RMSE for the estimated YM and PR of the inclusion was performed using the following formula [146].

$$\text{RMSE} = \sqrt{\frac{\sum_n^N (\Lambda_e(n) - \Lambda_t(n))^2}{N}} \times \frac{100 \times N}{\sum_n^N \Lambda_t(n)}, \tag{4.10}$$

where Λ_e is the vectorized (reshaped from 2D to 1D) YM or PR of the inclusion from YM and PR images estimated by different methods and Λ_t is the vectorized true YM or PR of the inclusion. N is the total number of points inside the inclusion of the estimated YM or PR image.

4.2.7 Calculation of surface area and solidity of the tumors

The surface area of the tumor, A_s is calculated in cm^2 as

$$A_s = \frac{n_p \times 16}{n_t}, \tag{4.11}$$

where n_p is the pixel number inside cancer tumor and n_t is the total number of pixels in the elastogram.

The solidity of the tumor is calculated as

$$s_t = \frac{a}{c_a}, \tag{4.12}$$

where a is the area and c_a is the convex area of the tumor.

4.2.8 Simulation procedures

The methods of FE and ultrasound simulations for the results in this section are discussed in detail in [198].

4.2.9 Specifications of the samples

The material properties of all samples are chosen based on values of YM and PR for tumors and normal tissues available in the literature [13, 16, 40, 115, 116]. In samples A-M, the normal tissues have YM equal to 32.78 kPa. A, D, E and F have tumors with YM equal to 97.02 kPa. B, C, H, I, J, K, L and M have tumors with YM equal to $50, 163.90, 491.7, 819.5, 1639, 3278, 16.39, 6.556$ and 3.78 kPa, respectively. The PR of normal tissues in A, B and C is equal to 0.49, in D is equal to 0.45 and in E-M is equal to 0.2. The PR of tumor is equal to 0.4 in A-C, 0.45 in D and E, 0.3 in F, 0.45 in G-J and 0.3 in K-M. These mechanical parameters are shown in tabulated form in Table 4.1 in the supplementary material.

Table 4.1: YM and PR of samples A-M used in the FEA and ultrasound simulations

Sample name	E_b (kPa)	E_i (kPa)	ν_b	ν_i
A	32.78	97.02	0.49	0.40
B	32.78	50.00	0.49	0.40
C	32.78	163.90	0.49	0.40
D	32.78	97.02	0.45	0.45
E	32.78	97.02	0.20	0.45
F	32.78	97.02	0.20	0.30
G	32.78	491.70	0.20	0.45
H	32.08	819.50	0.20	0.45
I	32.78	1639.00	0.20	0.45
J	32.78	3278.00	0.20	0.45
K	32.08	16.39	0.20	0.30
L	32.78	6.556	0.20	0.30
M	32.78	3.278	0.20	0.30

For samples Z1-Z8, H1-H3, B1-B3 and R1-R4, the YM and PR of tumor are set to 97.02 kPa and 0.3, whereas the YM and PR of the normal tissue are set to 32.78 kPa and 0.2. For samples X1-X9, the YM and PR of tumor are set to 97.02 kPa and 0.45 and the YM and PR of the normal tissue are set to 32.78 kPa and 0.2.

All the samples simulated are of 4 cm height and 2 cm width in an axisymmetric setup. In samples A-M and X1-X9, the radius of the spherical inclusion is 0.3 cm. In sample Z1, the radius of the inclusion is 0.3 cm, the lengths of elliptical axes along lateral and axial direction in inclusions of samples Z2 and Z3 are 0.2 cm and 0.5 cm and 0.5 cm and 0.2 cm, respectively. The radius and height of the cylindrical inclusion of sample Z4 are 0.3 cm and 0.55 cm. The radius of the penny-shaped inclusion of sample Z5 is 0.5 cm and the height is 0.05 cm. The length of each side of tetragonal, pentagonal and hexagonal inclusions in samples Z6, Z7 and Z8 are 0.45 cm. The dimensions of the inclusions and boundary conditions of samples B1-B3, H1-H3 and R1-R4 are described in detail in supplementary material.

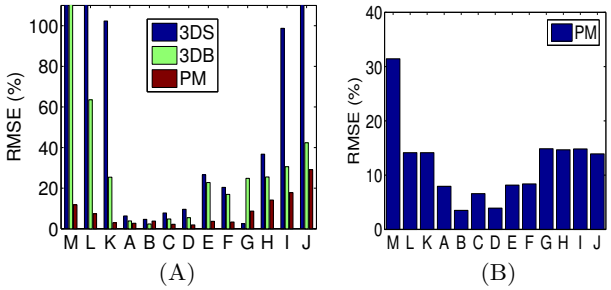

Figure 4.4: (A) Percent root mean squared errors (RMSE) of estimated YM images and (B) RMSEs of estimated PR images from three different methods for samples A-M using ultrasound simulated data. RMSEs greater than 100% have been masked to 100%. PM stands for: proposed method. Samples A-J are with tumors harder than the surrounding normal tissue, and K-M are with tumors softer than the surrounding normal tissue. RMSE is higher in case of samples with soft tumors. The RMSEs for 3DB and 3DS method are less than 5% for Sample C, whereas the RMSEs are more than 60% for sample L. RMSE for the proposed method is below 3% for sample C and below 6% for sample L. Sample C and sample L have 5 and $\frac{1}{5}$ contrast of YM between the tumor and normal tissue. For hard tumors, RMSE in estimating the YM for all three methods increases as the contrast of YM between the tumor and normal tissue increases. The RMSE in estimating the YM by the proposed method is the lowest in all cases in comparison to the other two methods.

4.3 Results

4.3.1 Simulations

The YM distributions in samples with different mechanical properties reconstructed using the proposed method were compared with the results obtained using two other 3D reconstruction methods, which are referred to as "3DB" [192] and "3DS" [176]. Eight samples of different shapes (Z1-Z8), nine samples of different inclusion/background YM contrasts (fixed inclusion/background PR contrast) (X1-X9), three samples with different boundary conditions (B1-B3), three samples with different YM heterogeneity percentages (H1-H3), four samples with different non-uniform loadings (R1-R4) and thirteen samples of different inclusion/background YM and PR contrasts (A-M) were simulated and analyzed.

The percent root mean squared errors (RMSE) occurring when reconstructing the YM distribution in tumors of different shapes using the 3 approaches are shown in Table 4.2. We observe that, within the results obtained using the proposed approach, the highest RMSE is observed when

the shape of the tumor is cylindrical (9.91%) and the lowest (0.8%) when the shape of the tumor is spherical. In comparison, the RMSE associated to the other two YM reconstruction approaches are much higher than the one associated to the proposed method and typically higher than 20% for tumors of all shapes. The RMSEs occurring when reconstructing the PRs using the proposed approach are also shown in the table, and they are found to be less than 9% in all simulated samples.

The RMSEs computed for the three methods in the case of tumors having different YM contrast (CTYM) with respect to the background are reported in Table 4.3. We see that the RMSE associated to the proposed approach is below 5% for contrast of $0.1 - 100$, whereas the RMSEs for the 3DB and 3DS approaches are higher than 20% in most cases.

A typical problem of elastography-based reconstruction methods is the effect of boundary conditions on the reconstructed mechanical parameters. The RMSEs computed when the YM of the tumor is reconstructed using data obtained with different boundary conditions are shown in Table 4.4. We see that, even in the case of very complex boundary conditions, the proposed approach can reconstruct the YM with about 90% accuracy. The other two reconstruction methods, instead, show larger RMSEs for all boundary conditions when compared to the proposed one.

Table 4.2: RMSEs in estimating the YM of inclusions of different shapes using different methods when the YM inclusion/background contrast (CTYM) is 3. RMSEs in estimating the PR in the same inclusions using the proposed method (PM) are shown in parentheses.

Sample	Shape	3DB (%)	3DS (%)	PM (%)
Z1	spherical	16.95	2.38	0.8(0.5)
Z2	prolate	26.86	3.28	2.69 (2.31)
Z3	oblate	56.00	27.06	5.01 (2.66)
Z4	cylindrical	21.57	22.18	9.91 (8.88)
Z5	penny	62.95	129.73	8.29 (12.67)
Z6	3D tetragon	27.39	43.00	9.39 (7.04)
Z7	3D pentagon	21.34	24.75	8.55(7.31)
Z8	3D hexagon	41.73	46.42	8.12(6.75)

Effect of heterogeneity in the YM distribution inside the tumor on the reconstructed parameters

Table 4.3: RMSEs in estimates of YM of spherical shaped inclusions by different methods for different CTYM values. RMSEs in estimating the PR in the same inclusions using the proposed method (PM) are shown in parentheses.

Sample	CTYM	3DB (%)	3DS (%)	PM (%)
X1	0.1	888.97	885.69	3.54(0.34)
X2	0.2	47.59	393.18	2.25 (0.19)
X3	0.5	4.54	97.71	1.34 (0.08)
X4	3	22.77	26.60	0.56 (0.05)
X5	5	23.77	26.35	0.64 (0.39)
X6	15	24.58	2.52	1.71 (0.94)
X7	25	24.53	36.54	2.34(3.36)
X8	50	25.15	98.72	3.85(11.98)
X9	100	24.59	115.81	4.75(2.41)

has been investigated, and the results are reported in Table 4.5. Sample H3 has the highest heterogeneity, where YM reduces by 30% from the center to the periphery of the tumor. The proposed method is capable of reconstructing the YM of the tumor with high accuracy ($> 94\%$) in all cases analyzed in this study whereas the other two approaches introduce more than 14% error in most cases.

The results related to the non-uniform compression conditions are shown in Table 4.6. Once again, the proposed method is robust to load variations, as opposed to the other two methods.

In Fig. 4.4(A), we report the RMSEs of the estimated YM images using the three reconstruction techniques for thirteen samples A-M when using simulated ultrasound data, and the RMSEs of the estimated PRs in the same samples using the proposed technique are shown in Fig. 4.4(B). We see from Fig. 4.4 that the error incurred in all the reconstruction methods increases as the inclusion/background YM contrast increases. However, the RMSE for the proposed method is below or around 15% for inclusion/background YM contrasts up to 50 (sample H). The RMSE for the estimated PR also increases as the inclusion/background YM contrast increases but remains around 10% even in case of a YM contrast of 100 (sample J). The other two methods can introduce errors greater than 25% even in case of a contrast as low as 3 (sample E). The RMSE for all methods increases for the samples with a soft inclusion (samples K-M). However, the error is significantly

Table 4.4: RMSEs in estimating the YM of spherically shaped inclusions with a CTYM of 3 by using different methods for different complex boundary conditions. RMSEs in estimating the PR in the same inclusions using the proposed method (PM) are shown in parentheses.

Sample	Boundary condition	3DB (%)	3DS (%)	PM (%)
B1	zig-zag stiffer tissue in background	19.25	21.82	7.74(8.32)
B2	14 different shaped inclusions in background	30.90	34.91	10.94 (3.67)
B3	strip of hard tissue on top of the tumor	16.56	19.94	0.9 (2.14)
B4	multiple layers of tissue on top of the tumor	12.03	14.87	5.06 (5.02)
B5	multiple layers of tissue on top of the tumor	21.86	24.15	5.55 (6.37)

Table 4.5: RMSEs in estimating the YM of the spherical shaped inclusions of CTYM of 3 by different methods for different heterogeneity conditions. RMSEs in estimating the PR in the same inclusions using the proposed method (PM) are shown in parentheses.

Sample	Heterogeneity (%)	3DB (%)	3DS (%)	PM (%)
H1	10	16.12	18.98	2.27(4.13)
H2	20	14.79	16.78	3.91 (5.25)
H3	30	13.95	14.91	6.22 (11.45)

lower for the proposed method in comparison to other two techniques. For sample M, where the inclusion is 10 times softer than the background, the RMSEs are higher than 100% for 3DB and 3DS methods, while the RMSE for the proposed technique is below 10%. These results prove that the proposed approach is more accurate, more precise and more robust than previously proposed 3D YM reconstruction methods and has the advantage to provide estimates of both the YM and the PR distributions.

4.3.2 Controlled experiments

Fig. 4.5 shows selected results from controlled experiments performed on a breast-mimicking phantom containing different spherical inclusions simulating incompressible tumors with similar stiffness. In Fig. 4.5, the estimated axial strain, lateral strain, reconstructed YM and PR distri-

Table 4.6: RMSEs in estimating the YM of spherical shaped inclusions with CTYM of 3 by different methods under non-uniform loading. RMSEs in estimating the PR in the same inclusions using the proposed method (PM) are shown in parentheses. In these cases, the load is increased or decreased from the center to the periphery of the compressor plate.

Sample	Non-uniformity of loading (%)	3DB (%)	3DS (%)	PM (%)
R1	20% reduction	31.84	35.54	9.47(1.89)
R2	10% reduction	24.68	28.26	5.24 (1.02)
R3	20% increment	7.94	10.86	9.52 (3.20)
R4	10% increment	12.96	15.94	6.45 (3.32)

butions for one of the inclusions inside the breast phantom are shown. The mean and standard deviation values of the reconstructed YM and PR distributions as obtained from this experiment can be found in Table 4.7. According to the manufacturer's specifications for this breast phantom [199, 200], the YM of the background is 20 ± 5 kPa while the YM in the inclusion is approximately 50 kPa. The PR is approximately 0.5 both in the inclusion and in the background [201]. Thus, our reconstructed YM and PR have errors less than 7% and 15%, respectively.

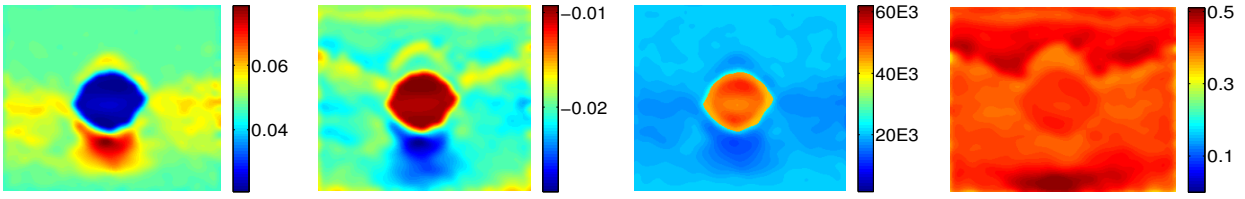

(A1) (A2) (A3) (A4)

Figure 4.5: Estimated axial strain (A1), lateral strain (A2), YM image (A3) and PR image (A4) from the controlled experiment (CE1). This figure shows results for applied compression of 0.97 kPa. The estimated YM is in the range of $45 - 55$ kPa in the inclusion and in the range of $17 - 21$ kPa in the background region. The estimated PR is around 0.44 in the inclusion region and 0.43 in the background region.

4.3.3 In vivo experiments

B-mode images and reconstructed YM and PR distributions obtained from data acquired from three untreated mice at three different time points (week 1, week 2 and week 3) are shown in

Table 4.7: Mean and standard deviation of the reconstructed YM and PR distributions in controlled experiment

Exp no	Applied load (kPa)	Est YM of inclusion (kPa)	Est PR of inclusion	Est YM of background (kPa)	Est PR of background
CE1	0.97	46.72 $\pm$3.59	0.432 $\pm$0.02	19.27 $\pm$1.61	0.427 $\pm$0.03

Fig. 4.6 (A1-A9, B1-B9 and C1-C9). We see from this figure that, in general, the YM increases significantly from week 1 (A2, A5, A8) to week 3 (C2, C5, C8) in the untreated mice, while the PR values are around 0.25 to 0.35. Based on prior literature on elastography, we expect most cancers to be stiffer than the normal tissue. However, to the best of our knowledge, our results are the first ones to experimentally demonstrate the actual increase of YM as the cancer progresses using ultrasound elastography.

B-mode images and reconstructed YM and PR distributions obtained from data acquired from three treated mice at three different time points (week 1, week 2 and week 3) are shown in Fig. 4.7 (A1-A9, B1-B9 and C1-C9). We see from this figure that, in most treated mice, the YM decreases or does not change with time. Also, the YM contrast between cancer and background tissue is not as high as in the case of the untreated mice. The PR values are in the range $0.3 - 0.4$ in most of the cases. However, the PR appears to increase in the first or second week and then to decrease in the third week in most of the cases. Once again, to our knowledge, these YM and PR trends in tumors following a treatment have not been experimentally investigated using elastography prior to this study.

The YM mean values with the corresponding standard deviations for twelve treated mice and seven untreated mice at the three different time points (week 1, week 2 and week 3) are shown in Fig. 4.8 (A1). In the first week, the mean YM in the untreated tumors was found to be below 50 kPa. In the second week, the mean YM in the untreated tumors increased significantly (above 60 kPa) and in the third week was found to be above 75 kPa. The mean YM in the treated tumors at the three different weeks was found to be close to 25 kPa, which is a value close to the one measured for the YM in the normal tissue (background).

The mean values of PR with the corresponding standard deviations for all the treated and un-

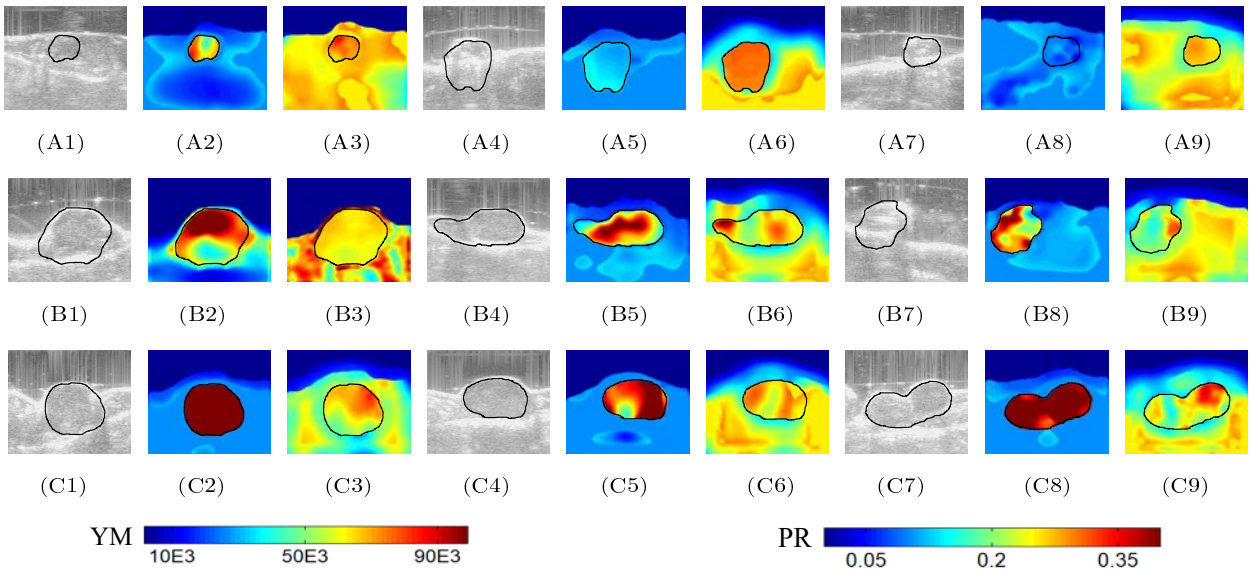

Figure 4.6: B-mode images of untreated mouse $\#1$ at three time points (week 1, week 2, week 3) are shown in (A1), (B1) and (C1). Reconstructed YM and PR distributions at the same time points are shown in (A2), (B2) and (C2), and (A3), (B3) and (C3), respectively. B-mode images of untreated mouse $\#2$ at three time points (week 1, week 2, week 3) are shown in (A4), (B4) and (C4). Reconstructed YM and PR distributions at the same time points are shown in (A5), (B5) and (C5), and (A6), (B6) and (C6), respectively. B-mode images of untreated mouse $\#3$ at three time points (week 1, week 2, week 3) are shown in (A7), (B7) and (C7). YM and PR distributions at the same time points are shown in (A8), (B8) and (C8), and (A9), (B9) and (C9), respectively. The YMs for the three cases increase from week 1 to week 3. More specifically, the YMs for the shown untreated mice are below 50 kPa in the first week, around 80 kPa in the second week and more than 90 kPa in the third week. These results indicate the increasing hardening of the tumor as the cancer progresses. The PRs do not change significantly at the three time points (≈ 0.3).

treated mice at the three different time points (week 1, week 2 and week 3) are shown in Fig. 4.8 (A2). In all these time points, the treated mice were found to have higher PR than the untreated ones. For both the treated and untreated mice, the mean PR does not appear to change significantly at the different time points.

Fig. 4.8 (A3) shows the tumor/background YM contrast for the twelve treated and seven untreated cancers, while Fig. 4.8 (A4) shows the tumor/background PR contrast (CTPR) for the twelve treated and seven untreated cancers. In Fig. 4.8 (A3), we see that the CTYM for untreated cancers is higher than that for the treated ones in all three weeks, which confirms previously reported findings [204].

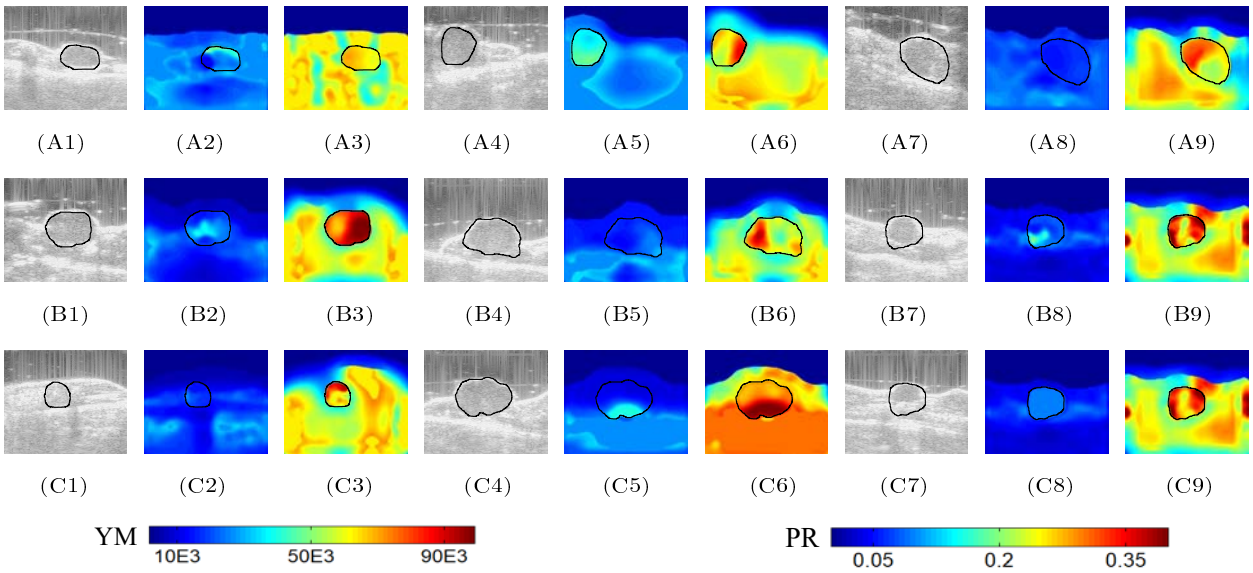

Figure 4.7: B-mode images of treated mouse $\#1$ at three time points (week 1, week 2, week 3) are shown in (A1), (B1) and (C1). Reconstructed YM and PR distributions at the same time points are shown in (A2), (B2) and (C2), and (A3), (B3) and (C3), respectively. B-mode images of treated mouse $\#2$ at three time points (week 1, week 2, week 3) are shown in (A4), (B4) and (C4). Reconstructed YM and PR distributions at the same time points are shown in (A5), (B5) and (C5), and (A6), (B6) and (C6), respectively. B-mode images of treated mouse $\#3$ at three time points (week 1, week 2, week 3) are shown in (A7), (B7) and (C7). Reconstructed YM and PR distributions at the same time points are shown in (A8), (B8) and (C8), and (A9), (B9) and (C9), respectively. The YMs for these treated mice are around 20 kPa for all time points, and the PRs are around 0.35 for all time points. Overall, the YM values of the treated mice are significantly lower than that of the untreated mice, whereas the PR values of the treated mice are higher than that of the untreated ones. The reduction/non-increment of stiffness of the treated tumors may be a sign of the efficacy of the treatment in controlling the growth of the cancer.

Mean surface areas of the tumors with the corresponding standard deviations for all the treated and untreated mice at the three time points are shown in Fig. 4.9 (A1). The mean surface area of the treated tumors does not change significantly with time, whereas the mean surface area of the untreated tumors increases with time.

The solidity of the tumor is a measure of the regularity of the shape of the tumor, and the mean values of solidity for all the tumors at the three time points are shown in Fig. 4.9 (A2). Solidity is higher in the case of the treated tumors than in the case of the untreated tumors at all time points. In a previous study, lower values of solidity have been associated to malignancy [205].

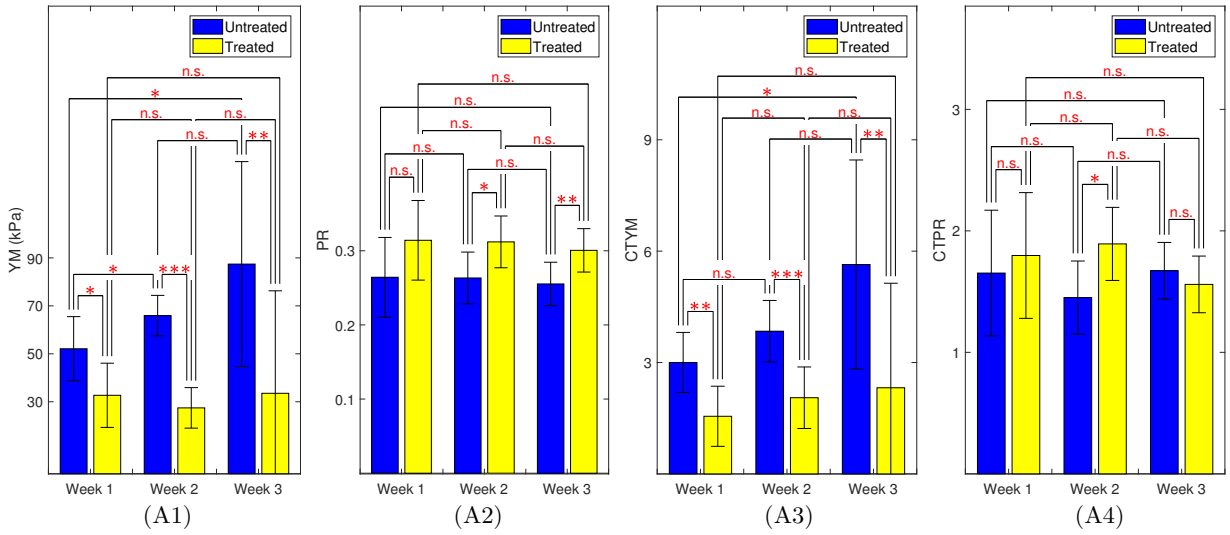

Figure 4.8: (A1) Mean YM values for the treated and untreated mice at week 1, week 2 and week 3. (A2) Mean PR values for the treated and untreated mice at week 1, week 2 and week 3. (A3) Mean YM contrast between tumor and normal tissue for treated and untreated mice at week 1, week 2 and week 3. (A4) Mean PR contrast between tumor and normal tissue for treated and untreated mice at week 1, week 2 and week 3. n.s. means not statistically significant. One, two and three stars correspond to p-value less than $0.05, 0.01, 0.001$, respectively. The mean values of YM and CTYM of the tumors increase from week 1 to week 3 for untreated mice and remain almost constant for the treated ones. Mean values of PR and CTPR of the tumors are consistently higher for the treated tumors than the untreated ones.

4.4 Discussion

In this paper, we propose a new, non-invasive, three dimensional method for reconstructing both the YM and PR in tumors. The YM is a mechanical parameter that has been investigated as a marker for cancer diagnosis, prognosis and treatment monitoring and planning. PR is another mechanical parameter, whose role in cancer assessment has not been fully elucidated yet, but it has been shown to have potentials in cancer-related diseases such as lymphedema [10, 177]. Both these parameters are needed to estimate other important properties of a tumor such as interstitial permeability and vascular permeability [13].

The proposed method has many advantages compared to previously proposed reconstruction techniques, which are currently used in elastography. It can accurately reconstruct the YM and

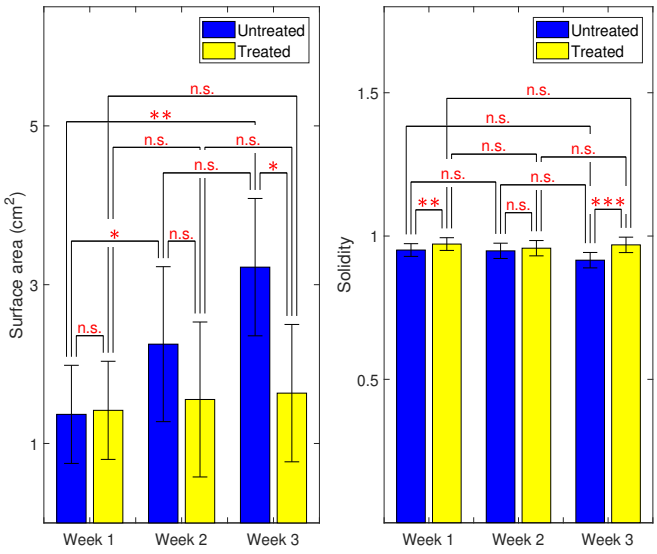

Figure 4.9: (A1) Mean surface areas of the tumors for the treated and untreated mice at week 1, week 2 and week 3. (A2) Mean values of solidity for all treated and untreated mice at week 1, week 2 and week 3. n.s. means not statistically significant. One, two and three stars correspond to p-value less than $0.05, 0.01, 0.001$, respectively. The mean value of surface area of the tumors increases from week 1 to week 3 for untreated mice and remains almost constant for the treated ones. Mean value of solidity of the tumors is consistently higher for the treated tumors than the untreated ones.

PR of a tumor for a wide range of tumor/background YM contrast, in many complex boundary conditions and independently of the shape of the tumor. The proposed method is also robust to practical experimental conditions that may deviate from the ideal ones such as non-uniform loading and when the YM inside the tumor is heterogeneous. Thus, the proposed method has the potential to significantly improve the way the YM of tumors is currently imaged and quantified as well as to provide a new means to image and quantify the PR of tumors and normal tissues in vivo.

Based on our in vivo animal results, YM in the untreated tumors was found to be increasing with time, whereas the YM in the treated ones did not change significantly with time. In most of the cancers (both treated and untreated), we found out that the PR is higher in the tumor than in the soft tissue. The values of PR found in this study match well with those previously reported in the literature as estimated using invasive techniques [16, 115, 116, 187, 206]. The shape regularity

index (solidity) and surface area of the tumors were also used to further characterize the in vivo results.

It is a common assumption in many studies reported in the literature pertaining elastography to treat tumors and soft tissues as incompressible elastic solids [19, 171–176]. Our study shows that such assumption can lead to significant errors in the reconstructed YM values (Table 4.3 sample X4) even in the case of small YM tumor/background contrasts, and that this error increases as the YM tumor/background contrast increases. Thus, accurate estimation of the PR is not only important because of its potential to provide new clinical information but also to obtain accurate estimates of the YM distribution.

There are several factors that can affect the accuracy of the reconstructed YM and PR values using the proposed approach. The first one is the quality of the axial strain and lateral strain estimates. The proposed method is able to reconstruct YM and PR with an error of below 5% for a tumor/background YM contrast of $0.1 - 100$, when the estimations of the axial and lateral strains are error- and noise-free such as those directly obtained from FE simulations. However, it is known that lateral strain estimation in elastography is typically noisier than axial strain estimation [120]. We have recently proposed a new method capable of providing high quality lateral strain estimations [146]. This method has been used in the study reported in this paper. Another important factor affecting reconstruction is the YM contrast between the tumor and the background. The axial strain ratio and lateral strain ratio between the tumor and normal tissue saturate for very small or large contrast of YM between the tumor and normal tissue (discussed in [198]), which is a fundamental limitation also referred to as "contrast transfer efficiency" in elastographic problems dealing with non-uniform materials [176, 195]. Because of this fundamental limitation, all elastographic reconstruction algorithms including the proposed one fail to accurately determine the YM and PR when the YM contrast is very small or large. In this paper, we demonstrate that our method can estimate the YM and PR with moderate accuracy (error around 15%) for YM tumor/background contrasts in the range of $0.1 - 50$, even in the presence of ultrasound noise (Fig. 4.4 (A)). We believe that this range should cover practical cancer imaging scenarios [104] and denotes a far

superior performance with respect to previously reported reconstruction methods.

When a compressor of finite size is used to excite a tissue, the applied stress is the highest near the top boundary and decreases with depth in the sample [192, 195]. This 'stress decay' leads to an overestimation of the reconstructed YM in the bottom part of the sample. This problem has been previously observed in elastography and has been referred to as 'target hardening effect' [2, 207]. Using our current experimental setup, we found this effect to be insignificant on the reconstructed results as proven in [198].

As the proposed method to estimate the YM and PR requires optimization of a cost function in every pixel inside the tumor, the computation time for the proposed technique is higher in comparison to previously reported 3DB and 3DS methods. The present configuration of the simultaneous reconstruction of YM and PR requires 1.7 s on average in an Intel Xeon 3.5 GHz PC with 32 GB RAM for each pixel inside the tumor and less than 1 s for all the pixels outside the tumor (with FE simulation axial and lateral strain data for the computational setup described in the Methods section), whereas the competing two methods require less than 1 s for the whole image.

4.5 Conclusion

In this paper, we have developed a three dimensional reconstruction method based on Eshelby's formulation for materials with inclusion. Our proposed method can accurately estimate and image both the PR and YM of tumors and surrounding tissue in vivo and is robust to changes of complex boundary conditions of the tumor environment and the shape of the tumor. Simulations and controlled ultrasound elastography experiments unequivocally demonstrate that the proposed method is capable of reconstructing these parameters accurately in many experimental scenarios of clinical relevance. Based on the potential role of YM and PR as markers for cancer diagnosis, prognosis and treatment efficacy, the proposed method can have a significant impact in the assessment of cancers and, in general, in the field of elasticity cancer imaging.

5. FINITE ELEMENT MODEL OF TUMOR [1]

5.1 Background

Elevated interstitial fluid pressure (IFP) inside cancers has been identified as one of the major barriers to cancer treatments [30, 31]. In chemo- and immunotherapy, interstitial fluid flow from the center to the periphery of the tumor induced by the IFP prevents the drug molecules to reach the central portion of the tumor and thus affects the efficacy of drug delivery [32, 33, 50]. Interstitial hypertension caused by the IFP can cause failure to radiation therapy [34, 35]. Interstitial fluid flow due to the IFP may also promote metastasis by applying shear stress to cancerous cells and forcing them to move toward the lymphatic system adjacent to the solid tumor [50, 208]. It has been shown that many cancers exhibit elevated values of IFP in comparison to normal tissue, where the measured IFP is in the range of $-0.5 - 3$ mmHg. These include: breast carcinoma (6-24 mmHg) [209, 210], metastatic melanoma (19-47 mmHg) [209, 211], head and neck carcinoma (4-33 mmHg) [212], cervical carcinoma (3-48 mmHg) [213] and colorectal carcinoma (9-33 mmHg) [209]. It is also known, from previous studies, that the IFP in cancers is spatially uniform throughout the tumor but drops steeply at its periphery [214, 215]. The actual mechanisms causing the IFP in cancers are not completely clear but it has been hypothesized that blood-vessel leakiness, lymph-vessel abnormalities, interstitial fibrosis and a contraction of the interstitial space mediated by stromal fibroblasts may be the primary factors affecting this parameter [31]. Despite the clinical relevance of the IFP, methods to assess this parameter non-invasively and in vivo are still lacking.

Analytical and numerical models of tumors provide a tool to better understand the way cancers develop and their response to drugs and treatments [83, 216–219]. Analytical models have some advantages with respect to numerical models as they allow to assess and extract individual material properties. Typically, it is not possible to extract individual material properties of poroelastic materials using FE methods alone because it requires minimizing multiple equations along with

[1] Islam, M.T., Reddy, J.N. and Righetti, R., 2018. A model-based approach to investigate the effect of elevated interstitial fluid pressure on strain elastography. Physics in Medicine & Biology, 63(21), p.215011, ©Institute of Physics and Engineering in Medicine. Reproduced with permission. All rights reserved.

satisfying the boundary and initial conditions. These issues often result in non-convergence of the numerical algorithms and erroneous local minima estimates [220]. In many cases, however, developing analytical models of tumors is not possible because of the complexity of the geometry and physics of the problem and the testing conditions. In such cases, numerical modeling may be the only option to obtain insights into the behavior of these tissues.

The first works on numerical modeling of cancers can be found in [21–23]. In these studies, the authors used a single dimensional poroelastic model to describe the stress, strains and fluid pressure inside the tumor. Three dimensional numerical modeling of cancers can be found in [221, 222], where the authors considered the effect of IFP and blood and lymphatic drainage on the drug delivery to the tumors. Zhao [223] studied the impact of inhomogeneous material properties of the tumor on fluid transport and drug delivery inside the tumor. Several other models have been proposed to study fluid transport mechanisms in the interstitial space of the tumor [21, 86, 224–226]. The importance of tumor shape, size and tissue transport properties on drug delivery has been studied in [227–230]. The spatial dependence of the IFP has been studied extensively using numerical models in [21, 21–23, 224]. While strains and displacements occurring inside a cancer due to the IFP have been analyzed in works retrievable in the literature, no analysis has been reported yet for the case of an externally applied load, which is typically the case for elastography techniques.

A few works on analytical and FE modeling of tumor/soft tissues for application in elastography have been reported [13, 101]. In [13], the authors incorporated both interstitial and vascular permeabilities in the model to show their effect on the poroelastic behavior of a tumor. However, IFP inside the tumor was not considered in this work. In our previous works related to analytical modeling of tumors [15, 93, 101, 109], we developed expressions for the displacements, strains and fluid pressure inside and outside a cylindrical tumor under different testing conditions, but did not incorporate the IFP in these models. In a preliminary FE model study from our group, the effect of the IFP on the axial normal and axial shear strains in a tumor has been qualitatively evaluated [231]. However, this study was limited to considering the elastographic parameters at

$t = 0^+$ s (i.e., immediately after the application of compression) only, while the temporal behavior of the strains and steady state response of the tissue due to the IFP were not investigated. The effect of vascular permeability of the tumor and normal tissue on their strain response was also not included in this study.

In this section, we design and implement a FE model, which incorporates relevant mechanical properties of the cancer, including Young's modulus, Poisson's ratio, interstitial permeability, vascular permeability and the IFP under the testing conditions typical for ultrasound elastography experiments. The model is developed using ABAQUS. The sample consists of a spherical inclusion, which represents the tumor, embedded in a background with different mechanical properties, representing normal tissue. The model is then used to assess the effect of IFP on various elastographic parameters and images.

5.2 Geometry of the model

A schematic of the poroelastic sample containing a spherical inclusion used in the study reported in this section is shown in Fig. 5.1 (A). The sample is assumed to be of cylindrical shape, whereas the inclusion inside the sample is of spherical shape of radius a. Because of the cylindrical and spherical symmetry of the sample and the inclusion, a 2D axisymmetric solution plane for this problem can be assumed as shown in Fig. 5.1 (B). The sample is compressed from the top, and the bottom side is fixed. Two frictionless compressor plates are used for holding up the sample and exert compression upon it.

The boundary conditions for a poroelastic sample in an elastography experiment are: 1) on the bottom plane of the sample, there is no axial displacement, i.e., the axial normal component of the displacement vector is zero; 2) on the right edge of the sample, there is zero fluid pressure [96] and 3) a constant uniaxial stress is present at the top boundary of the sample, i.e., only the axial normal component of the stress vector is non-zero and equal to the applied uniaxial stress. Other components of the stress vector are zero at the top boundary of the sample. Perfect bonding as well as continuous stress, fluid pressure and displacement between cancer and normal tissue should also be considered [23, 50]. Currently, no analytical solution is available for strains/fluid pressure

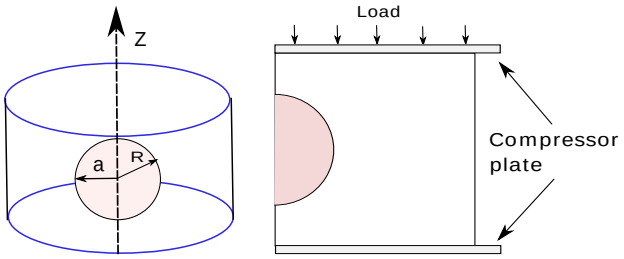

Figure 5.1: (A) A cylindrical sample of a poroelastic material with a spherical inclusion of radius a. (B) The 2D solution plane for the three dimensional sample.

inside a spherical poroelastic inclusion due to the complexity of the boundary conditions and the incorporation of the IFP inside the inclusion [101]. Therefore, finite element simulations remain the only option to examine the impact of the IFP on the displacements and strains in the inclusion (tumor) and background (normal tissue).

Table 5.1: Mechanical parameters of samples A-F. Here, E, ν and k denote the Young's modulus, Poisson's ratio and interstitial permeability and $\chi = \frac{L_p S}{V}$. L_p is the vascular permeability and $\frac{S}{V}$ is the surface area to volume ratio of the capillary walls. P_e is the IFP and α depends on the ratio of interstitial and vascular permeability and the radius of the tumor. The parameters corresponding to the background region are denoted with subscript b and the parameters without subscript correspond to the inclusion region.

Sample	E_b (kPa)	E (kPa)	ν_b	ν	k_b ($m^4N^{-1}s^{-1}$)	k ($m^4N^{-1}s^{-1}$)	χ_b (Pa s)$^{-1}$	χ (Pa s)$^{-1}$	$P_{e,b}$ $(mmHg)$	P_e $(mmHg)$	α
A	32.78	54.99	0.49	0.3	6.4×10^{-15}	3.1×10^{-14}	5.4×10^{-8}	2.79×10^{-6}	0	0	711
B	32.78	54.99	0.49	0.3	6.4×10^{-15}	3.1×10^{-14}	5.4×10^{-8}	2.79×10^{-6}	0	5	711
C	32.78	54.99	0.49	0.3	6.4×10^{-15}	3.1×10^{-14}	5.4×10^{-8}	2.79×10^{-6}	0	10	711
D	32.78	54.99	0.49	0.3	6.2×10^{-8}	6.27×10^{-11}	5.4×10^{-8}	2.79×10^{-6}	0	5	5
E	32.78	54.99	0.49	0.3	1.56×10^{-7}	1.56×10^{-10}	5.4×10^{-9}	2.79×10^{-7}	0	5	1
F	32.78	54.99	0.49	0.3	1.56×10^{-7}	1.56×10^{-10}	5.4×10^{-9}	2.79×10^{-8}	0	5	0.1

5.3 Finite element simulations

A commercial finite element simulation software namely ABAQUS, Abaqus Inc, Providence, RI, USA is used for our problem [232]. For our analysis, we have used the 'coupled pore fluid diffusion and stress analysis' module of ABAQUS. Details of this simulation module along with

necessary equations can be found in the documentation provided by ABAQUS [232, 6.7.1]. In brief, a poroelastic material saturated with a fluid is modeled in ABAQUS as a biphasic material (consisting of a solid phase and a fluid phase) and an effective stress principle is adopted to describe its behavior. The material is modeled by attaching the finite element mesh to the solid phase, and fluid can flow through the mesh. The mechanical part of the model is based on the effective stress principle, which can be described as, "the total stress acting at a point, $\boldsymbol{\sigma}$, is assumed to be made up of an average pressure stress in the wetting fluid, p, called the 'wetting fluid pressure' and an 'elastic stress' $\boldsymbol{\sigma}_e$ on the solid matrix". The effective stress principle can be expressed mathematically as [232, 2.8.1]

$$\boldsymbol{\sigma}_e = \boldsymbol{\sigma} + p\boldsymbol{I}. \tag{5.1}$$

The model also uses a continuity equation for the mass of wetting fluid in a unit volume of the poroelastic material,

$$\int_V \left[\delta p\big((\rho_w n_w)_{t+\Delta t} - \frac{1}{J_{t+\Delta t}}\big(J\rho_w n_w\big)_t\right] dV + \Delta t \int_V \delta p \left[\frac{d}{d\boldsymbol{x}} \cdot (\rho_w n_w \boldsymbol{v}_w)\right]_{t+\Delta t} dV = 0, \tag{5.2}$$

where ρ_w is the density of the fluid, $n_w = \frac{dV_w}{dV}$, V_w is the volume of the wetting fluid, $\boldsymbol{v}_w$ is the average velocity of the wetting liquid relative to the solid phase and J is the ratio of the material's volume in the current configuration to its volume in the reference configuration $J = \frac{dV}{dV^0} \sim 1 + div(\mathbf{u})$, where $\mathbf{u}$ is the solid phase displacement vector [232, 2.8.1]. The constitutive behavior for the pore fluid flow in the above-mentioned biphasic model is governed by Darcy's law stated as [232, 6.7.1]

$$n_w \boldsymbol{v}_w = -\frac{k}{\gamma_f}\nabla p, \tag{5.3}$$

where k and γ_f are the interstitial permeability of the solid phase and volumetric weight of pore fluid, respectively.

Six samples (described in Table 5.1) with different material properties and IFP are simulated to examine the response of the tumor in elastography experimental conditions. Both the inclusion and background of the samples are modeled as linearly elastic, isotropic, permeable solid phases fully saturated with a fluid.

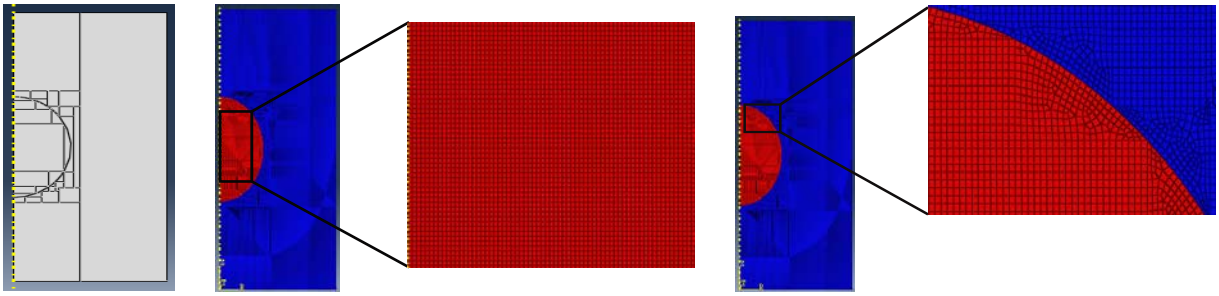

(A) (B) (C)

Figure 5.2: (A) Proposed model with rectangular partitions created inside the inclusion and background. Mesh structure in ABAQUS (B) inside inclusion (C) at the interface between inclusion and background.

The sample is compressed from the top with a load of 4500 Pa. Given the properties of the samples, this compression creates an approximate mean axial strain of $\approx 10\%$ in the inclusion region. Although this value of strain is high comparing to the strain values normally used in elastography experiments ($2-6$%), this value is within the range of strain values typical for a ultrasound poroelastography experiment [13,154,233]. In poroelastography experiments, the strain between two successive frames can be very low ($< 0.1\%$) even the applied load/strain is high ($> 10\%$). As in the poroelastography experiments, the strain value at any time point can be estimated as the cumulative sum of strain values between successive frames upto that time point, large value of applied strain can be used in poroelastography experiments without compromising the quality of strain images [146]. The permeability of the sample is assumed to be independent of the strain and void ratio. Following [96], a 2D plane of the 3D cylinder is modeled in ABAQUS. The solution plane of the sample is 2 cm in radius and 4 cm in height. The radius of the spherical inclusion is 0.75 cm. The quadrilateral pore pressure mesh element CAX4RP is used to model the sample with

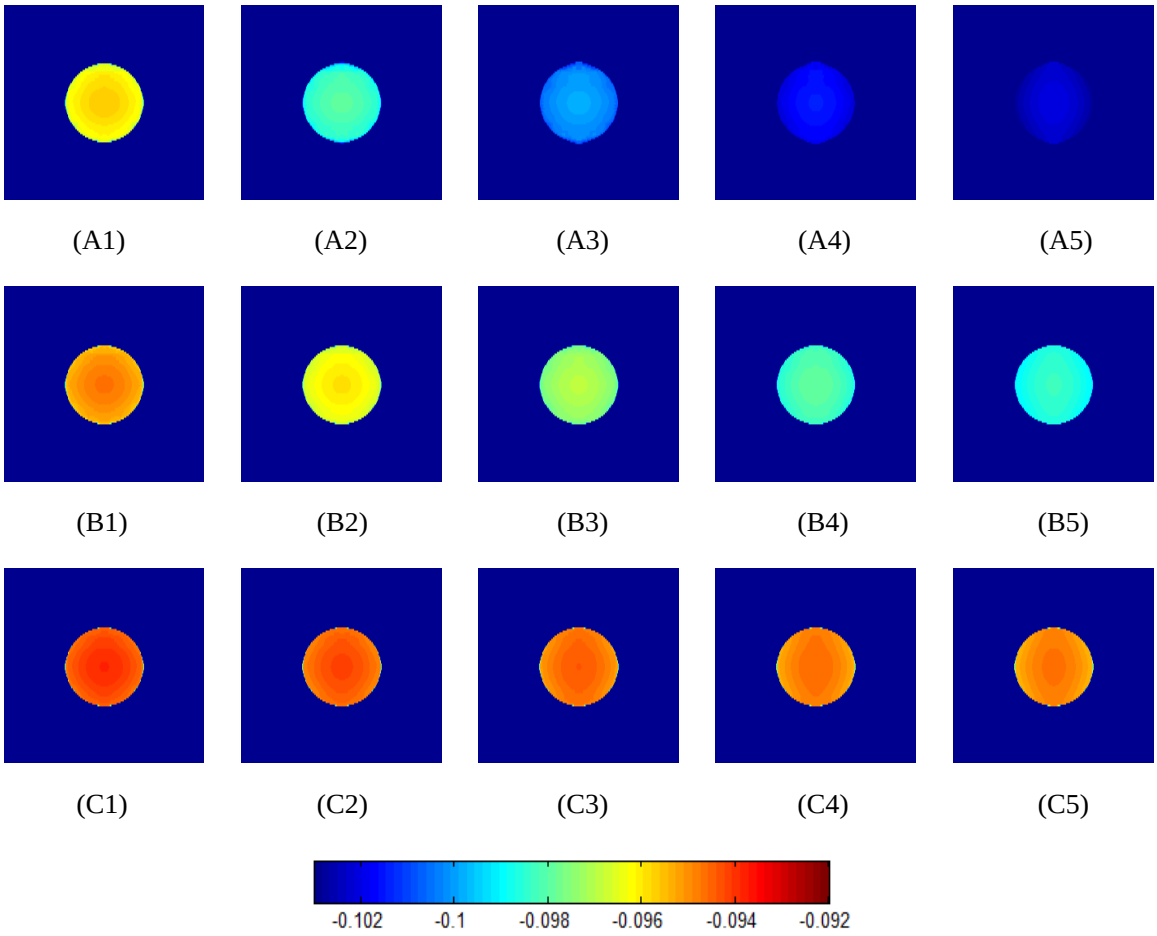

Figure 5.3: Axial strains at time points of 1.8 s, 4.8 s, 9 s, 18 s and 57.6 s for samples A, B and C are shown in (A1-A5), (B1-B5) and (C1-C5), respectively.

$81,799$ elements in the solution plane. We have used quadrilateral elements CAX4RP to model our sample since high order approximations such as the quadratic approximation lead to smaller errors in the solution of finite element problems in comparison to the linear approximation. A zero fluid pressure boundary condition is imposed on the right hand side of the sample following [96]. A perfect bonding condition between the inclusion and background has been assumed in all samples. Perfect bonding conditions between cancers and normal tissue have been assumed in most of the studies regarding poroelastic/elastic modeling of cancers retrievable in the literature and match well with experimental observations [16, 21, 22].

The model used in ABAQUS is shown in Fig. 5.2 (A). The particularity of the model is the

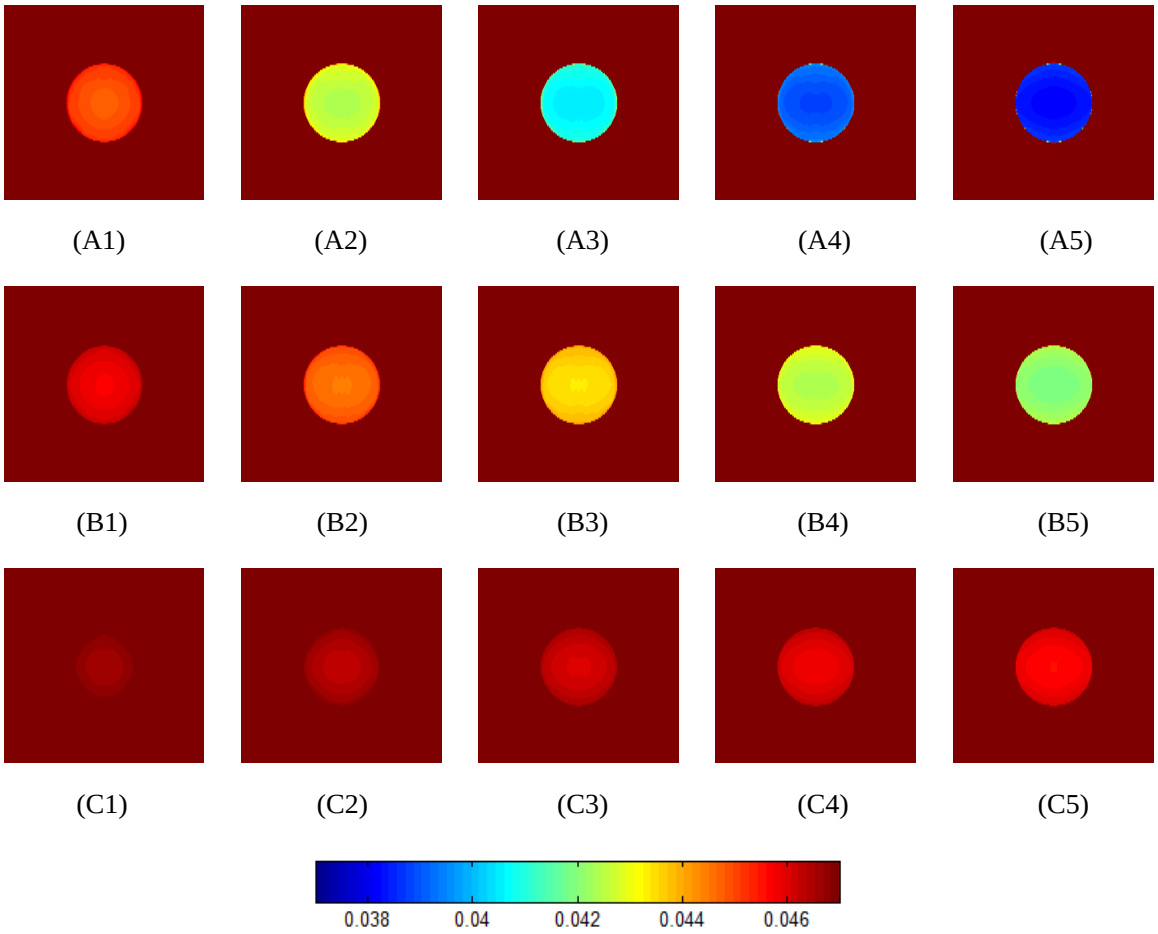

Figure 5.4: Radial strains at time points of 1.8 s, 4.8 s, 9 s, 18 s and 57.6 s for samples A, B and C are shown in (A1-A5), (B1-B5) and (C1-C5), respectively.

use of rectangular partition inside and outside the tumor. Such partition is necessary since square mesh elements (quadrilateral mesh elements with aspect ratio of 1) of same size inside the tumor (inclusion) and normal tissue (background) are required due to the following reason. The vascular permeability in the inclusion and background is modeled through the seepage coefficient. As the seepage coefficient is defined for each mesh element in ABAQUS, the length of each square mesh element must be same to achieve the same vascular permeability in the whole inclusion or whole background. Generally, in ABAQUS, the size of the mesh element is determined based on the geometry of the region. Without imposing any rectangular partition in the model, typically, in a rectangular region with partition of a spherical inclusion, the aspect ratio of the quadrilateral

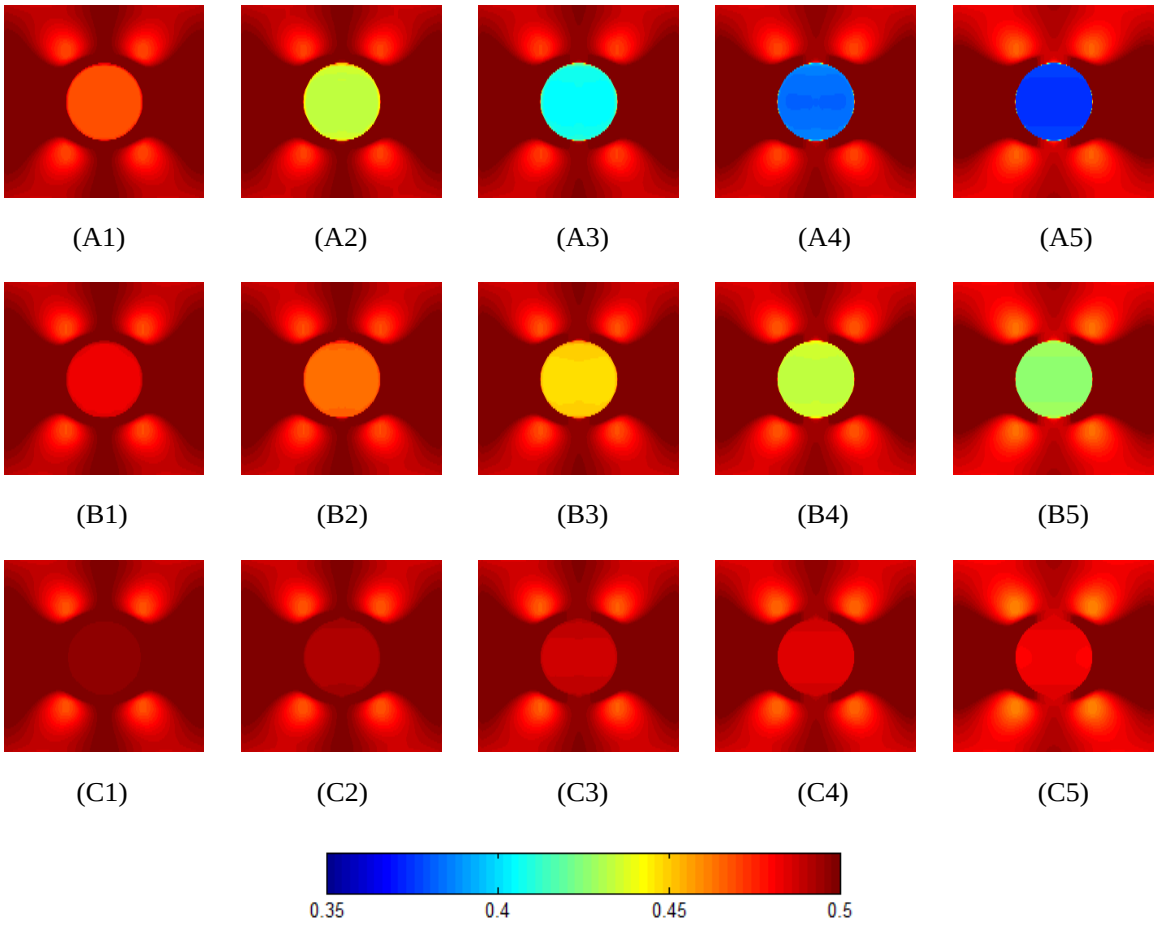

Figure 5.5: EPRs at time points of 1.8 s, 4.8 s, 9 s, 18 s and 57.6 s for samples A, B and C are shown in (A1-A5), (B1-B5) and (C1-C5), respectively.

mesh element is not kept to 1 and the lengths/widths of these mesh elements become highest at the center of the inclusion and reduce towards the periphery of the inclusion. Similarly, in the background region, the mesh elements are smaller closer to the inclusion while they increase in size away from the inclusion. This creates a non uniform mesh inside and outside the inclusion. However, with the imposition of rectangular partition, the partitioned rectangles are considered independent by ABAQUS, i.e., ABAQUS does not consider the outer geometry while meshing the rectangle. As rectangles are regular geometry (geometry without curve and discontinuity), ABAQUS can assign square mesh elements of the same length (length prescribed by the user) to all the rectangles. The mesh inside the inclusion of the FE model is shown in Fig. 5.2 (B), where the

uniform rectangular shaped mesh elements inside the spherical inclusion can be clearly seen. To ensure the uniformity of mesh size in the inclusion and background region, we measured the mesh element size at different points by measuring the distance between border pixels along vertical and horizontal directions in a mesh element in MATLAB, Mathworks Inc., Natick, MA, USA after importing the meshed model as an image from ABAQUS. We also show the mesh structure close to the interface between the inclusion and background in Fig. 5.2 (C), where a number of non-uniform mesh elements can be seen.

We have used reduced integration to calculate the element stiffness matrix in our FE analysis. Reduced integration is more appropriate when second-order elements are used, as it gives more accurate results and is less computationally expensive than full integration [232, 9.1.3]. We have used implicit integration techniques as our problem is dynamic in nature, and implicit integration techniques are reported to be more accurate than explicit techniques in solving dynamic problems [232, 2.4.1].

The spatial mesh resolution in the finite element model has been determined based on a mesh convergence study. As a part of the mesh convergence study, a mesh refinement analysis was performed and the resulting strain/fluid pressure response of the samples analyzed with increment of the mesh density. We found that changes in the output strains and fluid pressure are insignificant if the mesh density is increased (even up to 20 times) from the value used to generate the results reported in this paper. The temporal time step of the analyses was determined in such a way that important events can be clearly observable.

The poroelastic response was recorded for 60 s with a 0.6 s time step for samples A, B and C. For sample D, the total time of analysis was 30 s at 0.3 s step and for sample E, the total analysis time was 10 s at 0.1 s step. The total analysis was done in two steps. In the first step, an instantaneous load of 4500 Pa was applied which is constant in the next step. The duration of the first step was of 0.01 s, while the second step lasted up to 60.01 s, 30.01 s or 10.01 s depending on the sample. The specific weight of the fluid was taken as 1Nm^{-3} to match the definitions of permeability in ABAQUS and in the poroelastic theory [101]. The void ratio in all the samples

used was set to 0.4.

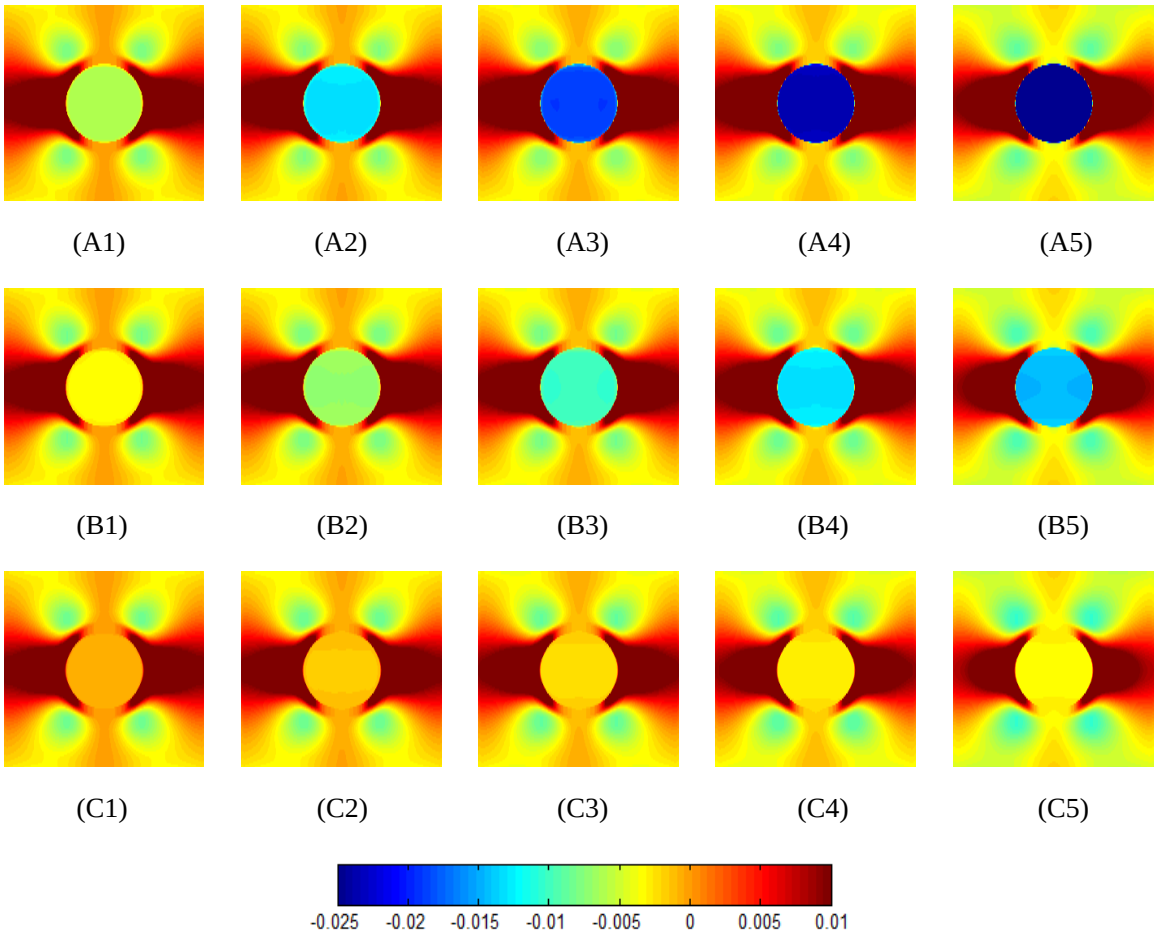

Figure 5.6: Volumetric strains at time points of 1.8 s, 4.8 s, 9 s, 18 s and 57.6 s for samples A, B and C are shown in (A1-A5), (B1-B5) and (C1-C5), respectively.

In a poroelastic sample, the fluid pressure generated by the applied compression becomes zero after a certain time interval. After that time, the poroelastic sample behaves as a perfectly linear elastic material [15]. However, the IFP exists inside the tumor independently of the experimental protocol or applied compression. The IFP does not change during or because of the experimental procedure. Moreover, as IFP is an isotropic stress [20] and works in the opposite direction to the solid stresses, we applied an isotropic stress equal to $-p_0$ to model the IFP. The isotropic

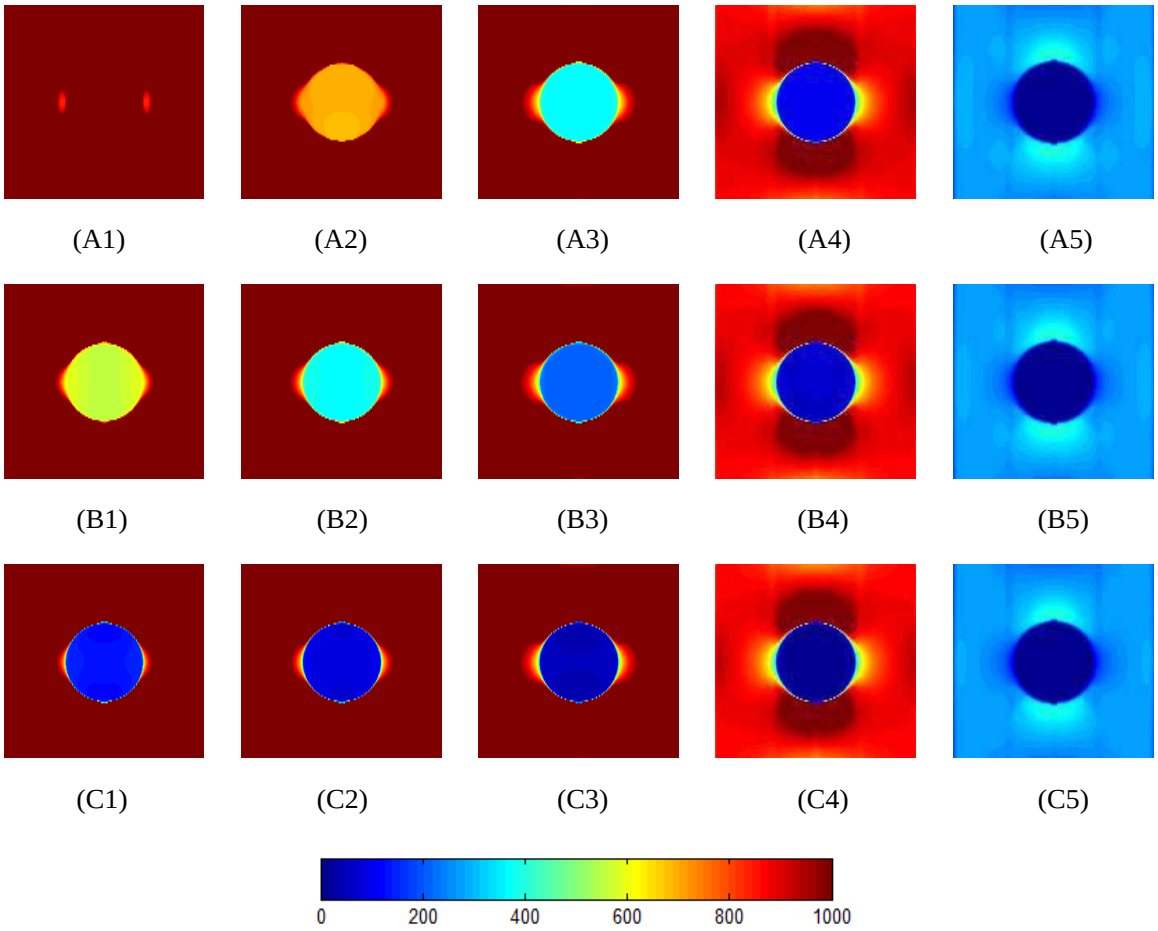

Figure 5.7: Fluid pressure (Pa) at time points of 1.8 s, 4.8 s, 9 s, 18 s and 57.6 s for samples A, B and C are shown in (A1-A5), (B1-B5) and (C1-C5), respectively.

stress is created in ABAQUS by a predefined initial stress field (available in CAE), which has six components. Following the definition of isotropic stress, the values of the first three components (axial, radial and tangential) are set to $-p_0$ and the other components are set to zero to create an isotropic stress of $-p_0$. The IFP is assumed to be uniform over the tumor radius ($p_0(R) = P_e$) and falls abruptly to zero at the boundary [36, 214].

When an initial stress is given as input in ABAQUS, the initial stress state may not be an exact equilibrium state for the finite element model. Therefore, an initial step should be included to allow ABAQUS to check for equilibrium and iterate, if necessary, to achieve equilibrium [232, 27.2.1]. We have included a small step of 0.01 s for this purpose in our simulations. After this

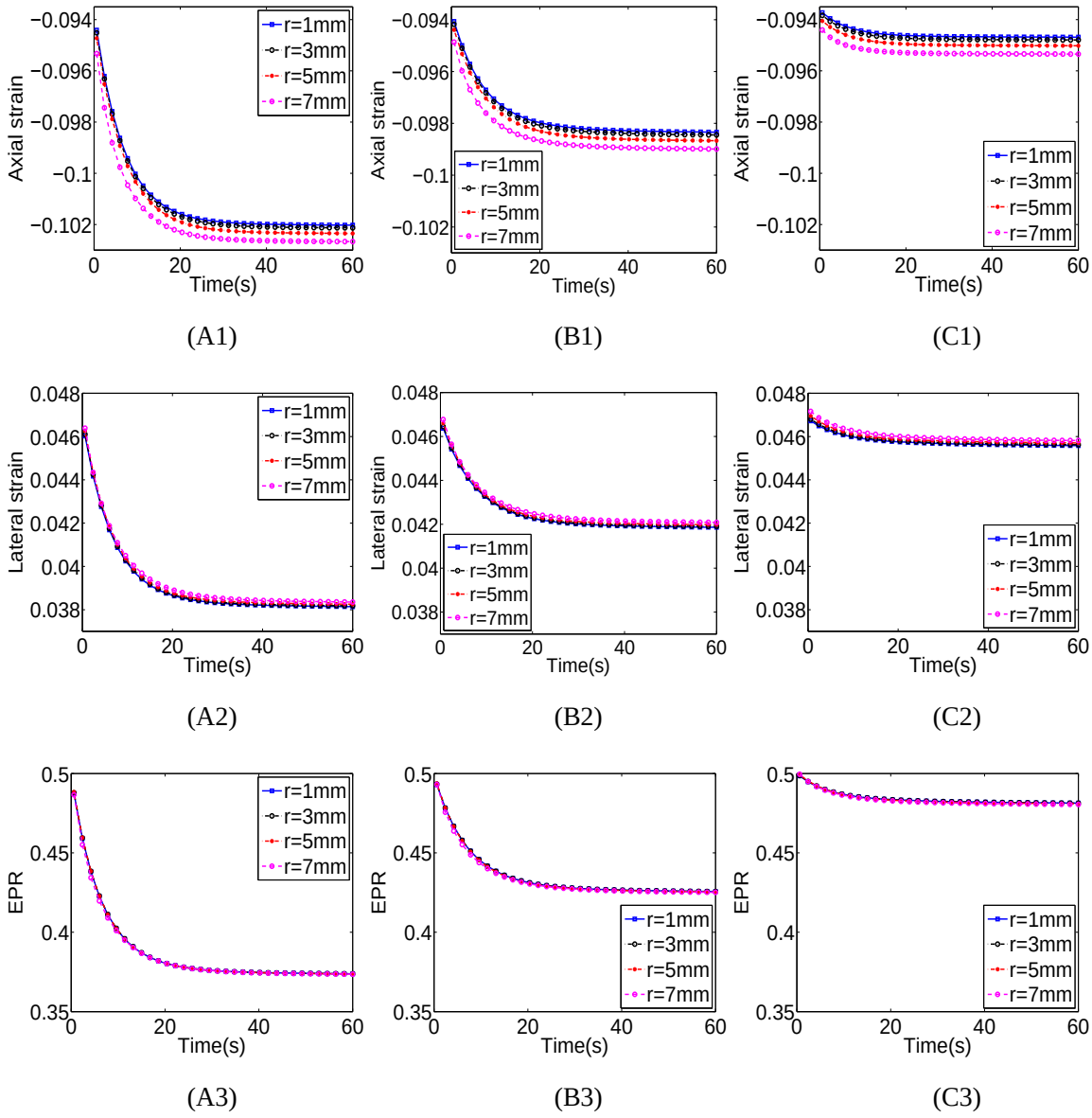

Figure 5.8: Time profiles of the axial strain at different radii inside the tumor of samples A, B and C are shown in (A1), (B1) and (C1). Time profiles of the radial strain at different radii inside the tumor of samples A, B and C are illustrated in (A2), (B2) and (C2). Time profiles of the EPR at different radii inside the tumor of samples A, B and C are shown in (A3-C3).

first step, the solution of stress and fluid pressure in equilibrium is achieved based on the applied compression and initial stress given as input. The solution of the stress, fluid pressure and strain for successive time depends on the computed stress and fluid pressure after the first step. The total

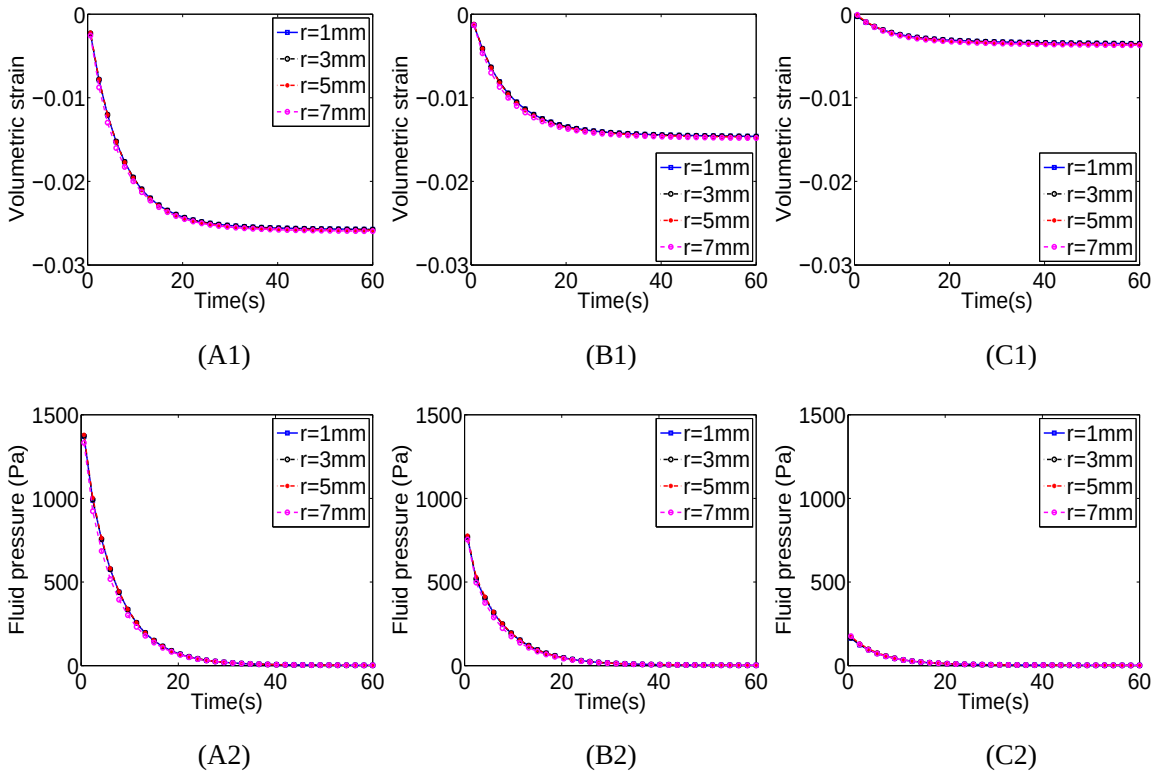

Figure 5.9: Time profiles of the volumetric strain at different radii inside the tumor of samples A, B and C are shown in (A1), (B1) and (C1). Time profiles of the fluid pressure at different radii inside the tumor of samples A, B and C are illustrated in (A2), (B2) and (C2).

axial, radial and tangential components of stress (computed as sum of elastic stress component and fluid pressure [15]) inside the tumor after first step become the total stress components created by the applied stress from the top of the sample minus the negative IFP (assuming the applied stress is negative). The fluid pressure inside the tumor after first step becomes the fluid pressure created by the applied stress minus the IFP. As 1) the initial isotropic stress given as input impacts the solution of the first step only, 2) ABAQUS finds an equilibrium solution at the end of the first step and 3) the solution for rest of the experimental duration depends on the first step, continuity of fluid pressure and stress at the interface of inclusion and background is satisfied at all time points after first step.

The material properties of cancers and normal tissues are reported in the literature to have broad

ranges. Young's modulus of the normal tissue in all samples is chosen as 32.78 kPa, based on previous literature [13, 40]. As in the literature, the cancers are reported to have Young's modulus of $1.1 - 20$ times the Young's modulus of normal tissue, the tumors in the samples are assumed to have a Young's modulus equal to 54.99 kPa (1.67 times the Young's modulus of normal tissue) [113, 114]. The Poisson's ratio is reported in the literature to have a range of values between $0.2 - 0.49$ for both tumors and normal tissues [13,16,115,116]. We assume the normal tissue to be almost incompressible with Poisson's ratio of 0.49 and the tumor to be compressible with Poisson's ratio of 0.3 based on [16,116,191]. It should be noted that the main goal of our study is to investigate the effect of the IFP and the spatial parameter of IFP α on the mechanical response of the cancer [59]. α can be expressed as $\alpha = a\sqrt{\frac{L_p}{k}\frac{S}{V}}$, where L_p is the vascular permeability and $\frac{S}{V}$ is the surface area to volume ratio of capillary walls. Therefore, the values of Young's modulus and Poisson's ratio in the tumor (inclusion) and normal tissue (background) were kept fixed in all samples. Only the values of IFP and α, which depends on the interstitial permeability and vascular permeability, were varied in this study to assess their effect on the strain parameters. Interstitial and vascular permeability of the normal tissue were chosen following [13, 59]. In many tumors, vascular permeability is reported to be dominant over interstitial permeability [59]. However, interstitial permeability can be dominant with respect to the vascular permeability in tumors at initial stages of cancer formation and after drug administration [50, 81]. Based on these observations, in our study, we varied both the vascular permeability and the interstitial permeability and considered both cases when vascular permeability is dominant over interstitial permeability and opposite cases and created different values of α [40]. Two values of IFP (5 and 10 mmHg in samples B and C (see Table 5.1))) were chosen following [16]. Four different values of α, namely 711, 5, 1 and 0.1 in samples A-C, D, E and F (see Table 5.1), respectively, were chosen. The surface area to volume ratio $\frac{S}{V}$ in calculation of α was set at 200 cm^{-1} [40, 58].

We analyze and report the effective Poisson's ratio (EPR), i.e., radial to axial strain ratio in all samples [8, 10, 146]. At steady state, when the poroelastic material behaves as a perfectly linear elastic material, the EPR becomes the Poisson's ratio if the poroelastic material is uniform. If the

poroelastic material is not uniform, the steady state EPR value is related to the actual Poisson's ratio in a more complex manner [110]. We also report the volumetric strain in the results section of this study. In the axisymmetric model, the tangential component of the strain may be assumed to be equal to the radial component. Thus, the volumetric strain is computed as the sum of the axial strain and two times the radial strain.

5.4 Results

Although we analyzed the 2D axisymmetric solution plane (one half plane from the center line) of the sample in ABAQUS, we will display a full 2D plane of the 3D cylindrical sample to visualize the results applying the angular symmetry of the sample with respect to the center line. According to the angular symmetry condition, the right half of any 2D plane along the center of the sample is same as its left half. In this way, the displayed results are similar to practical elastography images, where a linear transducer is used to image a 2D plane.

The axial strain elastograms corresponding to different time points for sample A, B and C are shown in Fig. 5.3. From this figure, we see that the magnitude the axial strain at different time points inside the tumor reduces as IFP increases in sample A, B and C, and, consequently, the axial strain contrast between tumor and normal tissue increases as IFP increases. For sample A, in which IFP=0 inside the tumor, we see that, at steady state, the difference between the axial strain in the tumor and the axial strain in the normal tissue is very small. However, at the same time point, in sample B and sample C, which have IFP inside the tumor equal to 5 and 10 mmHg, respectively, the differences between axial strains of the tumor and normal tissues are much larger. This observation confirms that IFP can affect the axial strain intensity and distribution inside the tumor.

Radial strain elastograms at time points of 1.8 s, 4.8 s, 9 s, 18 s and 57.6 s are shown for samples A, B and C in Fig. 5.4. Unlike the axial strain case, the radial strain contrast between tumor and normal tissue decreases as the IFP inside the tumor increases. In Fig. 5.5, we see that, as the IFP increases, the EPR inside the tumor at steady state increases and becomes close to 0.5. In general, immediately after compression, a poroelastic material behaves as an incompressible

material with EPR close to 0.5. As time progresses, EPR decreases to reach the steady state value, which, for a poroelastic material, is by definition lower than 0.5. However, our results show that, in the presence of high IFP (sample C), the tumor behaves as an incompressible material even at steady state manifesting a EPR close to 0.5 at all time points.

Volumetric strain elastograms at different time points for samples A, B and C are shown in Fig. 5.6. In sample A, we see that, since IFP is zero, the volumetric strain contrast between tumor and normal tissue is large at steady state. The volumetric strain contrast at steady state decreases in samples B and C. This effect is a direct consequence of the fact that the tumor tends to behave more as an incompressible material when its IFP is high. Note that the volumetric strain contrast is small at $t = 0^+$ in all samples, since immediately after compression both the tumor and normal tissue behave as incompressible materials.

Fluid pressure maps at different time points for the samples A, B and C are shown in Fig. 5.7. As the IFP increases, the fluid pressure inside the tumor reduces. In sample A, fluid pressure is higher than 1000 Pa at $t = 0^+$, whereas in sample C, which is the sample with highest IFP in the tumor (10 mmHg), the fluid pressure is almost zero at $t = 0^+$. In all the samples, the fluid pressure becomes zero at infinity.

The temporal profiles of the axial strains in samples A, B and C for different radii of the tumor are shown in Fig. 5.8 (A1-C1). From this figure, we see that the axial strain of sample A starts with a value of 9.4% and saturates around 20 s at value of 10.2% (Fig. 5.8 (A1)). For sample B, the axial strain starts at 9.4% and goes to 9.8% at steady state (Fig. 5.8 (B1)). For sample C, the axial strain does not change with time significantly (Fig. 5.8 (C1)). Note the decrease in value of the axial strain at steady state as IFP increases.

Time profiles of the radial strains at different radial positions for samples A, B and C are shown in Fig. 5.8 (A2)-(C2). Note the increase in value of the radial strain at steady state as IFP increases.

The time profiles of EPR for different samples are shown in Fig. 5.8 (A3-C3). The EPR starts at 0.5 for all samples and reaches 0.38 in sample A, 0.43 in sample B and 0.49 in sample C, which shows increased EPR at steady state for increased values of IFP.

The temporal behavior of the volumetric strains inside the tumor for samples A-C are shown in Fig. 5.9 (A1-C1). Decreasing values of volumetric strain with higher values of IFP are seen at different radii inside the tumor. If we quantify the change in volumetric strains due to IFP ($p_0(R) = P_e$), we find out that the volumetric strain decreases by an amount of 1.3% and 2.5% in samples B and C, which are close to $\frac{P_e}{K}$, where K is the compression modulus of the tumor in samples B and C. For both these samples, K is equal to 45.825 kPa.

The time profiles of the fluid pressure at different radial positions inside the tumor for the samples A, B and C are shown in Fig. 5.9 (A2-C2). It can be seen from this figure that the instantaneous fluid pressure in sample A is 1500 Pa, whereas in sample B and sample C the instantaneous fluid pressures are 700 Pa and 100 Pa, respectively. The fluid pressure goes to zero at the steady state in all the samples.

The EPRs, volumetric strains and fluid pressures for samples D, E and F at five different time points are shown in Figs. 5.10 and 5.11. As samples D, E and F have the same IFP and mechanical properties except the interstitial and vascular permeabilities inside the tumor, the EPRs and volumetric strains at steady state are identical. However, at different time points, spatial distributions of the EPR, volumetric strain and fluid pressure inside the tumor are different. This is because of the different α values, which is related to the ratio of vascular permeability to interstitial permeability. In sample D, the effect of interstitial permeability and vascular permeability are comparable whereas, in sample E and F, the effect of interstitial permeability is dominant. The radial dependence of the EPRs, volumetric strains and fluid pressures in samples D, E and F is also in contrast with the lack of such spatial dependence in samples A, B and C, where all the mechanical fields are radially constant. With lower values of α, i.e., the dominance of vascular permeability over interstitial permeability reduces and the mechanical fields become more radially dependent (sample D-F). For the vascular permeability dominant cases (samples A-C), the fluid flows through the capillary walls independently of the geometry of the tumor or the normal tissue and the mechanical field does not show any radial dependence. For the cases where interstitial permeability is important (sample D-F), instead, the fluid needs to pass the interstitium and, depending on the boundary

conditions, different fluid pressure gradients are created at different radial positions resulting in radially dependent mechanical fields inside the tumor. This finding is in agreement with the results reported in [13].

The spatial dependence of the EPR, volumetric strain and fluid pressure for samples D-F can be clearly seen in the radial profiles of these field parameters at different time points, which are shown in Fig. 5.12. In Fig. 5.12 (A1)-(A4), (B1)-(B4) and (C1)-(C4), we see that, at all time points, as the value of α increases, the fluid pressure, volumetric strain and EPR become more flat along the radial position inside the tumor. For $\alpha = 711$, the radial distributions of the EPR, volumetric strain and EPR become almost constant throughout the whole radius, whereas for $\alpha = 0.1$, these field parameters consistently reduce in magnitude as the radial position increases.

5.5 Discussion

In this section, we propose a new FE model for cancers surrounded by normal tissues in a typical elastography imaging experiment. While several FE models have been proposed in the past to study the mechanical behavior of cancers, to our knowledge, this is the first FE model applicable to poroelastography that takes into consideration the contribution of the IFP in the cancer. In addition, the proposed model includes both the interstitial permeability and the vascular permeability of the tumor, which is incorporated through the seepage coefficient in the established FE software ABAQUS. IFP is a parameter of great clinical relevance. While in normal tissues, the IFP remains close to the atmospheric pressure, the IFP in tumors is typically elevated. This elevated value of IFP has been found to be the major impediment to drug delivery therapies, a major cause of failure of radiation therapy and one of the causes of cancer metastasis. The parameter that defines the spatial distribution of the IFP is α, which depends on the ratio between the vascular permeability and the interstitial permeability, and that in itself may be a diagnostic or prognostic marker of malignancy and cancer progression [50, 224]. Therefore, the ability to measure IFP and α in cancers using a non-invasive imaging method as ultrasound elastography could have a large impact in cancer diagnosis, prognosis and treatment.

The proposed FE model is then used to assess the effect of the IFP inside the a tumor on the

axial, radial and volumetric strains and EPR created by external loading. Our results show: (1) in the presence of the increasing IFP, the magnitude of the steady state axial strain decreases and the magnitude of the steady state radial strain increases; (2) the volumetric strain inside the tumor reduces by the value of IFP divided by the compression modulus of the tumor; (3) as IFP increases, the volumetric strain of the tumor decreases and the EPR increases, i.e., the tumor behaves more as an incompressible material; and (4) as the ratio between the vascular permeability and interstitial permeability increases, the strains become less space-dependent and for very large values of this ratio, they become almost spatially invariant inside the tumor.

It is clear from these results that knowledge of the effects of IFP in the strain elastograms is of great importance for a correct interpretation of the results and for a correct reconstruction of the underlying mechanical properties of a tissue. For example, if IFP is not considered in the model, the reduction of steady state axial strain would result in the determination of an incorrect (higher) Young's modulus value, as it has also been observed by [234].

Interstitial permeability and vascular permeability are two important mechanical parameters, which have a significant impact on the mechanical microenvironment of a tumor [16]. As demonstrated by our results in the spherical tumor model, the dominance of the interstitial permeability over vascular permeability creates spatial dependent strains. This is contrasted with the case where vascular permeability dominates leading to spatially invariant strain fields. These observations may have important implications in cancer diagnosis and prognosis as the dominance of interstitial or vascular permeability determined from the spatial profile of the strains obtained from an elastography experiment may provide information to assess cancer stage and help in the identification of suitable treatments [50, 235].

Our results demonstrate that, as IFP increases, the effective volumetric stress (because of external stress) and volumetric strain inside the tumor decrease. When the effective volumetric stress is equal to the IFP inside the tumor, the volumetric strain becomes zero, the EPR becomes 0.5 and the axial and radial strain become constant with time. At this point, the tumor works as a perfectly incompressible material. If the IFP is higher than the effective volumetric stress, volumetric strain

remains zero, the EPR remains 0.5 and the axial and radial strains remains constant. Therefore, any value of IFP higher than the effective volumetric stress does not produce appreciable changes in the strains inside the tumor and may not be measurable using elastography. Thus, the upper limit of measurable IFP in an elastography experiment is given by the effective volumetric stress inside the tumor, which depends on the applied stress as well as the stiffness of the tumor and normal tissue. To translate this statement into numbers, we can consider the following hypothetical examples. Assuming a tumor with a Young's modulus contrast of 20 with respect to the normal tissue and assuming that the applied stress is $1 - 6$ kPa, the effective volumetric stress inside the tumor is around the range $0.67 - 4$ kPa. Thus, the highest measurable IFP would be in the range $5 - 30$ mmHg. If the Young's modulus contrast between tumor and normal tissue is lower, the effective volumetric stress decreases. Therefore, the highest measurable IFP would be lower. For example, for a Young's modulus contrast between tumor and normal tissue of 2, the measurable upper limit of the IFP would be 19.2 mmHg for an applied stress of 6 kPa. Therefore, the upper limit of the measurable IFP depends on the the applied stress and underlying mechanical properties of the tumor and normal tissue.

Based on the results from our finite element simulation study, the axial strain changes by 1%, when an IFP of 10 mmHg is simulated inside the tumor. The change in the axial strain would be higher for higher values of IFP. Such strain changes should be detectable by current elastographic strain estimation techniques, which have theoretically very high sensitivity and can easily detect strain changes as low as 0.05% [146].

The proposed model was derived under the assumption of a spherical model of the tumor, which is not always true in practical cases. However, we expect the observations regarding the effects of IFP and α on the strains and EPR to qualitatively hold also for tumors of shapes such as ellipse and cylinder. We also have assumed that the tumor and background tissue are poroelastic and isotropic, and they behave as linearly elastic solids at steady state. These two assumptions - spherical model and poroelastic isotropy - have been used in numerous studies reported in the literature [16, 21, 22, 40]. These models have also been found to provide results correlating well

with experimental observations. A limitation of our model is that we have not considered the lymphatic drainage inside the tumor. However, based on reported values in the literature, lymphatic permeability inside the tumor is very small and typically negligible in comparison to the value of vascular permeability [16]. In addition, in our proposed model, we have assumed that IFP and its spatial parameters α are independent of each other. In reality, with decrements of α, the peak value of the IFP reduces, but the spatial nature of the IFP does not change much [224]. Since our observations do not depend on the peak value of the IFP, this assumption does not change the major observations obtained from this study.

We divided the inclusion and background in rectangular regions having all the same mesh element length. However, as the inclusion has curved geometry, in small regions in proximity of the inclusion boundary, it was not possible to maintain a uniform mesh element length and, as such, uniform vascular permeability. However, such regions are very small compared to the size of the inclusion and can be neglected. Hourglass effect may arise if reduced integration elements are used in solving a finite element problem [236]. However, this effect was not present in our analysis as we used the mesh refinement. Our observation that the results were same with and without reduced integration elements also proved that.

We could not directly validate the finite element model because of the difficulty in fabricating controlled phantoms with elevated IFP and desired values of interstitial/vascular permeability. Since our work is very new and the IFP is a parameter that has been completely neglected in elastography so far despite its enormous clinical significance, there is very limited literature that can be used to corroborate our simulation results. In [234], a study of Young's modulus estimation by shear wave elastography in the presence of IFP has been performed, and it has been found that the measured Young's modulus increases in the presence of IFP. The increment of Young's modulus implies a reduction of the axial strain in elastography experiment, which would validate our observations of reduced axial strain in the presence of IFP. It should also been noted that, as our observations are based on finite element simulations incorporating practical experimental conditions and experimentally obtained mechanical properties of the samples, we can expect the observations

to hold in elastography experiments. However, experiments directly linking the IFP and strains would require an in vivo animal study and availability of invasive methods to assess IFP, which is beyond the scope of this paper and left for future work.

In all our simulated samples, we have assumed that the normal tissue and the tumor are poroelastic and isotropic and behave as linearly elastic solids at the steady state. If the tumor is linearly elastic but not isotropic, the incompressible behavior will be same as the one observed for the poroelastic case. Thus, our observation that tumors exhibit increased incompressibility if they have high IFP would still hold. However, in these anisotropic tumors the material properties (Young's modulus/Poisson's ratio) are different along different directions [237] leading to strain responses much more complicated than those reported in this study. On the other hand, if the material is not linearly elastic, the stress/strain behavior in the material would be different than that reported for the materials analyzed in this study, but we still expect the ratio between radial to axial strain (i.e., EPR) to increase as IFP increases (i.e., the tumor would become more incompressible as IFP increases).

Based on the work of Leiderman et al. [13] and some of our recent works [15, 93], if the vascular permeability is dominant over the interstitial permeability inside the tumor, then the time constant of the axial strain, radial strain and fluid pressure can be computed as $\frac{1}{H_A \chi}$, where H_A is the aggregate modulus and χ is the microfiltration coefficient (product of vascular permeability and $\frac{S}{V}$) of the tumor. However, when the interstitial permeability cannot be neglected with respect to the vascular permeability, the expression of the time constant of the strains and fluid pressure becomes much more complex. We have derived a formulation for cylindrical tumors [15, 93], but a formulation for spherical tumors is not currently available. Technically, the duration of data acquisition in a practical poroelastography experiment depends on the mechanical properties (aggregate modulus/vascular permeability) of the tumor/tissue. However, these parameters are often unknown in vivo and change from tissue to tissue. Thus, in most cases, preliminary experiments are required to have a rough estimate of the strain time constants in the tissue of interest and successive acquisitions can be based on these preliminary data or values previously reported in the literature (if

available). Based on previous studies [202] and recent experiments performed on mouse tumors in our lab [198], a data acquisition time interval of one minute is sufficient for in vivo tumorous tissues to reach steady state.

5.6 Conclusion

In this section, we have proposed a FE model for imaging of cancers using elastography, which incorporates the effect of IFP inside a tumor. Using this model, we have investigated the impact of the IFP and its spatial parameter α on the strain responses inside the tumor. The developed model and results reported in this paper may be helpful to understand the effect of IFP and related parameters in the elastographic images and may lead to new methods to assess this parameter with potentially important implications in cancer diagnosis, prognosis and treatment.

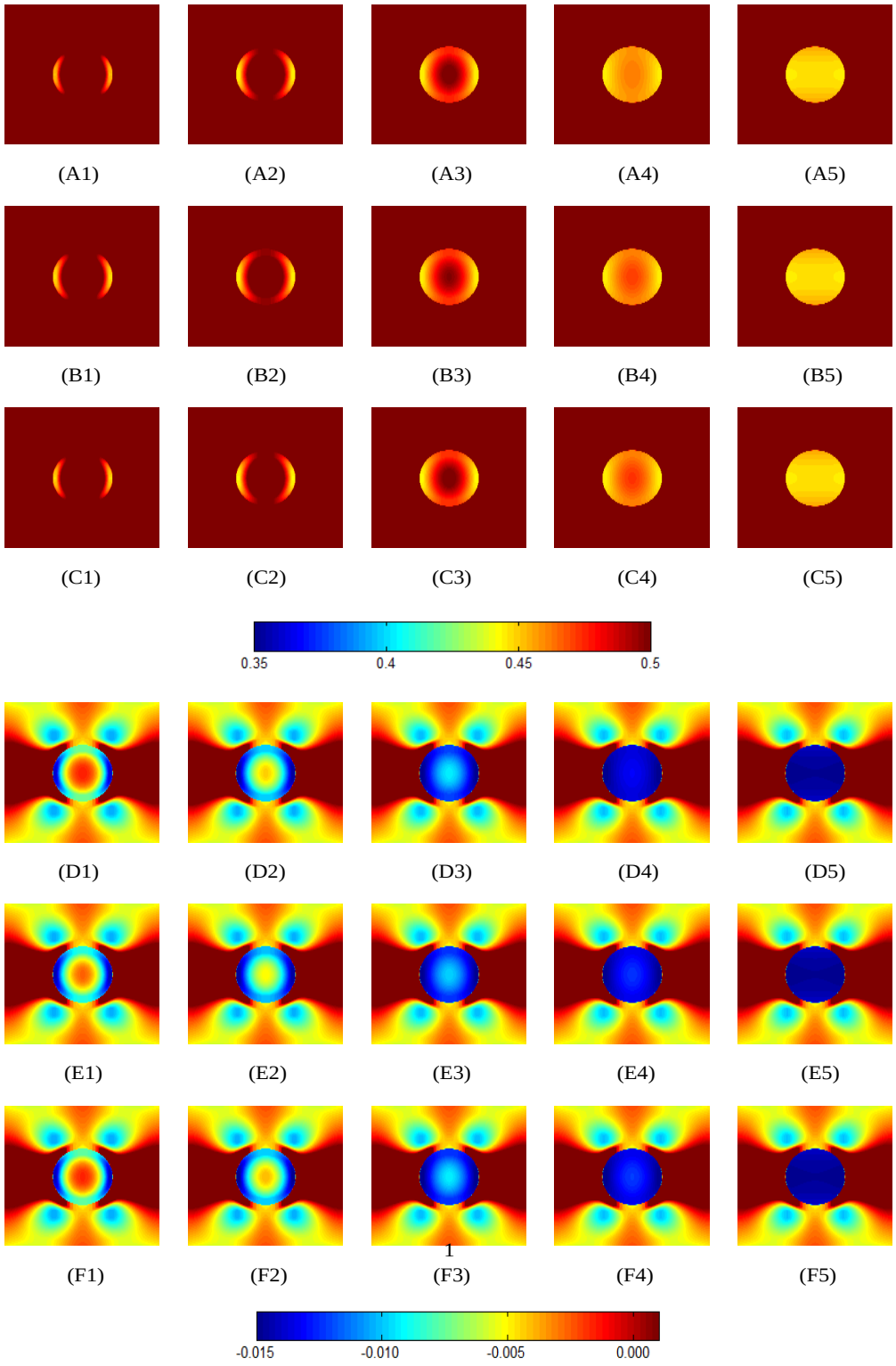

Figure 5.10: EPRs at time points of 0.6 s, 1.2 s, 2.4 s, 4.5 s and 28.8 s for sample D are shown in (A1-A5). EPRs at time points of 0.2 s, 0.4 s, 0.8 s, 1.5 s and 9.6 s for sample E and F are shown in (B1-B5) and (C1-C5). Volumetric strains at time points of 0.6 s, 1.2 s, 2.4 s, 4.5 s and 28.8 s for sample D are shown in (D1-D5). Volumetric strains at time points of 0.2 s, 0.4 s, 0.8 s, 1.5 s and 9.6 s for sample E and F are shown in (E1-E5) and (F1-F5).

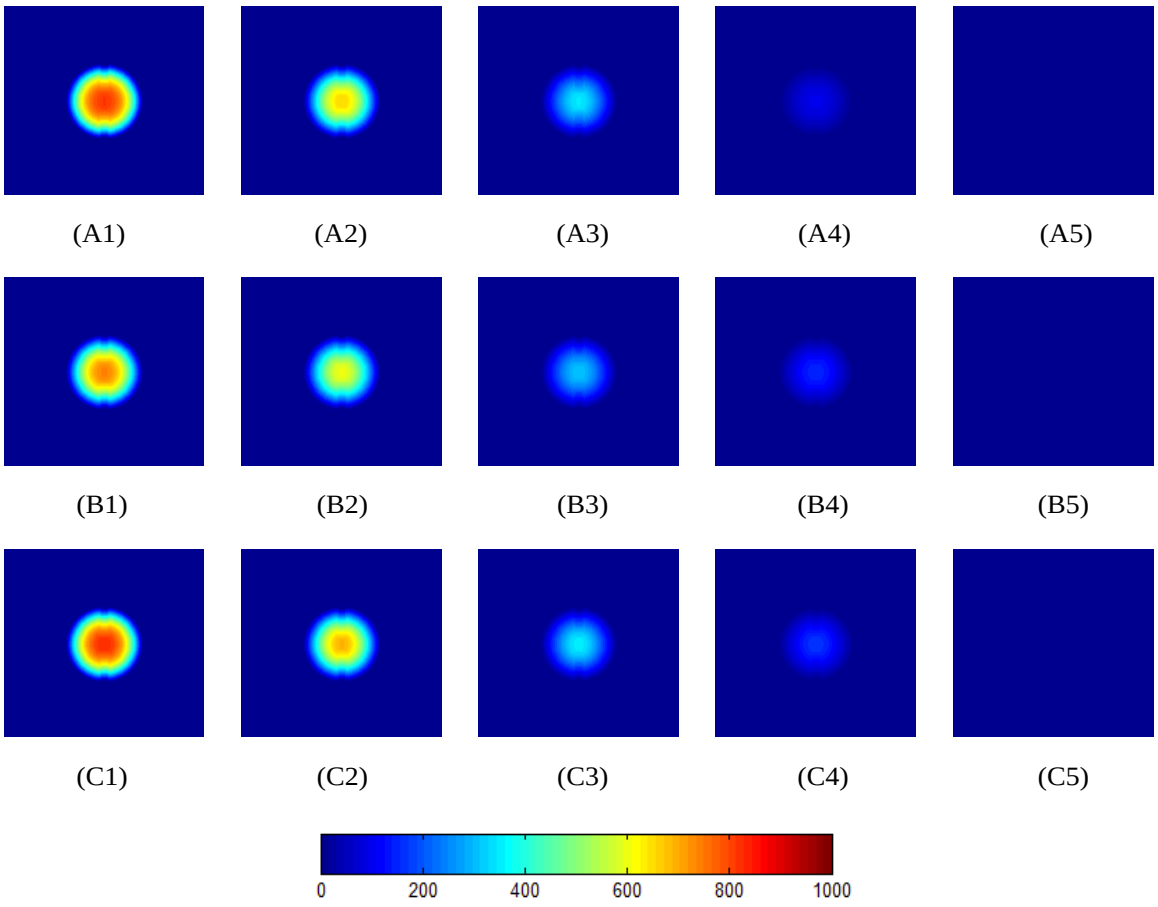

Figure 5.11: Fluid pressure (Pa) at time points of 0.6 s, 1.2 s, 2.4 s, 4.5 s and 28.8 s for sample D are shown in (A1-A5). Fluid pressure (Pa) at time points of 0.2 s, 0.4 s, 0.8 s, 1.5 s and 9.6 s for sample E and F are shown in (B1-B5) and (C1-C5), respectively.

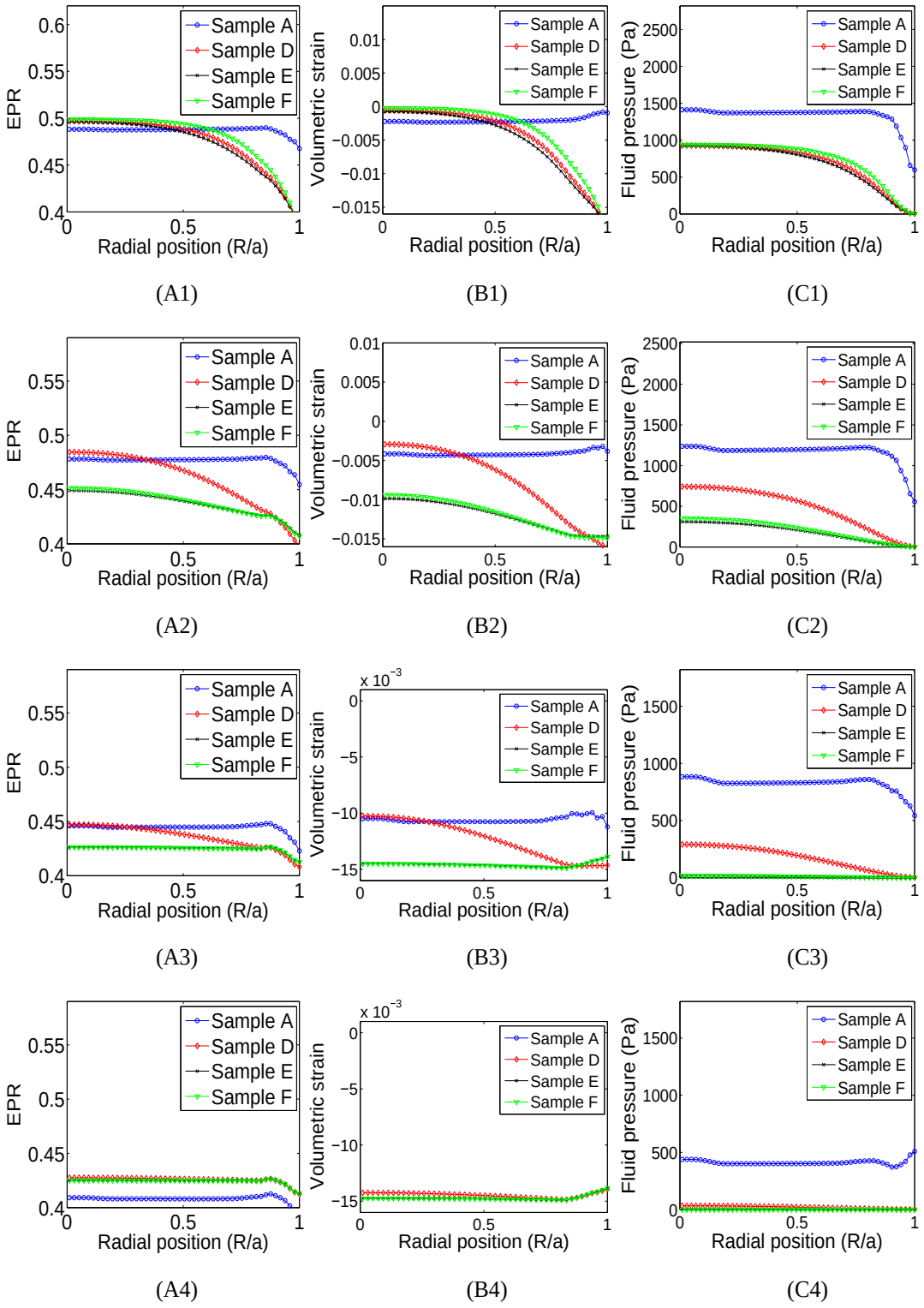

Figure 5.12: The radial profiles of the EPR, volumetric strain and fluid pressure are shown in (A1), (B1) and (C1), respectively in samples A, D, E and F at time point of 0^+ s. The radial profiles of the EPR, volumetric strain and fluid pressure are shown in (A2-A4), (B2-B4) and (C2-C4), respectively in samples A, D, E and F at time point of 1, 3 and 7 s.

6. ESTIMATION OF IFP

6.1 Methods

6.1.1 Estimation of IFP

From the developed analytical model of poroelastic media with spherical inclusion (see Section 2), we can write for the volumetric strain inside a tumor with IFP P_e

$$\epsilon_i(R,t) = -\frac{\sigma_T - P_e}{K_e} \times \left(1 + \frac{4}{3}\sum_{n=1}^{\infty} \frac{(1-2\nu_e)(1+\nu_e)}{[2(1+\nu_e)(1-2\nu_e) - (1-\nu_e)^2 x_n]} \times \frac{\sinh(\frac{R}{a}\sqrt{x_n})\exp\left(-x_n \frac{H_{Ai}k_i t}{a^2}\right)}{\frac{R}{a}\sinh(\sqrt{x_n})} \exp\left(-H_{Ai}\chi_i t\right)\right),$$

where σ_T is the applied effective volumetric stress inside the tumor, P_e is the IFP, K_e and ν_e are the effective compression modulus and Poisson's ratio, H_{Ai}, χ_i and k_i are the aggregate modulus, microfiltration coefficient and interstitial permeabilities inside the tumor, respectively. x_n is the root of the tangent characteristics function (see Section 2) and a is the radius of the tumor. This equation in steady state for spatially dependent elevated fluid pressure can be written as

$$\epsilon_i(R) = -\frac{\sigma_T - P_e(R)}{K_e}.$$

For the IFP, we can write

$$P_e(R) = K_e\epsilon_i(R) + \sigma_T.$$

σ_T is computed as $K_e\epsilon_i(a)$, where $\epsilon_i(a)$ is the volumetric strain at the radial boundary. In radial boundary, there is no IFP.

6.1.2 Time constant elastograms

The equation for the axial strain can be written as

$$\epsilon_y(r,z,t) = f(r,z)\exp(-\frac{t}{\tau}), \tag{6.1}$$

where $f(r,z)$ is the spatial function that determines the spatial variation of the fluid pressure and τ is the effective time constant of the relaxation of the poroelastic tumor defined as

$$\tau = \frac{\Omega}{H_{Ai}k_i} + \frac{1}{H_{Ai}\chi_i}. \tag{6.2}$$

Here, Ω is a constant which depends on the volumetric weight of the pore fluid, Poisson's ratio of the solid material and geometry of the sample, i.e., fluid path [13]. In this case, $\Omega = \frac{a^2}{x_1}$. Here, $\chi_i = \chi_V + \chi_L$, with $\chi_V = \frac{L_p S}{V}$ and $\chi_L = \frac{L_{PL}S_L}{V}$. $L_p$and L_{pL} are the hydraulic conductivities of capillary and lymphatic walls, respectively. $\frac{S_V}{V}$ and $\frac{S_L}{V}$ are the surface area to volume ratio of the capillary and lymphatic walls, respectively. Based on the values of the hydraulic conductivities of capillary and lymphatic walls reported in the literature, $\chi_V >> \chi_L$ [18]. This results in $\chi_i \approx \chi_V$, and the microfiltration coefficient becomes the hydraulic conductivity of the capillary wall (vascular hydraulic conductivity/permeability) multiplied by the surface area to volume ratio.

6.1.3 Interstitial fluid velocity (IFV)

The parameter V_{eR} is the IFV with respect to the solid and can be expressed as [14]

$$V_{eR}(R,z) = -k_i\frac{dP_e(R,z)}{dR}, \tag{6.3}$$

where k_i is the interstitial permeability of the tumor.

The parameter V_{ez} is the axial fluid velocity with respect to the solid and can be expressed as

$$V_{ez}(R,z) = -k_i\frac{dP_e(R,z)}{dz}. \tag{6.4}$$

6.1.4 Determination of the ratio between the interstitial and vascular permeabilities

For the elevated IFP inside tumor, we can write

$$P_e(R) = P_{ev}\big(1 - \frac{\sinh(\alpha R)}{R\sinh(R)}\big), \tag{6.5}$$

where

$$\alpha = a\sqrt{\frac{L_p}{k_i}\frac{S}{V}}. \tag{6.6}$$

Here P_{ev} is the effective vascular pressure inside the cancer tumor. L_p and k_i are the vascular and interstitial permeabilities and S/V is the ratio of cross-sectional area to volume of the tumor [40].

Using curve fitting technique, we determined the value of α. We choose at least 5 different lines from the center to periphery inside the tumor and fit eq. 6.5 onto the IFP curve to estimate α. The obtained 5 α values are then averaged to compute mean value of α.

6.1.5 Determination of interstitial and vascular permeabilities

We know from the model that

$$\frac{1}{\tau} = H_{Ai}\big(\chi_i + x_1\frac{k_i}{a^2}\big), \tag{6.7}$$

which can be written as

$$\frac{1}{H_{Ai}\tau} = \alpha k_i + x_1\frac{k_i}{a^2}. \tag{6.8}$$

The equation of the interstitial permeability can be written as

$$k_i = \frac{1}{H_{Ai}\tau(\alpha + \frac{x_1}{a^2})}. \tag{6.9}$$

The expression for vascular permeability can be written as

$$L_{pi} = \chi_i \frac{V}{S} = \alpha k_i \frac{V}{S} = \frac{V}{S} \frac{\alpha}{H_{Ai}\tau(\alpha + \frac{x_1}{a^2})}, \tag{6.10}$$

where $\frac{S}{V}$ is the surface area to volume ratio inside the tumor, which is determined using theory developed in [238].

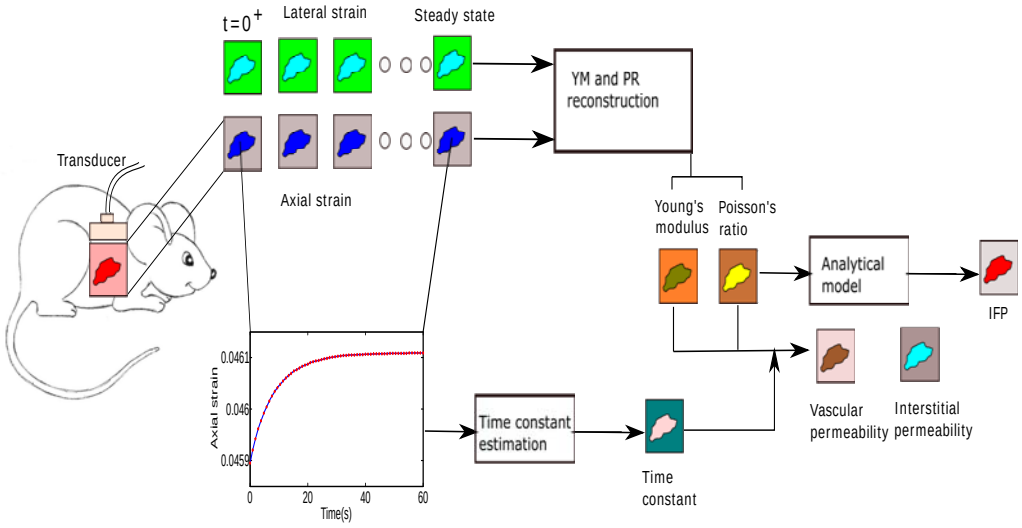

Figure 6.1: Estimation of mechanopathological parameters from a poroelastography experiment

6.1.6 In vivo experiments

Experiments on nineteen mice with triple negative breast cancer cells injected in the mammary fat pad were carried out on a weekly basis for three consecutive weeks. The cancers were created at the Houston Methodist Research Institute by injection of the cancerous cells beneath the mouse's mammary fat pad [159]. In vivo data acquisition was approved by the Houston Methodist Research Institute, Institutional Animal Care and Use Committee (ACUC-approved protocol # AUP-0614-0033). Seven mice were kept untreated and twelve mice were treated by injecting them intravenously with one of the following drugs: 1. Epirubicin alone, 2. Liposomes loaded with Epirubicin and 3. Liposomes loaded with Epirubicin and conjugated with Lox antibody on the

particle surface. The dose of each drug was 3 mg/kg body weight once a week. Prior to ultrasound data acquisition, each mouse was anesthetized with isoflurane. Each data acquisition session was 5 minutes long, and several RF data acquisitions could be performed during this period (for reliability purposes).

Elastography was carried out using a 38-mm linear array transducer (Sonix RP, Ultrasonix, Richmond, BC, Canada) with a center frequency of 6.6 MHz and $5-14$ MHz bandwidth. To compensate for the surface geometry as well as facilitate positioning the focus inside the superficial tumors, an aqueous ultrasound gel pad (Aquaflex, Parker Laboratories, NJ, USA) was placed between the compressor plate and the developed tumor. It should be noted that such use of gel pad does not change the stress distribution inside the sample significantly and thus does not change the estimated parameters. This has been proved in [198]. A force sensor (Tekscan FlexiForce) was inserted between the gel pad's top surface and the compressor plate to record the applied force during the compression. Creep compression was performed manually on the animals and monitored using the force sensor, with the duration of each compression being one minute. Duration of the experiment was selected based on the temporal behavior of the soft tissue and tumor reported in the literature [202] and to ensure that both the tumor and surrounding tissues reached steady state conditions. Ultrasound radio-frequency (RF) data acquisition was synchronized to the application of the compression. The sampling period of the data was set at 0.1 s. The axial and lateral strain data were calculated at steady state, when both the tumor and normal tissues behave as elastic materials [203]. An expert radiologist is employed to segment the in vivo axial strain elastograms in Matlab for determining the tumor areas.

6.1.7 Estimation of axial and lateral displacements and strains

To compute the axial and lateral displacements and strains from ultrasound simulation and in vivo experiment data, DPHS technique developed in our lab is used [146].

6.1.8 Computation of Young's modulus and Poisson's ratio

We used our previously developed technique to reconstruct the Young's modulus and Poisson's ratio simultaneously from axial and lateral strain elastograms as described in [198].

6.2 Results

We performed in vivo poroelastography experiments on six untreated and nine treated mice and reconstructed the IFP, IFV and interstitial and vascular permeabilities inside the tumor using our developed technique. The important images along with statistical analyses are shown and discussed below.

The reconstructed IFP, IFV along with the interstitial and vascular permeabilities and B-mode images for two untreated mice are shown in Figs. 6.2 and 6.3. The B-mode images for the first untreated tumor at three time points are shown in Fig. 6.2 A1, B1 and C1. From these images, the increment of size of the tumor with time can be clearly seen. The estimated IFP images for this tumor at week 1, 2 and 3 are shown in Fig. 6.2 A2, B2 and C2. The peak IFP is very low (around 0.5 kPa) inside the tumor in the first week. The IFP increases in the second week and its peak value becomes more than 1 kPa. The IFP can also be seen at multiple locations inside the tumor at this time point. In third week, the IFP becomes highest and is all over the tumor. The peak value of the IFP at this time point is more than 2.5 kPa. The estimated IFPs inside the tumor in this untreated tumor by our technique are similar to the values of IFP in untreated tumors of rodents reported by [239]. The consistent increment of the estimated IFP with cancer progression also matches with the results in [16].

The IFVs for the first untreated tumor are shown in Fig. 6.2 A3, B3 and C3. In these figures, we see that with increment of the magnitude of the IFP, the IFV also increases in subsequent weeks. In the first two weeks, the IFV is prominent around the periphery of the tumor. However, in the third week, the IFV increases at most of the points inside the tumor. The IFV values obtained using our technique corroborate with the reported values (in scale of $10^{-6}/10^{-7}$ ms^{-1}) in the literature [82, 224]. The IFVs seem increasing in the periphery regions of this tumor shown in subsequent

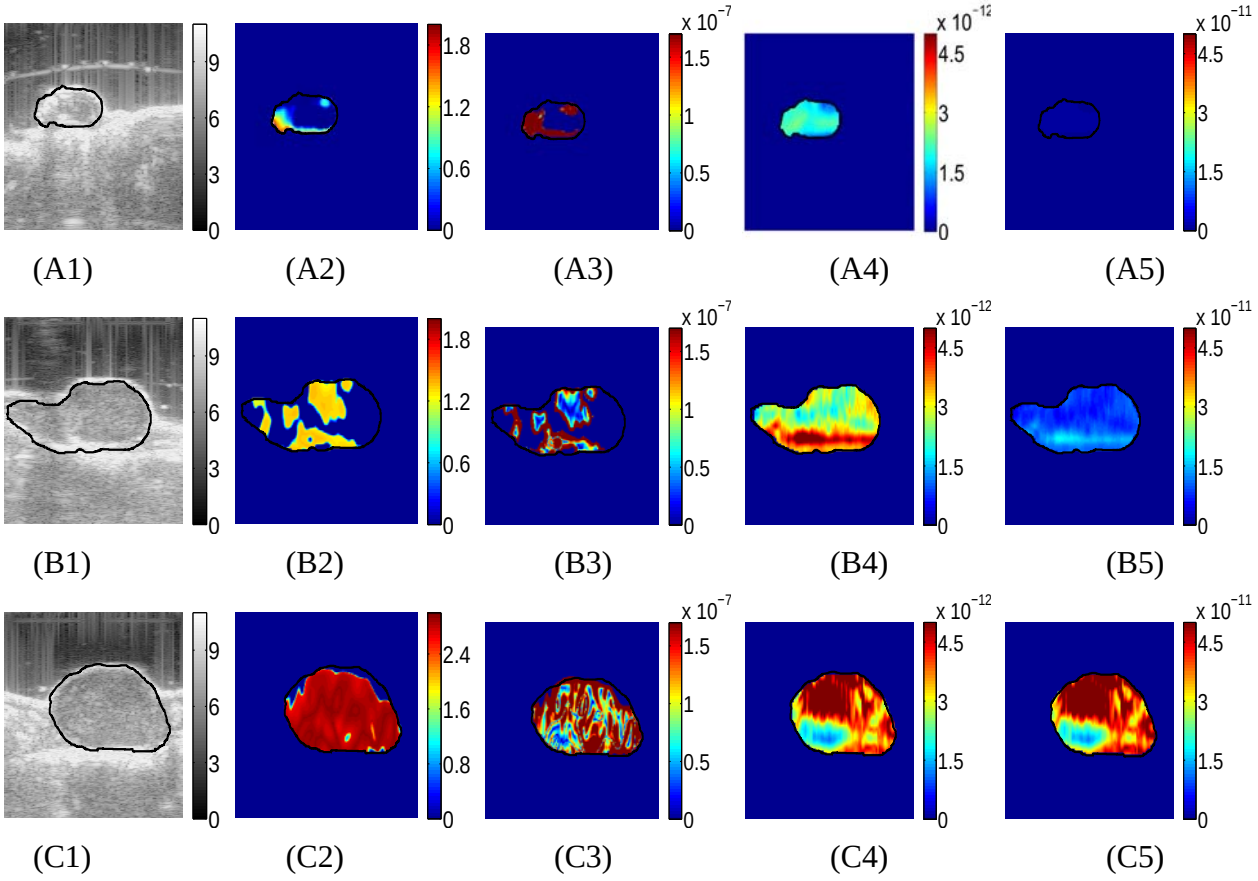

Figure 6.2: Ultrasound B-mode images of the first untreated tumor at three time points (week 1, week 2 and week 3) are shown in A1, B1 and C1, respectively. IFP images at these time points are shown in A2, B2 and C2. IFV images inside the tumor of the same mouse at three time points (week 1, week 2 and week 3) are shown in A3, B3 and C3, respectively. Interstitial permeabilities of the same tumor at three time points (week 1, week 2 and week 3) are shown in A4, B4 and C4, respectively. Vascular permeabilities of the same tumor at three time points (week 1, week 2 and week 3) are shown in A5, B5 and C5, respectively. The IFPs and IFVs are in scales of kPa and ms^{-1}. The interstitial and vascular permeabilities are in the scales of $m^4\ N^{-1}\ s^{-1}$ and $m(Pa\ s)^{-1}$. The IFP, IFV and interstitial and vascular permeabilities in the untreated tumor are all seen increasing in consecutive weeks. In the first week, both the IFP and IFV are almost zero everywhere inside the tumor. In the second week, the IFP and IFV increase at different locations inside the tumor and in the third week, both the IFP and IFV seem to spread all over the tumor with high values. The interstitial permeability seems to increase by 5 times from first to third week, whereas the vascular permeability increases by almost 10 times from first to third week.

weeks. This observation also matches with the reported profiles of IFV [50, 224].

The interstitial permeabilities for the first untreated tumor are shown in Fig. 6.2 A4, B4 and C4. We see from these images that the interstitial permeability of this tumor increases with time.

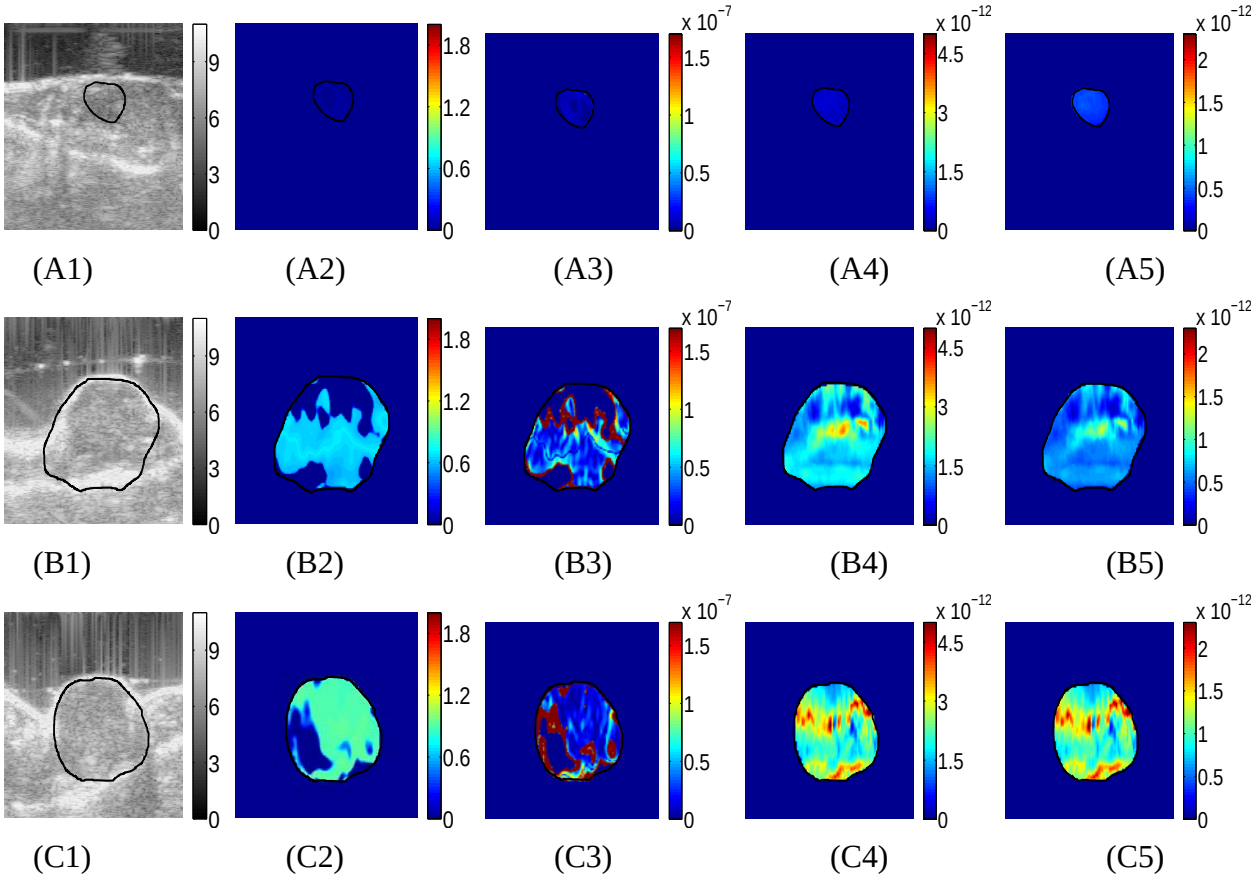

Figure 6.3: Ultrasound B-mode images of the second untreated tumor at three time points (week 1, week 2 and week 3) are shown in A1, B1 and C1, respectively. IFP images at these time points are shown in A2, B2 and C2. IFV images inside the tumor of the same mouse at three time points (week 1, week 2 and week 3) are shown in A3, B3 and C3, respectively. Interstitial permeabilities of the same tumor at three time points (week 1, week 2 and week 3) are shown in A4, B4 and C4, respectively. Vascular permeabilities of the same tumor at three time points (week 1, week 2 and week 3) are shown in A5, B5 and C5, respectively. The IFPs and IFVs are in scales of kPa and ms^{-1}. The interstitial and vascular permeabilities are in the scales of m^4 N^{-1} s^{-1} and m(Pa s)$^{-1}$. Similar to the first untreated tumor, the IFP, IFV and interstitial and vascular permeabilities in the untreated tumor are all seen increasing in consecutive weeks. In the first week, both the IFP and IFV are almost zero inside the tumor. In the second and third week, the IFP and IFV increase almost everywhere inside the tumor. The interstitial permeability seems to increase by 6 times from first to third week, whereas the vascular permeability increases by almost 8 times from first to third week.

At first week the interstitial permeability remains much below 1×10^{-12} m$^4 N^{-1}$ s^{-1}, whereas in third week, the interstitial permeability becomes more than 5 times of it, i.e., 5×10^{-12} m$^4 N^{-1}$ s^{-1}. The estimated values of the interstitial permeability correlate with the reported values (in scale of

10^{-12} m$^4 N^{-1}$ s^{-1}) obtained by invasive estimation methods [59]. The increment of the interstitial permeability with cancer progression is expected as it is known that the interstitial permeability increases in tumors in comparison to the normal tissue [40, 240].

The vascular permeability of the first untreated tumor at three time points are shown in Fig. 6.2 A5, B5 and C5. Like the interstitial permeability, the vascular permeability of the tumor also increases with time. In the first week, the vascular permeability of the tumor is much below than 0.5×10^{-11} m(Pas)$^{-1}$, whereas the vascular permeability becomes more than 10 times of this value in the third week, i.e., $> 5 \times 10^{-11}$ m(Pas)$^{-1}$. The obtained values of the vascular permeability are in the range of values (in scale of 10^{-11} m(Pas)$^{-1}$) reported in the literature [11, 40]. Similar to the interstitial permeability, the increment of vascular permeability in tumor tissues in comparison the normal tissues has been shown in many studies [40, 240], which corroborates with our results.

Similar scenarios for the IFP, IFV, interstitial and vascular permeabilities for the first untreated tumor are seen in case of the second untreated tumor, which are shown in Fig. 6.3. The IFP for this tumor is almost zero everywhere at the first week, which increases to about 0.5 kPa in the second week and further increases to about 0.8 kPa at the third week. The IFV is zero everywhere for this tumor is the first week but increases mostly around the periphery in the next two weeks. The interstitial and vascular permeability increases by 6 and 8 times in this tumor from first to third week as shown in Fig. 6.3 (A4-B4) and (A5-B5).

The estimated IFP, IFV, interstitial and vascular permeabilities of the first treated tumor along with the B-mode images are shown in Fig. 6.4 for three time points (week 1, 2 and 3). In the first week, we see that the IFP is zero inside the tumor and then it increases to 0.4 and then 1 kPa in second and third week. The spatial nature of the IFP for this tumor is different from the IFP of the untreated tumor. In this case, the IFP is radially decreasing, whereas for the untreated tumor, the IFP was constant throughout or at some locations inside the tumor. In this case, the IFP is highest at the center of the tumor and then goes down at the periphery. This may be because of the lower value of the spatial parameter α. This observation matches with results found in [50, 224] and means less metastatic nature of the tumor. The IFP in the treated tumor is also less than the

untreated tumors. This reduction of the IFP because of application of drug matches with the results reported in [239].

The IFV for the treated tumor is shown in Fig. 6.4 (A3, B3, C3). We see that the IFV is again high at the periphery of the tumor in all three time points of the tumor. The interstitial permeability of the tumor at three time points are shown in Fig. 6.4 (A4, B4, C4). We see that in contrast to the untreated tumors, the interstitial and vascular permeabilities both goes down for the treated tumors. The interstitial permeability of this tumor is around 5×10^{-12} m$^4 N^{-1}$s^{-1} at the first week, which becomes around 0.5×10^{-12} m$^4 N^{-1}$s^{-1} in the third week. On the other hand, the vascular permeability of this tumor is around 5×10^{-12} m(Pas)$^{-1}$ at the first week, which becomes around 0.1×10^{-12} m(Pas)$^{-1}$ in the third week. Therefore, the reduction of the interstitial permeability is around 10 times, where the reduction in vascular permeability is around 50 times from first to third week. This reduction of vascular permeability with treatment corroborates with the results reported in the work of Goel et al. [241].

The IFP, IFV and interstitial and vascular permeabilities of the second treated tumor along with the B-mode images are shown in Fig. 6.5 at three time points. The IFP for this tumor is almost zero in the first week, which becomes around 1 kPa in the third week. The IFV seems also increasing and becomes almost 10 times from the first to third week. The interstitial and vascular permeabilities for this tumor reduce consistently from first to third week. In the third week, both interstitial and vascular permeabilities of this tumor becomes very small i.e., $< 0.5 \times 10^{-12}$.

The summary of all the results obtained in our in vivo experiments can be seen in the bar plots of mean values of IFP (A1), interstitial permeability (A2), vascular permeability (A3), α (B1), Young's modulus (B2) and surface area (B3) shown in Fig. 6.6. In Fig. 6.6 (A1), we see that the IFP is much higher for the untreated tumors than the treated ones. The IFP increases with time for both the treated and untreated tumors. The mean value of α inside the untreated tumors is higher than that inside the treated ones in all three weeks, but is much higher in the third week. The mean values of α for the treated tumors do not change much with time. These observations match with the results obtained beforehand in invasive studies reported in the literature [50]. The interstitial

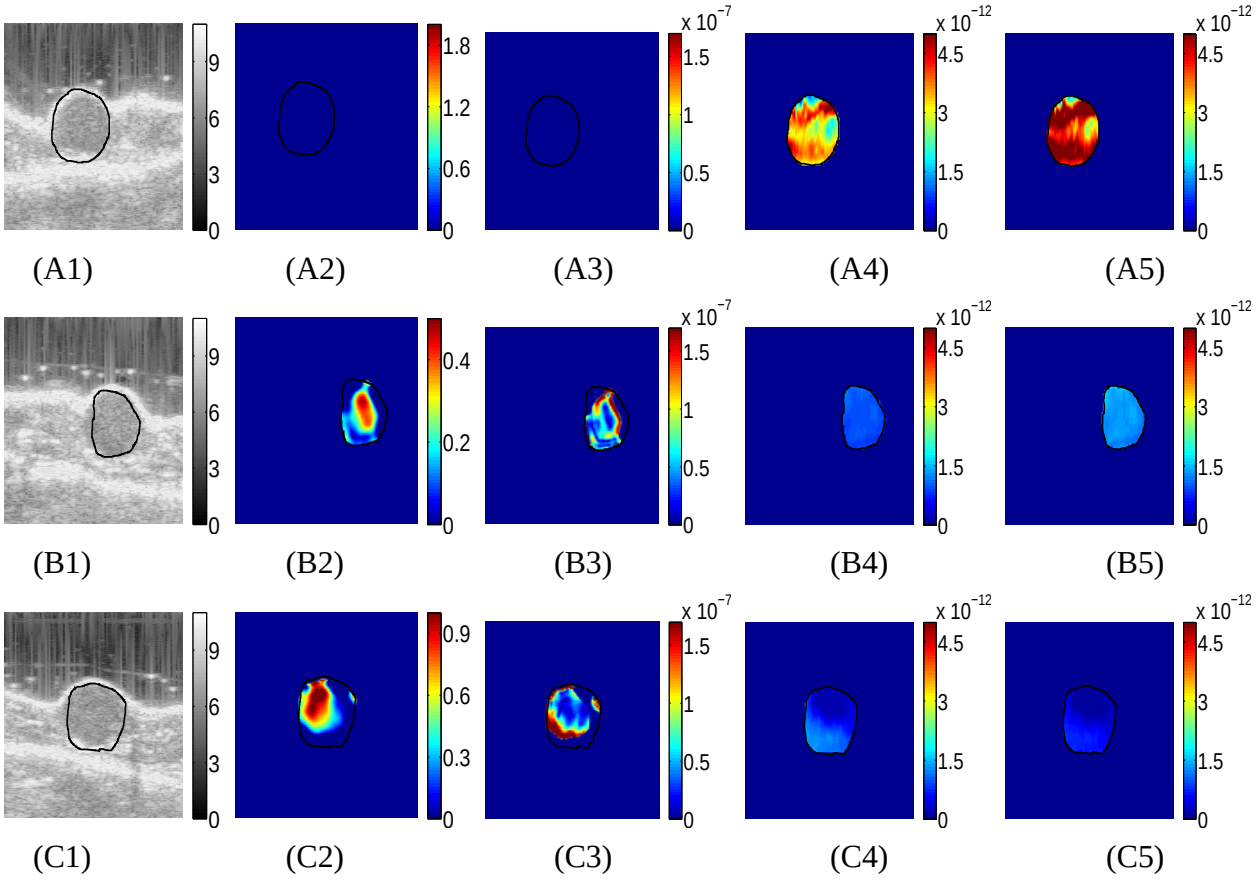

Figure 6.4: Ultrasound B-mode images of the first treated tumor at three time points (week 1, week 2 and week 3) are shown in A1, B1 and C1, respectively. IFP images at these time points are shown in A2, B2 and C2. IFV images inside the tumor of the same mouse at three time points (week 1, week 2 and week 3) are shown in A3, B3 and C3, respectively. Interstitial permeabilities of the same tumor at three time points (week 1, week 2 and week 3) are shown in A4, B4 and C4, respectively. Vascular permeabilities of the same tumor at three time points (week 1, week 2 and week 3) are shown in A5, B5 and C5, respectively. The IFPs and IFVs are in scales of kPa and ms^{-1}. The interstitial and vascular permeabilities are in the scales of $m^4\ N^{-1}\ s^{-1}$ and $m(Pa\ s)^{-1}$. Starting from zero in the first week, both the IFP and IFV increase in subsequent weeks for the treated tumor. However, the IFP never becomes more than 1 kPa. The interstitial permeability for this tumor is around $5 \times 10^{-12}\ m^4\ N^{-1}\ s^{-1}$ in the first week, which reduces by almost 10 times in the third week. The vascular permeability reduces by 50 times from the first to third week.

permeability is higher for the treated tumors in all three weeks than the untreated ones. This can be the direct impact of the treatment on the reduction of cell proliferation in the interstitium of the tumor. However, the interstitial permeability seems decreasing for the treated tumors with time, whereas the interstitial permeability of the untreated tumors seems to decrease by a small amount

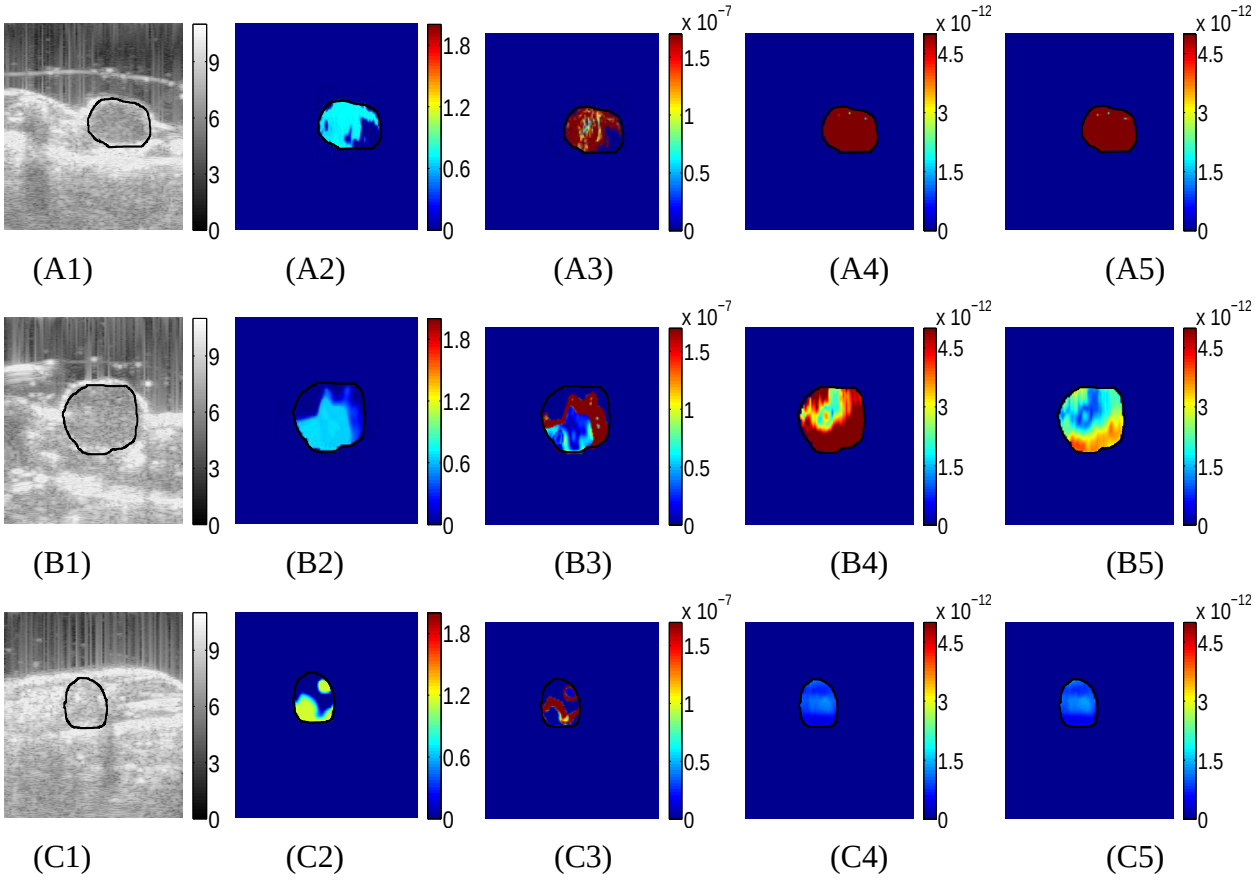

Figure 6.5: Ultrasound B-mode images of the second treated tumor at three time points (week 1, week 2 and week 3) are shown in A1, B1 and C1, respectively. IFP images at these time points are shown in A2, B2 and C2. IFV images inside the tumor of the same mouse at three time points (week 1, week 2 and week 3) are shown in A3, B3 and C3, respectively. Interstitial permeabilities of the same tumor at three time points (week 1, week 2 and week 3) are shown in A4, B4 and C4, respectively. Vascular permeabilities of the same tumor at three time points (week 1, week 2 and week 3) are shown in A5, B5 and C5, respectively. The IFPs and IFVs are in scales of kPa and ms^{-1}. The interstitial and vascular permeabilities are in the scales of $m^4\ N^{-1}\ s^{-1}$ and $m(Pa\ s)^{-1}$. The IFP and IFV are very small in both first and second week in this case. In third week, as the tumor becomes much smaller, the IFP and IFV increase at some locations inside the tumor. Unlike other tumors, the interstitial and vascular permeabilities increase at first to second week and then decrease at the third week.

from the first to second week but increases from second to third week. The vascular permeability for the treated tumors seems decreasing, whereas for the untreated tumors seems increasing with time as shown Fig. 6.6 (A3). The mean vascular permeability of the untreated tumors at third week is much higher than that at first and second week and can be high by one or two scale. We also

report the Young's modulus and surface area of these tumors in (B2) and (B3) to support the results of IFP, IFV and permeabilities obtained with the progression of cancer. Both of them increase consistently in case of the untreated tumors with time, which proves the consistent progression of cancers in the untreated tumors. On the other hand, for the treated tumors, the Young's modulus and surface area of the tumor seem at the same level in all three weeks, which proves that because of the drugs, the progression of cancer may have been halted or the cancer has been cured.

6.3 Discussion

In this section, we propose a novel noninvasive technique to image important mechanopathological parameters of cancers: IFP, IFV and interstitial and vascular permeabilities using ultrasound poroelastography. Based on developed analytical model, the IFP has been estimated from the estimated volumetric strain at steady state and the interstitial and vascular permeabilities have been estimated using a curve fitting technique on the temporal profile of the axial strain. The proposed technique incorporates all the advantages of ultrasound based imaging techniques such as cost-effectiveness, no radiation, user friendly, less time consuming etc.

The estimation of the IFP is important for cancer diagnosis, prognosis and treatment. IFP can be used as a strong marker to diagnose the malignancy of the tumor [242]. The image of IFP values inside the tumor can help the physicians to estimate the progression of tumor and decide the required treatment. For tumors with high IFP, the chemotherapy and immunotherapy may not be the good choice because the IFP creates hindrance for the therapeutic agents to enter into the tumor and thus reduces the effect of the treatment significantly [32, 50]. The value of IFP can also be helpful in assessing the efficacy of the treatment used. Decrement of IFP with application of drugs has been used as a indicator of the efficacy of the drugs in treating cancers in many works [243, 244].

The IFV is an important parameter in drug delivery. High IFV inside the tumor indicates the higher possibility of the drug to penetrate inside the tumor. We observed in many cases, in the untreated tumors, the IFV is higher inside the tumor and the drug has higher chance to enter into the tumor. This effect is called 'enhanced permeability and retention' (EPR) and has been

thoroughly investigated in the literature [245]. EPR effect increases the chance of drug penetration to tumor tissue than the normal tissue and has been been exploited to facilitate delivery of high-molecular-weight drugs to the cancer sites. We also observed extremely low IFV in some treated cases, which means that with increasing effect of drug, the further probability of successful drug delivery reduces. This phenomenon has been discussed in [50].

The interstitial and vascular permeabilities are effective diagnostic markers and important information for the decision of treatment type to used. High value of vascular permeability is connected with metastasis and cancer progression [40]. Interstitial permeability is also shown to change in tumors in comparison to the normal tissue [58]. In our study, we found out that the interstitial and vascular permeabilities of the untreated tumors increase, whereas of the treated tumors decrease with time. To our knowledge, this is the first report of change in values of interstitial and vascular permeabilities with cancer progression and with time after application of drug.

For the results of second treated tumor (Fig.6.5), the interstitial and vascular permeabilities are seen increasing from the first to second week and then decreasing from second to third week, which is different from the other tumor shown and the general trend shown in Fig. 6.6. However, the increment of the interstitial permeability from the first week to second week and then decrement from second to third week can be justified by the change in both Young's modulus and surface area of the tumor. The Young's modulus of this tumor increases from 29.05 to 35.93 kPa and then decreases to 21.24 kPa in the third week. Similarly, the surface area of the tumor increases from 0.945 to 1.616 cm^2 from first to second week and then decreases to 0.664 cm^2 in the third week. Therefore, for this tumor, it can be stated that from the first week to second week, the drug could not control the cancer progression but the drug became effective after second week and was able to control the cancer growth and reduce the tumor area, stiffness and permeabilities significantly.

In some treated cases, we found out that the IFP image has moderate values (≈ 0.6 kPa) in second and (≈ 1.2 kPa) in third week (Fig. 6.5). The Young's moduli of this tumor at three subsequent week are $23.39, 22.99$ and 16.58 kPa. We see that although the size and Young's modulus of this tumor are decreasing and values of Young's modulus are close to the Young's modulus of normal

tissues, the IFP inside the tumor is never zero and has increasing values in consecutive weeks. This phenomena can be an indicator of possible recurrance of the cancer. This also proves that the IFP can be an independent diagnostic and prognostic marker when the Young's modulus and size of the tumor fail to provide any information about the cancer progression.

Based on the results shown in Fig. 6.6, the mean Young's modulus and surface area increase consistently for the untreated tumors with time, but remain almost same for the treated tumors. Therefore, these markers may fail to show the impact of the drug on many treated tumors, whereas the mean values of the IFP, interstitial and vascular permeabilities are clearly seen to change for application drugs with time. Based on these results, it can be stated that these mechanopathological parameters may be more effective markers than the stiffness/surface area to show the treatment efficacy inside cancer tumor.

While estimating the IFP in this section, we did not consider the effect of the solid stress inside the tumor. There are two reasons behind that. Firstly, the solid stress value is generally much lower than the IFP inside the tumor [18, 185]. Secondly, the solid stress (both radial and circumferential stress) is normally uniform over the tumor and goes to zero far outside of the tumor [18]. Therefore, the value of solid stress can be assumed to be same at the inside and at the periphery of the tumor. As in our technique, IFP is estimated by subtracting the volumetric stress (created because of applied external stress) values inside the tumor from the volumetric stress of periphery, the volumetric solid stress (sum of radial and circumferential solid stress) would affect both of them equally and will be nullified because of subtraction. Therefore, the estimated IFP by our technique would be same even if the solid stress is considered and as a result our measurement of IFP is independent of presence of solid stress inside the tumor.

Although we have validated our technique through finite element and ultrasound simulations, we could not validate it experimentally and in vivo. The reason behind this is the lack of suitable phantom available with interstitial and vascular permeabilities and IFP inside it. We also believe that if the tumor is brought outside and the IFP measured invasively, the obtained result may not represent the accurate values of IFP. The presence of the normal tissue around the tumor is

important for obtaining the correct values of IFP. This observation has recently been verified by Nia et al. for solid stress inside the tumor [185]. It should be noted that the IFP and solid stress work inside the tumor and create expansive stress inside the tumor [20]. The main difference between them is that the IFP creates a isotropic stress, whereas the solid stress creates different stress along axial and lateral directions.

The main limitations of the proposed approach are the assumptions taken for developing the theory, i.e., the tumor and normal tissues have uniform mechanical properties and the tumor is of spherical shape. Although these assumptions are used frequently in cancer tumor modeling, they may not hold strictly in practical scenarios always. However, the obtained values of the mechanopathological parameters still would be accurate to a moderate degree and the proposed technique can be an attractive replacement for the time-consuming, costly invasive techniques and biopsy.

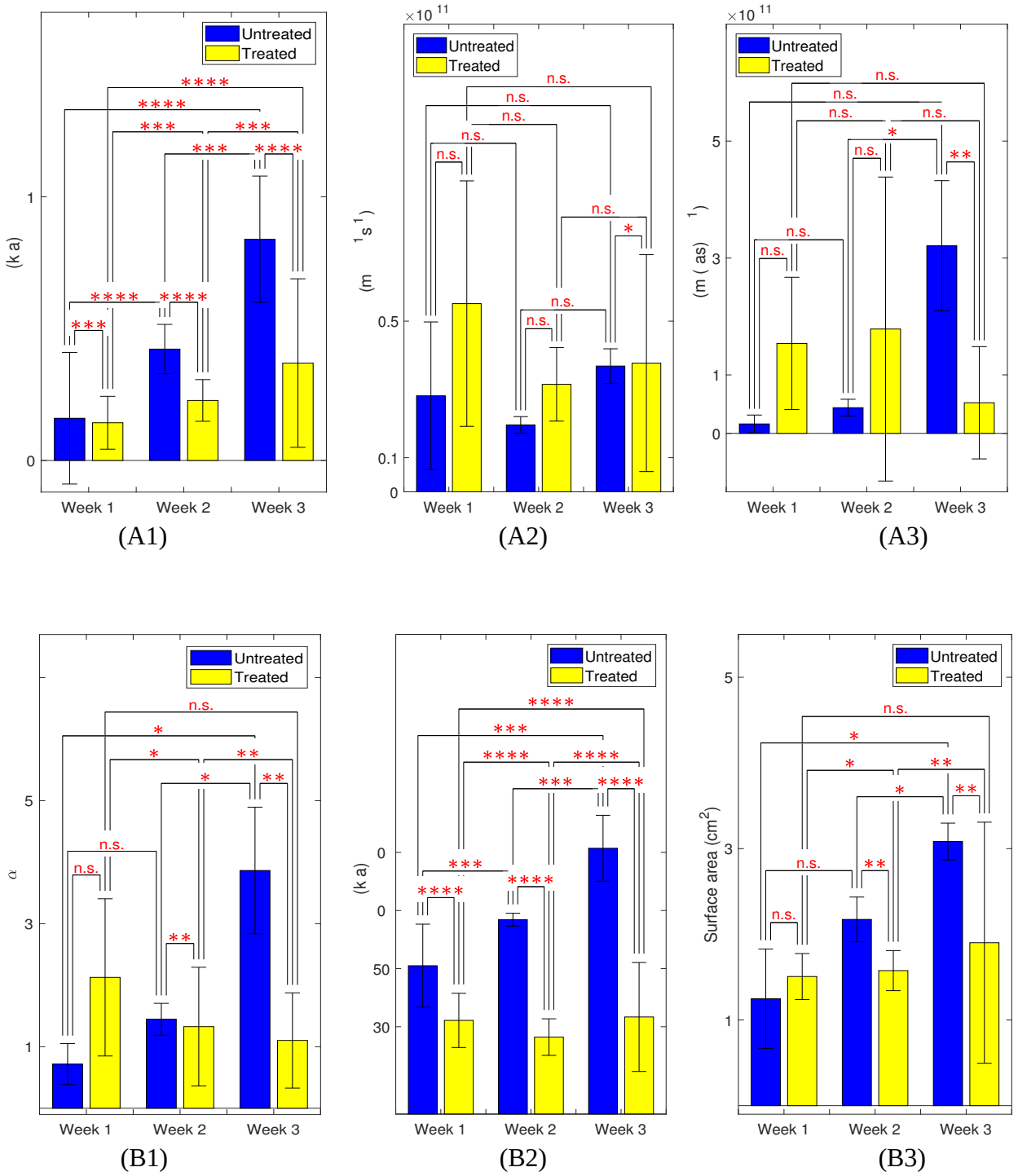

Figure 6.6: (A1) Mean IFP inside the tumors of the treated and untreated mice at week 1, week 2 and week 3. (A2) Mean interstitial permeability (IP) inside the tumors of the treated and untreated mice at week 1, week 2 and week 3. (A3) Mean vascular permeability (VP) inside the tumors of the treated and untreated mice at week 1, week 2 and week 3. (B1) Mean values of α inside the tumors of the treated and untreated mice at week 1, week 2 and week 3. (B2) Mean Young's moduli of the tumors of the treated and untreated mice at week 1, week 2 and week 3. (B3) Mean surface areas of the tumors of the treated and untreated mice at week 1, week 2 and week 3. n.s. means not statistically significant. One, two, three and four stars corresponds to p-value less than $0.05, 0.01, 0.001, 0.0001$, respectively.

7. CONCLUSION

In this dissertation, I demonstrated a non invasive technique for imaging the IFP, IFV and interstitial and vascular permeabilities inside cancer tumor based on ultrasound poroelastography. Based on the importance of these parameters in cancer treatment, diagnosis and prognosis and widespread popularity and low expense of ultrasound imaging systems, the developed method may be the preferable technique for imaging these parameters to the clinicians and researchers.

REFERENCES

[1] J.-L. Gennisson, T. Deffieux, M. Fink, and M. Tanter, "Ultrasound elastography: principles and techniques," *Diagnostic and Interventional Imaging*, vol. 94, no. 5, pp. 487–495, 2013.

[2] J. Ophir, I. Cespedes, H. Ponnekanti, Y. Yazdi, and X. Li, "Elastography: a quantitative method for imaging the elasticity of biological tissues," *Ultrasonic Imaging*, vol. 13, no. 2, pp. 111–134, 1991.

[3] J. Ophir, S. Alam, B. Garra, F. Kallel, E. Konofagou, T. Krouskop, and T. Varghese, "Elastography: ultrasonic estimation and imaging of the elastic properties of tissues," *Proceedings of the Institution of Mechanical Engineers, Part H: Journal of Engineering in Medicine*, vol. 213, no. 3, pp. 203–233, 1999.

[4] J. Bercoff, M. Tanter, and M. Fink, "Supersonic shear imaging: a new technique for soft tissue elasticity mapping," *IEEE Transactions on Ultrasonics, Ferroelectrics, and Frequency Control*, vol. 51, no. 4, pp. 396–409, 2004.

[5] K. Nightingale, M. S. Soo, R. Nightingale, and G. Trahey, "Acoustic radiation force impulse imaging: in vivo demonstration of clinical feasibility," *Ultrasound in Medicine & Biology*, vol. 28, no. 2, pp. 227–235, 2002.

[6] A. Goddi, M. Bonardi, and S. Alessi, "Breast elastography: a literature review," *Journal of Ultrasound*, vol. 15, no. 3, pp. 192–198, 2012.

[7] S. R. Mousavi, H. Rivaz, G. J. Czarnota, A. Samani, and A. Sadeghi-Naini, "Ultrasound elastography of the prostate using an unconstrained modulus reconstruction technique: A pilot clinical study," *Translational Oncology*, vol. 10, no. 5, pp. 744–751, 2017.

[8] R. Righetti, J. Ophir, S. Srinivasan, and T. A. Krouskop, "The feasibility of using elastography for imaging the poisson's ratio in porous media," *Ultrasound in Medicine & Biology*, vol. 30, no. 2, pp. 215–228, 2004.

[9] A. Chaudhry, "Effect of boundary conditions on performance of poroelastographic imaging techniques in non homogeneous poroelastic media," Master's thesis, Texas A&M University, 2010.

[10] R. Righetti, B. S. Garra, L. M. Mobbs, C. M. Kraemer-Chant, J. Ophir, and T. A. Krouskop, "The feasibility of using poroelastographic techniques for distinguishing between normal and lymphedematous tissues in vivo," *Physics in Medicine and Biology*, vol. 52, no. 21, p. 6525, 2007.

[11] R. K. Jain, "Transport of molecules in the tumor interstitium: a review," *Cancer Research*, vol. 47, no. 12, pp. 3039–3051, 1987.

[12] S. Nair, J. Varghese, A. Chaudhry, and R. Righetti, "Effect of temporal acquisition parameters on image quality of strain time constant elastography," *Ultrasonic Imaging*, p. 0161734614539665, 2014.

[13] R. Leiderman, P. E. Barbone, A. A. Oberai, and J. C. Bamber, "Coupling between elastic strain and interstitial fluid flow: ramifications for poroelastic imaging," *Physics in Medicine and Biology*, vol. 51, no. 24, p. 6291, 2006.

[14] C. Armstrong, W. Lai, and V. Mow, "An analysis of the unconfined compression of articular cartilage," *Journal of Biomechanical Engineering*, vol. 106, no. 2, pp. 165–173, 1984.

[15] M. T. Islam, J. Reddy, and R. Righetti, "An analytical poroelastic model of a non-homogeneous medium under creep compression for ultrasound poroelastography applications - part i," *In press, Journal of Biomechanical Engineering*, 2018. doi:10.1115/1.4040603.

[16] T. Stylianopoulos, J. D. Martin, M. Snuderl, F. Mpekris, S. R. Jain, and R. K. Jain, "Coevolution of solid stress and interstitial fluid pressure in tumors during progression: implications for vascular collapse," *Cancer Research*, vol. 73, no. 13, pp. 3833–3841, 2013.

[17] T. Stylianopoulos, "The solid mechanics of cancer and strategies for improved therapy," *Journal of Biomechanical Engineering*, vol. 139, no. 2, p. 021004, 2017.

[18] M. Sarntinoranont, F. Rooney, and M. Ferrari, "Interstitial stress and fluid pressure within a growing tumor," *Annals of Biomedical Engineering*, vol. 31, no. 3, pp. 327–335, 2003.

[19] M. E. Fernández-Sánchez, S. Barbier, J. Whitehead, G. Béalle, A. Michel, H. Latorre-Ossa, C. Rey, L. Fouassier, A. Claperon, L. Brullé, *et al.*, "Mechanical induction of the tumorigenic [bgr]-catenin pathway by tumour growth pressure," *Nature*, vol. 523, no. 7558, pp. 92–95, 2015.

[20] T. Stylianopoulos, J. D. Martin, V. P. Chauhan, S. R. Jain, B. Diop-Frimpong, N. Bardeesy, B. L. Smith, C. R. Ferrone, F. J. Hornicek, Y. Boucher, *et al.*, "Causes, consequences, and remedies for growth-induced solid stress in murine and human tumors," *Proceedings of the National Academy of Sciences*, vol. 109, no. 38, pp. 15101–15108, 2012.

[21] L. T. Baxter and R. K. Jain, "Transport of fluid and macromolecules in tumors. i. role of interstitial pressure and convection," *Microvascular Research*, vol. 37, no. 1, pp. 77–104, 1989.

[22] L. T. Baxter and R. K. Jain, "Transport of fluid and macromolecules in tumors. ii. role of heterogeneous perfusion and lymphatics," *Microvascular Research*, vol. 40, no. 2, pp. 246–263, 1990.

[23] L. T. Baxter and R. K. Jain, "Transport of fluid and macromolecules in tumors. iv. a microscopic model of the perivascular distribution," *Microvascular Research*, vol. 41, no. 2, pp. 252–272, 1991.

[24] G. Griffon-Etienne, Y. Boucher, C. Brekken, H. D. Suit, and R. K. Jain, "Taxane-induced apoptosis decompresses blood vessels and lowers interstitial fluid pressure in solid tumors," *Cancer Research*, vol. 59, no. 15, pp. 3776–3782, 1999.

[25] T. P. Padera, A. Kadambi, E. di Tomaso, C. M. Carreira, E. B. Brown, Y. Boucher, N. C. Choi, D. Mathisen, J. Wain, E. J. Mark, *et al.*, "Lymphatic metastasis in the absence of functional intratumor lymphatics," *Science*, vol. 296, no. 5574, pp. 1883–1886, 2002.

[26] T. P. Padera, B. R. Stoll, J. B. Tooredman, D. Capen, E. di Tomaso, and R. K. Jain, "Pathology: cancer cells compress intratumour vessels," *Nature*, vol. 427, no. 6976, pp. 695–695, 2004.

[27] R. K. Jain, "Barriers to drug delivery in solid tumors," *Scientific American*, vol. 271, no. 1, pp. 58–65, 1994.

[28] J. M. Brown and A. J. Giaccia, "The unique physiology of solid tumors: opportunities (and problems) for cancer therapy," *Cancer Research*, vol. 58, no. 7, pp. 1408–1416, 1998.

[29] M. Milosevic, A. Fyles, D. Hedley, M. Pintilie, W. Levin, L. Manchul, and R. Hill, "Interstitial fluid pressure predicts survival in patients with cervix cancer independent of clinical prognostic factors and tumor oxygen measurements," *Cancer Research*, vol. 61, no. 17, pp. 6400–6405, 2001.

[30] S. J. Lunt, A. Fyles, R. P. Hill, and M. Milosevic, "Interstitial fluid pressure in tumors: therapeutic barrier and biomarker of angiogenesis," *Future Oncology*, vol. 4, no. 6, pp. 793–802, 2008.

[31] C.-H. Heldin, K. Rubin, K. Pietras, and A. Östman, "High interstitial fluid pressure–an obstacle in cancer therapy," *Nature Reviews Cancer*, vol. 4, no. 10, p. 806, 2004.

[32] R. K. Jain, "Delivery of molecular medicine to solid tumors," *Science*, vol. 271, no. 5252, pp. 1079–1080, 1996.

[33] Y. Boucher and R. K. Jain, "Microvascular pressure is the principal driving force for interstitial hypertension in solid tumors: implications for vascular collapse," *Cancer Research*, vol. 52, no. 18, pp. 5110–5114, 1992.

[34] E. K. Rofstad, J.-V. Gaustad, K. G. Brurberg, B. Mathiesen, K. Galappathi, and T. G. Simonsen, "Radiocurability is associated with interstitial fluid pressure in human tumor xenografts," *Neoplasia*, vol. 11, no. 11, pp. 1243–1251, 2009.

[35] E. K. Rofstad, E.-B. M. Ruud, B. Mathiesen, and K. Galappathi, "Associations between radiocurability and interstitial fluid pressure in human tumor xenografts without hypoxic tissue," *Clinical Cancer Research*, vol. 16, no. 3, pp. 936–945, 2010.

[36] E. K. Rofstad, S. H. Tunheim, B. Mathiesen, B. A. Graff, E. F. Halsør, K. Nilsen, and K. Galappathi, "Pulmonary and lymph node metastasis is associated with primary tumor interstitial fluid pressure in human melanoma xenografts," *Cancer Research*, vol. 62, no. 3, pp. 661–664, 2002.

[37] C. Ellingsen, T. Hompland, B. Mathiesen, and E. K. Rofstad, "Microenvironment-associated lymph node metastasis of human cervical carcinoma xenografts," *Acta Oncologica*, vol. 51, no. 4, pp. 465–472, 2012.

[38] S.-G. Yeo, J.-S. Kim, M.-J. Cho, K.-H. Kim, and J.-S. Kim, "Interstitial fluid pressure as a prognostic factor in cervical cancer following radiation therapy," *Clinical Cancer Research*, vol. 15, no. 19, pp. 6201–6207, 2009.

[39] A. Fyles, M. Milosevic, M. Pintilie, A. Syed, W. Levin, L. Manchul, and R. P. Hill, "Long-term performance of interstial fluid pressure and hypoxia as prognostic factors in cervix cancer," *Radiotherapy and Oncology*, vol. 80, no. 2, pp. 132–137, 2006.

[40] P. A. Netti, L. T. Baxter, Y. Boucher, R. Skalak, and R. K. Jain, "Macro-and microscopic fluid transport in living tissues: Application to solid tumors," *AIChE Journal*, vol. 43, no. 3, pp. 818–834, 1997.

[41] U. Ozerdem and A. R. Hargens, "A simple method for measuring interstitial fluid pressure in cancer tissues," *Microvascular Research*, vol. 70, no. 1-2, pp. 116–120, 2005.

[42] P. Scholander, A. R. Hargens, and S. L. Miller, "Negative pressure in the interstitial fluid of animals," *Science*, vol. 161, no. 3839, pp. 321–328, 1968.

[43] A. R. Hargens, *Tissue fluid pressure and composition*. Williams & Wilkins, 1981.

[44] S. Mubarak and A. Hargens, "Clinical use of the wick-catheter technique," in *Tissue fluid pressure and composition*, pp. 261–268, The William & Wilkins Company, Baltimore, 1981.

[45] H. Fadnes, R. Reed, and K. Aukland, “Interstitial fluid pressure in rats measured with a modified wick technique,” *Microvascular Research*, vol. 14, no. 1, pp. 27–36, 1977.

[46] H. Wiig, R. K. Reed, and K. Aukland, “Measurement of interstitial fluid pressure in dogs: evaluation of methods,” *American Journal of Physiology-Heart and Circulatory Physiology*, vol. 253, no. 2, pp. H283–H290, 1987.

[47] C. A. Wiederhielm, J. W. Woodbury, S. Kirk, and R. F. Rushmer, “Pulsatile pressures in the microcirculation of frog’s mesentery,” *American Journal of Physiology–Legacy Content*, vol. 207, no. 1, pp. 173–176, 1964.

[48] A. C. Guyton, M. Frank, and B. Abernathy, “A concept of negative interstitial pressure based on pressures in implanted perforated capsules,” *Circulation Research*, vol. 12, no. 4, pp. 399–414, 1963.

[49] U. Ozerdem, “Measuring interstitial fluid pressure with fiberoptic pressure transducers,” *Microvascular Research*, vol. 77, no. 2, pp. 226–229, 2009.

[50] R. K. Jain, R. T. Tong, and L. L. Munn, “Effect of vascular normalization by antiangiogenic therapy on interstitial hypertension, peritumor edema, and lymphatic metastasis: insights from a mathematical model,” *Cancer Research*, vol. 67, no. 6, pp. 2729–2735, 2007.

[51] Y. Hassid, E. Furman-Haran, R. Margalit, R. Eilam, and H. Degani, “Noninvasive magnetic resonance imaging of transport and interstitial fluid pressure in ectopic human lung tumors,” *Cancer Research*, vol. 66, no. 8, pp. 4159–4166, 2006.

[52] K. Gulliksrud, K. G. Brurberg, and E. K. Rofstad, “Dynamic contrast-enhanced magnetic resonance imaging of tumor interstitial fluid pressure,” *Radiotherapy and Oncology*, vol. 91, no. 1, pp. 107–113, 2009.

[53] K. Gulliksrud, K. Galappathi, and E. K. Rofstad, “Interstitial fluid pressure and vascularity of intradermal and intramuscular human tumor xenografts,” *International Journal of Radiation Oncology* Biology* Physics*, vol. 80, no. 1, pp. 258–264, 2011.

[54] M. A. Haider, I. Sitartchouk, T. P. Roberts, A. Fyles, A. T. Hashmi, and M. Milosevic, "Correlations between dynamic contrast-enhanced magnetic resonance imaging–derived measures of tumor microvasculature and interstitial fluid pressure in patients with cervical cancer," *Journal of Magnetic Resonance Imaging*, vol. 25, no. 1, pp. 153–159, 2007.

[55] M. A. Haider, M. Milosevic, A. Fyles, I. Sitartchouk, I. Yeung, E. Henderson, G. Lockwood, T. Y. Lee, and T. P. Roberts, "Assessment of the tumor microenvironment in cervix cancer using dynamic contrast enhanced ct, interstitial fluid pressure and oxygen measurements," *International Journal of Radiation Oncology* Biology* Physics*, vol. 62, no. 4, pp. 1100–1107, 2005.

[56] A. Miles and E. M. Miles, "Vascular reactions to histamine, histamine-liberator and leukotaxine in the skin of guinea-pigs," *The Journal of Physiology*, vol. 118, no. 2, pp. 228–257, 1952.

[57] C. Michel, J. Mason, F. Curry, J. Tooke, and P. Hunter, "A development of the landis technique for measuring the filtration coefficient of individual capillaries in the frog mesentery," *Experimental Physiology*, vol. 59, no. 4, pp. 283–309, 1974.

[58] E. A. Swabb, J. Wei, and P. M. Gullino, "Diffusion and convection in normal and neoplastic tissues," *Cancer Research*, vol. 34, no. 10, pp. 2814–2822, 1974.

[59] P. A. Netti, D. A. Berk, M. A. Swartz, A. J. Grodzinsky, and R. K. Jain, "Role of extracellular matrix assembly in interstitial transport in solid tumors," *Cancer Research*, vol. 60, no. 9, pp. 2497–2503, 2000.

[60] M. Milosevic, S. J. Lunt, E. Leung, J. Skliarenko, P. Shaw, A. Fyles, and R. P. Hill, "Interstitial permeability and elasticity in human cervix cancer," *Microvascular Research*, vol. 75, no. 3, pp. 381–390, 2008.

[61] H. C. Roberts, T. P. Roberts, R. C. Brasch, and W. P. Dillon, "Quantitative measurement of microvascular permeability in human brain tumors achieved using dynamic contrast-

enhanced mr imaging: correlation with histologic grade," *American Journal of Neuroradiology*, vol. 21, no. 5, pp. 891–899, 2000.

[62] L. J. Liu, S. L. Brown, J. R. Ewing, B. D. Ala, K. M. Schneider, and M. Schlesinger, "Estimation of tumor interstitial fluid pressure (tifp) noninvasively," *PloS One*, vol. 11, no. 7, p. e0140892, 2016.

[63] R. Elmghirbi, T. N. Nagaraja, S. L. Brown, K. A. Keenan, S. Panda, G. Cabral, H. Bagher-Ebadian, G. W. Divine, I. Y. Lee, and J. R. Ewing, "Toward a noninvasive estimate of interstitial fluid pressure by dynamic contrast-enhanced mri in a rat model of cerebral tumor," *Magnetic Resonance in Medicine*, vol. 80, no. 5, pp. 2040–2052, 2018.

[64] H. Chen, X. Tong, L. Lang, O. Jacobson, B. C. Yung, X. Yang, R. Bai, D. O. Kiesewetter, Y. Ma, H. Wu, *et al.*, "Quantification of tumor vascular permeability and blood volume by positron emission tomography," *Theranostics*, vol. 7, no. 9, p. 2363, 2017.

[65] M. A. Biot, "General theory of three-dimensional consolidation," *Journal of Applied Physics*, vol. 12, no. 2, pp. 155–164, 1941.

[66] M. A. Biot, "Mechanics of deformation and acoustic propagation in porous media," *Journal of Applied Physics*, vol. 33, no. 4, pp. 1482–1498, 1962.

[67] V. C. Mow and W. M. Lai, "Recent developments in synovial joint biomechanics," *Siam Review*, vol. 22, no. 3, pp. 275–317, 1980.

[68] V. C. Mow, A. Ratcliffe, and S. L. Woo, *Biomechanics of diarthrodial joints*, vol. 1. Springer Science & Business Media, 2012.

[69] V. C. Mow, S. Kuei, W. M. Lai, and C. G. Armstrong, "Biphasic creep and stress relaxation of articular cartilage in compression: theory and experiments," *Journal of Biomechanical Engineering*, vol. 102, no. 1, pp. 73–84, 1980.

[70] V. Mow, N. Bachrach, L. Setton, and F. Guilak, "Stress, strain, pressure and flow fields in articular cartilage and chondrocytes," in *Cell Mechanics and Cellular Engineering*, pp. 345–379, Springer, 1994.

[71] A. Chaudhry, G. Unnikrishnan, J. Reddy, T. A. Krouskop, and R. Righetti, "Effect of permeability on the performance of elastographic imaging techniques," *IEEE Transactions on Medical Imaging*, vol. 32, no. 2, pp. 189–199, 2013.

[72] J. Eshelby, "Elastic inclusions and inhomogeneities," *Progress in Solid Mechanics*, vol. 2, no. 1, pp. 89–140, 1961.

[73] J. Rice, J. Rudnicki, and D. A. Simons, "Deformation of spherical cavities and inclusions in fluid-infiltrated elastic materials," *International Journal of Solids and Structures*, vol. 14, no. 4, pp. 289–303, 1978.

[74] Y. Song, H. Hu, and J. W. Rudnicki, "Shear properties of heterogeneous fluid-filled porous media with spherical inclusions," *International Journal of Solids and Structures*, vol. 83, pp. 154–168, 2016.

[75] Y. Song, H. Hu, J. W. Rudnicki, and Y. Duan, "Dynamic transverse shear modulus for a heterogeneous fluid-filled porous solid containing cylindrical inclusions," *Geophysical Journal International*, vol. 206, no. 3, pp. 1677–1694, 2016.

[76] J. G. Berryman, "Scattering by a spherical inhomogeneity in a fluid-saturated porous medium," *Journal of Mathematical Physics*, vol. 26, no. 6, pp. 1408–1419, 1985.

[77] M. Kanj and Y. Abousleiman, "Porothermoelastic analyses of anisotropic hollow cylinders with applications," *International Journal for Numerical and Analytical Methods in Geomechanics*, vol. 29, no. 2, pp. 103–126, 2005.

[78] L. Cui and Y. Abousleiman, "Time-dependent poromechanical responses of saturated cylinders," *Journal of Engineering Mechanics*, vol. 127, no. 4, pp. 391–398, 2001.

[79] G. Ateshian, W. Lai, W. Zhu, and V. Mow, "An asymptotic solution for the contact of two biphasic cartilage layers," *Journal of Biomechanics*, vol. 27, no. 11, pp. 1347–1360, 1994.

[80] P. A. Netti, L. T. Baxter, Y. Boucher, R. Skalak, and R. K. Jain, "Time-dependent behavior of interstitial fluid pressure in solid tumors: implications for drug delivery," *Cancer Research*, vol. 55, no. 22, pp. 5451–5458, 1995.

[81] M. A. Swartz, A. Kaipainen, P. A. Netti, C. Brekken, Y. Boucher, A. J. Grodzinsky, and R. K. Jain, "Mechanics of interstitial-lymphatic fluid transport: theoretical foundation and experimental validation," *Journal of Biomechanics*, vol. 32, no. 12, pp. 1297–1307, 1999.

[82] R. K. Jain, J. D. Martin, and T. Stylianopoulos, "The role of mechanical forces in tumor growth and therapy," *Annual Review of Biomedical Engineering*, vol. 16, p. 321, 2014.

[83] R. K. Jain, "Delivery of molecular and cellular medicine to solid tumors," *Journal of Controlled Release*, vol. 53, no. 1, pp. 49–67, 1998.

[84] R. K. Jain and L. T. Baxter, "Mechanisms of heterogeneous distribution of monoclonal antibodies and other macromolecules in tumors: significance of elevated interstitial pressure," *Cancer Research*, vol. 48, no. 24 Part 1, pp. 7022–7032, 1988.

[85] M. F. Milosevic, A. W. Fyles, and R. P. Hill, "The relationship between elevated interstitial fluid pressure and blood flow in tumors: a bioengineering analysis," *International Journal of Radiation Oncology* Biology* Physics*, vol. 43, no. 5, pp. 1111–1123, 1999.

[86] P. Netti, L. Baxter, Y. Coucher, R. Skalak, and R. Jain, "A poroelastic model for interstitial pressure in tumors," *Biorheology*, vol. 32, no. 2, pp. 346–346, 1995.

[87] H. Byrne and M. A. Chaplain, "Modelling the role of cell-cell adhesion in the growth and development of carcinomas," *Mathematical and Computer Modelling*, vol. 24, no. 12, pp. 1–17, 1996.

[88] A. Jones, H. Byrne, J. Gibson, and J. Dold, "A mathematical model of the stress induced during avascular tumour growth," *Journal of Mathematical Biology*, vol. 40, no. 6, pp. 473–499, 2000.

[89] S. K. Kyriacou, C. Davatzikos, S. J. Zinreich, and R. N. Bryan, "Nonlinear elastic registration of brain images with tumor pathology using a biomechanical model [mri]," *IEEE Transactions on Medical Imaging*, vol. 18, no. 7, pp. 580–592, 1999.

[90] A. Bertuzzi, A. Fasano, and A. Gandolfi, “A mathematical model for tumor cords incorporating the flow of interstitial fluid,” *Mathematical Models and Methods in Applied Sciences*, vol. 15, no. 11, pp. 1735–1777, 2005.

[91] I. M. Saeed *et al.*, “Structure and growth of tumors: the effect of cartesian, cylindrical, and spherical geometries,” *Annals of the New York Academy of Sciences*, vol. 858, no. 1, pp. 127–136, 1998.

[92] G. Sciumè, S. Shelton, W. G. Gray, C. T. Miller, F. Hussain, M. Ferrari, P. Decuzzi, and B. Schrefler, “A multiphase model for three-dimensional tumor growth,” *New Journal of Physics*, vol. 15, no. 1, p. 015005, 2013.

[93] M. T. Islam, J. Reddy, and R. Righetti, “An analytical poroelastic model of a non-homogeneous medium under creep compression for ultrasound poroelastography applications - part ii,” *In press, Journal of Biomechanical Engineering*, 2018. doi:10.1115/1.4040604.

[94] M. A. Swartz and M. E. Fleury, “Interstitial flow and its effects in soft tissues,” *Annual Review of Biomedical Engineering*, vol. 9, pp. 229–256, 2007.

[95] A. Verruijt, “Theory and problems of poroelasticity,” *Delft University of Technology*, 2013.

[96] G. P. Berry, J. C. Bamber, C. G. Armstrong, N. R. Miller, and P. E. Barbone, “Towards an acoustic model-based poroelastic imaging method: I. theoretical foundation,” *Ultrasound in Medicine & Biology*, vol. 32, no. 4, pp. 547–567, 2006.

[97] G. A. Ateshian, K. D. Costa, and C. T. Hung, “A theoretical analysis of water transport through chondrocytes,” *Biomechanics and Modeling in Mechanobiology*, vol. 6, no. 1-2, pp. 91–101, 2007.

[98] H. S. Carslaw and J. C. Jaeger, “Conduction of heat in solids,” *Oxford: Clarendon Press, 1959, 2nd ed.*, 1959.

[99] A. Segall, “Thermoelastic analysis of thick-walled vessels subjected to transient thermal loading,” *Journal of Pressure Vessel Technology*, vol. 123, no. 1, pp. 146–149, 2001.

[100] J. P. Guerrero, E. Pontedeiro, M. T. van Genuchten, and T. Skaggs, "Analytical solutions of the one-dimensional advection–dispersion solute transport equation subject to time-dependent boundary conditions," *Chemical Engineering Journal*, vol. 221, pp. 487–491, 2013.

[101] M. T. Islam, A. Chaudhry, G. Unnikrishnan, J. Reddy, and R. Righetti, "An analytical poroelastic model for ultrasound elastography imaging of tumors," *Physics in Medicine & Biology*, vol. 63, no. 2, p. 025031, 2018.

[102] D. Simulia, "Abaqus version 6.10 documentation," *Dassault Systems Simulia Corp, Providence, RI, USA*, 2010.

[103] A. Nabavizadeh, R. R. Kinnick, M. Bayat, C. Amador, M. W. Urban, A. Alizad, and M. Fatemi, "Automated compression device for viscoelasticity imaging.," *IEEE Transactions on Biomedical Engineering*, vol. 64, pp. 1535–1546, July 2017.

[104] M. Lekka, "Discrimination between normal and cancerous cells using afm," *Bionanoscience*, vol. 6, no. 1, pp. 65–80, 2016.

[105] A. Grodzinsky, V. Roth, E. Myers, W. Grossman, and V. Mow, "The significance of electromechanical and osmotic forces in the nonequilibrium swelling behavior of articular cartilage in tension," *Journal of Biomechanical Engineering*, vol. 103, no. 4, pp. 221–231, 1981.

[106] M. Muskat and R. D. Wyckoff, *Flow of homogeneous fluids through porous media*. McGraw-Hill Book Company, Inc., 1937.

[107] J. E. Schmidt and G. Sonnemann, "Transient temperatures and thermal stresses in hollow cylinders due to heat generation," *Journal of Heat Transfer*, vol. 82, no. 4, pp. 273–278, 1960.

[108] D. G. Duffy, *Advanced engineering mathematics with MATLAB*. CRC Press, 2010.

[109] M. T. Islam, A. Chaudhry, G. Unnikrishnan, J. Reddy, and R. Righetti, "An analytical model of tumors with higher permeability than surrounding tissues for ultrasound elastography

imaging," *Journal of Engineering and Science in Medical Diagnostics and Therapy*, vol. 1, no. 3, p. 031006031006, 2018.

[110] J. D. Eshelby, "The determination of the elastic field of an ellipsoidal inclusion, and related problems," in *Proceedings of the Royal Society of London A: Mathematical, Physical and Engineering Sciences*, vol. 241, pp. 376–396, The Royal Society, 1957.

[111] D. Mason, A. Solomon, and L. Nicolaysen, "Evolution of stress and strain during the consolidation of a fluid-saturated porous elastic sphere," *Journal of Applied Physics*, vol. 70, no. 9, pp. 4724–4740, 1991.

[112] M. T. Islam, J. Reddy, and R. Righetti, "A model-based approach to investigate the effect of elevated interstitial fluid pressure on strain elastography," *Physics in Medicine & Biology*, vol. 63, no. 21, p. 215011, 2018.

[113] H. Zhi, B. Ou, B.-M. Luo, X. Feng, Y.-L. Wen, and H.-Y. Yang, "Comparison of ultrasound elastography, mammography, and sonography in the diagnosis of solid breast lesions," *Journal of Ultrasound in Medicine*, vol. 26, no. 6, pp. 807–815, 2007.

[114] P. Rzymski and T. Opala, "Elastography as a new diagnostic tool to detect breast cancer–evaluation of research and clinical applications," *Prz. Menopauzalny*, vol. 5, pp. 357–362, 2011.

[115] F. Mpekris, J. W. Baish, T. Stylianopoulos, and R. K. Jain, "Role of vascular normalization in benefit from metronomic chemotherapy," *Proceedings of the National Academy of Sciences*, vol. 114, no. 8, pp. 1994–1999, 2017.

[116] Y.-C. Fung, "Mechanical properties and active remodeling of blood vessels," in *Biomechanics*, pp. 321–391, Springer, 1993.

[117] T. Varghese, E. Konofagou, J. Ophir, S. Alam, and M. Bilgen, "Direct strain estimation in elastography using spectral cross-correlation," *Ultrasound in Medicine & Biology*, vol. 26, no. 9, pp. 1525–1537, 2000.

[118] S. K. Alam, J. Ophir, and E. E. Konofagou, "An adaptive strain estimator for elastography," *IEEE Transactions on Ultrasonics, Ferroelectrics, and Frequency Control*, vol. 45, no. 2, pp. 461–472, 1998.

[119] H. Rivaz, E. Boctor, P. Foroughi, R. Zellars, G. Fichtinger, and G. Hager, "Ultrasound elastography: a dynamic programming approach," *IEEE Transactions on Medical Imaging*, vol. 27, no. 10, pp. 1373–1377, 2008.

[120] H. Rivaz, E. M. Boctor, M. A. Choti, and G. D. Hager, "Real-time regularized ultrasound elastography," *IEEE Transactions on Medical Imaging*, vol. 30, no. 4, pp. 928–945, 2011.

[121] Y. Zhou and Y.-P. Zheng, "A motion estimation refinement framework for real-time tissue axial strain estimation with freehand ultrasound," *IEEE Transactions on Ultrasonics, Ferroelectrics, and Frequency Control*, vol. 57, no. 9, pp. 1943–1951, 2010.

[122] X. Pan, J. Gao, S. Tao, K. Liu, J. Bai, and J. Luo, "A two-step optical flow method for strain estimation in elastography: Simulation and phantom study," *Ultrasonics*, vol. 54, no. 4, pp. 990–996, 2014.

[123] S. K. Alam, F. L. Lizzi, T. Varghese, E. J. Feleppa, and S. Ramachandran, "Adaptive spectral strain estimators for elastography," *Ultrasonic Imaging*, vol. 26, no. 3, pp. 131–149, 2004.

[124] F. Viola and W. F. Walker, "A comparison of the performance of time-delay estimators in medical ultrasound," *IEEE Transactions on Ultrasonics, Ferroelectrics, and Frequency Control*, vol. 50, no. 4, pp. 392–401, 2003.

[125] T. Varghese and J. Ophir, "A theoretical framework for performance characterization of elastography: The strain filter," *IEEE Transactions on Ultrasonics, Ferroelectrics, and Frequency Control*, vol. 44, no. 1, pp. 164–172, 1997.

[126] C. Pellot-Barakat, F. Frouin, M. F. Insana, and A. Herment, "Ultrasound elastography based on multiscale estimations of regularized displacement fields," *IEEE Transactions on Medical Imaging*, vol. 23, no. 2, pp. 153–163, 2004.

[127] T. J. Hall, Y. Zhu, and C. S. Spalding, "In vivo real-time freehand palpation imaging," *Ultrasound in Medicine & Biology*, vol. 29, no. 3, pp. 427–435, 2003.

[128] J. Jiang and T. J. Hall, "A regularized real-time motion tracking algorithm using dynamic programming for ultrasonic strain imaging," in *2006 IEEE Ultrasonics Symposium*, pp. 606–609, IEEE, 2006.

[129] S. Chikayoshi, A. Suzuki, and K. Nakayama, "Phantom experiment on estimation of shear modulus distribution in soft tissue from ultrasonic measurement of displacement vector field," *IEICE TRANSACTIONS on Fundamentals of Electronics, Communications and Computer Sciences*, vol. 78, no. 12, pp. 1655–1664, 1995.

[130] C. Sumi, "Fine elasticity imaging utilizing the iterative rf-echo phase matching method," *IEEE Transactions on Ultrasonics, Ferroelectrics, and Frequency Control*, vol. 46, no. 1, pp. 158–166, 1999.

[131] H. Shi and T. Varghese, "Two-dimensional multi-level strain estimation for discontinuous tissue," *Physics in Medicine and Biology*, vol. 52, no. 2, p. 389, 2007.

[132] H. Chen, H. Shi, and T. Varghese, "Improvement of elastographic displacement estimation using a two-step cross-correlation method," *Ultrasound in Medicine & Biology*, vol. 33, no. 1, pp. 48–56, 2007.

[133] H. Zhu, S. Zhou, P. Yang, L. He, and J. Zhou, "An efficient optimal method for a 2d strain estimation of ultrasound tissue-mimicking material phantom," *Polymer Engineering & Science*, vol. 55, no. 12, pp. 2751–2760, 2015.

[134] T. Zakaria, Z. Qin, and R. L. Maurice, "Optical-flow-based b-mode elastography: Application in the hypertensive rat carotid," *IEEE Transactions on Medical Imaging*, vol. 29, no. 2, pp. 570–578, 2010.

[135] M. A. Lubinski, S. Y. Emelianov, K. Raghavan, A. E. Yagle, A. R. Skovoroda, and M. O'Donnell, "Lateral displacement estimation using tissue incompressibility," *IEEE*

Transactions on Ultrasonics Ferroelectrics and Frequency Control, vol. 43, no. 2, pp. 247–256, 1996.

[136] E. Konofagou and J. Ophir, "A new elastographic method for estimation and imaging of lateral displacements, lateral strains, corrected axial strains and poisson's ratios in tissues," *Ultrasound in Medicine & Biology*, vol. 24, no. 8, pp. 1183–1199, 1998.

[137] L. Chen, R. J. Housden, G. M. Treece, A. H. Gee, and R. W. Prager, "A hybrid displacement estimation method for ultrasonic elasticity imaging," *IEEE Transactions on Ultrasonics, Ferroelectrics, and Frequency Control*, vol. 57, no. 4, pp. 866–882, 2010.

[138] J. Jiang and T. J. Hall, "A coupled subsample displacement estimation method for ultrasound-based strain elastography," *Physics in Medicine and Biology*, vol. 60, no. 21, p. 8347, 2015.

[139] H. S. Hashemi and H. Rivaz, "Global time-delay estimation in ultrasound elastography," *IEEE Transactions on Ultrasonics, Ferroelectrics, and Frequency Control*, vol. 64, no. 10, pp. 1625–1636, 2017.

[140] H. S. Hashemia, M. Boilyb, P. A. Martineaub, and H. Rivaza, "Ultrasound elastography: Efficient estimation of tissue displacement using an affine transformation model," in *SPIE Medical Imaging*, pp. 1013903–1013903, International Society for Optics and Photonics, 2017.

[141] M. McCormick, T. Varghese, X. Wang, C. Mitchell, M. Kliewer, and R. Dempsey, "Methods for robust in vivo strain estimation in the carotid artery," *Physics in Medicine and Biology*, vol. 57, no. 22, p. 7329, 2012.

[142] A. Chaudhry, P. Shajudee, and R. Righetti, "Estimation of effective poisson's ratio in non-homogeneous porous media using two ultrasound transducers: A feasibility study," *Imaging in Medicine*, vol. 8, no. 4, pp. 105–111, 2017.

[143] R. L. Maurice, J. Ohayon, Y. Frétigny, M. Bertrand, G. Soulez, and G. Cloutier, "Non-invasive vascular elastography: Theoretical framework," *IEEE Transactions on Medical Imaging*, vol. 23, no. 2, pp. 164–180, 2004.

[144] H. Liebgott, J. Fromageau, J. E. Wilhjelm, D. Vray, and P. Delachartre, "Beamforming scheme for 2d displacement estimation in ultrasound imaging," *EURASIP Journal on Advances in Signal Processing*, vol. 2005, no. 8, p. 932740, 2005.

[145] M. Rao, Q. Chen, H. Shi, T. Varghese, E. Madsen, J. Zagzebski, and T. Wilson, "Normal and shear strain estimation using beam steering on linear-array transducers," *Ultrasound in Medicine & Biology*, vol. 33, no. 1, pp. 57–66, 2007.

[146] M. T. Islam, A. Chaudhry, S. Tang, E. Tasciotti, and R. Righetti, "A new method for estimating the effective poisson's ratio in ultrasound poroelastography," *IEEE Transactions on Medical Imaging*, vol. 37, no. 5, pp. 1178–1191, 2018.

[147] C.-C. Cheng, K.-H. Ho, H.-T. Li, and G.-L. Lin, "Image following using the feature-based optical flow approach," in *Intelligent Control, 2002. Proceedings of the 2002 IEEE International Symposium on*, pp. 350–355, IEEE, 2002.

[148] B. K. Horn and B. G. Schunck, "Determining optical flow," *Artificial Intelligence*, vol. 17, no. 1-3, pp. 185–203, 1981.

[149] E. Meinhardt-Llopis, J. S. Pérez, and D. Kondermann, "Horn-schunck optical flow with a multi-scale strategy," *Image Processing On Line*, vol. 2013, pp. 151–172, 2013.

[150] R. Dugad and N. Ahuja, "Video denoising by combining kalman and wiener estimates," in *Image Processing, 1999. ICIP 99. Proceedings. 1999 International Conference on*, vol. 4, pp. 152–156, IEEE, 1999.

[151] G. Welsh and G. Bishop, "An introduction to the kalman filter," *University of North Carolina at Chapel Hill Chapel Hill NC*, vol. 95, pp. 95–041, 1995.

[152] J. N. Reddy, *An introduction to the finite element method*, vol. 2. McGraw-Hill New York, 1993.

[153] R. Righetti, J. Ophir, and T. A. Krouskop, "A method for generating permeability elastograms and poisson's ratio time-constant elastograms," *Ultrasound in Medicine & Biology*, vol. 31, no. 6, pp. 803–816, 2005.

[154] S. P. Nair, X. Yang, T. A. Krouskop, and R. Righetti, "Performance analysis of a new real-time elastographic time constant estimator," *IEEE Transactions on Medical Imaging*, vol. 30, no. 2, pp. 497–511, 2011.

[155] F. Kallel, C. D. Prihoda, and J. Ophir, "Contrast-transfer efficiency for continuously varying tissue moduli: Simulation and phantom validation," *Ultrasound in Medicine & Biology*, vol. 27, no. 8, pp. 1115–1125, 2001.

[156] S. Tang, A. Chaudhry, N. Kim, J. Reddy, and R. Righetti, "Effect of bone-soft tissue friction on ultrasound axial shear strain elastography," *Physics in Medicine and Biology*, vol. 62, p. 6074, 2017.

[157] A. Sayed, G. Layne, J. Abraham, and O. Mukdadi, "Nonlinear characterization of breast cancer using multi-compression 3d ultrasound elastography in vivo," *Ultrasonics*, vol. 53, no. 5, pp. 979–991, 2013.

[158] T. Varghese and J. Ophir, "Performance optimization in elastography: Multicompression with temporal stretching," *Ultrasonic Imaging*, vol. 18, no. 3, pp. 193–214, 1996.

[159] R. Palomba, A. Parodi, M. Evangelopoulos, S. Acciardo, C. Corbo, E. De Rosa, I. Yazdi, S. Scaria, R. Molinaro, N. T. Furman, *et al.*, "Biomimetic carriers mimicking leukocyte plasma membrane to increase tumor vasculature permeability," *Scientific Reports*, vol. 6, p. 34422, 2016.

[160] R. R. Desai, T. A. Krouskop, and R. Righetti, "Elastography using harmonic ultrasonic imaging: a feasibility study," *Ultrasonic Imaging*, vol. 32, no. 2, pp. 103–117, 2010.

[161] R. Righetti, S. Srinivasan, A. T. Kumar, J. Ophir, and T. A. Krouskop, "Assessing image quality in effective poisson's ratio elastography and poroelastography: I," *Physics in Medicine and Biology*, vol. 52, no. 5, p. 1303, 2007.

[162] M. Bilgen and M. Insana, "Predicting target detectability in acoustic elastography," in *Ultrasonics Symposium, 1997. Proceedings., 1997 IEEE*, vol. 2, pp. 1427–1430, IEEE, 1997.

[163] J. S. Bendat and A. G. Piersol, *Random data: analysis and measurement procedures*, vol. 729. John Wiley & Sons, 2011.

[164] M. Amooshahi and A. Samani, "A fast constrained nonlinear elastography technique: Polyvinyl alcohol (pva) phantom study using the veronda-westman model," in *ASME 2010 International Mechanical Engineering Congress and Exposition*, pp. 815–824, American Society of Mechanical Engineers, 2010.

[165] X. Gong and S. Bansmer, "Horn–schunck optical flow applied to deformation measurement of a birdlike airfoil," *Chinese Journal of Aeronautics*, vol. 28, no. 5, pp. 1305–1315, 2015.

[166] T. Liu, A. Merat, M. Makhmalbaf, C. Fajardo, and P. Merati, "Comparison between optical flow and cross-correlation methods for extraction of velocity fields from particle images," *Experiments in Fluids*, vol. 56, no. 8, p. 166, 2015.

[167] F. Viola and W. F. Walker, "A spline-based algorithm for continuous time-delay estimation using sampled data," *IEEE Transactions on Ultrasonics, Ferroelectrics, and Frequency Control*, vol. 52, no. 1, pp. 80–93, 2005.

[168] J. Folkman, "Clinical applications of research on angiogenesis," *New England Journal of Medicine*, vol. 333, no. 26, pp. 1757–1763, 1995.

[169] F. Sebag, J. Vaillant-Lombard, J. Berbis, V. Griset, J. Henry, P. Petit, and C. Oliver, "Shear wave elastography: a new ultrasound imaging mode for the differential diagnosis of benign and malignant thyroid nodules," *The Journal of Clinical Endocrinology & Metabolism*, vol. 95, no. 12, pp. 5281–5288, 2010.

[170] R. Muthupillai and R. L. Ehman, "Magnetic resonance elastography," *Nature Medicine*, vol. 2, no. 5, pp. 601–603, 1996.

[171] F. Kallel and M. Bertrand, "Tissue elasticity reconstruction using linear perturbation method," *IEEE Transactions on Medical Imaging*, vol. 15, no. 3, pp. 299–313, 1996.

[172] M. Doyley, P. Meaney, and J. Bamber, “Evaluation of an iterative reconstruction method for quantitative elastography,” *Physics in Medicine and Biology*, vol. 45, no. 6, p. 1521, 2000.

[173] M. M. Doyley, S. Srinivasan, S. A. Pendergrass, Z. Wu, and J. Ophir, “Comparative evaluation of strain-based and model-based modulus elastography,” *Ultrasound in Medicine & Biology*, vol. 31, no. 6, pp. 787–802, 2005.

[174] A. A. Oberai, N. H. Gokhale, M. M. Doyley, and J. C. Bamber, “Evaluation of the adjoint equation based algorithm for elasticity imaging,” *Physics in Medicine and Biology*, vol. 49, no. 13, p. 2955, 2004.

[175] J. Fehrenbach, M. Masmoudi, R. Souchon, and P. Trompette, “Detection of small inclusions by elastography,” *Inverse Problems*, vol. 22, no. 3, p. 1055, 2006.

[176] B. Shin, D. Gopaul, S. Fienberg, and H. J. Kwon, “Application of eshelby’s solution to elastography for diagnosis of breast cancer,” *Ultrasonic Imaging*, vol. 38, no. 2, pp. 115–136, 2016.

[177] G. P. Berry, J. C. Bamber, P. S. Mortimer, N. L. Bush, N. R. Miller, and P. E. Barbone, “The spatio-temporal strain response of oedematous and nonoedematous tissue to sustained compression in vivo,” *Ultrasound in Medicine & Biology*, vol. 34, no. 4, pp. 617–629, 2008.

[178] K. Raghavan and A. E. Yagle, “Forward and inverse problems in elasticity imaging of soft tissues,” *IEEE Transactions on Nuclear Science*, vol. 41, no. 4, pp. 1639–1648, 1994.

[179] A. Skovoroda, S. Emelianov, and M. O’donnell, “Tissue elasticity reconstruction based on ultrasonic displacement and strain images,” *IEEE Transactions on Ultrasonics, Ferroelectrics, and Frequency Control*, vol. 42, no. 4, pp. 747–765, 1995.

[180] C. Sumi, A. Suzuki, and K. Nakayama, “Estimation of shear modulus distribution in soft tissue from strain distribution,” *IEEE Transactions on Biomedical Engineering*, vol. 42, no. 2, pp. 193–202, 1995.

[181] D. B. Plewes, J. Bishop, A. Samani, and J. Sciarretta, "Visualization and quantification of breast cancer biomechanical properties with magnetic resonance elastography," *Physics in Medicine and Biology*, vol. 45, no. 6, p. 1591, 2000.

[182] A. A. Oberai, N. H. Gokhale, and G. R. Feijóo, "Solution of inverse problems in elasticity imaging using the adjoint method," *Inverse Problems*, vol. 19, no. 2, p. 297, 2003.

[183] A. Samani, J. Bishop, and D. B. Plewes, "A constrained modulus reconstruction technique for breast cancer assessment," *IEEE Transactions on Medical Imaging*, vol. 20, no. 9, pp. 877–885, 2001.

[184] J. Fehrenbach, "Influence of poisson's ratio on elastographic direct and inverse problems," *Physics in Medicine and Biology*, vol. 52, no. 3, p. 707, 2007.

[185] H. T. Nia, H. Liu, G. Seano, M. Datta, D. Jones, N. Rahbari, J. Incio, V. P. Chauhan, K. Jung, J. D. Martin, *et al.*, "Solid stress and elastic energy as measures of tumour mechanopathology," *Nature Biomedical Engineering*, vol. 1, p. 0004, 2016.

[186] M. Bayat, A. Nabavizadeh, V. Kumar, A. Gregory, M. Insana, A. Alizad, and M. Fatemi, "Automatedin vivosub-hertz analysis of viscoelasticity (save) for evaluation of breast lesions," *IEEE Transactions on Biomedical Engineering*, vol. 65, no. 10, pp. 2237–2247, 2018.

[187] T. Roose, P. A. Netti, L. L. Munn, Y. Boucher, and R. K. Jain, "Solid stress generated by spheroid growth estimated using a linear poroelasticity model," *Microvascular Research*, vol. 66, no. 3, pp. 204–212, 2003.

[188] N. I. Nikolaev, T. Müller, D. J. Williams, and Y. Liu, "Changes in the stiffness of human mesenchymal stem cells with the progress of cell death as measured by atomic force microscopy," *Journal of Biomechanics*, vol. 47, no. 3, pp. 625–630, 2014.

[189] D. C. Stewart, A. Rubiano, K. Dyson, and C. S. Simmons, "Mechanical characterization of human brain tumors from patients and comparison to potential surgical phantoms," *PloS One*, vol. 12, no. 6, p. e0177561, 2017.

[190] D. Thanoon, M. Garbey, N.-H. Kim, and B. Bass, "A computational framework for breast surgery: application to breast conserving therapy," in *Computational Surgery and Dual Training*, pp. 249–266, Springer, 2010.

[191] C. Voutouri, C. Polydorou, P. Papageorgis, V. Gkretsi, and T. Stylianopoulos, "Hyaluronan-derived swelling of solid tumors, the contribution of collagen and cancer cells, and implications for cancer therapy," *Neoplasia*, vol. 18, no. 12, pp. 732–741, 2016.

[192] M. Bilgen and M. F. Insana, "Elastostatics of a spherical inclusion in homogeneous biological media," *Physics in Medicine and Biology*, vol. 43, no. 1, p. 1, 1998.

[193] P. E. Barbone and N. H. Gokhale, "Elastic modulus imaging: on the uniqueness and nonuniqueness of the elastography inverse problem in two dimensions," *Inverse Problems*, vol. 20, no. 1, p. 283, 2004.

[194] C. Jia, S. Alam, R. Azar, and B. Garra, "Estimation of shear modulus ratio between inclusion and background using strain ratios in 2-d ultrasound elastography," *IEEE Transactions on Ultrasonics, Ferroelectrics, and Frequency Control*, vol. 61, no. 4, pp. 611–619, 2014.

[195] F. Kallel, M. Bertrand, and J. Ophir, "Fundamental limitations on the contrast-transfer efficiency in elastography: an analytic study," *Ultrasound in Medicine & Biology*, vol. 22, no. 4, pp. 463–470, 1996.

[196] T. Liu, O. A. Babaniyi, T. J. Hall, P. E. Barbone, and A. A. Oberai, "Noninvasive in-vivo quantification of mechanical heterogeneity of invasive breast carcinomas," *PloS One*, vol. 10, no. 7, p. e0130258, 2015.

[197] T. Mura, *Micromechanics of defects in solids. Mechanics of Elastic and Inelastic Solids, second, revised edition*. Martinus Nijhoff Publishers, Dordrecht, The Netherlands, 1987.

[198] M. T. Islam, S. Tang, C. Liverani, E. Tasciotti, and R. Righetti, "Non-invasive imaging of the young's modulus and poisson's ratio of cancer tumor in vivo," *ArXiv Preprint arXiv:1809.02929*, 2018.

[199] J. Yue, M. Tardieu, F. Julea, L. Chami, O. Lucidarme, X. Maître, and C. Pellot-Barakat, "Comparison between 3d supersonic shear wave elastography and magnetic resonance elastography: a preliminary experimental study," in *Journées RITS 2015*, pp. pp–142, 2015.

[200] S. Cournane, A. Fagan, and J. Browne, "Review of ultrasound elastography quality control and training test phantoms," *Ultrasound*, vol. 20, no. 1, pp. 16–23, 2012.

[201] K. Hollerieth, B. Gaßmann, S. Wagenpfeil, P. Moog, M.-T. Vo-Cong, U. Heemann, and K. F. Stock, "Preclinical evaluation of acoustic radiation force impulse measurements in regions of heterogeneous elasticity," *Ultrasonography*, vol. 35, no. 4, p. 345, 2016.

[202] Y. Qiu, M. Sridhar, J. K. Tsou, K. K. Lindfors, and M. F. Insana, "Ultrasonic viscoelasticity imaging of nonpalpable breast tumors: preliminary results," *Academic Radiology*, vol. 15, no. 12, pp. 1526–1533, 2008.

[203] R. Righetti, J. Ophir, B. S. Garra, R. M. Chandrasekhar, and T. A. Krouskop, "A new method for generating poroelastograms in noisy environments," *Ultrasonic Imaging*, vol. 27, no. 4, pp. 201–220, 2005.

[204] E. Elyas, E. Papaevangelou, E. J. Alles, J. T. Erler, T. R. Cox, S. P. Robinson, and J. C. Bamber, "Correlation of ultrasound shear wave elastography with pathological analysis in a xenografic tumour model," *Scientific Reports*, vol. 7, p. 165, 2017.

[205] A. Tahmasbi, F. Saki, and S. B. Shokouhi, "Classification of benign and malignant masses based on zernike moments," *Computers in Biology and Medicine*, vol. 41, no. 8, pp. 726–735, 2011.

[206] J. Jurvelin, M. Buschmann, and E. Hunziker, "Optical and mechanical determination of poisson's ratio of adult bovine humeral articular cartilage," *Journal of Biomechanics*, vol. 30, no. 3, pp. 235–241, 1997.

[207] J. Ophir, I. Cespedes, B. Garra, H. Ponnekanti, Y. Huang, and N. Maklad, "Elastography: ultrasonic imaging of tissue strain and elastic modulus in vivo," *European Journal of Ultrasound*, vol. 3, no. 1, pp. 49–70, 1996.

[208] E. K. Rofstad, K. Galappathi, and B. S. Mathiesen, "Tumor interstitial fluid pressure—a link between tumor hypoxia, microvascular density, and lymph node metastasis," *Neoplasia*, vol. 16, no. 7, pp. 586–594, 2014.

[209] J. R. Less, M. C. Posner, Y. Boucher, D. Borochovitz, N. Wolmark, and R. K. Jain, "Interstitial hypertension in human breast and colorectal tumors," *Cancer Research*, vol. 52, no. 22, pp. 6371–6374, 1992.

[210] S. D. Nathanson and L. Nelson, "Interstitial fluid pressure in breast cancer, benign breast conditions, and breast parenchyma," *Annals of Surgical Oncology*, vol. 1, no. 4, pp. 333–338, 1994.

[211] B. D. Curti, W. J. Urba, W. G. Alvord, J. E. Janik, J. W. Smith, K. Madara, and D. L. Longo, "Interstitial pressure of subcutaneous nodules in melanoma and lymphoma patients: changes during treatment," *Cancer Research*, vol. 53, no. 10, pp. 2204–2207, 1993.

[212] R. Gutmann, M. Leunig, J. Feyh, A. E. Goetz, K. Messmer, E. Kastenbauer, and R. K. Jain, "Interstitial hypertension in head and neck tumors in patients: correlation with tumor size," *Cancer Research*, vol. 52, no. 7, pp. 1993–1995, 1992.

[213] M. F. Milosevic, A. W. Fyles, R. Wong, M. Pintilie, M.-C. Kavanagh, W. Levin, L. A. Manchul, T. J. Keane, and R. P. Hill, "Interstitial fluid pressure in cervical carcinoma," *Cancer*, vol. 82, no. 12, pp. 2418–2426, 1998.

[214] Y. Boucher, L. T. Baxter, and R. K. Jain, "Interstitial pressure gradients in tissue-isolated and subcutaneous tumors: implications for therapy," *Cancer Research*, vol. 50, no. 15, pp. 4478–4484, 1990.

[215] G. R. DiResta, J. Lee, S. M. Larson, and E. Arbit, "Characterization of neuroblastoma xenograft in rat flank. i. growth, interstitial fluid pressure, and interstitial fluid velocity distribution profiles," *Microvascular Research*, vol. 46, no. 2, pp. 158–177, 1993.

[216] J. K. Burton III, *Theoretical models for drug delivery to solid tumors*. PhD thesis, The University of Arizona, 2016.

[217] F. Iranmanesh and M. A. Nazari, "Finite element modeling of avascular tumor growth using a stress-driven model," *Journal of Biomechanical Engineering*, vol. 139, no. 8, p. 081009, 2017.

[218] S. Benzekry, C. Lamont, A. Beheshti, A. Tracz, J. M. Ebos, L. Hlatky, and P. Hahnfeldt, "Classical mathematical models for description and prediction of experimental tumor growth," *PLoS Computational Biology*, vol. 10, no. 8, p. e1003800, 2014.

[219] Y. Jiang, J. Pjesivac-Grbovic, C. Cantrell, and J. P. Freyer, "A multiscale model for avascular tumor growth," *Biophysical Journal*, vol. 89, no. 6, pp. 3884–3894, 2005.

[220] J. Laible, D. Pflaster, B. Simon, M. Krag, M. Pope, and L. Haugh, "A dynamic material parameter estimation procedure for soft tissue using a poroelastic finite element model," *Journal of Biomechanical Engineering*, vol. 116, no. 1, pp. 19–29, 1994.

[221] C.-H. Wang and J. Li, "Three-dimensional simulation of igg delivery to tumors," *Chemical Engineering Science*, vol. 53, no. 20, pp. 3579–3600, 1998.

[222] C.-H. Wang, J. Li, C. S. Teo, and T. Lee, "The delivery of bcnu to brain tumors," *Journal of Controlled Release*, vol. 61, no. 1, pp. 21–41, 1999.

[223] J. Zhao, H. Salmon, and M. Sarntinoranont, "Effect of heterogeneous vasculature on interstitial transport within a solid tumor," *Microvascular Research*, vol. 73, no. 3, pp. 224–236, 2007.

[224] M. Soltani and P. Chen, "Numerical modeling of fluid flow in solid tumors," *PloS One*, vol. 6, no. 6, p. e20344, 2011.

[225] M. Soltani and P. Chen, "Numerical modeling of interstitial fluid flow coupled with blood flow through a remodeled solid tumor microvascular network," *PloS One*, vol. 8, no. 6, p. e67025, 2013.

[226] L. Cattaneo and P. Zunino, "Computational models for fluid exchange between microcirculation and tissue interstitium," *Networks & Heterogeneous Media*, vol. 9, no. 1, pp. 135–159, 2014.

[227] M. Soltani and P. Chen, "Effect of tumor shape and size on drug delivery to solid tumors," *Journal of Biological Engineering*, vol. 6, no. 1, p. 4, 2012.

[228] M. Sefidgar, M. Soltani, K. Raahemifar, H. Bazmara, S. M. M. Nayinian, and M. Bazargan, "Effect of tumor shape, size, and tissue transport properties on drug delivery to solid tumors," *Journal of Biological Engineering*, vol. 8, no. 1, p. 12, 2014.

[229] M. Sefidgar, M. Soltani, H. Bazmara, M. Mousavi, M. Bazargan, and A. Elkamel, "Interstitial flow in cancerous tissue: effect of considering remodeled capillary network," *J Tissue Sci Eng S*, vol. 4, p. 2, 2014.

[230] M. Sefidgar, M. Soltani, K. Raahemifar, M. Sadeghi, H. Bazmara, M. Bazargan, and M. M. Naeenian, "Numerical modeling of drug delivery in a dynamic solid tumor microvasculature," *Microvascular Research*, vol. 99, pp. 43–56, 2015.

[231] A. Chaudhry, N. Kim, G. Unnikrishnan, S. Nair, J. Reddy, and R. Righetti, "Effect of interstitial fluid pressure on ultrasound axial strain and axial shear strain elastography," *Ultrasonic Imaging*, vol. 39, no. 2, pp. 137–146, 2017.

[232] D. Simulia, "Abaqus version 6.6 documentation," *Dassault Systems Simulia Corp, Providence, RI, USA*, 2006.

[233] R. Righetti, J. Ophir, A. T. Kumar, and T. A. Krouskop, "Assessing image quality in effective poisson's ratio elastography and poroelastography: Ii," *Physics in Medicine & Biology*, vol. 52, no. 5, p. 1321, 2007.

[234] S. Locke, *The effect of interstitial pressure on tumour stiffness*. PhD thesis, University of Toronto (Canada), 2014.

[235] S. R. Chary and R. K. Jain, "Direct measurement of interstitial convection and diffusion of albumin in normal and neoplastic tissues by fluorescence photobleaching," *Proceedings of the National Academy of Sciences*, vol. 86, no. 14, pp. 5385–5389, 1989.

[236] T. Belytschko, J. S.-J. Ong, W. K. Liu, and J. M. Kennedy, "Hourglass control in linear and nonlinear problems," *Computer Methods in Applied Mechanics and Engineering*, vol. 43, no. 3, pp. 251–276, 1984.

[237] K. F. Chernykh, *An introduction to modern anisotropic elasticity*. Begell House, 1998.

[238] W. Zhan, W. Gedroyc, and X. Y. Xu, "The effect of tumour size on drug transport and uptake in 3-d tumour models reconstructed from magnetic resonance images," *PloS One*, vol. 12, no. 2, p. e0172276, 2017.

[239] Y. Boucher, H. Salehi, B. Witwer, G. Harsh IV, and R. Jain, "Interstitial fluid pressure in intracranial tumours in patients and in rodents," *British Journal of Cancer*, vol. 75, no. 6, p. 829, 1997.

[240] L. E. Gerlowski and R. K. Jain, "Microvascular permeability of normal and neoplastic tissues," *Microvascular Research*, vol. 31, no. 3, pp. 288–305, 1986.

[241] S. Goel, D. G. Duda, L. Xu, L. L. Munn, Y. Boucher, D. Fukumura, and R. K. Jain, "Normalization of the vasculature for treatment of cancer and other diseases," *Physiological Reviews*, vol. 91, no. 3, pp. 1071–1121, 2011.

[242] T. Hompland, C. Ellingsen, K. M. Øvrebø, and E. K. Rofstad, "Interstitial fluid pressure and associated lymph node metastasis revealed in tumors by dynamic contrast-enhanced mri," *Cancer Research*, vol. 72, no. 19, pp. 4899–4908, 2012.

[243] R. K. Jain and T. Stylianopoulos, "Delivering nanomedicine to solid tumors," *Nature Reviews Clinical Oncology*, vol. 7, no. 11, p. 653, 2010.

[244] S. Ferretti, P. R. Allegrini, M. M. Becquet, and P. M. McSheehy, "Tumor interstitial fluid pressure as an early-response marker for anticancer therapeutics," *Neoplasia*, vol. 11, no. 9, pp. 874–881, 2009.

[245] J. Fang, H. Nakamura, and H. Maeda, "The epr effect: unique features of tumor blood vessels for drug delivery, factors involved, and limitations and augmentation of the effect," *Advanced Drug Delivery Reviews*, vol. 63, no. 3, pp. 136–151, 2011.

APPENDIX A

LIST OF PUBLICATIONS

A.1 Journal articles

1. Islam, M.T., Reddy, J.N. and Righetti, R., 2018. A model-based approach to investigate the effect of elevated interstitial fluid pressure on strain elastography. *Physics in Medicine & Biology*, 63(21), p.215011.

2. Islam, M.T. and Righetti, R.,"A novel filter for estimation of fluid pressure and fluid velocity". *Computers in Biology and Medicine*, 101, pp.90-99.

3. Tang S., Chaudhry A., Shajudeen P. S., Islam M.T., Kim N., Cabrera F. J., Reddy J. N., Tasciotti E. and Righetti, R. "A model-based approach to investigate the effect of a long bone fracture on ultrasound strain elastography" 2018. Accepted in *IEEE Transactions on Medical Imaging*.

4. Islam, M.T., Reddy, J.N. and Righetti, R. "An analytical poroelastic model of a non-homogeneous medium under creep compression for ultrasound poroelastography applications - Part I" 2018. In press, *Journal of Biomechanical Engineering*.

5. Islam, M.T., Reddy, J.N. and Righetti, R. "An analytical poroelastic model of a non-homogeneous medium under creep compression for ultrasound poroelastography applications - Part II" 2018. In press, *Journal of Biomechanical Engineering*.

6. Islam, M.T., Chaudhry, A., Unnikrishnan, G., Reddy, J.N. and Righetti, R., 2018. An analytical model of tumors with higher permeability than surrounding tissues for ultrasound elastography imaging. *Journal of Engineering and Science in Medical Diagnostics and Therapy*, 1(3), p.031006.

7. Islam, M.T., Chaudhry, A., Tang, S., Tasciotti, E. and Righetti, R., 2018. A new method for

estimating the effective Poisson's ratio in ultrasound poroelastography. *IEEE transactions on medical imaging*, 37(5), pp.1178-1191.

8. Islam, M.T., Chaudhry, A., Unnikrishnan, G., Reddy, J.N. and Righetti, R., 2018. An analytical poroelastic model for ultrasound elastography imaging of tumors. *Physics in Medicine & Biology*, 63(2), p.025031.

A.2 Journal articles under review

1. Islam, M.T., Tasciotti, E. and Righetti, R. "Estimation of vascular permeability in irregularly shaped cancers using ultrasound poroelastography", 2018, under review in *Medical Image Analysis*.

2. Islam, M.T., Chaudhry, A. and Righetti, R. "A robust method to estimate the time constant of elastographic parameters", 2018, under review in *IEEE Transactions on Medical Imaging*.

3. Islam, M.T., Chaudhry, A. and Righetti, R. "An analysis of the error associated to single and double exponential approximations of theoretical poroelastic models", 2018, under review in *Ultrasonic Imaging*.

4. Islam, M.T., Tang, S., Tasciotti, E. and Righetti, R. "Non-invasive imaging of Young's modulus and Poisson's ratio in cancers in vivo", 2018, under review in *IEEE Transactions on Biomedical Engineering*.

5. Islam, M.T., Tasciotti, E. and Righetti, R.,"Non-invasive assessment of the spatial and temporal distributions of mechanopathological parameters in cancers in vivo", 2018, under review in *IEEE Transactions on Medical Imaging*.

6. Islam, M.T. and Righetti, R.,"Estimation of mechanical parameters in cancers by empirical orthogonal function analysis of poroelastography data", 2018, under review in *IEEE Transactions on Medical Imaging*.

7. Tang S., Sabonghy E., Islam M.T., Shajudeen P. S., Chaudhry, A., Tasciotti E. and Righetti, R. “Assessment of the long bone inter-fragmentary gap size in ultrasound strain elastograms", 2018, under review in *Physics in Medicine & Biology*.